University of Southampton
Faculty of Social and Human Sciences
School of Mathematics

Seismology of Adolescent General Relativistic Neutron Stars

by

Christian Jürgen Krüger

Thesis for the degree of Doctor of Philosophy

July 2015

University of Southampton

ABSTRACT

Faculty of Social and Human Sciences
School of Mathematics

Doctor of Philosophy

Seismology of Adolescent General Relativistic Neutron Stars

by Christian Jürgen Krüger

Neutron stars are a unique laboratory for exciting physics under extreme conditions; after their birth in a violent supernova explosion or due to accretion of matter or other operative mechanisms during their lifetime, they are subject to oscillations. The identification of such oscillations, via their generated gravitational waves or their imprint on electromagnetic signals, establishes the field of neutron star asteroseismology and allows us to probe the otherwise unobservable interior of these stars.

In this study, we take the first steps towards the ambitious aim of developing the computational technology to determine accurate spectra of lifelike neutron stars. Starting from the widely used Detweiler & Lindblom formulation of the equations governing perturbations of a perfect fluid star, we extend this formalism to account for density discontinuities associated with distinct phase-transitions, an internal composition gradient, thermal pressure, the elastic crust and superfluidity in an npeμ-core described by a modern equation of state. The latter two require different sets of equations for their description and we show their derivation in detail, starting from a fundamental action principle. Furthermore, snapshots of detailed cooling simulations allow us to study the impact of thermal effects on the various oscillation modes.

We discover a new branch of short-lived w-modes; even though our results are unambiguous, there is the option that these modes are an artefact of the numerical algorithms employed. The simulations for single fluid stars show evidence for all expected oscillation modes and we can successfully extract the thermal evolution of the spectrum as the star cools. The multi-fluid calculations reveal the existence of g-modes in superfluid neutron star cores if at least one of fluids features an internal stratification. During the short period of time where there are two individual superfluid regions, we find evidence for two independent sets of superfluid modes. Our code proves to possess very high accuracy, be robust and is ready for extension to include more physics.

Contents

List of Figures

List of Tables

Declaration of Authorship

I, Christian Jürgen Krüger, declare that this thesis entitled *Seismology of Adolescent General Relativistic Neutron Stars* and the work presented in it are my own and has been generated by me as the result of my own original research. I confirm that:

- this work was done wholly or mainly while in candidature for a research degree at this University;
- where any part of this thesis has previously been submitted for a degree or any other qualification at this University or any other institution, this has been clearly stated;
- where I have consulted the published work of others, this is always clearly attributed;
- where I have quoted from the work of others, the source is always given. With the exception of such quotations, this thesis is entirely my own work;
- I have acknowledged all main sources of help;
- where the thesis is based on work done by myself jointly with others, I have made clear exactly what was done by others and what I have contributed myself;
- parts of this work have been published as: [1]

Signed:.....

Date:.....

Acknowledgements

I wish to take this opportunity to express my gratitude to a number of people without whom this thesis would not exist.

First and foremost, I wish to acknowledge my supervisor, Nils Andersson, for all his help throughout. I thank him for his fruitful guidance, unwavering patience and detailed explanations which have deepened my understanding of relativity in general and that of neutron stars in particular. He has remained friendly and supportive, even when things deviated from their intended path.

I wish to thank Ian Hawke; his thoughtful and detailed criticism has helped me improve my communication skills.

In addition, I would like to thank my two examiners, Ian Jones and Sanjay Reddy, for the thorough reading of my thesis and the very constructive suggestions and corrections.

The relativity group in Southampton has been a very enjoyable place to work; the entire community has been very welcoming and supportive. Among the group members, I would especially like to thank—in alphabetical order—Sam Lander for numerous coffee breaks of a very different kind, Stephanie Erickson for profound discussions on banalities, Stuart Wells for copious time spent on das climbing wall and Yafet Sanchez for entropic conversations regarding geometry and other things.

I also would like to thank Niki and Ian Reeves who I stayed with during my time in England and who were very supportive and made my entire stay very enjoyable.

Last but by no means least, my parents, Gisela and Jürgen, deserve special attention. They have always supported me in all my endeavours throughout all of my life, no matter what they were. Thank you very much for your unwavering and invaluable encouragement and support.

Chapter 1

Introduction

Neutron stars are a unique laboratory for exciting physics under extreme conditions; nowhere else can we test the behaviour of matter at densities several times the nuclear density. Due to their high compactness, a general relativistic treatment is inevitable for an accurate investigation of their dynamics and it is believed that their vibrations serve as a continuous source for gravitational waves. These waves, predicted by Einstein's theory of gravity, are a purely relativistic effect in the sense that they have no Newtonian counterpart and their existence has as yet been proved only indirectly, e.g. by the observation of the binary pulsar PSR B1913+16 in 1974 [2, 3]; this system is also called *Hulse-Taylor binary pulsar* after its discoverers who were awarded with the Nobel Prize in 1993. A direct detection of gravitational waves, however, is still pending. The hope is that their direct observation will open up the new field of *gravitational wave asteroseismology* which will help unveil details of the internal structure of distant stars.

The larger field of asteroseismology is a part of modern astronomy that studies stellar oscillations in order to gain further insight into the internal structure of stars. Such oscillations penetrate the star to different depths and thus can provide information about the otherwise unobservable interior of stars. This might be the density profile of the region in which the wave is travelling or a hint about the chemical composition.

Asteroseismology can be traced back over nearly one century to the realisation in 1918 that the periodic changes in the luminosity of Delta Cephei discovered by John Goodricke in 1786 are the result of radial pulsations [4, 5]. A vast number of pulsating stars have been discovered ever since; the most famous of them being the Sun for which it is known that pressure modes and probably modes of other classes are excited. The impressive success of so-called helioseismology, a branch of asteroseismology, fuelled research in these fields; the combination of theoretical models and observations of the Sun's oscillations have enabled researchers to deduce a detailed model of its internal structure. We have a precise knowledge of, for example, the sound speed at different depths or the Sun's rotational profile [6].

The observation of oscillations of neutron stars is disproportionately more difficult;

not only are these stars considerably smaller, they are also much less bright since they do not have powerful heat sources as a stellar remnant. Gravitational waves emitted by these stars are a promising source of information; unlike electromagnetic waves which are scattered and absorbed during their travel from source to detector, gravitational waves propagate virtually unaffected through the entirety of the universe. However, since matter couples only very weakly to space-time, the amount of gravitational wave radiation is usually quite limited and therefore hard to detect. Five decades have passed since the first attempts were made by Weber in the 1960s to detect gravitational waves. Nowadays, there are several modern gravitational wave detectors online (VIRGO, GEO600 and Advanced LIGO [under construction]) which are huge Michelson-Morley interferometers with two several kilometre long orthogonal arms. The strength of the waves is usually quantified in the relative change of spatial separation, $h = \Delta l/l$; however, even at sensitivities of $h \approx 10^{-22}$ of the present detectors in relevant frequency bands, no gravitational wave signal has been detected as of today. There is strong hope that with the improved versions Advanced LIGO and Advanced VIRGO coming online within the next couple of years, finally gravitational waves will be observed. Such detection would be a significant step towards gravitational wave asteroseismology and finally verify a central prediction of the 100 years old theory of general relativity. The identification of neutron star oscillations, in particular their frequency and damping time, will help us understand their internal structure and to adjust our current theoretical models of neutron star matter.

The detection of continuous gravitational wave signals emitted by neutron stars is not the only channel through which we may detect oscillations of these compact objects; we also expect them to have an impact on signals in the electromagnetic spectrum. The first evidence for such observations are the quasiperiodic oscillations (hereafter referred to as QPOs) seen in the X-ray tails that accompany magnetar giant flares. Magnetar giant flares are highly energetic subsecond duration bursts of electromagnetic radiation of soft gamma repeaters (which are believed to be magnetars) in the soft gamma and hard X-ray spectrum. As of today, three giant flares have been observed: one of SGR 0526-66 in 1979, one of SGR 1900+14 in 1998 and one of SGR 1806-20 in 2004. The analysis of the latter two revealed a number of QPOs in the decaying X-ray tail; whilst most of them have frequencies of a few tens of Hertz, oscillations of up to about 1.8 kHz were discovered. These frequencies, in particular the ones with longer time periods, fit those of torsional oscillations of the solid crust well; however, it was soon established that not all of the observed QPOs can be explained purely by crustal oscillations as the first overtones of these already have frequencies in the kHz regime [7, 8]. Other models are necessary in order to fit the observations, the most promising being Alfvén oscillations of magnetised neutron stars. The observations of these QPOs, which are promising candidates for the first ever observations of oscillations of neutron stars, are very exciting: not only do they provide the first credible example of actual neutron

star asteroseismology, they also emphasise the significance of oscillation modes which we would not expect to detect via their emission of gravitational waves due to their extremly weak coupling to space-time.

The detection of these QPOs has triggered a series of theoretical studies, in particular regarding torsional oscillations of the crust and Alfvén modes in magnetars, the latter of which we will briefly summarise in the following. While the dynamics of non-rotating neutron stars without magnetic field can be investigated by the solution of one-dimensional ordinary differential equations, the study of magnetised neutron stars is somewhat more difficult since the presence of the magnetic field breaks the spherical symmetry of the physical system and requires more involved calculations. Levin pointed out based on toy model simulations that the Alfvén modes of magnetars could form a continuum [9] and another subsequent toy model calculation indicated that the edges or turning point of the continuum could correspond to long-lived QPOs [10]. Sotani et al. have performed more detailed two-dimensional calculations in the framework of general relativity but ignoring the solid crust [11]; they find different series of oscillation modes in the Fourier spectrum where the frequencies depend on the location within the star; this is to be expected as the frequency of Alfvén modes varies throughout the star. For a particular location, the identified oscillation modes have frequencies with nearly integer multiples of the respective fundamental frequency. Subsequently, they extended the calculations to study the effect of an entirely type I superconducting core that expels the magnetic field and confines it to the crust [12]. They find that such a magnetic field geometry strongly affects the torsional modes and shifts their frequencies to higher values, thereby ruling out such a geometry as the frequency shift makes it impossible to explain all of the identified modes in the giant flare of SGR 1806-20. Colaiuda et al. thoroughly examined the system of partial differential equations describing the Alfvén modes and discovered a coordinate transformation that not only reduces the number of dimensions by one but also removed the necessity to use artificial viscosity in order to achieve a stable time evolution of the perturbations [13]. All of these findings cited above have been qualitatively confirmed through non-linear simulations by Cerdá-Durán et al. [14]. Whilst the above mentioned calculations were regarding poloidal or mixed poloidal-toroidal fields, Lander et al. investigated the oscillations of rotating neutron stars with purely toroidal fields in Newtonian theory on consistent background configurations, i.e. taking into account the deformation of the equilibrium model due to rotational or magnetic effects [15]. It was only recently when Gabler et al. built a magnetar model that includes the crust, superfluidity in the core and a magnetic field such that the whole range of observed QPOs in magnetar giant flares, those with low frequencies ($f < 150\,\mathrm{Hz}$) as well as high frequencies ($f > 500\,\mathrm{Hz}$), can be explained by axisymmetric, torsional magnetoelastic oscillations [16].

These exciting observations in the electromagnetic spectrum, paired with the prospect of an advanced generation of gravitational wave detectors coming online soon, provide

strong motivation for the improvement of the theoretical modelling of neutron star dynamics towards realistic simulations. However, this is a complicated venture, due to, firstly, the rich catalogue of physical aspects to be considered, and secondly, the still remaining uncertainties regarding in particular the deep core (at several times the nuclear saturation density).

The history of relativistic seismology spans nearly half a century and has been pioneered by Thorne & Campolattoro in the late 1960s who derived for the first time the equations governing vibrations of a perfect fluid star in first order perturbation theory [17]. For many years, the focus lay on the mathematical formulation of the problem as well as the investigation of qualitative features of the spectra of such stars rather than a detailed consideration of the involved physics. In fact, most of the literature is on perfect fluid stars assuming a highly simplified polytropic equation of state that resembles a realistic one only in the bulk properties. This is, nevertheless, a natural start towards the understanding of the increasingly difficult problem and the studies on the simple models revealed several fundamental facts of the stellar spectrum. The first proof of existence of the fundamental f-mode and the pressure restored p-modes by Detweiler & Lindblom came along with another milestone, namely the reduction of the equations to a fourth order system [18, 19]. While these modes were well-known from studies conducted in Newtonian theory (see e.g. Cowling [20] who also introduced the nomenclature for the different classes of modes), the fundamentally new class of gravitational wave w-modes was discovered by Kokkotas & Schutz in 1992 when they extended the mode search for strongly damped modes [21] for which numerical challenges concerning the exterior solution had to be overcome. While they adopted a method that had originally been developed for solutions of problems within the framework of quantum mechanics, their findings were confirmed by Leins et al. [22] by borrowing a method from black hole calculations; furthermore, they located another small set of so-called w_{II}-modes at even shorter damping times than the w-modes.

The spectrum of a general relativistic perfect fluid is hereby exhausted; new classes of modes enter the spectrum only upon the inclusion of more physics. A naturally existing composition gradient leads to the rise of gravity g-modes due to buoyancy in the core which were first identified by Reisenegger & Goldreich [23]; the nature of these modes has numerically been studied to more detail in simple (rotating) neutron star models using polytropic equations of state in Newtonian theory [24] as well as general relativity [25]. More complex neutron star models have not yet been considered in detail regarding composition g-modes. Closely related are the interface i-modes which arise due to density discontinuities associated with phase transitions that occur predominantly in the crust [26, 27, 28, 29, 30]. In a sufficiently old star, when the crust has crystallised, it supports shear stresses and hence the spectrum will be enriched by shear modes; the equations describing crustal oscillations have been laid out by Schumaker & Thorne [31] for axial perturbations and by Finn [32] for the polar

counterpart. The first numerical solutions (in yet another formulation) for torsional modes were presented by Samuelsson & Andersson [7] for the Cowling approximation and a bit later by the same authors even taking a superfluid neutron component (see following explanation) permeating the crust into account [33]. Furthermore, it is widely accepted that parts of a neutron star's core and its inner crust exhibit superfluidity at sufficiently low temperatures; there are already constraints on the superfluid pairing gaps (or equivalently, the critical temperatures) from the observed real-time cooling of the remnant in Cassiopeia A [34]. The density dependence of the critical temperature for the onset of superfluidity causes a layering of the star where different regions of the star require a different mathematical description (like in the case of the elastic crust); the mandatory multi-fluid description for neutron stars has been developed by Comer et al. [35] who discovered a second set of superfluid modes, which bear similarity to the pressure modes, in an entirely two-fluid star. This description was later refined by deriving appropriate junction conditions between layers of different nature within the star to account for a perfect fluid envelope as well as a single fluid (central) core [36, 37] where the latter also have taken further steps towards the investigation of the temperature dependence of the superfluid modes and the inclusion of more sophisticated entrainment models. While a zoo of different realistic equations of state has been proposed over the decades, they all came with the drawback of being applicable to single fluid stars only. In order to study oscillations of a realistic neutron star, access to a realistic equation of state which accounts for the two-fluid nature of a neutron star's core, including information about the superfluid energy gaps and the entrainment, is a basic requirement. It was only recently, when Chamel provided the first ever consistent equation of state model including entrainment [38]; this PhD project will be the first to use this modern equation of state for the numerical simulation of oscillations of multi-fluid neutron stars.

A real neutron star features even more physics which is essential for a full grasp of its dynamics: it supports a strong magnetic field (see discussion above) and it will certainly rotate. Rotation has a severe impact on a neutron star's spectrum and its dynamics; first of all, the star loses its spherical symmetry owing to the centrifugal force which enforces completely different numerical techniques for the solution of the perturbation equations unless the slow-rotation approximation (in which the star is assumed to be spherically symmetric) is applied. The oscillations of fast rotating (and highly deformed) stars are investigated by time evolutions that are subject to numerical instabilities which is why such calculations have been performed only using numerous simplifications as of today; most notably the Cowling approximation, in which perturbations of the space-time are neglected, is widely applied. Jones et al. [39] were the first to develop a numerical code that stably evolves the perturbations of a fast rotating Newtonian polytrope in time. For the general relativistic counterpart, some numerical difficulties had to be overcome in order to achieve a stable evolution [40]. In

both studies, the effect of rotation on the fundamental mode, i.e. the breaking of the degeneracy at zero spin frequency, as well as the emerging of the inertial modes, which are due to the Coriolis force, have been considered. Both codes were later extended to account for stratification [24, 25] and qualitatively similar results have been found; as the star spins faster, the buoyancy driving the g-modes becomes increasingly dominated by the Coriolis force and the modes of both classes approach each other. Effort has also been made to investigate inertial modes in non-linear simulations [41]. Rotating stars also have the freedom to rotate differentially; this allows to store considerably more rotational energy in the neutron star than in a rigidly rotating star. The effect of differential rotation on the so-called *f-mode instability* has been investigated in the framework of general relativity [42]; this CFS instability, discovered by Chandrasekhar, Friedman & Schutz [43, 44], of the fundamental mode may drive a fast rotating neutron star unstable due to the emission of gravitational waves given that the star's spin frequency exceeds a certain threshold. Subsequently, this code has been extended by Doneva et al. [45] for the use with realistic equations of state in order to investigate the f-mode instability window in more realistic neutron stars. There are also a few studies of neutron star oscillations in full non-linear general relativity, however, their number is still very limited due to the computationally extremely costly simulations; radial oscillations of fast and differentially rotating stars in the Cowling approximation have been investigated by Stergioulas et al. [46] whereas Zink et al. [47] studied the CFS instability of the non-axisymmetric fundamental mode. Dimmelmeier et al. [48] considered axisymmetric modes in differentially rotating stars in the so-called conformal flatness approximation. If one is interested only in slowly rotating neutron stars, the deviation from spherical can be neglected, and thus the angular dependence of the problem vanishes. Such calculations have been performed regarding the rotational or r-mode (which is generically unstable due to the CFS instability) [49, 50] and slowly and differentially rotating stars have been studied, too [51, 52].

We take these studies as a starting point to take the first steps towards true realism and to develop a comprehensive numerical code. The inclusion of all above mentioned physical aspects would go well beyond the scope of this thesis, which is why we will constrain ourselves to the following: we will start from the classic fluid formalism of Detweiler & Lindblom [19] and extend it to account for density discontinuities associated with distinct phase transitions, interior composition gradients, thermal pressure, the elastic crust and superfluidity in the core. The determination of the elastic or superfluid regions requires a temperature profile of our model neutron star; in order to remain consistent, we use snapshots of detailed cooling simulations based on our actual neutron star model provided by Ho [53]. With this thermal evolution of our neutron star at hand, we are able to track the different modes as the star matures. This exercise sheds light on the influence of thermal effects on the various oscillations modes of the star.

The thesis will essentially be divided into two substantial chapters which are preceded by Chapter 2 that is devoted to the construction of our background model and the equation of state we use.

In the following Chapter 3, we discuss the extension of the perfect fluid formalism provided by Detweiler & Lindblom [19] and the derivation of perturbation equations for the elastic crust for both polar and axial perturbations. We also revise the junction condition problem and discuss associated puzzling findings. The last part of this chapter comprises the results; firstly, we compare our new code against literature values and perform a comprehensive high resolution scan for w-modes in the first quadrant of the complex plane, after which we progress to increase the complexity of our neutron star model until we reach the stage where we can extract the time evolution of the spectrum of a single fluid neutron star.

The next big Chapter 4 covers the multi-fluid formalism and our subsequent results. We start by revisiting an action principle from which we derive the equations of motion; we show in detail how to account for leptons in the core which are electromagnetically locked to the protons. We then produce a comprehensive matrix of junction conditions for all possible cases. The results section again starts with sanity checks of our code for different special cases, after which we turn to the low frequency spectrum in multi-fluid stars and explain why such stars do support g-modes. Last, we produce the time evolution of the spectrum of a multi-fluid star.

In Chapter 5, we conclude our work and provide an outlook on future research.

1.1 Conventions

- Greek indices run from 0 to 3 and denote space-time components (with 0 being the time component), Latin indices run from 1 to 3 and denote spatial components. We use the Einstein sum convention for these indices.

- Latin indices in roman typeset, e.g. $\mathrm{n}, \mathrm{p}, \mathrm{x}, \ldots$ are constituent indices. We place them liberally upstairs or downstairs in order to avoid cluttering and they do not obey any kind of summation convention.

- The signature of the metric is $(-,+,+,+)$ which means that time-like vectors have a negative length.

- Unless stated otherwise, we carry out our calculations in units in which $G = c = M_\odot = 1$. Whenever appropriate, we quote physical quantities in cgs-units; occasionally we use MeV.

- Covariant derivatives of an arbitrary quantity f with respect to x^μ are written as $\nabla_\mu f$, and we occasionally use the abbreviations $\partial_\mu f$ or $f_{,\mu}$ for partial derivatives.

- We abbreviate radial derivatives with a prime, $f' = \partial_r f$, and temporal derivatives with a dot, $\dot{f} = \partial_t f$.
- For brevity, we will occasionally make use of the following short-hand notation regarding tensor indices: for any tensor $t_{\mu\nu}$, round brackets denote symmetrisation, $2t_{(\mu\nu)} := t_{\mu\nu} + t_{\nu\mu}$, whereas square brackets are used to denote anti-symmetrisation, $2t_{[\mu\nu]} := t_{\mu\nu} - t_{\nu\mu}$.

Chapter 2

The Background Model

The investigation of oscillations of neutron stars is very complicated. First, because many different physical properties have to be taken into account, second, due to their high compactness it is essential to encounter the problem within the framework of general relativity. A well-known feature of these equations is their non-linearity which poses different numerical challenges. However, since oscillations of a neutron star are thought to be small, a widely used approach is to linearise the equations. Physically, the problem has been reduced to studying the evolution of small perturbation on a star in equilibrium. We will generally refer to the equilibrium as the *background configuration* or short *the background*; mathematically, this removes the difficulty in dealing with non-linear equations and allows us to consider the background and the perturbations separately—their equations are fully decoupled.

In this chapter, we will describe the background model that we will use for our studies. Aside from the fundamental equations describing the general structure of the star, the essential piece that strongly affects the bulk properties of the star like mass and radius is the equation of state (EoS hereafter). It connects pressure and energy density in a one-to-one relation, $p = p(\rho)$; while this relation is fairly well known for lower densities which we find in the crust of the star, there are large uncertainties at high densities in the deep core of neutron stars at several times the nuclear saturation density. These uncertainties stem from our lack of knowledge of the behaviour of matter at these extreme densities and they become apparent by the fact that many different EoSs for the core of a neutron star have been proposed over the past decades. The resulting background configurations (as well as the oscillation modes) may obviously vary significantly when a different EoS is employed. Many studies on neutron star oscillations use several different EoSs and investigate differences and similarities in the results. However, our study has a different aim: Our focus lies on demonstrating how our current understanding of physics relevant for neutron stars can be implemented and incorporating more physics in a single simulation rather than trying to calculate precise (as in realistic) oscillation frequencies. We are aware that the oscillation frequencies we

calculate can only be exemplary as the EoS is still largely unknown. We will, therefore, treat the EoS as a parameter in our study that can easily be exchanged once a more accurate EoS has been developed. Until then, we choose one particular EoS that suits our problem best and hope that it is somewhat realistic.

Apart from the EoS, we are going to account for several other physical properties that influence the background model and the oscillations. In this part of the study, we will account for density discontinuities in the background, stratification, a finite temperature and an elastic crust. In the following we describe the construction of the background model.

2.1 The Mathematical Description

The structure—i. e. the pressure and density profile—of a neutron star can be calculated using the Einstein equations

$$G_{\mu\nu} = 8\pi T_{\mu\nu}, \tag{2.1}$$

where $G_{\mu\nu}$ is the Einstein tensor expressing the curvature of the space-time and $T_{\mu\nu}$ the stress-energy tensor being the source of the gravitational field. The latter has to satisfy the conservation law of energy and momentum, which reads

$$\nabla_\nu T^{\mu\nu} = 0. \tag{2.2}$$

In order to solve the Einstein equations (2.1), a stress-energy tensor must be specified. A neutron star (without heat or superfluidity taken into account) is well described as a perfect fluid, for which $T_{\mu\nu}$ is given by

$$T_{\mu\nu} = (\rho + p)\, u_\mu u_\nu + p g_{\mu\nu}. \tag{2.3}$$

Here, ρ and p are the energy density and the pressure, respectively, and u_μ is the 4-velocity of the object. We point out that while we will account for elasticity of the crust in the oscillations, we assume that the background configuration is unstrained. If we were to consider a strained star, we would need to account for shear stresses in the background stress-energy tensor. In the simplest case—a non-rotating star—the 4-velocity takes the form

$$u^\mu = e^{-\nu/2} t^\mu, \tag{2.4}$$

with $t^\mu = (\partial_t)^\mu$ being the time-like Killing vector of the space-time. This particular form is a result of the normalisation condition $u^\mu u_\mu = -1$ and the fact that $u^r = u^\theta = u^\phi = 0$. The spherical symmetry of the problem allows to reduce the number of non-vanishing metric components and, by using spherical coordinates (r, θ, ϕ), the line-element takes

the form

$$ds^2 := g_{\mu\nu}\,\mathrm{d}x^\mu\,\mathrm{d}x^\nu \tag{2.5}$$

$$= -e^\nu\,\mathrm{d}t^2 + e^\lambda\,\mathrm{d}r^2 + r^2\left(\mathrm{d}\theta^2 + \sin^2\theta\,\mathrm{d}\phi^2\right), \tag{2.6}$$

where λ and ν are two *metric potentials* depending only on r.

These ingredients finally lead to the following three equations for the unknowns λ, ν, ρ and p governing the structure of a compact object,

$$\lambda' = \frac{1-e^\lambda}{r} + 8\pi r e^\lambda \rho, \tag{2.7a}$$

$$\nu' = \frac{e^\lambda - 1}{r} + 8\pi r e^\lambda p, \tag{2.7b}$$

$$p' = -\frac{1}{2}(\rho + p)\nu'. \tag{2.7c}$$

We refer to these equations as the *Tolman-Oppenheimer-Volkov* equations (abbreviated TOV), even though the original TOV equations have been published in a slightly different form.

Obviously, the system is under-determined, because there are only three equations for four variables. The missing bit is an equation of state, which relates pressure and energy density in a unique way. We will explain the actual EoS used in more detail in Section 4.2.

We also define the mass inside a ball of radius r to be

$$M(r) := \frac{1}{2}r\left(1 - e^{-\lambda}\right). \tag{2.8}$$

Differentiating with respect to r and using (2.7a) yields

$$M' = 4\pi r^2 \rho, \tag{2.9}$$

which can be written in the more concise form

$$M(r) = 4\pi \int_0^r \rho(\mathring{r})\mathring{r}^2\,\mathrm{d}\mathring{r}. \tag{2.10}$$

We find the reasonable result that the mass we have defined can be calculated from integrating the energy density over the volume of a ball of radius r.

Numerical Implementation. The TOV equations (2.7) represent an initial value problem. They are solved from the centre of the star ($r = 0$), with some initial values given, outwards to the surface.

As initial values, we take $\lambda(0) = 0$, $\nu(0) = 0$ and the pressure $p(0)$ is set as desired (usually by specifying a central energy density ρ_c). $\lambda(0) = 0$ is equivalent to $M(0) = 0$

(the mass within the ball of radius zero vanishes) and the initial value of $\nu(0)$ is irrelevant at this point as ν does not appear in the background equations (only its derivative ν' does); after the integration, we will shift this metric potential by a constant value in order to meet some boundary condition at the surface of the star, see below. The equations are then integrated outwards using the Dormand-Prince method (DOPRI) which is a member of the Runge-Kutta family of ODE solvers and has order eight; high accuracy adaptive mesh refinement is used which generally leads to a higher resolution close to the surface of the star. The surface is reached as the pressure reaches zero. In the case of realistic EoSs, a different threshold must be applied since tabulated EoSs usually have a cut-off at some positive pressure. It turned out to be reasonable to stop integration at a very low mass density, e. g. $\rho \leq 10^6\,\mathrm{g\,cm^{-3}}$. There will be a thin atmosphere at densities lower than that, but in comparison to the star it contains negligible mass and will not affect the oscillation modes. We can, therefore, safely neglect its presence for this problem.

In the exterior of the star, the metric potentials λ and ν are given by the Schwarzschild solution (if the star is non-rotating),

$$e^{-\lambda} = e^{\nu} = 1 - \frac{2M}{r} \quad \text{for } r \geq R, \tag{2.11}$$

where M is the mass of the neutron star and R its radius. The value of $\nu(R)$ at the star's surface right after the integration will in general not fulfil this condition (because we chose $\nu(0) = 0$); since ν itself does not appear in the background equations, we can add any constant to ν and we choose this constant so that $\nu(R) = -\lambda(R)$.

The solution of the TOV equations for an exemplary neutron star with a central energy density of $\rho_c = 1 \cdot 10^{15}\,\mathrm{g\,cm^{-3}}$ using our chosen EoS is depicted in Figure 2.1 by showing some quantities throughout the star. That star has a gravitational mass of $M = 1.447\,M_\odot$ and a circumferential radius of $R = 11.77\,\mathrm{km}$. In Figure 2.2, we show a magnification of parts of the outer crust which makes the density discontinuities, present in the crustal EoS, visible; see following section for details.

2.2 The Equation of State

To model our neutron star, we use a realistic equation of state. As our main interest is a proof of principle rather than providing a truly accurate spectrum of a real neutron star (which would be impossible given the large uncertainties in the equation of state), we focus on a single, realistic equation of state for which we make use of different proposed models for the different regions of the star, i.e. the crust and the core. We will match these different pieces in a rather ad hoc fashion but we will see that this particular equation of state perfectly serves the purpose of our study. In the following, we will briefly explain the different EoSs. For the sake of brevity and clarity, we will refer to

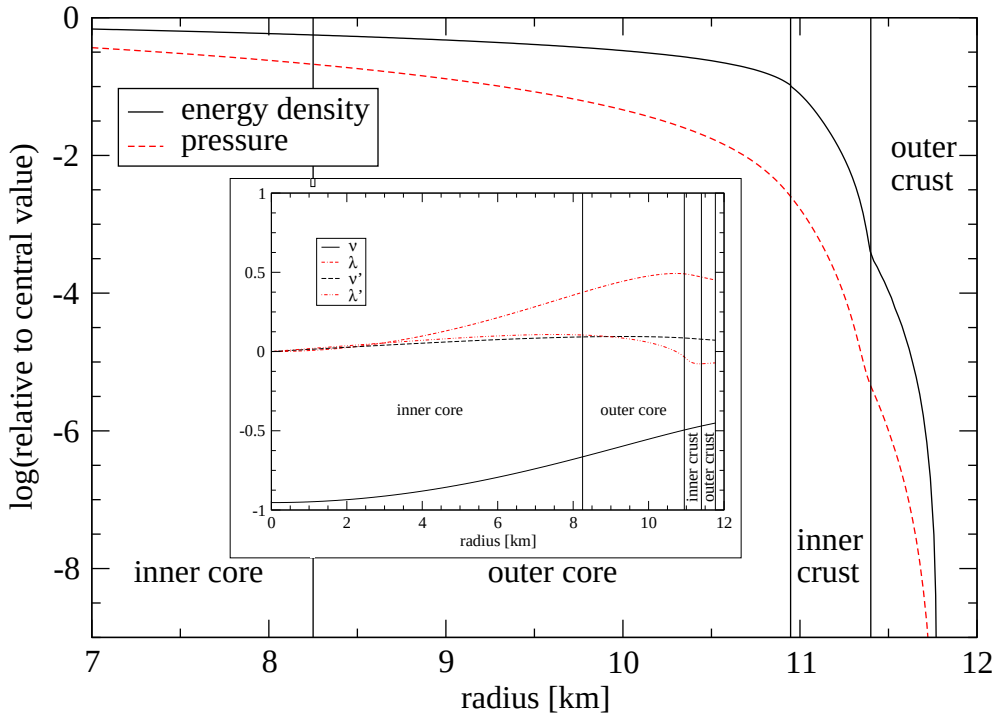

Figure 2.1: Pressure and energy mass density relative to their central values throughout the star. The small inset depicts the metric potentials and their first derivative. The vertical lines separate the different regions in the neutron star.

the low density region of a neutron star with $\rho \lesssim 1 \cdot 10^{14}\,\mathrm{g\,cm^{-3}}$ simply as *the crust* or the *crustal region*, regardless of whether or not an elastic lattice has already shaped during the ageing process of the star. Whenever we mean the solid/elastic region, we designate this by explicitly using the adjective.

The Crustal Equation of State

We calculate our background model for densities as low as $\rho = 10^6\,\mathrm{g\,cm^{-3}}$; the neutron star envelope with $\rho < 10^6\,\mathrm{g\,cm^{-3}}$ has a tiny mass of about $10^{-10}\,M_\odot$ and is largely irrelevant for the calculation of oscillation modes [54]. The composition of the outer crust (up to the neutron drip, $\rho_{\mathrm{drip}} \approx 3.4{\cdot}10^{11}\,\mathrm{g\,cm^{-3}}$) is characterised by the presence of a sequence of nuclei: at a given pressure p, the ground state of matter is determined by the condition that the Gibbs energy is minimised. The obvious fact that the number of neutrons, N, and the mass number, Z, are discrete, leads to abrupt changes in composition within the outer crust. Detailed calculations by Jog & Smith [55] have revealed that a phase transition between two layers occurs over a very small pressure range, Δp. Typically, this pressure range Δp is about four orders of magnitude smaller than the pressure p at which it occurs, $\Delta p \lesssim 10^{-4} p$. In a real neutron star, this corresponds to a transition layer with a width of a few millimetres only; hence, the approximation of implementing sharp density jumps is a very good representation of

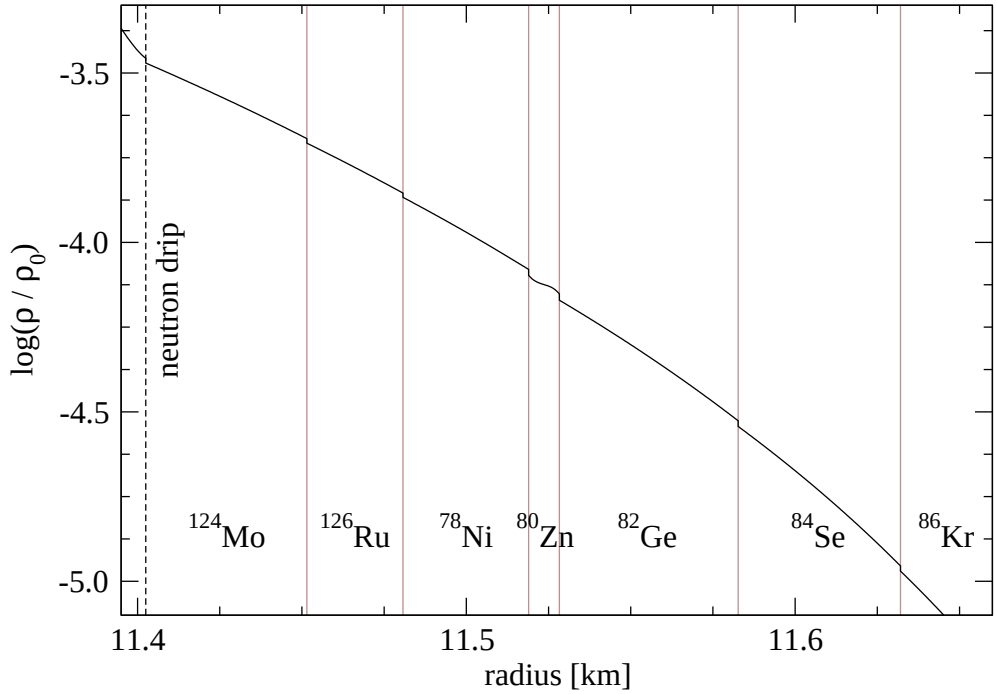

Figure 2.2: A strong magnification on a small layer within the outer crust touching the inner crust; the vertical dashed line depicting the neutron drip separates the outer from the inner crust. The density discontinuities due to the phase transitions become visible; we emphasise them with brown vertical lines. We also show the predominant nucleus present in each layer.

the nuclear composition in the crust. The sequence of nuclei (and the eleven induced density discontinuities) in our equation of state is shown in Table 2.1.

For the inner crust, we use an EoS which has been calculated using the Compressible Liquid Drop Model to approximate the composition of the matter in this region of the star. Instead of a layered structure where the layers are composed of mainly one particular type of ions, this model results in a continuous function for the proton and neutron number in the nuclei; these functions grow quickly and the atomic number reaches values of around 600 at the crust-core boundary. Also, as this region is beyond the neutron drip, the large number of neutrons results in neutrons dripping out of the nuclei and forming a neutron fluid beside the ions. When we consider superfluids in the second part of this study, this neutron fluid will become superfluid in sufficiently old stars.

The models for the EoS which we use for the outer and inner crust have been proposed by Douchin & Haensel [56] and we will refer to it as DH hereafter. In our study, we use the crustal EoS as provided by Samuelsson [57], who provides the calculations by Douchin & Haensel with a higher resolution, matched the EoSs for the inner and outer crust at the neutron drip, and attached the shear modulus as given by Baym & Pines [58].

Table 2.1: The sequence of nuclei in the ground state of dense matter. Z is the atomic number, N is the number of neutrons, $\rho_{\max}$ is the maximum density at which the corresponding nucleus is present and the last column shows the fractional increase of density at the phase transition.

Element	Z	N	$\rho_{\max}$ $[\mathrm{g\,cm^{-3}}]$	$\Delta\rho/\rho$ [%]
^{56}Fe	26	30	$7.83 \cdot 10^{6}$	3.0
^{62}Ni	28	34	$2.71 \cdot 10^{8}$	3.2
^{64}Ni	28	36	$1.31 \cdot 10^{9}$	3.1
^{66}Ni	28	38	$1.44 \cdot 10^{9}$	2.0
^{86}Kr	36	50	$3.14 \cdot 10^{9}$	3.3
^{84}Se	34	50	$1.07 \cdot 10^{10}$	3.6
^{82}Ge	32	50	$2.86 \cdot 10^{10}$	3.9
^{80}Zn	30	50	$6.75 \cdot 10^{10}$	4.3
^{78}Ni	28	50	$8.00 \cdot 10^{10}$	4.1
^{126}Ru	44	82	$1.36 \cdot 10^{11}$	3.0
^{124}Mo	42	82	$1.96 \cdot 10^{11}$	3.2

The Core

At densities $\rho_{\mathrm{cc}} > 1.03 \cdot 10^{14}\,\mathrm{g\,cm^{-3}}$ (which is about 37 % of nuclear saturation density, $\rho_{\mathrm{nuc}} = 2.8 \cdot 10^{14}\,\mathrm{g\,cm^{-3}}$), we use the SLy4 equation of state for which an analytical representation is given by Chamel [38]. The EoS is calculated at zero temperature and accounts for the presence of a mixture of superfluid neutrons and superconducting protons in the core, also including entrainment effects. We opt for this particular EoS as it will be essential when we extend our work to account for a superfluid core in the second part of the study. We are going to sketch the idea of the calculation in more detail in Section 4.2. For the single fluid calculations, a detailed insight is not essential, we will merely give a brief overview of the fundamental ingredients.

The internal energy density of the core fluid is calculated, based on the assumption that it consists of a mixture of neutrons, protons, electrons and muons (we will see that the latter only exist above a certain threshold). From this quantity (which depends on a number of parameters), we can deduce all other necessary quantities, which in the single fluid case are the pressure, p, and the adiabatic index, γ_0; the adiabatic index of perturbed matter, γ, which is the mathematical manifestation of stratification, can also be calculated (see Section 4.2 for details).

Matching the Different EoSs

As explained above, the EoS we use for our simulations consists of three pieces. We have to "glue" these pieces together at the interface between the outer and the inner crust ($\rho_{\text{drip}} \approx 3.4 \cdot 10^{11}\,\text{g}\,\text{cm}^{-3}$) and at the crust-core interface ($\rho_{\text{cc}} = 1.03 \cdot 10^{14}\,\text{g}\,\text{cm}^{-3}$) (the matching within the crust has already been performed by Samuelsson [57], so we will simply cite the result). We have to take into account that the pressure profile of a neutron star must be a continuous and strictly monotonic (increasing towards the centre, obviously) function of the radius for physical reasons: a hypothetical pressure discontinuity could not persist since the different pressures on either side of the discontinuity would cause a motion of the neutron star matter towards the side with lower pressure (which means the star is not in equilibrium). Secondly, the pressure gradient is in such a way that it exactly balances the gravitational pull; if the pressure were to decrease towards the centre of the star in some region, this would again imply a motion of matter towards the centre of star and hence contradict the assumption of equilibrium. However, the density is allowed to have discontinuities and we have seen that these jumps are physically realised in the outer crust. By matching the three pieces at their interfaces, we introduce two density discontinuities (at the neutron drip and at the crust-core interface) which are listed in Table 2.2. While the new density discontinuity at the neutron drip is artificial due to the matching of two different EoS models and does not exist in a lifelike neutron star, at the crust-core interface matter, in fact, undergoes a first order phase transition which comes with a jump in density; however, since we picked two independent models for the crustal and core EoSs, we can only guarantee that the resulting density discontinuity resembles reality qualitatively (but not quantitatively).

Table 2.2: The density discontinuities introduced by matching the different EoSs at the respective interfaces.

Interface	ρ_{max} $[\text{g}\,\text{cm}^{-3}]$	$\Delta\rho/\rho$ [%]
outer/inner crust	$3.38 \cdot 10^{11}$	3.3
crust-core	$1.03 \cdot 10^{14}$	3.0

This piecing together of different EoSs might appear ad hoc; however, for different reasons, we will use our 'made-up' EoS: the first reason being that the core EoS is still largely unknown and we have to choose one of the available EoSs. Since the SLy4 EoS is one of the most elaborate ones at present and more importantly, its multi-fluid approximation proposed by Chamel [38] will be essential for our future work, this is our number one choice. Secondly, and as a consequence of the former reason, this study aims to be a proof of technology rather than providing an accurate stellar spectrum

of a lifelike neutron star: once our understanding of a neutron star's core has grown and a more accurate EoS is derived, we can plug it into our code and calculate the corresponding stellar spectrum.

2.3 Adding Temperature

The above derived equations do not require temperature to be taken into consideration; they work for an idealised neutron star at zero temperature. However, in the early stages of a neutron star's life, temperature cannot be neglected and gives a substantial contribution to the pressure leading to a bigger star; in more adolescent stars, the static thermal pressure does not influence the background model anymore but will certainly have an impact on the neutron star oscillation spectrum.

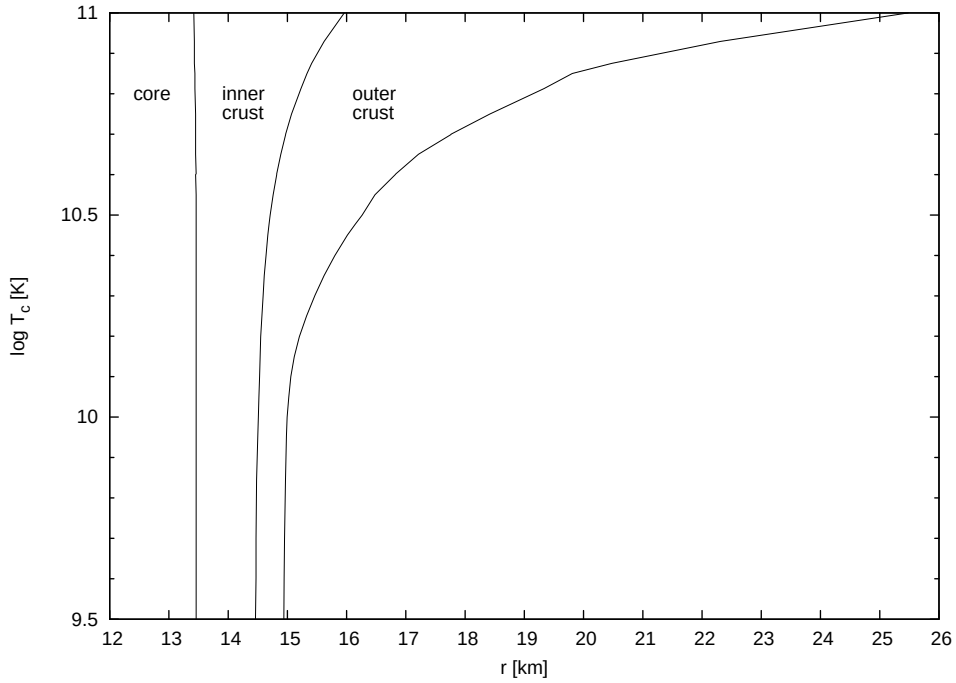

Figure 2.3: Impact of thermal pressure on the neutron star's size. The graph shows at which radii the boundaries between the different regions in a neutron star, as well as its radius, are found.

How strongly does the thermal pressure affect the background model? The answer to this question can help us decide about the importance of thermal pressure in the background model. Shen et al. [59] proposed a hot EoS which we can use to construct background models at different temperatures. For simplicity, we assume the star to be in an isothermal state (which in relativistic terms means that we take the red-shifted temperature, Te^{ν}, to be constant). Our focus in this calculation lies on the bulk properties of the star, here its radius R. We calculate a sequence of neutron stars for temperatures between 10^9 and 10^{11} K; the results are shown in Figure 2.3.

The graph shows that, as soon as the star has cooled to approximately $T_c \approx 10^{10}\,\mathrm{K}$, thermal pressure has almost no effect on the neutron star's size anymore. A neutron star cools to these temperature within seconds after its birth and reaches its final size. As our focus lies on the adolescent neutron stars rather than very young neutron stars, we will in this study neglect the effect of thermal pressure on the background model and take it into account only for the perturbations.

2.3.1 A Sequence of Temperature Profiles

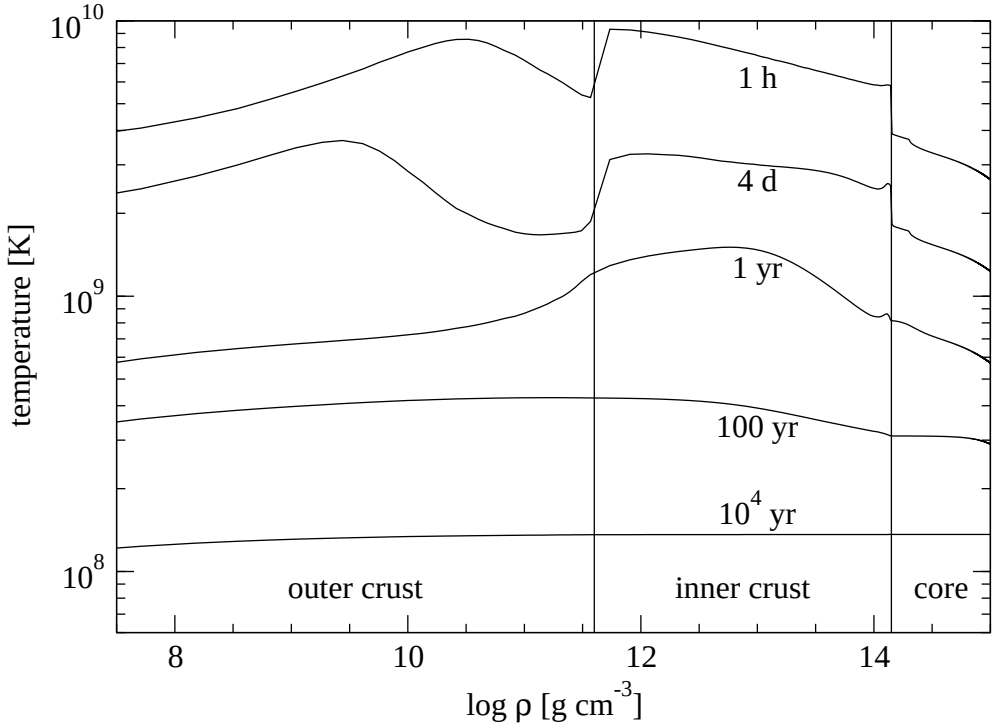

Figure 2.4: The thermal evolution of our neutron star model with $M = 1.447\,M_\odot$. As is apparent from this graph, which shows the red-shifted temperature, the neutron star is nearly isothermal after 100 years (without heat sources). Data courtesy of Wynn Ho.

According to the previous discussion, we will not include the thermal pressure in the background model. This means that we can construct our equilibrium configuration using a cold EoS and we will use separately provided temperature profiles from which we calculate the corrections to the pressure perturbations. We use thermal profiles from cooling simulations which are kindly provided by Wynn Ho [53]. As an initial temperature profile, we start from a uniform temperature $T = 10^{10}\,\mathrm{K}$, at which point the thermal pressure can be neglected compared to the static pressure. Starting from this initial temperature profile (this is artificial but filters out of the system very rapidly), we evolve the interior temperature $T(r,t)$ of the neutron star using the relativistic

equations of energy balance and heat flux [60]

$$\frac{e^{-\lambda/2-\nu}}{4\pi r^2}\frac{\mathrm{d}}{\mathrm{d}r}\left(e^{\nu}L_r\right) = -e^{-\nu/2}C\frac{\partial T}{\partial t} - \varepsilon_\nu, \tag{2.12}$$

$$\frac{L_r}{4\pi r^2} = -e^{-(\lambda+\nu)/2}K\frac{\partial}{\partial r}\left(e^{\nu/2}T\right), \tag{2.13}$$

where L_r is the luminosity at radius r, C is the heat capacity, ϵ_ν is the neutrino emissivity and K is the thermal conductivity. Note that we do not include internal heat sources, which would appear as a further source term in Equation (2.12); without these, neutron stars become essentially isothermal after about 100 years, as is apparent in Figure 2.4 where we show the thermal evolution of our chosen neutron star.

As is apparent from Figure 2.4, the core of the neutron star cools more quickly than the crust in the very early stages of its life. This is due to stronger neutrino emission in the core and hence the crust is generally hotter than the core. In these very early stages, thermal conductivity does not play a major role in the cooling evolution and the cooling of the core and the crust can be considered more or less decoupled; this leads to the rather big jumps in temperature at the crust-core transition, see Figure 2.4. The jump between the outer and inner crust is due to the neutron drip. After about one year or so, the star has cooled considerably, so that the cooling mechanisms become less efficient and conductivity will smooth the temperature profile throughout the star, finally bringing it into an isothermal state after about 100 years.

Chapter 3

Perturbations of Single Fluid Stars

In our calculations we will account for different physical properties of a neutron star, each of which will result in a certain, distinct class of modes visible in the stellar spectrum. Additionally to the well-studied f- and p-modes [18, 19, 61] (due to the density gradient) and the w-modes [21, 62] (which are present due to a non-static space-time), we will find four classes of modes which will arise due to the following physical properties: we will account for composition gradients (leading to composition g-modes), a finite temperature (thermal g-modes), an elastic crust (s-modes) and density discontinuities (i-modes).

In this section we will start with an overview about the general ingredients needed to derive the equations which govern perturbations around equilibrium. In the following, we will briefly go into the perturbation equations for the simplest case of a non-rotating perfect fluid which were derived by Detweiler & Lindblom [19] (which we will refer to as DL85 hereafter); in the remainder of that section we will discuss how we incorporate the different pieces of physics and how the perturbation equations are affected or derived.

3.1 Linear Perturbation Theory: Eulerian and Lagrangian Perturbations

A system needs to be described by an observer and usually there are some preferred observers or frames. These are called *Eulerian* or *Lagrangian* observers and they describe the system as follows. An Eulerian observer sits at a fixed point in space and watches fluid elements pass by, measuring their properties like velocity, density and so on; everything at the given location. A Lagrangian observer, on the other hand, is fixed to a particular fluid element and keeps track of the changes of that fluid element as it travels through space and time.

In the following, we will lay out the mathematically precise description of these

concepts on an arbitrary manifold; we will follow the analysis of Friedman & Schutz [44] as well as Frescura & Engelbrecht [63]. Our explanation will obviously be motivated by the application to neutron stars and therefore rely more on intuitive explanations than mathematical rigorousness, however, it will be formal enough so that it can be extended to the general case without much effort.

While the definition of the Eulerian perturbation will not pose serious difficulties, the Lagrangian perturbation needs a more careful treatment. As is clear from the explanation above, we need to compare quantities at different points on the manifold in order to define it; this is straightforward for scalars but not for vectors or tensors on a general manifold. We need to find a way to uniquely transport a tensor, T, from the current fluid element's position, x'^i, to its original position, x^i. This will lead us to the *Lie derivative*.

Let $F(x,t)$ be a flow and denote by ϕ_t the induced diffeomorphisms, $\phi_t(x) = F(x,t)$. The fluid element which at time $t = 0$ occupies the position x, will be found at the position $F(x,t)$ at time t. The tensor field T at this position has the value $T(F(x,t)) = T(\phi_t(x))$, while it has the value $T(x)$ at its original position. We now have to transport the value $T(\phi_t(x))$ backwards ("against the flow") to x in order to compare it with $T(x)$. This procedure is called *pull-back* and is performed by the operator $T\phi_t^{-1}$; The result is more briefly denoted by $\phi_t^* T(x) = T\phi_t^{-1}(T(\phi_t(x)))$. We can now define the Lie derivative of T along X (where X is the velocity field of the flow F) by

$$\mathcal{L}_X T := \lim_{\epsilon \to 0} \frac{\phi_\epsilon^* T - \phi_0^* T}{\epsilon} \tag{3.1}$$

$$= \lim_{\epsilon \to 0} \frac{\phi_\epsilon^* T - T}{\epsilon}, \tag{3.2}$$

since ϕ_0 is by definition the identity map, $\phi_0^* T = T$.

Let us now come back to the perturbations. Suppose first that Q denotes the equilibrium solution of our neutron star, i.e. it denotes a set of quantities, e.g. $Q = \{g_{\mu\nu}, u^\mu, \rho, p\}$; for simplicity we can think of it as a single quantity. Furthermore, let Q_λ be a smooth family of solutions (with $Q_0 = Q$) to the time-dependant equations of our system and we will suppose that this family of solutions is such that all of its members can be reached by a family of maps $\psi_\lambda(x^i, t)$ which track a given fluid element; i.e. if $\gamma(t)$ is the world line of a fluid element in the equilibrium configuration then $\psi_\lambda(\gamma(t), t)$ will be the world line in the perturbed configuration. The Eulerian perturbation of Q can now be defined as

$$\delta Q := Q_\lambda(x,t) - Q(x,t). \tag{3.3}$$

The difference is taken at the same point in space and is, hence, well defined.

The maps ψ_λ naturally define a family of vector fields η_λ which at every point is tangent to the flow, $\eta_\lambda(\psi_\lambda(x^i,t),t) = \psi'_\lambda(x^i,t)$. The Lagrangian displacement vector ξ is related to the vector field η_λ for the parameter value $\lambda = 0$. If we restrict ourselves

to small perturbations, we can approximate the flows ψ_λ by

$$\psi_\lambda(x^i,t) = \psi_0(x^i,t) + \lambda\frac{\partial\psi_0}{\partial\lambda}(x^i,t) + \mathcal{O}(\lambda^2) \tag{3.4}$$

$$= x^i + \lambda\eta_0(x^i,t), \tag{3.5}$$

where we used that $\lambda = 0$ corresponds to the equilibrium configuration and hence $\psi_0(x^i,t) = x_i$. Thus, we have $\xi = \psi_\lambda - \psi_0 = \lambda\eta_0$.

Let us now define the Lagrangian perturbation of a quantity Q. In the unperturbed flow, this quantity has the value $Q(x,t)$ for a fluid element occupying position x at time t. We want to compare this value to the value of Q of that fluid element in the perturbed flow; this value is given by $Q_\lambda(\psi_\lambda(x,t),t)$. On a general manifold, we need to pull-back this value along the flow ψ_λ to the position x; this yields $Q\psi_\lambda^{-1}(Q_\lambda(x,t),t)) = \psi_\lambda^* Q_\lambda(x,t)$. We can now define the Lagrangian variation of Q by

$$\Delta Q := \psi_\lambda^* Q_\lambda(x,t) - Q(x,t) \tag{3.6}$$

and as motivated above, this a well defined quantity. In order to connect this definition to the Eulerian perturbation, we rewrite this equation as (we omit the arguments for clarity)

$$\Delta Q = \psi_\lambda^* Q_\lambda - Q_\lambda + Q_\lambda - Q \tag{3.7}$$

$$= \left[\psi_\lambda^* Q_\lambda - \psi_0^* Q_\lambda\right] + \left[Q_\lambda - Q\right]. \tag{3.8}$$

The first bracket is related to the Lie derivative while the second bracket is the Eulerian perturbation δQ,

$$= \lambda\mathcal{L}_\eta Q + \delta Q, \tag{3.9}$$

where η_λ is the velocity field of the flow ψ_λ. Using $\xi = \lambda\eta_0$, we find the formula

$$\Delta Q = \delta Q + \mathcal{L}_\xi Q. \tag{3.10}$$

The relation $\lambda\mathcal{L}_\eta Q = \mathcal{L}_{(\lambda\eta)}Q$ can easily be shown from the definition of the Lie derivative.

3.2 Perturbation Equations for a Non-Rotating, Perfect Fluid Star

In order to study oscillations of neutron stars, one usually considers small deviations from equilibrium in order to avoid non-linearities of the Einstein equations. The metric

for a non-rotating, spherically symmetric neutron star, reads

$$\mathrm{d}s^2 = -e^{\nu}\,\mathrm{d}t^2 + e^{\lambda}\,\mathrm{d}r^2 + r^2\,\mathrm{d}\theta^2 + r^2\sin^2\theta\,\mathrm{d}\phi^2. \tag{3.11}$$

Together with the normalisation condition $u_\mu u^\mu = -1$, the 4-velocity takes the form $u^\mu = e^{-\nu/2}(1,0,0,0)$. The Lagrangian perturbation formalism will turn out to be the essential method in order to study multi-fluid systems. As the basic ingredients, it needs the metric perturbation $\delta g_{\mu\nu}$ and the displacement vector ξ^μ. In the case of a non-rotating star, the full solution can be decomposed into Legendre polynomials, P_l, and the perturbations of different degrees l are fully decoupled. It is, therefore, possible to consider perturbations of one particular degree l individually; we will define all quantities for arbitrary degrees $l \geq 2$ and derive the perturbation equations accordingly, however, in the actual calculations we will with no exception consider the case $l = 2$.

We write the displacement vector for polar perturbations as

$$\xi^\mu = r^l \begin{pmatrix} 0 \\ W r^{-1} e^{-\lambda/2} \\ -V r^{-2}\partial_\theta \\ -\frac{V}{r^2\sin^2\theta}\partial_\phi \end{pmatrix} P_l(\cos\theta) e^{i\omega t}, \tag{3.12}$$

where W and V are functions of r.

The metric perturbation in the Regge-Wheeler gauge [64] is

$$\delta g_{\mu\nu} = -r^l \begin{pmatrix} H_0 e^{\nu} & i\omega r H_1 & 0 & 0 \\ i\omega r H_1 & H_2 e^{\lambda} & 0 & 0 \\ 0 & 0 & r^2 K & 0 \\ 0 & 0 & 0 & r^2\sin^2\theta K \end{pmatrix} P_l(\cos\theta) e^{i\omega t}, \tag{3.13}$$

where P_l is the Legendre polynomial of degree l.

The perturbation equations which we have to solve are the perturbed Einstein equations

$$\delta G_{\mu\nu} = 8\pi \delta T_{\mu\nu}. \tag{3.14}$$

In order to solve these equations, we need expressions for the perturbed Einstein tensor, $\delta G_{\mu\nu}$, and the perturbed stress-energy tensor, $\delta T_{\mu\nu}$. The calculation of the perturbed Einstein tensor δG^ν_μ is tedious and not very insightful which is why we simply state the result (cf. [49])

$$\begin{aligned} 2\delta G^\nu_\mu = &-\nabla_\lambda\nabla^\lambda \delta g^\nu_\mu + \nabla^\nu\nabla_\lambda \delta g^\lambda_\mu + \nabla_\mu\nabla^\lambda \delta g^\nu_\lambda - g^{\lambda\sigma}\nabla_\mu\nabla^\nu \delta g_{\lambda\sigma} \\ &- R^\lambda_\mu \delta g^\nu_\lambda - \left(\nabla^\lambda\nabla^\sigma \delta g_{\lambda\sigma} - g^{\tau\sigma}\nabla_\lambda\nabla^\lambda \delta g_{\tau\sigma} - R^{\lambda\sigma}\delta g_{\lambda\sigma}\right)\delta^\nu_\mu, \end{aligned} \tag{3.15}$$

with $R_{\mu\nu}$ being the Ricci tensor.

The perturbed stress-energy tensor is given by

$$\delta T^{\nu}_{\mu} = (\delta\rho + \delta p)u_{\mu}u^{\nu} + \delta p\delta^{\nu}_{\mu} + (\rho + p)(u^{\nu}\delta u_{\mu} + u_{\mu}\delta u^{\nu} + u^{\nu}u^{\lambda}\delta g_{\mu\lambda}). \tag{3.16}$$

The velocity perturbations can be derived in the following way: Let t^{μ} be the time-like Killing vector of the space-time which is tangent to the unperturbed world lines of the fluid elements. The velocity then is

$$u^{\mu} = t^{\mu}/|t^{\mu}| = t^{\mu}\left(-g_{\nu\sigma}t^{\nu}t^{\sigma}\right)^{-1/2}. \tag{3.17}$$

As t^{μ} is constant, its Lagrangian variation vanishes, $\Delta t^{\mu} = 0$. This immediately implies the relation

$$\Delta u^{\mu} = \frac{1}{2}u^{\mu}u^{\nu}u^{\sigma}\Delta g_{\nu\sigma} \tag{3.18}$$

for the Lagrangian perturbation of the velocity field and thus we have

$$\delta u^{\mu} = q^{\mu}_{\nu}\mathcal{L}_{u}\xi^{\nu} + \frac{1}{2}u^{\mu}u^{\nu}u^{\sigma}\delta g_{\nu\sigma}, \tag{3.19}$$

where

$$q^{\mu\nu} = g^{\mu\nu} + u^{\mu}u^{\nu}, \tag{3.20}$$

and the Lie derivative of a vector field ξ^{ν} along u^{μ} is given by

$$\mathcal{L}_{u}\xi^{\nu} = u^{\mu}\nabla_{\mu}\xi^{\nu} - \xi^{\mu}\nabla_{\mu}u^{\nu}. \tag{3.21}$$

We still need to find expressions for δp and $\delta\rho$. We start from the Lagrangian perturbation of the baryon number density, n_b, [17]

$$\frac{\Delta n_b}{n_b} = -\frac{1}{2}q^{\mu\nu}\Delta g_{\mu\nu}. \tag{3.22}$$

The Lagrangian perturbation of the metric is given by

$$\Delta g_{\mu\nu} = \delta g_{\mu\nu} + \mathcal{L}_{\xi}g_{\mu\nu} \tag{3.23}$$

$$= \delta g_{\mu\nu} + \nabla_{\mu}\xi_{\nu} + \nabla_{\nu}\xi_{\mu} \tag{3.24}$$

$$= \delta g_{\mu\nu} + 2\nabla_{(\mu}\xi_{\nu)}, \tag{3.25}$$

where we have used the compatibility of the metric with the covariant derivative, $\nabla_{\sigma}g_{\mu\nu} = 0$. The round brackets in the last equation denote symmetrisation; for any tensor $t_{\mu\nu}$,

$$2t_{(\mu\nu)} := t_{\mu\nu} + t_{\nu\mu}. \tag{3.26}$$

Given the definitions (3.12) of the displacement vector, and the metric perturbations

(3.13), we find

$$\frac{\Delta n_b}{n_b} = r^{l-2} P_l e^{i\omega t} \left[r^2 \left(K + \frac{1}{2} H_0 \right) - l(l+1)V - (l+1)e^{-\lambda/2} W - r e^{-\lambda/2} W' \right]. \quad (3.27)$$

The fundamental laws of thermodynamics relate the Lagrangian perturbations of the energy density and the number density to each other

$$\Delta\rho = \frac{\rho + p}{n_b} \Delta n_b, \quad (3.28)$$

from which we can calculate $\delta\rho$ to be

$$\delta\rho = (\rho + p) \frac{\Delta n_b}{n_b} - \rho' \xi^r. \quad (3.29)$$

The Eulerian pressure perturbation can be obtained from the definition of the adiabatic index,

$$\gamma_0 = \frac{\rho + p}{p} \left(\frac{\partial p}{\partial \rho} \right)_\beta, \quad (3.30)$$

where the index β indicates that the partial derivative is to be taken in β-equilibrium. The meaning of β-equilibrium being that the composition of the star is stationary with regards to the Urca processes (see Section 4.2.1 for a detailed discussion). Then, we have

$$\delta p = \gamma_0 p \frac{\Delta n_b}{n_b} - p' \xi^r. \quad (3.31)$$

For the derivation of the perturbation equations, it turns out to be useful to define a quantity which is closely related to the Lagrangian pressure perturbation,

$$X := -r^{-l} e^{\nu/2} \Delta p. \quad (3.32)$$

This makes sense as the Lagrangian pressure appears naturally and it has the positive side effect that the derivative of the energy density, ρ', which is not necessarily continuous and hence may pose numerical difficulties, does not appear in the perturbation equations.

The equations governing small perturbations of a perfect fluid are then given by the Einstein equations and have been under thorough investigation already [19, 21, 61, 29]. We write them in the following form (which has first been derived in this form by Detweiler & Lindblom and we refer to this formulation as DL85 hereafter):

$$H_1' = \left[\frac{1}{2} \left(\lambda' - \nu' \right) - \frac{l+1}{r} \right] H_1 + \frac{e^\lambda}{r} \left[H_0 + K - 16\pi(\rho + p)V \right], \quad (3.33a)$$

$$K' = \frac{1}{r} H_0 + \frac{n+1}{r} H_1 + \left[\frac{1}{2} \nu' - \frac{l+1}{r} \right] K - \frac{8\pi}{r} e^{\lambda/2} (\rho + p) W, \quad (3.33b)$$

$$W' = -\frac{l+1}{r}W + re^{\lambda/2}\left[\frac{e^{-\nu/2}}{\gamma_0 p}X - \frac{l(l+1)}{r^2}V + \frac{1}{2}H_0 + K\right], \tag{3.33c}$$

$$\begin{aligned} X' = &-\frac{l}{r}X + \frac{1}{2}(\rho+p)e^{\nu/2}\left\{\left[\frac{1}{r} - \frac{\nu'}{2}\right]H_0 + \left[r\omega^2 e^{-\nu} + \frac{n+1}{r}\right]H_1\right. \\ &+ \left[\frac{3}{2}\nu' - \frac{1}{r}\right]K - \nu'\frac{l(l+1)}{r}V - \frac{1}{r}\left[8\pi(\rho+p)e^{\lambda/2} + 2\omega^2 e^{\lambda/2-\nu}\right. \\ &\left.\left. - r^2\left(r^{-2}e^{-\lambda/2}\nu'\right)'\right]W\right\}, \end{aligned} \tag{3.33d}$$

where we have defined

$$n := \frac{1}{2}(l+2)(l-1). \tag{3.34}$$

The Einstein equations imply that not all five perturbation quantities H_0, H_1, K, V and W are linearly independent, but there is the following relation between them:

$$\begin{aligned} \left[\frac{re^{-\lambda}}{2}(r\nu' - 2) + (n+1)r\right]H_0 = r^2 e^{-\lambda}&\left[\omega^2 re^{-\nu} - \frac{n+1}{2}\nu'\right]H_1 \\ &+ \left[nr - \omega^2 r^3 e^{-\nu} - \frac{1}{4}r^2 e^{-\lambda}\nu'(r\nu' - 2)\right]K + 8\pi r^3 e^{-\nu/2}X. \end{aligned} \tag{3.35a}$$

The definition of X gives us another algebraic relation,

$$X = \omega^2(\rho+p)e^{-\nu/2}V - \frac{1}{r}p'e^{(\nu-\lambda)/2}W + \frac{1}{2}(\rho+p)e^{\nu/2}H_0. \tag{3.35b}$$

We describe the perturbations of a perfect fluid by the six variables H_0, H_1, K, V, W and X for which we have two algebraic relations plus four differential equations. These are enough for a complete description of the problem. Furthermore, we can understand the four first-order ODEs as a system of two (second-order) wave equations; one for each wave degree of freedom. We obviously have oscillations of the perfect fluid, which are covered by the ODEs for W and X and lead to the well-known f-modes and p-modes. Due to general relativity, we also have two ODEs for the metric perturbations, H_1 and K, which leads to the appearance of w-modes [21].

3.2.1 The Taylor Expansion at the Centre of the Star

Since the perturbation equations (3.33) are singular at the origin due to the use of spherical coordinates, we will expand all variables by Taylor series near the origin, $r = 0$, in order to approximate the solution of the ODEs; we will comment on the accuracy of this approximation at the end of this subsection. For all our perturbation variables H_0, H_1, K, V, W and X, we will use an expansion of the form

$$q(r) = q_0 + \frac{1}{2}r^2 q_2 + \frac{1}{4}r^4 q_4 + \mathcal{O}\left(r^4\right), \tag{3.36}$$

and insert this expansion into perturbation equations. This will lead, in general, to polynomial expressions in r on both sides of the equation. The conditions for the coefficients then follow by equating the coefficients of the same power of r on either side of the equation.

Note that in this subsection regarding the Taylor expansion (and consistently throughout all subsections of similar type), subscripts of the background quantites (and only these) will denote the order of the coefficient within its corresponding Taylor expansion around the origin. E.g. ν_2 denotes the second Taylor coefficient of the (background) metric potential ν. In order to avoid confusion, we will not adopt this convention for the adiabatic index, γ_0, the zeroth-order coefficient of which we will simply refer to as $\gamma_0(0)$, as well as the perturbation variables, for the coefficients of which we will write $H_0(0)$, $H_0''(0)$ and so on.

The procedure is nearly straightforward; only the exponential function requires a little extra care. The term e^{ν} and similar terms appear often in the perturbation equations. The Taylor expansion follows by using the Taylor expansion of the exponential function,

$$e^{\nu} = e^{\nu_0+\frac{1}{2}r^2\nu_2+\frac{1}{4}r^4\nu_4+\mathcal{O}\left(r^6\right)} \tag{3.37}$$

$$= e^{\nu_0}\sum_{k=0}^{\infty}\frac{1}{k!}\left(\frac{1}{2}r^2\nu_2+\frac{1}{4}r^4\nu_4+\mathcal{O}\left(r^6\right)\right)^k \tag{3.38}$$

$$= e^{\nu_0}\left[1+\frac{1}{2}\nu_2 r^2+\left(\frac{1}{4}\nu_4+\frac{1}{8}\nu_2^2\right)r^4+\mathcal{O}\left(r^6\right)\right]. \tag{3.39}$$

Similar expressions can be obtained for the terms $e^{\nu/2}$, $e^{-\nu}$, e^{λ} etc. We note that in expression (3.36), we have omitted the coefficients q_1, q_3, and so on for odd orders. This is for simplicity as the background and perturbation equations imply that all odd orders vanish in our problem, $q_1 = q_3 = 0$. We do not show the proof for this as the proof itself is purely technical and does not give further insight into the problem.

Here and in the following, we need the expansion coefficients of the background quantities, ν, λ, p and ρ as well which can be obtained from the background equations (the TOV equations plus the EoS). We have expanded them in the same way as specified in (3.36); their zeroth-order coefficients are simply their values at the centre of the star, $\lambda_0 = 0$, $\nu_0 = \nu(0)$, $p_0 = p(0)$ and $\rho_0 = \rho(0)$; their second- and fourth-order coefficients are given by

$$\lambda_2 = \frac{16}{3}\pi\rho_0, \tag{3.40}$$

$$\nu_2 = \frac{8}{3}\pi\left(\rho_0+3p_0\right), \tag{3.41}$$

$$p_2 = -\frac{1}{2}\nu_2\left(\rho_0+p_0\right), \tag{3.42}$$

$$\rho_2 = \frac{p_2\,(\rho_0 + p_0)}{\gamma_0(0)p_0}, \tag{3.43}$$

$$\lambda_4 = \frac{4}{5}\left[4\pi(\rho_2 + \lambda_2\rho_0) - \frac{1}{8}\lambda_2^2\right], \tag{3.44}$$

$$\nu_4 = 4\pi\left[\rho_2 + p_2 + \lambda_2(\rho_0 + p_0)\right] - \lambda_4, \tag{3.45}$$

$$p_4 = -\frac{1}{2}\nu_4(\rho_0 + p_0) - \frac{1}{4}\nu_2(\rho_2 + p_2). \tag{3.46}$$

We make use of the fourth-order coefficients for the background quantities as they will shorten the equations for the second-order coefficients of the perturbation variables a little.

The zeroth-order constraints imposed on the perturbation variables by the perturbation equations are

$$H_1(0) = \frac{2lK(0) + 16\pi\,(\rho_0 + p_0)\,W(0)}{l(l+1)}, \tag{3.47a}$$

$$X(0) = (\rho_0 + p_0)e^{\nu_0/2}\left[\frac{1}{2}K(0) + \left(\frac{1}{2}\nu_2 - \frac{\omega^2}{l}e^{-\nu_0}\right)W(0)\right], \tag{3.47b}$$

$$V(0) = -\frac{1}{l}W(0), \tag{3.47c}$$

$$H_0(0) = K(0), \tag{3.47d}$$

which demonstrates that, once $K(0)$ and $W(0)$ are chosen, the remaining expansion coefficients, $H_0(0)$, $H_1(0)$, $V(0)$ and $X(0)$ are determined. We define two auxiliary variables Q_0 and Q_1 so that

$$H_0''(0) = K''(0) + Q_0, \tag{3.48}$$

$$V''(0) = Q_1 - \frac{l+3}{l(l+1)}W''(0). \tag{3.49}$$

These two variables are given by

$$Q_0 = \frac{2}{n}\left\{\left[\omega^2 e^{-\nu_0} - \frac{n+1}{2}\nu_2\right]H_1(0) - \left[\omega^2 e^{-\nu_0} + \frac{1}{2}\lambda_2\right]K(0) + 8\pi e^{-\nu_0/2}X(0)\right\}, \tag{3.50a}$$

$$Q_1 = \frac{1}{n+1}\left\{\frac{3}{2}K(0) + \frac{l+1}{4}\lambda_2 W(0) + \frac{e^{-\nu_0/2}}{\gamma_0(0)p_0}X(0)\right\}, \tag{3.50b}$$

where (3.50a) and (3.50b) stem from (3.35a) and (3.33c), respectively. The second-order coefficients of the perturbation variables are then given by the following linear system:

$$-\frac{1}{2}(\rho_0 + p_0)K''(0) + \left[p_2 + (\rho_0 + p_0)\frac{\omega^2(l+3)}{l(l+1)}e^{-\nu_0}\right]W''(0) + e^{-\nu_0/2}X''(0)$$

$$= \frac{1}{2}(\rho_2 + p_2)K(0) - \left[2p_4 - \frac{1}{2}\lambda_2 p_2 + \frac{\omega^2}{l}(\rho_2 + 3p_2)e^{-\nu_0}\right] W(0)$$
$$+ \frac{1}{2}\nu_2 e^{-\nu_0/2}X(0) + \frac{1}{2}(\rho_0 + p_0)Q_0 + \omega^2(\rho_0 + p_0)e^{-\nu_0}Q_1, \tag{3.51a}$$

$$-\frac{n+1}{2}H_1''(0) + \frac{l+2}{2}K''(0) + 4\pi(\rho_0 + p_0)W''(0)$$
$$= \frac{1}{2}\nu_2 K(0) - 4\pi\left[\rho_2 + p_2 + \frac{1}{2}\lambda_2(\rho_0 + p_0)\right] W(0) + \frac{1}{2}Q_0, \tag{3.51b}$$

$$\frac{l+3}{2}H_1''(0) - K''(0) - 4\pi(\rho_0 + p_0)\frac{l+3}{n+1}W''(0)$$
$$= 4\pi\left[\frac{2l+3}{3}\rho_0 - p_0\right] H_1(0) + \frac{8\pi}{l}(\rho_2 + p_2)W(0) + \frac{1}{2}Q_0$$
$$- 8\pi(\rho_0 + p_0)Q_1, \tag{3.51c}$$

$$-(\rho_0 + p_0)e^{\nu_0/2}\left[\frac{l+2}{4}\nu_2 - 2\pi(\rho_0 + p_0) - \frac{\omega^2}{2}e^{-\nu_0}\right] W''(0)$$
$$-\frac{n+1}{4}(\rho_0 + p_0)e^{\nu_0/2}H_1''(0) + \frac{l+2}{2}X''(0)$$
$$= \frac{l}{2}\frac{\rho_2}{\rho_0 + p_0}X(0) + (\rho_0 + p_0)e^{\nu_0/2}\left[\frac{\omega^2}{2}e^{-\nu_0}H_1(0) + \frac{1}{2}\nu_2 K(0)\right.$$
$$+ \left[\frac{l+1}{2}\nu_4 - \frac{1}{2}\lambda_4 + \frac{1}{8}\lambda_2^2 + \frac{\omega^2}{4}e^{-\nu_0}(2\nu_2 - \lambda_2)\right] W(0) + \frac{1}{4}Q_0$$
$$\left. - \frac{n+1}{2}\nu_2 Q_1\right]. \tag{3.51d}$$

The individual equations (3.51a) to (3.51d) are derived from (3.35b), (3.33b), (3.33a) and (3.33d), respectively. These expressions look messy but the linear system can be understood in the simple form

$$TY''(0) = UY(0), \tag{3.52}$$

where $Y(0) = (H_1(0), K(0), W(0), X(0))$ is a vector representing the zeroth-order coefficients of the Taylor expansion. $Y''(0)$ is the second-order counterpart; T and U are 4×4 matrices which depend only on background quantities like ν_0, λ_0, p_0, ν_2 and so on as well as parameters of the problem like ω, l etc. Keep in mind that U is a 4×4 matrix if we insert the expressions for Q_0 and Q_1 into (3.51) whereby the right-hand sides are linear combinations of only the components of $Y(0)$. The solution to this linear system is then simply given by

$$Y''(0) = T^{-1}UY(0). \tag{3.53}$$

The most computational effort in solving this linear system, hence, is inverting the 4×4 matrix T, which is negligible compared to the solution of the differential equations.

Using the zeroth-order and second-order coefficients of the Taylor expansion, we can approximate the solution of the differential equations using equation (3.36) near the origin where these equations are singular. We have to keep in mind that this is only

a second-order approximation and we should use it only in the close vicinity of $r = 0$. In fact, in our simulations, we use the Taylor expansion up to about $R_{\text{Tayl}} \approx R/1000$ (the actual value depends slightly on the chosen EoS by virtue of the implementation) where R is the star's radius; then we switch to the differential equations and we use the values obtained from the Taylor expansion as initial values for the numerical integration. For the modes we are interested in (mainly low order modes), this poses an excellent approximation as their eigenfunctions display a very regular behaviour close to the origin. We can confirm this from our simulations and have also investigated the effect of choosing a different radius R_{Tayl} at which to switch from the Taylor approximation to integrating the ODEs: The obtained frequencies are highly insensitive to such changes and the discrepancy is less than one part in a million even for modes of order ten and $R_{\text{Tayl}} = R/20$. However, one has to keep in mind that if one were to investigate higher order modes which display a strong oscillatory behaviour even close to the origin, this approximation becomes less accurate and one has to either retain more terms in the Taylor expansion or choose a smaller R_{Tayl} (or both) in order to obtain accurate results.

We will not go into further detail about these equations since they already have been studied thoroughly. Instead, we will investigate how we have to modify these equations if we want to study perturbations of a more realistic neutron star model. This will be subject of the following sections.

3.3 Accounting for Stratification

As a first step, we will account for stratification; the composition of a neutron star changes with depth inside the neutron star. Let us consider an oscillating fluid element. Weak interaction processes ought to adjust its composition to the surrounding matter which is in β-equilibrium as it moves into different layers during one oscillation period. However, as Reisenegger & Goldreich [23] have argued, the timescale of the relevant weak interaction processes is much longer than typical oscillation periods and thus perturbed fluid elements are not able to equilibrate during one oscillation period. Hence, the assumption that the composition of a perturbed fluid element is frozen, is accurate and the adiabatic index γ of the perturbed fluid is

$$\gamma = \frac{\rho + p}{p} \left(\frac{\partial p}{\partial \rho} \right)_{n,T}, \tag{3.54}$$

where we assumed that the temperature T of the considered fluid element does not change as well. This is the so-called *slow reaction* limit. We note that we, in contrast to definition (3.30) which we evaluate in β-equilibrium, have kept the composition constant (via the number density).

Closely related to the study of g-modes is the Schwarzschild discriminant

$$S = \frac{\mathrm{d}p}{\mathrm{d}r} - \frac{\gamma p}{\rho + p}\frac{\mathrm{d}\rho}{\mathrm{d}r} = \left(1 - \frac{\gamma}{\gamma_0}\right)\frac{\mathrm{d}p}{\mathrm{d}r}, \tag{3.55}$$

which determines the local stability of a pulsating star [65]; all normal modes are stable as long as $S \geq 0$ throughout the star. For our particular equation of state this condition holds as we have $\gamma \geq \gamma_0$ everywhere. Note that we have used equation (3.30) in order to achieve the last equality of equation (3.55).

In the opposite limit of *fast reactions* the weak interaction is considered sufficiently fast to fully adjust the perturbed fluid element's composition such that it stays in β-equilibrium at all times. Such a star is called barotropic and both adiabatic indices, γ and γ_0, then coincide and as a consequence, the Schwarzschild discriminant vanishes, $S = 0$. In this case, perturbed fluid elements are not subject to buoyancy and all g-modes due to stratification will be degenerate at zero frequency and therefore absent from the stellar spectrum.

In order to account for stratification, the perturbation equations will only be marginally modified. In the expression for the Eulerian pressure perturbation (3.31), γ_0 has to be replaced by γ; this leads to the same substitution in the differential equation (3.33c) for W and likewise in equation (3.50b) for the Taylor expansion. No other modification to the perturbation equations need to be made; we will, hence, not repeat the equations. The modified value of γ will result in the appearance of g-modes in the low frequency domain of the spectrum; more precisely, it enforces the g-modes to have a non-zero frequency whilst they are still existent but degenerate at zero frequency when $\gamma = \gamma_0$ [49].

3.4 Including the Thermal Pressure

Acting in a fashion similar to that of composition gradients, the presence of a finite temperature leads to a thermal pressure that influences the fluid dynamics. This effect may be important in young neutron stars. Since our equation of state models zero temperature physics, we will account for thermal effects by adding the thermal pressure of a Fermi liquid of the form [66]

$$p^{\mathrm{x}}_{th}(n_{\mathrm{x}}, T) = \frac{\pi^2}{6} n_{\mathrm{x}} kT \frac{kT}{E^{\mathrm{x}}_F} \tag{3.56}$$

to the pressure at zero temperature. Here, n_{x} is the number density of the relevant species, x=n, p, e and μ for neutrons, protons, electrons and muons, respectively, k is the Boltzmann constant and E^{x}_F is the Fermi energy of the given species. Note that, in our case $kT/E^{\mathrm{x}}_F \ll 1$ throughout most of the star (as our thermal evolutions begin at $kT \approx 1$ MeV), whereas, e.g., [67] consider the thermal pressure when $kT \gtrsim 1$ MeV. As

the electrons are relativistic, their Fermi energy is much higher than that of protons or neutrons and as a result their contribution to the thermal pressure is much lower in comparison. Hence, we will only account for thermal pressure due to neutrons and protons. The non-relativistic nucleon Fermi energy is given by $E_F^{\mathrm{x}} = p_{F\mathrm{x}}^2/2m_{\mathrm{x}}^*$ with $p_{F\mathrm{x}} = \hbar k_{F\mathrm{x}}$ and $k_{F\mathrm{x}} = \left(3\pi^2 n_{\mathrm{x}}\right)^{1/3}$ and m_{x}^* being the Landau effective mass of the corresponding species (for simplicity, we will take the effective mass to be constant in the following and secondly, that these of neutrons and protons coincide, $m^* := m_{\mathrm{n}}^* = m_{\mathrm{p}}^*$) [68]. Since the EoS gives us information about the composition of the neutron star core, we have all the information we need to account for the thermal pressure due to neutrons and protons, and the total pressure p becomes

$$p = p_0(\rho, x_{\mathrm{p}}) + \sum_{\mathrm{x=n,p}} p_{th}^{\mathrm{x}}(n_{\mathrm{x}}, T), \tag{3.57}$$

where p_0 is the pressure of the zero temperature equation of state described in Section 2.2 and $x_{\mathrm{p}} = n_{\mathrm{p}}/n_b$ is the proton fraction ($n_b = n_{\mathrm{n}} + n_{\mathrm{p}}$ is the baryon number density). In order to see how the thermal pressure enters the perturbation equations, we have to calculate the pressure perturbation. Since we are assuming the composition to be frozen we have $\Delta x_{\mathrm{p}} = 0$, where Δ represents a Lagrangian perturbation. The perturbed pressure then is

$$\begin{aligned}\Delta p = \left(\frac{\partial p_0}{\partial \rho}\right)_{x_{\mathrm{p}}} \Delta\rho + \left(\frac{\partial p_{th}^{\mathrm{n}}}{\partial n_{\mathrm{n}}}\right)_T \Delta n_{\mathrm{n}} + \left(\frac{\partial p_{th}^{\mathrm{n}}}{\partial T}\right)_{n_{\mathrm{n}}} \Delta T \\ + \left(\frac{\partial p_{th}^{\mathrm{p}}}{\partial n_{\mathrm{p}}}\right)_T \Delta n_{\mathrm{p}} + \left(\frac{\partial p_{th}^{\mathrm{p}}}{\partial T}\right)_{n_{\mathrm{p}}} \Delta T.\end{aligned} \tag{3.58}$$

It is, of course, the case that the (cold) energy density ρ is a function of the baryon density only. We need to transform the Lagrangian perturbations Δn_{n}, Δn_{p} and ΔT into known ones. For the former two, we resort to (3.22), which also holds for the different species (neutrons and protons) separately. Since we consider a single fluid star in which protons and neutrons are unconditionally comoving, they obviously have the same displacement vector and thus we have

$$\frac{\Delta n_{\mathrm{n}}}{n_{\mathrm{n}}} = \frac{\Delta n_{\mathrm{p}}}{n_{\mathrm{p}}}. \tag{3.59}$$

We need to relate each fraction to the entire baryon density $n_b = n_{\mathrm{n}} + n_{\mathrm{p}}$. We start from the fraction $\frac{\Delta n_{\mathrm{n}}}{n_{\mathrm{n}}}$ and extend it with the baryon density n_b,

$$\frac{\Delta n_{\mathrm{n}}}{n_{\mathrm{n}}} = \frac{\Delta n_{\mathrm{n}}}{n_{\mathrm{n}}} \frac{n_{\mathrm{n}}}{n_{\mathrm{n}} + n_{\mathrm{p}}} + \frac{\Delta n_{\mathrm{n}}}{n_{\mathrm{n}}} \frac{n_{\mathrm{p}}}{n_{\mathrm{n}} + n_{\mathrm{p}}}. \tag{3.60}$$

Making use of (3.59) for the second term yields

$$= \frac{\Delta n_{\mathrm{n}}}{n_{\mathrm{n}} + n_{\mathrm{p}}} + \frac{\Delta n_{\mathrm{p}}}{n_{\mathrm{n}} + n_{\mathrm{p}}} \tag{3.61}$$

$$= \frac{\Delta n_b}{n_b}. \tag{3.62}$$

Altogether, we have

$$\frac{\Delta n_{\mathrm{n}}}{n_{\mathrm{n}}} = \frac{\Delta n_{\mathrm{p}}}{n_{\mathrm{p}}} = \frac{\Delta n_b}{n_b}. \tag{3.63}$$

At last, we need to find a relation that translates ΔT into Δn_b. The assumption of adiabatic oscillations, $\Delta S = 0$, will give this final link. The total entropy is given by $S = S_{\mathrm{n}} + S_{\mathrm{p}}$ with [69]

$$S_{\mathrm{x}} = \frac{\pi^2}{2}\frac{T}{T_F^{\mathrm{x}}}, \tag{3.64}$$

where the Fermi temperature, $T_F^{\mathrm{x}} = E_F^{\mathrm{x}}/k$, is a function of the number density only, $T_F^{\mathrm{x}} = T_F^{\mathrm{x}}(n_{\mathrm{x}})$. From the total entropy, we find the temperature

$$T = \frac{2}{\pi^2} S \left[\frac{1}{T_F^{\mathrm{n}}} + \frac{1}{T_F^{\mathrm{p}}}\right]^{-1}. \tag{3.65}$$

Later, we will need the following partial derivative

$$\frac{\partial T_{F\mathrm{x}}}{\partial n_{\mathrm{x}}} = \frac{1}{2k}\frac{\partial}{\partial n_{\mathrm{x}}}\left(\frac{k_{F\mathrm{x}}^2}{m^*}\right) \tag{3.66}$$

$$= \frac{1}{2k}\left[\frac{1}{m^*}\frac{2k_{F\mathrm{x}}^2}{3n_{\mathrm{x}}} - \frac{k_{F\mathrm{x}}^2}{m^{*2}}\frac{\partial m^*}{\partial n_{\mathrm{x}}}\right] \qquad \text{with} \quad \frac{\partial k_{F\mathrm{x}}}{\partial n_{\mathrm{x}}} = \frac{k_{F\mathrm{x}}}{3n_{\mathrm{x}}} \tag{3.67}$$

$$= \frac{1}{k}\frac{k_{F\mathrm{x}}^2}{2m^*}\left[\frac{2}{3n_{\mathrm{x}}} - \frac{1}{n_{\mathrm{x}}}\frac{n_{\mathrm{x}}}{m^*}\frac{\partial m^*}{\partial n_{\mathrm{x}}}\right] \tag{3.68}$$

$$= \frac{T_{F\mathrm{x}}}{n_{\mathrm{x}}}\left[\frac{2}{3} - \left(\frac{m^*}{m} - 1\right)\right] \tag{3.69}$$

$$= \frac{T_{F\mathrm{x}}}{n_{\mathrm{x}}}\left[\frac{5}{3} - \frac{m^*}{m}\right]. \tag{3.70}$$

In this derivation, we have used the logarithmic derivative $\frac{\mathrm{d}\ln m^*}{\mathrm{d}\ln n_{\mathrm{x}}} = \frac{m^*}{m} - 1$ given by Prakash et al. [69]. We can now calculate the Lagrangian temperature variation

$$\Delta T = \frac{2}{\pi^2}\left[\frac{1}{T_{F\mathrm{n}}} + \frac{1}{T_{F\mathrm{p}}}\right]^{-1} \underbrace{\Delta S}_{=0} \tag{3.71}$$

$$+ \frac{2}{\pi^2} S \left[\frac{1}{T_{F\mathrm{n}}} + \frac{1}{T_{F\mathrm{p}}}\right]^{-2} \left(\frac{1}{T_{F\mathrm{n}}^2}\frac{\partial T_{F\mathrm{n}}}{\partial n_{\mathrm{n}}}\Delta n_{\mathrm{n}} + \frac{1}{T_{F\mathrm{p}}^2}\frac{\partial T_{F\mathrm{p}}}{\partial n_{\mathrm{p}}}\Delta n_{\mathrm{p}}\right), \tag{3.72}$$

where we have used $\Delta T_{F\mathrm{x}} = \frac{\partial T_{F\mathrm{x}}}{\partial n_{\mathrm{x}}} \Delta n_{\mathrm{x}}$. Using (3.65) and (3.70) for both neutrons and protons yields

$$= T \left[\frac{1}{T_{F\mathrm{n}}} + \frac{1}{T_{F\mathrm{p}}} \right]^{-1} \left[\frac{5}{3} - \frac{m^*}{m} \right] \left(\frac{1}{T_{F\mathrm{n}}} \frac{\Delta n_{\mathrm{n}}}{n_{\mathrm{n}}} + \frac{1}{T_{F\mathrm{p}}} \frac{\Delta n_{\mathrm{p}}}{n_{\mathrm{p}}} \right), \tag{3.73}$$

and finally applying (3.63) gives us the simple result

$$= T \left[\frac{5}{3} - \frac{m^*}{m} \right] \frac{\Delta n_b}{n_b}. \tag{3.74}$$

The last thing we need to note is that from the specific form of the thermal pressure (3.56), it immediately follows that

$$\left(\frac{\partial p_{th}^{\mathrm{x}}}{\partial T} \right)_{n_{\mathrm{x}}} = \frac{6 n_{\mathrm{x}}}{T} \left(\frac{\partial p_{th}^{\mathrm{x}}}{\partial n_{\mathrm{x}}} \right)_T. \tag{3.75}$$

Using the relations (3.63), (3.74) and (3.75) we can eliminate Δn_{n}, Δn_{p} and ΔT from the perturbed pressure given in (3.58) and arrive at

$$\Delta p = \left[\gamma p_0 + M^* n_{\mathrm{n}} \left(\frac{\partial p_{th}^{\mathrm{n}}}{\partial n_{\mathrm{n}}} \right)_T + M^* n_{\mathrm{p}} \left(\frac{\partial p_{th}^{\mathrm{p}}}{\partial n_{\mathrm{p}}} \right)_T \right] \frac{\Delta n_b}{n_b}, \tag{3.76}$$

where we introduced the abbreviation $M^* = 11 - 6\frac{m^*}{m}$. For the first term, which accounts for the EoS at zero temperature ($T = 0$), we made use of the thermodynamic relation

$$\Delta \rho = \frac{\rho + p}{n_b} \Delta n_b \tag{3.77}$$

and the definition (3.54) of γ. This provides us with a straightforward way to incorporate the thermal pressure in the perturbation problem. In our simulations, we account for the individual thermal pressures of neutrons and protons in the core. In the crust, there are free neutrons as well as ions present. For simplicity, we assume all baryons contribute as a single Fermi liquid. This is a simplification which in essence implies a maximal thermal component of the pressure. This assumption will be relaxed in future work using the results of, e.g., [67].

Regarding the perturbation equations, the thermal pressure can be incorporated by the simple substitution

$$\gamma p_0 \quad \rightarrow \quad \gamma p_0 + M^* n_{\mathrm{n}} \left(\frac{\partial p_{th}^{\mathrm{n}}}{\partial n_{\mathrm{n}}} \right)_T + M^* n_{\mathrm{p}} \left(\frac{\partial p_{th}^{\mathrm{p}}}{\partial n_{\mathrm{p}}} \right)_T. \tag{3.78}$$

Effectively, this substitution just modifies the value of γ; it could be absorbed into the adiabatic index via

$$\gamma \quad \rightarrow \quad \gamma + \frac{1}{p_0} \left[M^* n_{\mathrm{n}} \left(\frac{\partial p_{th}^{\mathrm{n}}}{\partial n_{\mathrm{n}}} \right)_T + M^* n_{\mathrm{p}} \left(\frac{\partial p_{th}^{\mathrm{p}}}{\partial n_{\mathrm{p}}} \right)_T \right]. \tag{3.79}$$

Since all quantities in this expression are positive, there is no doubt that the inclusion of the thermal pressure will lead to convectively stable g-modes, according to an analysis of the Schwarzschild discriminant (3.55).

3.5 The Crust Elasticity

The approximation of the neutron star to be a perfect fluid has to be abandoned in view of the solid crust which forms in the very early stages of a neutron star's life. This elastic crust supports shear stresses which by definition do not exist in a perfect fluid. Accounting for such stresses means to introduce off-diagonal terms in the stress-energy tensor. As we are assuming the background to be in a relaxed, unstrained state, these alterations appear in the perturbed stress-energy tensor only and leave the equilibrium configuration untouched.

Following [32], the shear strain tensor is given by

$$\delta s^{\nu}_{\mu} = \frac{1}{2}\left(\perp^{\sigma}_{\mu}\perp^{\lambda\nu} - \frac{1}{3}\perp^{\nu}_{\mu}\perp^{\sigma\lambda}\right)\Delta g_{\sigma\lambda} \tag{3.80}$$

and enters the stress-energy tensor via the anisotropic stress tensor

$$\delta\pi^{\nu}_{\mu} = -2\check{\mu}\delta s^{\nu}_{\mu}, \tag{3.81}$$

where $\check{\mu}$ is the shear modulus and the projection operator $\perp^{\sigma}_{\mu}$ is given by

$$\perp^{\sigma}_{\mu} = \delta^{\sigma}_{\mu} - N^{\sigma}N_{\mu}. \tag{3.82}$$

We have assumed a Hookean relationship between the shear strain and stress. The total perturbed stress-energy tensor then takes the form

$$\delta T^{\mathrm{tot}}_{\mu\nu} = \delta T_{\mu\nu} + \delta\pi_{\mu\nu}, \tag{3.83}$$

which leads to severe alterations of the perturbation equations when compared to the set of equations (3.33) and (3.35) which govern the perturbations of a perfect fluid.

It turns out to be useful to define two new variables which are related to the traction. The radial traction, T_1, and the tangential traction, T_2, are defined by

$$T_1 := \delta\pi^{r}_{r} \quad \text{and} \quad T_2 := \delta\pi^{\theta}_{r}. \tag{3.84}$$

Both traction variables vanish in the perfect fluid case. However, we will later see that they are crucial in the implementation of the junction conditions at the crustal interfaces (see Section 3.6).

The perturbations of the elastic crust are governed by the perturbed Einstein equa-

tions and hence the pulsation equations follow from

$$\delta G_{\mu\nu} = 8\pi\delta T_{\mu\nu} \quad \text{and} \quad \delta\left(\nabla_\mu T^{\mu\nu}\right) = 0, \tag{3.85}$$

where $\delta T^{\mu\nu}$ denotes the *total* stress-energy tensor as given in equation (3.83). In addition, we have the definitions of the two traction variables, T_1 and T_2, which in their expanded form read

$$T_1 = \frac{4}{3}\check{\mu}\left[e^{-\lambda/2}(2l-4)W + 2re^{-\lambda/2}W' + r^2(K-H_2) - l(l+1)V\right], \tag{3.86}$$

$$T_2 = -2\check{\mu}\left[e^{\lambda/2}W - (l-2)V - rV'\right]. \tag{3.87}$$

Furthermore and identically to the perfect fluid case [18], we will use the Lagrangian variation of the pressure as an independent variable

$$X := -\frac{1}{r^l}e^{\nu/2}\Delta p \tag{3.88}$$

$$= \frac{\gamma p}{r^2}e^{\nu/2}\left[e^{-\lambda/2}(l+1)W + re^{-\lambda/2}W' - r^2(K+\frac{1}{2}H_2) + l(l+1)V\right]. \tag{3.89}$$

For brevity and clarity, we have suppressed the angular dependence.

The full set of perturbation equations for the elastic crust (we have used the background equations in order to simplify the expressions) then reads:

$$H_1' = \left[\frac{1}{2}(\lambda'-\nu') - \frac{l+1}{r}\right]H_1 + \frac{e^\lambda}{r}\left[H_2 + K - 16\pi(\rho+p)V\right], \tag{3.90a}$$

$$K' = \frac{1}{r}H_2 + \frac{n+1}{r}H_1 + \left[\frac{1}{2}\nu' - \frac{l+1}{r}\right]K - \frac{8\pi}{r}e^{\lambda/2}(\rho+p)W, \tag{3.90b}$$

$$H_0' = K' - re^{-\nu}\omega^2 H_1 - \left[\frac{1}{2}\nu' + \frac{l-1}{r}\right]H_0 - \left[\frac{1}{2}\nu' + \frac{1}{r}\right]H_2 + \frac{l}{r}K - \frac{16\pi}{r}T_2, \tag{3.90c}$$

$$W' = -\frac{l+1}{r}W + re^{\lambda/2}\left[\frac{e^{-\nu/2}}{\gamma p}X - \frac{l(l+1)}{r^2}V + \frac{1}{2}H_2 + K\right], \tag{3.90d}$$

$$V' = \frac{1}{2\check{\mu}r}T_2 + \frac{e^{\lambda/2}}{r}W + \frac{2-l}{r}V, \tag{3.90e}$$

$$T_2' = -\frac{1}{2}re^\lambda(\rho+p)H_0 + \left[\frac{4ne^\lambda\check{\mu}}{r} - e^{\lambda-\nu}r\omega^2(\rho+p)\right]V + e^{\lambda/2}p'W$$
$$+ re^{\lambda-\nu/2}\left(X - \frac{1}{2r^2}e^{\nu/2}T_1\right) + \left[\frac{1}{2}(\lambda'-\nu') - \frac{l+1}{r}\right]T_2. \tag{3.90f}$$

In addition to these six ODEs, we have three algebraic relations:

$$H_2 = H_0 + 64\pi\check{\mu}V, \tag{3.91a}$$

$$\left[\frac{re^{-\lambda}}{2}(r\nu'-2) + (n+1)r\right]H_0 = r^2e^{-\lambda}\left[\omega^2re^{-\nu} - \frac{n+1}{2}\nu'\right]H_1$$

$$+\left[nr-\omega^2 r^3 e^{-\nu}-\frac{1}{4}r^2 e^{-\lambda}\nu'(r\nu'-2)\right]K$$
$$+8\pi r^3 e^{-\nu/2}X+8\pi r T_1-16\pi r e^{-\lambda}T_2, \tag{3.91b}$$
$$\frac{2}{3}e^{-\nu/2}\check{\mu}r^2X-\frac{1}{4}\gamma p T_1=\check{\mu}\gamma p\left[2e^{-\lambda/2}W-r^2K+l(l+1)V\right]. \tag{3.91c}$$

The origin of the equations are as follows (for brevity, we denote the components of the Einstein equations with $[\mu\nu]$ as a shortcut for $G_{\mu\nu}=8\pi T_{\mu\nu}$): Equations (3.90a), (3.90b) and (3.90c) are $[t\theta]$, $[tr]$ and $[r\theta]$, respectively; (3.90d) and (3.90e) are due to the definitions of X and T_2, respectively; (3.90f) is $\delta\left(\nabla_\mu T^\mu_\theta\right)=0$; (3.91a) is the difference $[\theta\theta]-[\phi\phi]$; (3.91b) is $[rr]$ and (3.91c) is obtained by removing W' from the definitions of X and T_1.

In comparison to the perfect fluid case, the differential equations for H_1', K' and W' are only slightly altered; merely H_0 got replaced by H_2. The equation for H_0'—which we do not use in the perfect fluid case—now involves the tangential traction as well as terms for H_0 and H_2 whose separation was not visible beforehand since we had $H_2=H_0$. The equation for V' is new and does not have a perfect fluid equivalent; it becomes a tautology in the $\check{\mu}\to 0$ case. The differential equation for T_2' used to be the algebraic relation between the variables H_0, V, W and X, cf. equation (3.35b). We do not use the equation $\delta\left(\nabla_\mu T^\mu_\theta\right)=0$ anymore; it used to serve as the evolution equation solely for X' and it now contains the radial derivatives of both X and T_1, neither of which can be isolated since they appear nowhere else. We could introduce a new variable

$$Y:=X+\frac{1}{r^2}e^{\nu/2}T_1 \tag{3.92}$$

and transform the latter equation into a differential equation for the derivative Y'. However, we choose not to do so since we would only extend the set of variables by a new one without gaining new insight or simplicity. For completeness, we show this equation here:

$$\begin{aligned}\left(X+\frac{1}{r^2}e^{\nu/2}T_1\right)'=&-\frac{l}{r}\left(X+\frac{1}{r^2}e^{\nu/2}T_1\right)+\frac{1}{2}(\rho+p)e^{\nu/2}\left\{\left[\frac{1}{r}-\frac{\nu'}{2}\right]H_0\right.\\&+\left[r\omega^2e^{-\nu}+\frac{n+1}{r}\right]H_1+\left[\frac{3}{2}\nu'-\frac{1}{r}\right]K-\nu'\frac{l(l+1)}{r}V\\&-\frac{1}{r}\left[8\pi(\rho+p)e^{\lambda/2}+2\omega^2e^{\lambda/2-\nu}-r^2\left(r^{-2}e^{-\lambda/2}\nu'\right)'\right]W\\&\left.-\frac{16\pi}{r}T_2\right\}-\frac{1}{r^3}e^{\nu/2}\left[3T_1+l(l+1)T_2\right],\end{aligned} \tag{3.93}$$

The algebraic equations (3.91a) and (3.91b) are not very different from their perfect fluid equivalents; they are simply corrected for the appearance of elastic stresses. Equation (3.91c) is new and has no equivalent in the non-elastic case.

In the limit of a vanishing shear modulus, $\check{\mu}\to 0$, it can easily be shown that the

equations for the solid crust reduce to the fluid equations. We will, however, use this new set of equations only in the region where the elastic crust is present; for both the core and the fluid ocean, we still use the perfect fluid equations.

The simple relation $H_0 = H_2$ between these two metric perturbations, which is valid for the perfect fluid, is broken up by the presence of the crust. Instead, we now have

$$H_2 = H_0 + 64\pi\check{\mu}V. \tag{3.94}$$

Furthermore, we have to deal with six instead of four independent variables for which we have to solve differential equations. This makes sense in that we expect a third wave degree of freedom equation for the crustal oscillations giving us two more first order differential equations.

3.5.1 The Formation of the Crust

We have now derived the equations governing perturbations of the elastic crust. However, in which region do we have to apply them? This obviously depends on the temperature of the star and subsequently where the crust has crystallised during the star's ageing process.

In order to quantify the thermal effects on the star's oscillation spectrum, we use thermal profiles from cooling simulations; a detailed description of how these profiles were obtained can be found in Section 2.3.1. Using these temperature profiles and a model for the crust crystallisation, we can determine the region in which the crust is solid. The standard idealised model for the crust of a neutron star is a one-component plasma, in which ions of charge Ze, ion number density n_I and temperature T are free to move. The thermodynamics of such a plasma can be described by the dimensionless Coulomb coupling parameter

$$\Gamma = \frac{(Ze)^2}{akT}, \tag{3.95}$$

where $a = (4\pi n_I/3)^{-1/3}$ denotes the inter-ion spacing and k is the Boltzmann constant. Calculations by Farouki & Hamaguchi [70] show that the crust crystallises as Γ increases (due to cooling) above $\Gamma_m \approx 173$. The EoS (see Section 2.2) as provided by Samuelsson [57] we are using provides us with all parameters required to quantify the crust freezing. Given the temperature profiles from our thermal evolution we calculate Γ and assume the crust to be elastic in the region in which $\Gamma \geq \Gamma_m$. This must be seen as an approximation for two different reasons. Firstly, the quantity Γ_m is associated with uncertainties of a few percent; a slightly different value will affect the thickness of the crust and thereby the frequencies of the shear modes. Similar to the choice of the EoS, we do not further investigate these effects in this study and take the value of $\Gamma_m = 173$ as given. It can easily be adjusted once more accurate data are available. Secondly, we neglect the fact that the crystallisation does not happen immediately as

soon as Γ crosses a certain threshold, but is a process that happens over a certain period of time.

In Figure 3.1, we show how the crust region evolves as the star cools. The crust of the neutron star stays liquid for a bit more than a day; then the crust starts to crystallise close to the core-crust interface. The outer boundary of the solid crust is determined by the threshold $\Gamma_m = 173$ for the Coulomb coupling parameter, while we choose the crust-core interface at the fixed density of $\rho_{\rm cc} = 1.03 \cdot 10^{14}\,{\rm g\,cm^{-3}}$ as the inner boundary. Within the first three years the crust gains quickly in width up to about 580 m. After about hundred years without any significant further crystallisation, the temperature has dropped below the melting temperature also in the outer layers of the crust and the elastic crust eventually extends nearly to the surface of the star.

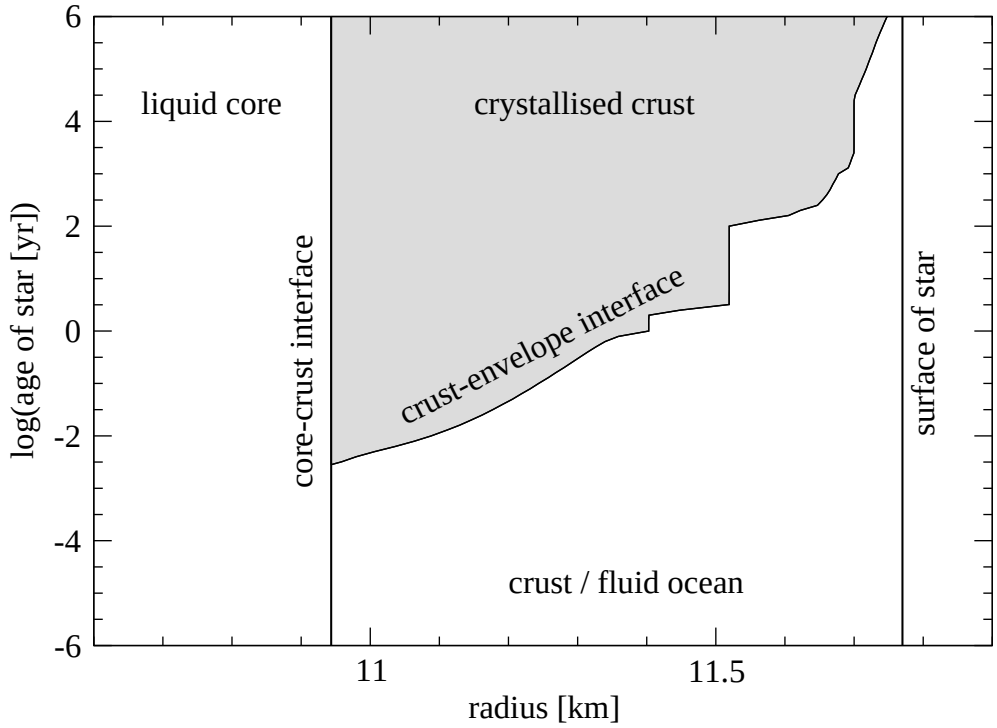

Figure 3.1: The formation of the solid crust over time. We show only the outer layer of our model star. The area where the crust is crystallised is shaded in grey; this region is calculated using a sharp threshold of $\Gamma > 173$ (see text).

3.6 The Implementation of Interfaces and Density Discontinuities

In a realistic neutron star, we expect phase transitions to occur; primarily in the crust where detailed calculations suggest a layering of the matter where each layer is composed of a certain type of ions. As we have described in Section 2.2 the transition happens over a very narrow pressure range. This requires a high resolution at the

phase transition in order to resolve the rapid change in density over a short distance—a TOV solver with adaptive mesh refinement will automatically lower the step size at these locations. Alternatively, we can approximate such phase transitions by an actual discontinuity in density rather than a sharp but continuous change.

Aside from the change of nuclear composition in the crust, we will have three interfaces in our particular neutron star model. There is the neutron drip in the crust, the appearance of muons in the core (see Section 4.2) and we also have an artificial density discontinuity at the crust-core interface due to our matching between the different EoSs. Furthermore, we need to account for the inner and outer edges of the solid crust.

In terms of our simulations, we need to evaluate how these different interfaces impact the perturbation variables. Some of the variables might be continuous whilst others may be discontinuous. We have to distinguish between interfaces where all background quantities are continuous and interfaces where the density has a discontinuity. Unfortunately, the analysis of the latter situation leads to a contradiction which we have not been able to resolve yet.

3.6.1 The Formalism to Determine the Junction Conditions across Interfaces

An essential tool for this analysis are the first and second fundamental forms which both have to be continuous across the perturbed interface [71] (we do not have "delta-function-like" discontinuities here). In order to calculate these, we have to describe the perturbed surface by a normal vector, N^μ. There are different possibilities to define these interfaces, e.g. their location given by $r = r_i + \xi^r$, or hypersurfaces given by level surfaces of the pressure or other scalar quantities. Since we need to do this analysis for several different cases (single fluid vs. multi-fluid, fluid-solid interface, density discontinuities, and so on), we will keep the analysis as general as possible and specialise to the actual variable defining the hypersurface only when necessary.

Let us consider level surfaces of a given scalar quantity q. The space-like normal to these surfaces is given by

$$N^\mu = \frac{g^{\mu\nu}\nabla_\nu q}{\sqrt{\nabla_\lambda q \nabla^\lambda q}}, \tag{3.96}$$

and by construction we have $N^\mu N_\mu = 1$. The first fundamental form (or the induced three-metric) on the level surfaces, $\gamma_{\mu\nu}$, is

$$\gamma_{\mu\nu} = \perp^\sigma_\mu \perp^\tau_\nu g_{\sigma\tau}, \tag{3.97}$$

where the projection operator $\perp^\sigma_\mu$ is given by

$$\perp^\sigma_\mu = \delta^\sigma_\mu - N^\sigma N_\mu. \tag{3.98}$$

The second fundamental form, $K_{\mu\nu}$, (the extrinsic curvature) is defined as

$$K_{\mu\nu} = -\perp^{\sigma}_{\mu}\perp^{\tau}_{\nu}\nabla_{(\sigma}N_{\tau)}. \tag{3.99}$$

We decompose the scalar quantity which defines our level surfaces into a background and a perturbed part,

$$q(t,r,\theta) = q_0(r) + \delta q(t,r,\theta). \tag{3.100}$$

To keep the analysis universally valid, we will use the bare components of the perturbed metric (for polar perturbations) and resort to our specific definition (3.13) only later. The non-trivial components of the first and second fundamental form are

$$\gamma_{tt} = -e^{\nu} + \delta g_{tt}, \tag{3.101a}$$
$$\gamma_{tr} = \delta g_{tr} - e^{\lambda}\frac{\delta\dot{q}}{q_0'}, \tag{3.101b}$$
$$\gamma_{r\theta} = -e^{\lambda}\frac{\delta q_{,\theta}}{q_0'}, \tag{3.101c}$$
$$\gamma_{\theta\theta} = r^2 + \delta g_{\theta\theta}, \tag{3.101d}$$
$$\gamma_{\phi\phi} = r^2\sin^2\theta + \delta g_{\phi\phi}, \tag{3.101e}$$

and

$$K_{tt} = \frac{\nu'}{2}e^{\nu-\lambda/2} - e^{\lambda/2}\frac{\ddot{q}}{q_0'} + \frac{1}{e^{\lambda/2}}\delta\dot{g}_{tr} - \frac{1}{2e^{\lambda/2}}\delta g_{tt}' - \frac{\nu'}{4}e^{\nu-3\lambda/2}\delta g_{rr}, \tag{3.102a}$$
$$K_{tr} = \frac{\nu'}{2}\left(e^{\lambda/2}\frac{\delta\dot{q}}{q_0'} - e^{-\lambda/2}\delta g_{tr}\right), \tag{3.102b}$$
$$K_{t\theta} = -e^{\lambda/2}\left(\frac{\delta\dot{q}_{,\theta}}{q_0'} - \frac{1}{2e^{\lambda}}\delta g_{tr,\theta}\right), \tag{3.102c}$$
$$K_{r\theta} = \frac{e^{\lambda/2}}{r}\frac{\delta q_{,\theta}}{q_0'}, \tag{3.102d}$$
$$K_{\theta\theta} = -\frac{r}{e^{\lambda/2}} - e^{\lambda/2}\frac{\delta q_{,\theta\theta}}{q_0'} - \frac{1}{2e^{\lambda/2}}\left(\delta g_{\theta\theta}' - \frac{r}{e^{\lambda}}\delta g_{rr}\right), \tag{3.102e}$$
$$K_{\phi\phi} = -\sin^2\theta\left(\frac{r}{e^{\lambda/2}} + \cot\theta e^{\lambda/2}\frac{\delta q_{,\theta}}{q_0'} + \frac{1}{2\sin^2\theta e^{\lambda/2}}\delta g_{\phi\phi}' - \frac{r}{2e^{3\lambda/2}}\delta g_{rr}\right). \tag{3.102f}$$

These components have to be continuous across the interfaces which allows us to impose junction conditions for the background variables as well as the perturbation variables (since we can construct a background independently of the oscillations).

Independent of the actual physical content of the quantity q as well as the nature of the interface, we can draw the first conclusions on the continuity of several variables. We start with the background variables (omitting the first-order terms in the above components for a moment). We denote by $[q]_r$ the jump of the quantity at the interface

located at the radius r,

$$[q]_r := \lim_{\varepsilon\to 0} q(r+\varepsilon) - \lim_{\varepsilon\to 0} q(r-\varepsilon). \tag{3.103}$$

The continuity of γ_{tt}, $K_{\theta\theta}$ and K_{tt} imply

$$[\nu]_r = 0, \qquad [\lambda]_r = 0, \qquad [\nu']_r = 0, \tag{3.104}$$

in that order. The latter two in combination with the background Einstein equations enforce continuity of the pressure in equilibrium

$$[p_0]_r = 0. \tag{3.105}$$

The equation (2.7c) governing the radial pressure derivative yields

$$\frac{p_0'(r)}{\tilde{p}_0'(r)} = \frac{p_0(r)+\rho_0(r)}{p_0(r)+\tilde{\rho}_0(r)}, \tag{3.106}$$

where we have used the tilde to distinguish between the values of the quantities on either side of the interface; a tilde denotes that the quantity is to be evaluated on the side of the interface which has the lower density (as seen from the surface of the star).

We now turn to the perturbation variables and hence consider the entire coefficients, as given in (3.101) and (3.102). We note that the temporal and angular derivatives of δq are irrelevant for this discussion since we consider single frequency modes and hence have

$$\delta\dot{q} = i\omega\delta q, \quad \text{and} \quad \delta q_{,\theta} = \delta q \frac{\mathrm{d}P_l}{\mathrm{d}\theta}, \tag{3.107}$$

and likewise for higher or mixed derivatives. In terms of continuity, we can treat these derivatives as if there simply appeared δq since the differential operators turn into continuous factors. In conjunction with the background junction conditions (3.104), we find that the components γ_{tt}, $\gamma_{\theta\theta}$, $\gamma_{r\theta}$ and γ_{tr} imply

$$[H_0]_r = 0, \qquad [K]_r = 0, \qquad [\frac{\delta q}{q_0'}]_r = 0, \qquad [H_1]_r = 0, \tag{3.108}$$

respectively, in that order.

We point out that up to this point, the analysis is completely generic and does not rely on any assumptions on the nature of the adjacent layers nor the physical content of the scalar quantity q. As a side note, if we follow Finn's [32] approach and let q describe the location of the perturbed surface, i.e. $q_0 = r$ and $\delta q = \xi^r$, then the generic condition in (3.108) turns into $[\xi^r]_r = 0$ which is equivalent to

$$[W]_r = 0. \tag{3.109}$$

The physical meaning of this condition is that there cannot be a gap in the perturbed matter.

It is also worth noting that we have fully exhausted the continuity of the first fundamental form, $\gamma_{\mu\nu}$, which already implies continuity of the components K_{tr}, $K_{t\theta}$ and $K_{r\theta}$ of the extrinsic curvature; merely the continuity conditions on K_{tt} and $K_{\theta\theta}$ potentially contain new information (the continuity of $K_{\phi\phi}$ is equivalent to the continuity of $K_{\theta\theta}$).

Let us first consider K_{tt}. After applying the previously derived junction conditions, the continuity of K_{tt} implies

$$\left[\delta g'_{tt} + \frac{\nu'}{2} e^{\nu-\lambda} \delta g_{rr}\right]_r = 0. \tag{3.110}$$

As per our definition of the perturbed metric, $\delta g_{tt} = -r^l e^{\nu} H_0$ and $\delta g_{rr} = -r^l e^{\lambda} H_2$, we find the condition

$$\left[H'_0\right]_r = -\frac{\nu'}{2} \left[H_2\right]_r . \tag{3.111}$$

In the same way, we can infer

$$\left[\delta g'_{\theta\theta} - \frac{r}{e^{\lambda}} \delta g_{rr}\right]_r = 0 \qquad \Rightarrow \qquad \left[K'\right]_r = \frac{1}{r} \left[H_2\right]_r \tag{3.112}$$

from the continuity of $K_{\theta\theta}$, where we have used $\delta g_{\theta\theta} = -r^{l+2} K$.

3.6.2 Interfaces Involving the Solid Crust

Depending on the temperature of the star, parts of the crustal region may be solid. We need to work out the junction conditions at the "surfaces" of the solid crust as well as junction conditions for the variables at interfaces within the solid crust which are due to phase transitions. As we have shown, we have $H_2 \neq H_0$ in the solid crust.

First, we combine the continuity conditions (3.112) and (3.111), by subtracting them to

$$\left[H'_0 - K'\right]_r = -\left(\frac{\nu'}{2} + \frac{1}{r}\right) \left[H_2\right]_r \tag{3.113}$$

and then apply this condition to differential equation (3.90c) for H'_0 which we recast into the following form

$$H'_0 - K' = -r e^{-\nu} \omega^2 H_1 - \left[\frac{\nu'}{2} + \frac{l-1}{r}\right] H_0 - \left[\frac{\nu'}{2} + \frac{1}{r}\right] H_2 + \frac{l}{r} K - \frac{16\pi}{r} T_2, \tag{3.114}$$

in order to make the application of the above continuity condition (3.113) obvious. After applying the other conditions, too, we find the continuity of the tangential traction,

$$\left[T_2\right]_r = 0. \tag{3.115}$$

Second, we apply condition (3.112) to the equation (3.90b) for K' which leads to

$$[(\rho_0 + p_0)W]_r = 0. \tag{3.116}$$

We keep the extra factor of $(\rho_0 + p_0)$ in here in order to account for possible density discontinuities. If the density is continuous, this condition reduces to the continuity of the radial displacement, $[W]_r = 0$. In contrast, at a phase transition with density discontinuity, we would expect a jump in the radial displacement. This seems paradoxical as a discontinuous displacement will lead to voids in the perturbed matter fluid; we will address this issue in detail in Section 3.6.4.

Additionally to these conditions, the equations of motion allow us to derive continuity conditions; these conditions, however, are not independent of the previously derived ones but they can give further insight into the problem. When implementing the junction conditions, we have to be careful not to select a non-independent set. We quote the algebraic condition (3.91b), recast into

$$\begin{aligned} 8\pi r^3 e^{-\nu/2} X + 8\pi r T_1 = &\left[\frac{r e^{-\lambda}}{2}(r\nu' - 2) + (n+1)r\right] H_0 + \left[\omega^2 r e^{-\nu} - \frac{n+1}{2}\nu'\right] H_1 \\ &- \left[nr - \omega^2 r^3 e^{-\nu} - \frac{1}{4} r^2 e^{-\lambda}\nu'(r\nu' - 2)\right] K + 16\pi r e^{-\lambda} T_2. \end{aligned} \tag{3.117}$$

As per the discussion above, the quantities on the right-hand side are continuous without exception; this implies continuity of the left-hand side as well, i.e.

$$[H_0]_r = [H_1]_r = [K]_r = [T_2]_r = 0 \qquad \Rightarrow \qquad \left[r^2 e^{-\nu/2} X + T_1\right]_r = 0. \tag{3.118}$$

Furthermore, the algebraic condition (3.91a) leads to

$$[H_2]_r = 64\pi \left[\check{\mu} V\right]_r. \tag{3.119}$$

3.6.3 Interfaces within a Perfect Fluid

We will now consider the case of a perfect fluid. In principle, this is a special case of the previous section, where we disregard the traction, $T_1 = T_2 = 0$, and set $H_2 = H_0$; however, as this case will become important again in the multi-fluid case, we will give it some consideration here.

At first, we will simply repeat the previous analysis and specialise it to the perfect fluid case. While the continuity of K_{tt} (which now implies $[H_0'] = 0$, cf. equation (3.111)) does not provide new information anymore, the continuity of $K_{\theta\theta}$ applied to (3.33b) for K' yields the same results as before,

$$[(\rho_0 + p_0)W]_r = 0. \tag{3.120}$$

However, this is in contrast to the unconditional continuity of W, as derived in (3.109). Since this condition physically makes more sense, we will opt for $[W]_r = 0$ in our implementation; see also Section 3.6.4.

We can also use the algebraic condition (3.35b) on the perturbation variables which now leads to the continuity of the Lagrangian pressure perturbation,

$$[H_0]_r = [H_1]_r = [K]_r = 0 \qquad \Rightarrow \qquad [X]_r = 0. \tag{3.121}$$

This is the reduced version of condition (3.118); we see that the continuity of H_0, H_1 and K immediately imply the continuity of X.

Altogether, we can choose the four independent conditions

$$[H_1]_r = [K]_r = [W]_r = [X]_r = 0 \tag{3.122}$$

for the matching at e.g. density discontinuities. These four variables are usually the ones we integrate within a perfect fluid layer (cf. the perturbation equations (3.33)). Since they have to be continuous, there is no need to slice the neutron star into more layers at a density discontinuity; the continuity conditions allow us to continue integrating the ODEs across the discontinuity without further ado.

3.6.4 More Junction Conditions and Undesirable Results

We have already highlighted that we have arrived at contradicting results. Using Finn's approach, where the hypersurfaces are located at $r_i = r + \xi^r$, we found the unconditional continuity of the radial displacement, see equation (3.109),

$$[W]_r = 0, \tag{3.123}$$

while the continuity of $K_{\theta\theta}$ and thence the continuity of K' implied

$$[(\rho_0 + p_0)W]_r = 0, \tag{3.124}$$

as shown in (3.120). The problem emerges as soon as we consider an interface at a density discontinuity; this is true for this entire discussion: as long as the density is continuous, no problem arises.

This is a clear mathematical contradiction: we have proved that a given function is continuous and discontinuous at one point at the same time, which obviously cannot be true. Physically, it makes sense that the radial displacement, W, is continuous as this condition ensures that no gap in the perturbed fluid emerges; and we will implement strictly this condition in our code.

We are unable to resolve this issue at the time, but we point out another related discrepancy. In his work on the elastic crust, Finn claims to arrive at the following two

junction conditions due to the extrinsic curvature (cf. equations (64) in [32]):

$$0 = \left[\frac{1}{2}\nu' H_2 + H_0' + r^{-2}\left(\nu' e^{-\lambda/2}\right)' W\right]_r, \tag{3.125}$$

$$0 = \left[H_2 - rK' + 2\left(r^{-1}e^{-\lambda/2}\right)' W\right]_r. \tag{3.126}$$

The appearance of H_0' as well as K' in both these conditions suggest that they stem from the continuity of K_{tt} and $K_{\theta\theta}$, respectively; this is in agreement with our analysis where exactly these two components remain (see general discussion at the beginning of this section). After a few algebraic manipulations and using our definition for the perturbed metric, we find

$$\frac{2e^{\lambda/2-\nu}}{r^2}K_{tt} = \frac{1}{2}\nu' H_2 + H_0' + \left(\nu' + \frac{2}{r}\right)H_0 + 2e^{-\nu}r\omega^2 H_1 - 2r^{-1}e^{-\nu-\lambda/2}\ddot{W}, \tag{3.127}$$

$$-\frac{2e^{\lambda/2}}{r^3}K_{\theta\theta} = H_2 - rK' + 4K + 2r^{-2}e^{-\lambda/2}W_{,\theta\theta}, \tag{3.128}$$

where we have specified to $l = 2$ for easier comparison. Our expressions and Finn's coincide to the first two terms but the remainders differ and we are unable to verify by means of algebraical transformations or using background and/or perturbation equations that they are identical (they have to differ anyway due to slightly different definitions of the displacement vector and the metric perturbations; however, these differences by continuous factors are irrelevant for this discussion here). In fact, we should not be able to prove their equality since, while the three remaining terms in (3.127) are continuous, this is not the case for the one remaining term in (3.126) due to the appearance of the discontinuous quantity $\lambda' \propto \rho$.

We can view that problem from a different perspective. If we assume continuity of the displacement, $[W]_r = 0$, then we can prove, using (3.108), that Finn's second condition (3.126) holds true. It further implies that K' is *not* continuous across interfaces where the density jumps. This contrasts our finding that $[K']_r = 0$, cf. equation (3.112) (remember that $[H_2]_r = 0$ in a perfect fluid).

Where is the flaw in our derivation of $[K']_r = 0$? The calculations are laid out by Finn [32] as well as Andersson et al. [36] to great detail and up to and including the first fundamental form we fully agree with both calculations. However, their results for the second fundamental form differs. While we are able to verify the results of Andersson et al. (and we are confident of the correctness due to the small steps taken in the derivation), knowledge of the precise derivation of Finn's results (of which we are not aware, unfortunately) would shed light on this issue. As a temporary solution, we will avoid using the continuity of K' in our study.

We are going to study multi-fluid stars at later stages of this project. In this case, it might make more sense to resort to a different scalar than the radial component of

the displacement vector in order to describe hypersurfaces. Andersson et al. [36] have opted for the pressure as scalar quantity. They have derived junction conditions for the multi-fluid problem; however, also in this case are we able to arrive at contradicting junction conditions.

They make extensive use of the Eulerian pressure perturbation which can be written as

$$\delta p = r^l \left[\frac{\nu'}{2re^{\lambda/2}} (\rho_0 + p_0) W - e^{-\nu/2} X \right]. \tag{3.129}$$

During the general analysis in Section 3.6.1 we have seen that it is not δp which is continuous but the fraction $\delta p / p_0'$. We use (3.106) in order to relate the Eulerian pressure on either side of the interface,

$$\frac{\delta p}{p_0'} = \frac{\delta \tilde{p}}{\tilde{p}_0'} \Rightarrow \delta p = \frac{\rho_0 + p_0}{\tilde{\rho}_0 + p_0} \delta \tilde{p}. \tag{3.130}$$

We insert expression (3.129) for the Eulerian pressure into this equation and after a few algebraic manipulations and making use of (3.109) we find

$$\tilde{X} = \frac{\tilde{\rho}_0 + p_0}{\rho_0 + p_0} X + \frac{\nu' e^{\nu/2}}{2R_c e^{\lambda/2}} \left(1 - \frac{\tilde{\rho}_0 + p_0}{\rho_0 + p_0} \right) (\rho_0 + p_0) W, \tag{3.131}$$

where R_c is the radius at the interface. This means that, in general, the Lagrangian pressure perturbation, X, is *not* continuous across interfaces where the density changes discontinuously. (If the density is continuous, $\tilde{\rho}_0 = \rho_0$, the last equality simplifies to $\tilde{X} = X$.) This is in contrast to the earlier result, $[X]_r = 0$ (cf. equation (3.121)), which holds independent of any density discontinuities.

We could go further and assume that both (3.121) and (3.131) are correct. Substituting the latter into the former, we arrive at the relation

$$X = \frac{\nu' e^{\nu/2}}{2R_c e^{\lambda/2}} (\rho_0 + p_0) W \qquad \text{at } r = R_c, \tag{3.132}$$

which links X and W to each other *at the interface*. This link, however, holds only at interfaces where the density is discontinuous; a similar condition cannot be deduced if the density is continuous. While such a condition is to be questioned from a physical point of view, we have not yet found a clear mathematical contradiction in this case.

At this moment, we are, unfortunately, unable to resolve this issue. The problem of the junction conditions has been addressed by several authors in different physical set-ups. Finn [27], Sotani et al. [29] as well as Miniutti et al. [30] considered the case of density discontinuities in neutron star matter in different settings; without showing a detailed calculation, they claim that the radial displacement, W, as well as the Lagrangian pressure perturbation, X, are continuous. Schutz [72] also considered density discontinuities (in general, without immediate application) and argues that X

must be continuous across such interfaces. Finn reconsidered the problem for an elastic crust [32] while Andersson et al. worked on the two-fluid case [36]; both articles show a fairly detailed calculation (which we followed to a great extent during the analysis in this section), however, neither of them uncover the contradictions stated above. The knowledge of the precise derivation of Finn's results for the components of the second fundamental form would probably help in resolving the contradictions and to understand why the results of Andersson et al. and Finn disagree.

We do not fully understand where precisely the problem lies, but we understand that it turns up once we take the continuity of $\delta q/q_0'$ or $K_{\theta\theta}$ into account. From a physical point of view, it makes sense that firstly, the radial displacement is continuous, $[W]_r = 0$, in order to "avoid a void" in the perturbed matter and, secondly, the Lagrangian pressure perturbation is continuous, $[X]_r = 0$, since a discontinuous pressure would lead to a net force at the considered location. However, the actual density discontinuities are small and whether we, e.g., implement $[W]_r = 0$ or $[(\rho_0 + p_0)W]_r = 0$ will most likely have only a negligible impact on the oscillations spectrum. Our solution to this problem will be to choose a healthy mix of junction conditions which are derived from the continuity of the fundamental forms or which appear physically more sensible. Nevertheless, a thorough analysis of this problem needs to be undertaken.

3.6.5 The Junction Conditions for a Single Fluid Star

Table 3.1: The junction conditions for the boundaries between a fluid and/or an elastic layer. The three generic conditions $[H_0]_r = [H_1]_r = [K]_r = 0$ are applied at every interface; we do not mention them in the table again.

	fluid	elastic
fluid	$[W]_r = 0$	$[W]_r = 0$ $[T_2]_r = 0$
elastic	$[W]_r = 0$ $[T_2]_r = 0$	$[W]_r = 0$ $[V]_r = 0$ $[T_2]_r = 0$

We have derived the junction conditions that tell us how to connect the solutions of two adjacent layers. In a single fluid star, each layer will be either fluid or elastic and we have to choose junctions conditions for three different combinations (it does not matter if an interface is fluid-elastic or elastic-fluid—the conditions will be the same in both cases). At each interface, we apply the three generic conditions, i.e. the continuity of H_0, H_1 and K. As the analysis above has shown, the radial displacement, W, has to be continuous in a single fluid star. This makes sense in order to "avoid a void" in the fluid. When at least one of the layers is elastic then the continuity of the tangential

traction, T_2, is another independent condition. Finally, we need one more condition in case we want to join two elastic layers. As such an interface is within the elastic medium, we follow Finn's [32] argument and demand the tangential displacement, V, to be continuous, too. We show the junction conditions in Table 3.1.

Besides the rather evident interfaces between the crust and the fluid as well as density discontinuities, we have to impose boundary conditions at the centre and the surface of the star, too. A Taylor expansion of the ODEs at the centre of the star, $r = 0$, reveals that not all quantities are independent, see Section 3.2.1. At the surface of the star, we demand the Lagrangian pressure variation to vanish, $X(R) = 0$. We will always have a fluid ocean in our neutron star model, which means that this boundary condition holds independent of the state of the matter inside the star.

3.7 Numerical Strategy

The numerical solution of the described problem is not straightforward and requires more steps than one might think at a first glance. It is natural to split the solution into two parts; one part concerns the solution in the interior of the star, the other one the solution in the matter-free exterior. Both regions require a conceptually different treatment.

The interior solution is a boundary value problem that has the centre and the surface of the star as its boundaries. The imposed boundary conditions determine the solution up to an arbitrary amplitude; this is not an issue since we work on a linear problem in which the amplitude does not play an essential role. We describe the interior solution in the first part of this section.

The second part of this section is devoted to the solution in the exterior of the star. Even though the mathematical description is considerably simpler due to the lack of matter, its numerical solution is peppered with difficulties; our aim is impose the boundary condition of no incoming waves "at infinity". Firstly, we have to "approximate" infinity by a large radial coordinate, secondly—and this poses the major challenge—we need to numerically separate two solutions, one of which is exponentially growing while the other one is exponentially decaying.

Once both part solutions are calculated, they can be matched at the surface of the star. The final result of the procedure is the knowledge of the two amplitudes of incoming and outgoing gravitational waves for a prescribed complex frequency ω. We then need to find such frequencies ω for which the incoming wave amplitude vanishes; these are the eigenfrequencies of our system.

3.7.1 The Inner Solution

Our numerical strategy to determine the oscillation modes is conceptually the same as in several previous studies about polar oscillations, the closest being Lin et al. [37]

where a three-layer star is considered. The essential difference is that the "middle" layer in their study is considered superfluid whereas in our case this layer shapes the elastic crust. However, we also have to deal with different sets of equations depending on whether a given layer is considered a perfect fluid or the elastic crust as well as junction conditions in order to connect the layers.

Now, we will describe the details of the numerical procedure for the interior solution. In this chapter, we consider a star with up to three layers. However, as more physics enters the arena, we will have to slice the neutron star into more layers, each of which extends over a region in which the neutron star matter is homogeneous in the sense that it can be described by one and the same set of equations. Thus, in prospect of extending our work to account for superfluidity, where we will certainly have more than three distinct regions within the star, we will for generality as well as for clarity consider a star with n layers. Furthermore, the same procedure with exactly the same underlying idea and very similar junction condition has already been explained to great detail for a three-layer star by Lin et al. [37]. Hence, using this n-layer description and applying it to our 3-layer star together with the junction conditions from Section 3.6 is straightforward.

Let us now consider a neutron star which radially consists of n layers. The interfaces between the layers, including the centre and the surface of the star, are located at the radii $0 = R_0 < R_1 < R_2 < \cdots < R_{n-1} < R_n = R$, where R is the star's radius. Within each of the different layers, the dynamics and the perturbations, respectively, are governed by a certain set of equations which obviously depends on the nature of the matter within this region. It could be, for instance, a perfect fluid, the elastic crust or a superfluid etc. We conveniently write the equations for layer $i \in \{1, 2, \ldots, n\}$ as

$$\frac{\mathrm{d}^{(i)}\mathbf{Y}}{\mathrm{d}r} = {}^{(i)}\mathbf{Q} \cdot {}^{(i)}\mathbf{Y} \quad \text{for} \quad r \in [R_{i-1}, R_i], \tag{3.133}$$

where ${}^{(i)}\mathbf{Y} = (y_1, \ldots, y_{k_i})$ is an abstract vector field with as many entries, say k_i, as there are independent variables in this layer (in most of the cases, we will have four or six independent variables); ${}^{(i)}\mathbf{Q} = {}^{(i)}\mathbf{Q}(r, l, \omega)$ is a $k_i \times k_i$ matrix (depending also on the background fields, which we have suppressed in this notation). The variables y_i are placeholders for the corresponding perturbations variables, like H_1, K, V, etc.

Let us now find the general solution in layer i. Since we, a priori, do not have any boundary conditions for this layer, we have to choose some set of values for ${}^{(i)}\mathbf{Y}(R_{i-1})$ and integrate through this layer using (3.133) until we reach $r = R_i$. In order to find the general solution, we have to repeat this procedure k_i times; each time starting with a different set of values for ${}^{(i)}\mathbf{Y}(R_{i-1})$, where all these 'start vectors' ought to be linearly independent. This generates k_i linearly independent solutions and the general

solution (within layer i) will be some linear combination of these, i.e.

$$ {}^{(i)}\mathbf{Y}(r) = \sum_{j=1}^{k_i} c_{i,j}\, {}^{(i)}\mathbf{Y}_j(r) \quad \text{for} \quad r \in [R_{i-1}, R_i], \tag{3.134} $$

where the coefficients $c_{i,j}$ with $i = 1, \ldots, n$ (denoting the layer) and $j = 1, \ldots, k_i$ (counting the different solutions inside a particular layer) are constants to be determined by interface and boundary conditions. Before we turn to these, we want to mention some peculiarities while integrating the different layers. Firstly, in some cases it is possible to reduce the computational effort. This happens if some interface condition essentially is a fixed boundary condition for this layer; for instance, a condition could require a variable to vanish at an interface and we will then, of course, apply this condition when choosing the 'start vectors', effectively reducing the number of linearly independent solutions. Secondly, the innermost layer at the centre of the star (number 1 in our way of counting) needs special treatment as the differential equations, due to the use of spherical coordinates, are singular at the origin. We will therefore expand the solutions at the origin into Taylor series, calculate the Taylor coefficients up to second-order and use this expansion up to a small radius at which the ODEs can safely be integrated numerically. The Taylor expansion also reveals that not all perturbation quantities are independent at the origin, whereby the number of solutions is reduced. Thirdly, the outermost layer n is traditionally integrated from the surface of the star inwards since in most of the cases the Lagrangian pressure perturbation, X, is used as a variable which has to vanish at the surface, $X(R) = 0$.

Finally, we use the (remaining) interface conditions in order to determine the $\sum_i k_i$ coefficients $c_{i,j}$. An interface condition connects the solutions between layer $i-1$ and i. After fixing the overall normalisation by choosing the value of one of the coefficients $c_{i,j}$, we expect to have $(\sum_i k_i) - 1$ interface and boundary conditions (less the conditions we have already used in order to reduce the computational effort) in order to uniquely determine the solution. We give a full list of the junction conditions used throughout the whole study and show that we have specified the right number in Section 4.9. The actual interface conditions can take a variety of forms and they become more complicated when we take superfluidity into account. We are going to write down the conditions in full (also for the multi-fluid case) but will not repeat conditions which differ from listed ones only by a different choice of variables.

We use the superscript "$-$" in R_i^- to denote that we consider the value of a quantity at the inner edge of the interface (as seen from the centre of the star) at radius R_i whereas the superscript "$+$" denotes the value at the outer edge of the interface (as seen from the surface), i.e.

$$ Q(R_i^-) := \lim_{\varepsilon \to 0} Q(R_i - \varepsilon), \qquad Q(R_i^+) := \lim_{\varepsilon \to 0} Q(R_i + \varepsilon). \tag{3.135} $$

Written in full length, the interface conditions read

$$[H_1]_{R_i} = 0 \quad \Leftrightarrow \quad \sum_{j=1}^{k_i} c_{i,j}{}^{(i)}H_1(R_i^-) = \sum_{j=1}^{k_{i+1}} c_{i,j}{}^{(i+1)}H_1(R_i^+), \tag{3.136}$$

and likewise for other continuous quantities. We also have

$$W_{\mathrm{x}}(R_i^-) - W_{\mathrm{y}}(R_i^-) = 0 \quad \Leftrightarrow \quad \sum_{j=1}^{k_i} c_{i,j}\left[{}^{(i)}W_{\mathrm{x}}(R_i^-) - {}^{(i)}W_{\mathrm{y}}(R_i^-)\right] = 0, \tag{3.137}$$

and likewise for $0 = W_{\mathrm{x}}(R_i^+) - W_{\mathrm{y}}(R_i^+)$ (which we obviously have to evaluate in the $(i+1)$-th layer). Finally,

$$W_{\mathrm{x}}(R_i^-) = W_{\mathrm{y}}(R_i^+) \quad \Leftrightarrow \quad \sum_{j=1}^{k_i} c_{i,j}{}^{(i)}W_{\mathrm{x}}(R_i^-) = \sum_{j=1}^{k_{i+1}} c_{i,j}{}^{(i+1)}W_{\mathrm{y}}(R_i^+). \tag{3.138}$$

This completes the general description of the interior problem.

We note that now, given this interface formalism, only the set of equations for each layer has to be specified and the interface conditions may be given in a short notation.

3.7.2 The Exterior Solution

In the previous section, we described how we find the solution (unique up to an arbitrary amplitude) in the interior of the star. There is a solution for each choice of ω but only a discrete set of values for ω correspond to actual eigenfrequencies of the star. At an arbitrary frequency ω, we can understand the oscillations of our star to be the reaction to incoming gravitational waves; and obviously it also emits gravitational waves. We have to continue our interior solution outside the star in order to decompose the solutions into incoming and outgoing waves. When the star oscillates even when there is no incoming radiation, then we have found an eigenfrequency of the star. For reasons that become clear soon, we will consider both polar and axial perturbations at the same time in this section.

The Analytic Description of the Exterior Problem

Outside the star, the fourth-order system of equations for a perfect fluid reduces to a second-order system since there is no matter and the fluid perturbations vanish. Fackerell [73] has shown that the perturbation equations (for polar perturbations) in the exterior can—by means of a suitable variable transformation—be put into the form of a one-dimensional wave equation

$$\frac{\mathrm{d}^2 Z}{\mathrm{d}r_*^2} + \left[\omega^2 - V_Z(r_*)\right] Z = 0, \qquad \text{(Zerilli's equation)} \tag{3.139}$$

where $r_* = r + 2M\log(r-2M)$ is the tortoise coordinate which naturally emerges in the study of black hole oscillations and the effective potential $V_Z(r_*)$ is given by

$$V_Z(r_*) = 2\left(1-\frac{2M}{r}\right)\frac{n^2(n+1)r^3+3n^2Mr^2+9nM^2r+9M^3}{r^3(nr+3M)^2}, \tag{3.140}$$

with n being the shortcut $n=\frac{1}{2}(l+2)(l-1)$. In order to integrate Zerilli's equation, we need to specify initial values for $Z(R)$ and $Z'(R)$ at the surface of the star. These are given by $H_1(R)$ and $K(R)$ from the interior solution by the transformation

$$\begin{pmatrix} Z \\ Z' \end{pmatrix} = \frac{1}{fk-h}\begin{pmatrix} k & -1 \\ -h & f \end{pmatrix}\begin{pmatrix} K \\ H_1 \end{pmatrix}, \tag{3.141}$$

where the functions f, h and k are

$$f = \frac{n(n+1)r^2+3nMr+6M^2}{r^2(nr+3M)}, \tag{3.142}$$

$$h = \frac{nr^2-3nMr-3M^2}{r(r-2M)(nr+3M)}, \tag{3.143}$$

$$k = \frac{r}{r-2M}. \tag{3.144}$$

Before we proceed to explain the further procedure, we cast an eye on the axial problem. Since a perfect fluid is not subject to axial perturbations, the problem is considerably easier to start with; the equations governing axial metric perturbations in the perfect fluid ocean continue to hold in the exterior of the star, too. As was shown by Regge & Wheeler [64], the equations can also be written as a one-dimensional wave equation

$$\frac{\mathrm{d}^2Q}{\mathrm{d}r_*^2} + \left[\omega^2 - V_R(r_*)\right]Q = 0, \qquad \text{(Regge-Wheeler equation)} \tag{3.145}$$

where the Regge-Wheeler potential $V_R(r_*)$ is given by

$$V_R(r_*) = 2\left(1-\frac{2M}{r}\right)\frac{(n+1)r-3M}{r^3}. \tag{3.146}$$

The initial values $Q(R)$ and $Q'(R)$ can be obtained from $h_0(R)$ and $h_1(R)$ by

$$\begin{pmatrix} Q \\ Q' \end{pmatrix} = R^l\begin{pmatrix} 0 & R-2M \\ -\omega^2 & -(R-2M)^2 \end{pmatrix}\begin{pmatrix} h_0 \\ h_1 \end{pmatrix}. \tag{3.147}$$

Chandrasekhar has shown that the physical content of Zerilli's equation and the Regge-Wheeler equation is identical and how the corresponding functions Z and Q are related [74]; while this statement has been proven with mathematical rigour, the deeper

physical origin of this link, however, remains obscure [75]. The relevance for us lies in the fact that we can solve the exterior problem for both polar and axial perturbations conveniently in the same way. We choose to work with the Regge-Wheeler equation as it is slightly simpler than Zerilli's equation. The Regge-Wheeler function Q can be obtained from the Zerilli function Z via the relations

$$Q = \frac{1}{\kappa - 2i\omega\beta}\left[\left(\kappa + 2\beta^2 f_r\right) Z - 2\beta Z'\right], \tag{3.148}$$

$$Q' = \frac{1}{2\beta}\left[\left(\kappa + 2i\omega\beta\right) Z - \left(\kappa + 2\beta^2 f_r\right) Q\right], \tag{3.149}$$

where the coefficients are

$$\beta = 6M, \tag{3.150}$$

$$\kappa = 4n(n+1), \tag{3.151}$$

$$f_r = \left(1 - \frac{2M}{r}\right)\frac{1}{2r(nr+3M)}. \tag{3.152}$$

The Numerical Solution of the Exterior Problem

We can now turn to the numerical solution in the exterior of the star. We will follow the approach by Andersson et al. [61] and outline the relevant ideas. They introduce a new independent variable Ψ where

$$Q = \left(1 - \frac{2M}{r}\right)^{-1/2}\Psi. \tag{3.153}$$

The Regge-Wheeler equation (3.145) for Q then turns into the new differential equation

$$\left(\frac{\mathrm{d}^2}{\mathrm{d}r^2} + U(r)\right)\Psi = 0, \tag{3.154}$$

where

$$U(r) = \left(1 - \frac{2M}{r}\right)^{-2}\left[\omega^2 - V_R(r) + \frac{2M}{r^3} - \frac{3M^2}{r^4}\right]. \tag{3.155}$$

The ansatz

$$\Psi^{\pm} = q^{-1/2}\exp\left[\pm i\int_R^r q(\mathring{r})\,\mathrm{d}\mathring{r}\right] \tag{3.156}$$

for the two linearly independent solutions yields the non-linear differential equation for q,

$$\frac{1}{2q}\frac{\mathrm{d}^2 q}{\mathrm{d}r^2} - \frac{3}{4q^2}\left(\frac{\mathrm{d}q}{\mathrm{d}r}\right)^2 + q^2 - U = 0. \tag{3.157}$$

Instead of a linear wave equation, we now have to solve a non-linear equation; this may seem more complicated at first sight. However, the new differential equation comes with favourable properties: even when the solution to (3.154) oscillates wildly, the

function q may be slowly varying only which makes a numerical solution much easier. Furthermore, when U is a slowly varying function of r (which is the case for $r \to \infty$) then by means of the ansatz (3.156), q is also varying slowly and its derivatives in (3.157) can be neglected; this means we can use $q \approx \sqrt{U}$ to generate initial values for the integration of (3.157) at a large distance from the star; they are $q(\text{“far away”}) = \sqrt{U}$ and $q'(\text{“far away”}) = U'/2\sqrt{U}$.

The next step is to solve (3.157) for a particular value of ω from a point sufficiently far away from the star; this gives us values for q as well as q' at the surface of the star. We assume that the physically acceptable solution for the interior of the star corresponds to a mixture of outgoing and ingoing waves at spatial infinity, i.e.

$$\Psi = A_{\text{in}}\Psi^{+} + A_{\text{out}}\Psi^{-}. \tag{3.158}$$

Using (3.153) and (3.156), we first find $\Psi^{\pm}(R) = q^{-1/2}$ and second, we can solve for the ingoing and outgoing amplitudes, A_{in} and A_{out}. Since the solution is determined only up to a constant factor due to the linearity of the problem, it is more reasonable to investigate the ratio of the amplitudes,

$$\frac{A_{\text{in}}}{A_{\text{out}}} = \frac{Q\left\{\left(1-\frac{2M}{R}\right)\left[iq+\frac{1}{2q}q'\right]+\frac{M}{R^2}\right\}+Q'}{Q\left\{\left(1-\frac{2M}{R}\right)\left[iq-\frac{1}{2q}q'\right]-\frac{M}{R^2}\right\}-Q'}, \tag{3.159}$$

where all variables are to be evaluated at the surface of the star. A quasi-normal mode corresponds to a zero of this ratio as a function of ω.

In this discussion, we have obscured the fact that the coordinate r is taken to be complex in the exterior. It is important for the method to integrate along a straight line in the complex plane rather than along the real x-axis. The slope of this straight line depends on the chosen value of ω and is optimally taken to be $\tan\theta = -\text{Im}\omega/\text{Re}\omega$. The derivatives with respect to (complex-valued) r can easily implemented numerically using the relation

$$\frac{\mathrm{d}q}{\mathrm{d}r} = e^{-i\theta}\frac{\mathrm{d}q}{\mathrm{d}\rho}, \tag{3.160}$$

where ρ is the real distance along the integration path from the surface of the star.

3.8 Reformulating the Perfect Fluid Equations for Low Frequencies

Having laid out the physics that goes into our problem and what the corresponding equations are that govern the perturbations, we should be able to find the oscillation modes. However, it turns out that, as we are considering low-frequency oscillations like g-modes or i-modes, we are running into numerical difficulties, which firstly lead

to undesirable noise in the very low frequency regime in the stellar spectrum (higher order g-modes or thermal g-modes of old neutron stars as well as i-modes would fall into this regime), preventing us entirely from determining any eigenmode. Secondly, in regions of slightly higher frequency but still well below the f-mode frequency, the stellar spectrum appears to be reasonable; however, we are unable to reliably calculate the eigenfunctions as a kink appears at the point near the origin where we switch from the Taylor expansion to actually solving the ODEs.

The problem is of purely numerical origin and it mainly stems from the algebraic equation, which is used to calculate the perturbation variable V (cf. equation (A14) in [18]):

$$\omega^2 (\rho + p) V = e^{\nu/2} X + \frac{1}{r} p' e^{\nu - \lambda/2} W - \frac{1}{2} (\rho + p) e^{\nu} H_0. \tag{3.161}$$

A Taylor expansion around the origin (see [19]) reveals that all perturbation variables appearing in this equation, H_0, V, W and X, are of the same order of magnitude in proximity of the origin. The same holds for the coefficients appearing on the right-hand side. As we are dealing with low frequencies, $\omega \approx 0.001$, the left-hand side of this algebraic relation forces the sum of the three terms on the right-hand side to be many orders of magnitude smaller than then sum's constituents, inevitably leading to numerical cancellation and hence inaccurate results.

This problem has already been addressed by Finn [26], who proposed a different set of equations for the study of low-frequency modes in which the Eulerian pressure perturbation rather than the Lagrangian pressure perturbation is used as an independent variable. The implementation certainly improves the accuracy of our results as the effect of the cancellation is not as severe; nevertheless, the outcome does not fully satisfy our demands. Instead, we derive a new set of equations where the independent variables are a subset of the "fundamental" variables, namely H_1, K, V and W. An algebraic equation like (3.161) does not appear in this formulation and thus the cancellation is avoided.

The perturbation equations for this set of variables then read

$$H_1' = \left[\frac{1}{2}\left(\lambda' - \nu'\right) - \frac{l+1}{r}\right] H_1 + \frac{e^{\lambda}}{r}\left[H_0 + K - 16\pi (\rho + p) V\right], \tag{3.162a}$$

$$K' = \frac{1}{r} H_0 + \frac{n+1}{r} H_1 + \left[\frac{1}{2}\nu' - \frac{l+1}{r}\right] K - \frac{8\pi\ (\rho + p)}{r} e^{\lambda/2} W, \tag{3.162b}$$

$$W' = -\left[\frac{l+1}{r} + \frac{p'}{F}\right] W + r e^{\lambda/2}\left[\frac{\rho + p}{F}\left(e^{-\nu}\omega^2 V + \frac{1}{2} H_0\right) - \frac{l(l+1)}{r^2} V + \frac{1}{2} H_0 + K\right], \tag{3.162c}$$

$$V' = \left[\bar{S} + \nu' - \frac{l}{r}\right] V + \frac{\bar{S}}{2\omega^2} e^{\nu}\left(H_0 + \frac{1}{r} e^{-\lambda/2} \nu' W\right) + r H_1 - \frac{1}{r} e^{\lambda/2} W, \tag{3.162d}$$

where $\bar{S}$ is closely related to the Schwarzschild discriminant S (corrected for the thermal

pressure) and given by

$$\bar{S} = \frac{S}{F} = \frac{p'}{F} - \frac{\rho'}{\rho + p}, \tag{3.163}$$

and we have introduced the abbreviation

$$F := \gamma p + M^* n_{\mathrm{n}} \frac{\partial p^{\mathrm{n}}_{th}}{\partial n_{\mathrm{n}}} + M^* n_{\mathrm{p}} \frac{\partial p^{\mathrm{p}}_{th}}{\partial n_{\mathrm{p}}}. \tag{3.164}$$

Here, $M^* = 11 - 6\frac{m^*}{m}$ as introduced in Section 3.4. The Einstein equations imply the following algebraic relation between the perturbation variables, which we use for the calculation of H_0:

$$\begin{aligned}\left[(n+1)r - \frac{re^{-\lambda}}{2}(r\lambda' + 2)\right] H_0 &= r^2 e^{-\lambda}\left[\omega^2 r e^{-\nu} - \frac{n+1}{2}\nu'\right] H_1 \\ &+ \left[nr - \omega^2 r^3 e^{-\nu} - \frac{1}{4}r^2 e^{-\lambda}\nu'(r\nu' - 2)\right] K + 4\pi r^2(\rho + p)\left(e^{-\lambda/2}\nu' W + 2\omega^2 e^{-\nu} V\right).\end{aligned} \tag{3.165}$$

The origin of the equations is basically the same as in the DL85 formulation but deserves a few comments. In order to arrive at this set of equations, we start at the DL85 set of equations. Since the algebraic relation (3.161) causes numerical problems, we solve it for X and substitute it into the other equations. After some algebraic manipulations and making use of the background equations as well as the other perturbation equations, we then arrive at our set of perturbation equations. In compact form: (3.162a), (3.162b) and (3.165) are $[t\theta]$, $[tr]$ and $[rr]$, respectively; (3.162c) is due to the definition of (the no longer appearing) X; (3.162d) is $\delta\left(\nabla_\mu T^\mu_r\right) = 0$ and (3.161), which has been used as an auxiliary equation only, is $\delta\left(\nabla_\mu T^\mu_\theta\right) = 0$.

Before we can solve (3.165) for H_0, we have to assure that its coefficient is non-singular at any point. In order to prove this, we rewrite the coefficient as

$$(n+1)r - \frac{re^{-\lambda}}{2}(r\lambda' + 2) = 3M - 4\pi r^3\rho + nr, \tag{3.166}$$

which we can easily achieve by using the background equations (2.7a) and (2.8). We then have

$$3M = 3\int_0^r 4\pi \mathring{r}^2 \rho(\mathring{r})\,\mathrm{d}\mathring{r} \geq 3\int_0^r 4\pi \mathring{r}^2 \rho(r)\,\mathrm{d}\mathring{r} = 4\pi r^3 \rho, \tag{3.167}$$

where we have used (2.10) for the first equality and monotonicity of the density inside the star, $\rho(\mathring{r}) > \rho(\breve{r})$ for $\mathring{r} < \breve{r}$, for the estimate. Thus, the coefficient will be singular only at the origin, $r = 0$, where we will use a Taylor expansion anyway.

The price we have to pay for eliminating the cancellation is the appearance of ρ' in the perturbation equations. Since this quantity is not known during the integration of the TOV equations, we have to calculate it numerically on an uneven grid; even worse, it may not be well-defined everywhere since $\rho(r)$ is not necessarily differentiable

as density discontinuities may occur inside the star. We use the method proposed by Sundqvist & Veronis [76] to tackle the former problem. In order to overcome the latter, we will use this new set of equations only in a region near the origin up to a certain radius R_V, up to which the perturbation variables have changed their order of magnitude sufficiently enough so that (3.161) can be applied without significant loss of accuracy and then switch back to the DL85 perfect fluid equations—this encourages a rather high value for R_V. However, when choosing R_V, we have to ensure that there are no discontinuities in ρ inside the interval $[0, R_V]$ and furthermore, the calculation of ρ' suffers from (however small but still present) numerical errors, which favours a low value for R_V. The "optimal" value for R_V can be found by trial and error only. In our simulations we find that $R_V \approx 5\,\mathrm{km}$ is a good choice as in this case we can reliably extract eigenmode frequencies down to $\approx 15\,\mathrm{Hz}$ (the actual lower limit slightly depends on the problem under consideration, see Section 3.10). For lower or higher values of R_V, either of the above discussed numerical issues becomes more severe and in the end the low frequency spectrum is spoiled by noise up to a higher frequency.

Altogether, our proposed set of equations allows us to calculate an unspoiled stellar spectrum down to lower frequencies and secondly, we are able to extract the eigenfunctions to higher accuracy also at intermediate frequencies.

3.8.1 The Taylor Expansion at the Centre of the Star

As in the previous formulation where equations (3.33) described the perturbations, the perturbation equations (3.162) are singular at the origin, too. We will use a Taylor expansion in exactly the same fashion as described in Section 3.2.1 which is why we will only state the results here. The entire procedure is completely identical.

We use an expansion of the form

$$q(r) = q_0 + \frac{1}{2}r^2 q_2 + \frac{1}{4}r^4 q_4 + \mathcal{O}\left(r^4\right), \tag{3.168}$$

and the coefficients for the background are the same as given in (3.40). The zeroth-order coefficients for the perturbation variables are

$$H_1(0) = \frac{2lK(0) + 16\pi\left(\rho_0 + p_0\right)W(0)}{l(l+1)}, \quad V(0) = -\frac{1}{l}W(0), \quad H_0(0) = K(0), \tag{3.169a}$$

which demonstrates that, once again that as soon as $K(0)$ and $W(0)$ are chosen, the remaining expansion coefficients, $H_0(0)$, $H_1(0)$ and $V(0)$ are determined. The second-order coefficients of the perturbation variables are then given by the following linear system:

$$-\frac{l+3}{2}H_1''(0) + \frac{1}{2}K''(0) - 8\pi(\rho_0 + p_0)V''(0) + \frac{1}{2}H_0''(0)$$

$$= \frac{1}{2}(\nu_2 - \lambda_2)H_1(0) - \lambda_2 K(0) + 8\pi\left[\rho_2 + p_2 + \lambda_2(\rho_0 + p_0)\right]V(0), \tag{3.170a}$$

$$\frac{n+1}{2}H_1''(0) - \frac{l+3}{2}K''(0) - 4\pi(\rho_0 + p_0)W''(0) + \frac{1}{2}H_0''(0)$$
$$= -\frac{1}{2}\nu_2 K(0) + 2\pi\left[2(\rho_2 + p_2) + \lambda_2(\rho_0 + p_0)\right]W(0), \tag{3.170b}$$

$$-(n+1)\gamma p_0 V''(0) - \frac{l+3}{2}\gamma p_0 W''(0)$$
$$= -\frac{1}{2}\left(3\gamma p_0 + p_0 + \rho_0\right)K(0) + \left[\frac{n+1}{2}\lambda_2\gamma p_0 - l p_2 - e^{-\nu_0}\omega^2(\rho_0 + p_0)\right]V(0), \tag{3.170c}$$

$$(l+2)V''(0) + W''(0)$$
$$= 2H_1(0) - \frac{e^{\nu_0}}{\omega^2}\left(\frac{\rho_2}{\rho_0 + p_0} - \frac{p_2}{\gamma p_0}\right)K(0) + \left[\frac{l}{2}\lambda_2 + 2\nu_2 + \left(2 - \frac{l e^{\nu_0}\nu_2}{\omega^2}\right)\left(\frac{p_2}{\gamma p_0} - \frac{\rho_2}{\rho_0 + p_0}\right)\right]V(0), \tag{3.170d}$$

$$\frac{n}{2}K''(0) - \frac{n}{2}H_0''(0) = \left[\frac{n+1}{2}\nu_2 - \omega^2 e^{-\nu_0}\right]H_1(0) + \left[\omega^2 e^{-\nu_0} - \frac{1}{2}\nu_2\right]K(0) - 8\pi e^{-\nu_0}\omega^2(\rho_0 + p_0)V(0) + 8\pi p_2 W(0). \tag{3.170e}$$

The five equations (3.170) are derived from the equations (3.162a), (3.162b), (3.162c), (3.162d) and (3.165) in that order.

3.9 The Perturbation Equations for Axial Perturbations

Additionally to the polar perturbations described in the previous section, there are axial perturbations. Axial perturbations in a non-rotating star change their sign like $(-)^{l+1}$ under space reflection. Comparably little attention is paid to axial perturbations in non-rotating stars for a simple reason: in the simplest case of modelling the star as a perfect fluid, there cannot be any axial perturbations connected to fluid motion since the pressure p is a scalar quantity and a space reflection would result in a sign change in the $l = 2$ case—which immediately implies $p = 0$ throughout the star. However, in contrast to Newtonian theory where the spectrum of a non-rotating perfect fluid star is actually void of modes, in general relativity there do exist axial perturbations in non-rotating stars; these are the axial w-modes.

We write the displacement vector for axial perturbations in the form

$$\xi^\mu = r^l \begin{pmatrix} 0 \\ 0 \\ -\frac{U}{\sin\theta}\partial_\phi \\ U\sin\theta\partial_\theta \end{pmatrix} P_l(\cos\theta)e^{i\omega t}, \tag{3.171}$$

where U is a function of r only, while the metric perturbation in the Regge-Wheeler gauge is [64]

$$\delta g_{\mu\nu} = -r^l \begin{pmatrix} 0 & 0 & 0 & i\omega r h_0 \sin\theta\partial_\theta \\ 0 & 0 & 0 & r^2 h_1 \sin\theta\partial_\theta \\ 0 & 0 & 0 & 0 \\ i\omega r h_0 \sin\theta\partial_\theta & r^2 h_1 \sin\theta\partial_\theta & 0 & 0 \end{pmatrix} P_l(\cos\theta)e^{i\omega t}. \tag{3.172}$$

Inserting these ingredients into the Einstein equations in the same way as we did for the polar perturbations, we find the perturbation equations

$$h_0' = \left[r - \frac{2ne^\nu}{\omega^2 r}\right] h_1 - \frac{l-1}{r} h_0, \tag{3.173a}$$

$$h_1' = -\frac{\omega^2}{r} e^{\lambda-\nu} h_0 + \left[\frac{1}{2}(\lambda' - \nu') - \frac{l+2}{r}\right] h_1, \tag{3.173b}$$

$$U = 0. \tag{3.173c}$$

One of the three unknowns, U, which describes the perturbation of the fluid, turns out to vanish throughout the star. The two metric perturbations, h_0 and h_1, however, are governed by a system of two first-order differential equations; this is the origin of the axial w-modes.

If we take the elastic crust into account, i.e. we use the modified stress-energy tensor (3.83), we end up at the following more complicated system of equations:

$$\begin{aligned} h_0'' = {} & \left[\frac{1}{2}(\nu' + \lambda') - \frac{2}{r}(l+1)\right] h_0' + \frac{1}{r}\left[\frac{l-1}{2}(\nu' + \lambda') + \frac{2n}{r}(e^\lambda - 1)\right] h_0, \\ & + r h_1' + \left[l + 4 - \frac{1}{2} r(\nu' + \lambda')\right] h_1 - 16\pi e^\lambda \frac{\rho + p}{r} U, \end{aligned} \tag{3.174a}$$

$$h_1' = -\frac{\omega^2}{r} e^{\lambda-\nu} h_0 + \left[\frac{1}{2}(\lambda' - \nu') - \frac{l+2}{r}\right] h_1 + \frac{32\pi\check{\mu} e^\lambda}{r^2} U, \tag{3.174b}$$

$$U' = +\frac{\omega^2 r e^{-\nu}}{32\pi\check{\mu}} h_0' + \frac{(l-1)\omega^2 e^{-\nu}}{32\pi\check{\mu}} h_0 + \left[\frac{2n - \omega^2 e^{-\nu} r^2}{32\pi\check{\mu}} + r^2\right] h_1 - \frac{l-2}{r} U. \tag{3.174c}$$

The system consists of two ODEs of first order and one ODE of second order; this is as expected as the elastic crust allows for torsional modes, or t-modes, for which we need

a second wave equation. It is worth noting, that the motion of the matter is confined to the elastic crust; in the perfect fluid regions of the star, we have $U = 0$.

3.9.1 The Taylor Expansion at the Centre of the Star

As in the polar case, the perturbation equations are singular at the origin; and again we tackle this issue by using a Taylor expansion around the origin for the perturbed quantities in the following way

$$h_0(r) = h_{00} + \frac{1}{2}r^2 h_{02} + \mathcal{O}(r^4), \tag{3.175}$$

$$h_1(r) = h_{10} + \frac{1}{2}r^2 h_{12} + \mathcal{O}(r^4). \tag{3.176}$$

As only two variables, h_0 and h_1, are involved—the third variable, U, vanishes—the expressions for the Taylor coefficients are relatively short. Again, the perturbation equations imply a relation between the zero-th order coefficients which means that the two perturbations are not independent. The behaviour at the origin is given by

$$h_{10} = -\frac{\omega^2}{(l+2)e^{\nu_0}} h_{00} \tag{3.177}$$

for the zero-th order coefficients, whereas the second-order coefficients follow from the linear system

$$\frac{1}{2}(l+1)\omega^2 h_{02} + n e^{\nu_0} h_{12} = \left(\omega^2 - n e^{\nu_0}\nu_2\right) h_{10}, \tag{3.178}$$

$$e^{-\nu_0}\omega^2 h_{02} + (l+4)h_{12} = e^{-\nu_0}\omega^2(\nu_2 - \lambda_2)h_{00} + (\lambda_2 - \nu_2)h_{10}. \tag{3.179}$$

3.9.2 The Junction Conditions

As in the polar case, we also have to find boundary conditions for the crustal interfaces and possibly density discontinuities. The analysis will be identical to the polar case, see Section 3.6; however, it comes with two considerable differences: firstly, the definition of the metric perturbations is obviously different, secondly, the scalar quantity which is being used to define the normal vector, N^μ, will be a purely background quantity since scalar quantities are not subject to axial perturbations. We will hence use the (unperturbed) location of an interface.

With the same definitions as before, we arrive at the following expressions for the non-trivial components of the first and second fundamental form,

$$\gamma_{00} = -e^{\nu}, \tag{3.180a}$$

$$\gamma_{03} = \delta g_{03}, \tag{3.180b}$$

$$\gamma_{13} = \delta g_{13}, \tag{3.180c}$$

$$\gamma_{22} = r^2, \tag{3.180d}$$

$$\gamma_{33} = r^2 \sin^2\theta, \tag{3.180e}$$

and

$$K_{00} = \frac{\nu'}{2} e^{\nu-\lambda/2}, \tag{3.181a}$$

$$K_{03} = \frac{1}{2} e^{-\lambda/2} \left(\delta\dot{g}_{13} - \delta g'_{03}\right), \tag{3.181b}$$

$$K_{13} = -\frac{e^{-\lambda/2}}{r} \delta g_{13}, \tag{3.181c}$$

$$K_{22} = -r e^{-\lambda/2}, \tag{3.181d}$$

$$K_{23} = \frac{e^{-\lambda/2}}{2} \left(\delta g_{13,\theta} - 2\frac{\cos\theta}{\sin\theta}\delta g_{13}\right), \tag{3.181e}$$

$$K_{33} = -r \sin^2\theta e^{-\lambda/2}. \tag{3.181f}$$

Again, these components have to be continuous across the interfaces. We repeat the background conditions only for completeness,

$$[\nu]_r = 0, \qquad [\lambda]_r = 0, \qquad [\nu']_r = 0. \tag{3.182}$$

The continuity of the components γ_{03}, γ_{13} and K_{03} then imply

$$[h_0]_r = 0, \qquad [h_1]_r = 0, \qquad \text{and} \qquad [h'_0]_r = 0, \tag{3.183}$$

in that order, where we have used (3.107) in order to remove the temporal derivative. The junction conditions are already exhausted and we note that there is no condition put on the tangential displacement, U; the solid crust can slip freely along the fluid core as well as the fluid ocean.

3.10 Results

In this first chapter, we have started from the well studied Detweiler & Lindblom formulation (DL85) of the perturbed perfect fluid and have gradually put in more physics. At first, we present several checks against literature values for a polytropic neutron star in order to prove the accuracy of our code and build an understanding of the different modes that are present in non-rotating neutron stars. This will not only show that our code is working in many different special cases, we will also highlight certain features of mode classes as well as limitations of the code. After our discussion of the special cases, we will take the key bits of physics into account step by step. This will gradually enrich the spectrum with more and more classes of oscillation modes. The natural steps are: (i) taking only composition gradients into account, (ii) switching on temperature using the thermal evolution and (iii) accounting for the crystallisation of the elastic crust. The density jumps, leading to i-modes, are built in to the EoS, so we cannot easily switch them on or off. Hence, these modes will always be present in the star's spectrum.

Let us briefly comment on the actual implementation of the density discontinuities. As discussed in Section 3.6 we have two alternatives. Either represent the phase transition by a real jump in density in the EoS, or have a continuous transition with a large gradient ρ' in the background model. We opt for the former variant, just by choice.

One feature of the frequency domain approach in solving the oscillation problem is that one finds both the oscillation frequency (real part) and the damping time (imaginary part) at the same time. This works very well for the strongly damped w-modes whose imaginary part is comparable (in order of magnitude) to their real part. All other modes are much more weakly damped, which is equivalent to a very small imaginary part; typically, it is between 6 and 12 orders of magnitude smaller than the real part (depending on the nature of the mode and its order), which makes a numerical determination due to the finite machine precision difficult and in many cases even impossible (with the current method). As in earlier work [19, 61], we will not actually calculate the complex frequencies of the quasinormal modes; we ignore the damping of the mode. Instead, we construct the asymptotic amplitude A_{in} for real-valued frequencies and locate the quasinormal modes by approximating the zeros of this function (essentially resonances in the problem). To visualise the spectrum, we plot the logarithm of the incoming amplitude, $\log |A_{\text{in}}|$ (log always refers to the logarithm to base 10 throughout this study), as a function of the frequency in arbitrary units (as e.g. in Figures 3.23, 3.28, 3.31 and 3.32). Since we have linearised the problem, the actual amplitude is arbitrary and has no physical content; thus we do not show any scaling on the y-axis in these graphs but mention only briefly that there is a factor of 10 between two large, adjacent tick marks. The logarithm turns the zeros into much more visible spikes or singularities and an eigenfrequency can be found where this function ideally tends to

$-\infty$. For brevity, we will occasionally refer to the plots of $\log|A_{\text{in}}|$ as a "spectrum", even though this is technically not correct.

We also comment here on the stability of our numerical procedure. As explained earlier, the calculation of the ingoing wave amplitude is spoilt by noise in the low frequency regime and, in practice, the lower limit for reliably extracting frequencies lies at about 18 Hz. In our simulations, we find that this lower limit gets shifted down to approximately 10 Hz when we include composition, i.e. when we use γ instead of γ_0 in the equations (see next subsection). This gives us a further hint to the origin of the instability in the equations. However, this is not the only crucial point since the noisy behaviour is almost non-existent for polytropic equations of state (which we implemented as a test of the numerics).

Note that, while our perturbation equations are valid for any degree $l \geq 2$, we will always use $l = 2$ in our simulations.

3.10.1 A Polytropic Neutron Star as Test Case

We start by calculating neutron star spectra for polytropic models; these kind of models employ the most basic EoS that lead to somewhat realistic neutron star models. They appeal by their simple analytic structure—the pressure-density relation is given by

$$p = K\bar{\rho}^{1+\frac{1}{N}}, \tag{3.184}$$

where N is the polytropic index and K is a constant that allows to scale the units. We intentionally avoid denoting the exponent $1 + \frac{1}{N}$ by γ for the following reason; in the literature, two subtly different variations of this EoS are used: several studies on neutron stars in general relativity interpret $\bar{\rho}$ as the energy density [77, 78] (which we denote by ρ throughout this thesis), whereas other literature understands $\bar{\rho}$ as the rest-mass density (for which we use ρ_0) and the energy density is then thermodynamically consistent given by $\rho = \rho_0 + Np$ (see e.g. Tooper [79]).

We will compare our results to the articles by Kokkotas & Schutz [21] (KS92 hereafter) and Andersson et al. [61] (AKS95 hereafter) and thus adopt their interpretation of $\bar{\rho}$ for our calculations when considering a polytropic EoS; both articles use the former version of the polytropic EoS where $\bar{\rho}$ denotes the energy density, which leads to the slightly odd-looking adiabatic index defined by (3.30)

$$\gamma_0 = \frac{\rho + p}{p}\frac{\mathrm{d}p}{\mathrm{d}\rho} = \left(1 + \frac{1}{N}\right)\left(1 + \frac{\rho}{p}\right). \tag{3.185}$$

We pick model 4 of KS92 which has a central energy density of $\rho = 1 \cdot 10^{16}\,\mathrm{g\,cm^{-3}}$; the parameters of the EoS are chosen to be $N = 1$ and $K = 45.85$. As a result, this model star has a mass of $M = 1.3\,M_\odot$ and a radius of $R = 6.466\,\mathrm{km}$.

Gravitational wave modes

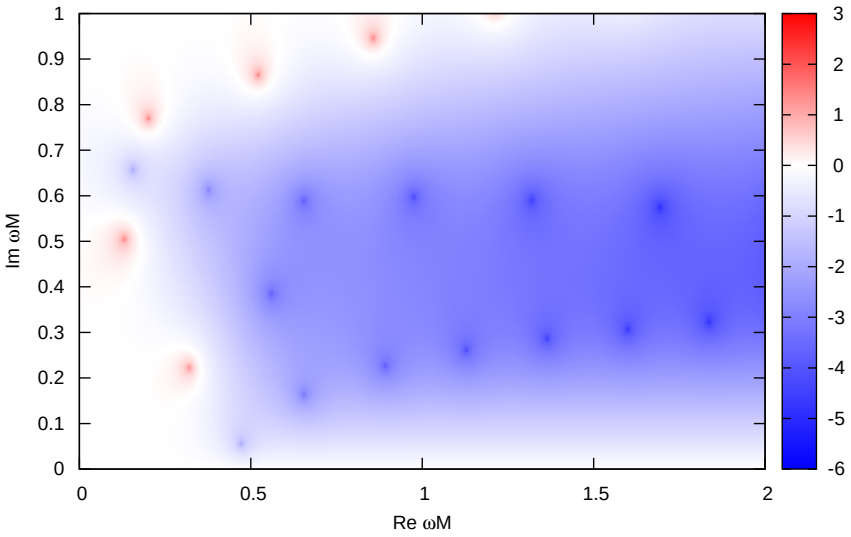

Figure 3.2: Logarithmic plot of $\log|A_{\text{in}}/A_{\text{out}}|$ for $\omega M \in [0,2]\times[0,1] \subset \mathbb{C}$. The resolution of this graph is $\Delta\omega M = 0.002$ (for both the real and the imaginary part). The blue dots indicate eigenfrequencies of the stellar system. The red dots are peaks of the plotted function. Their exact meaning is not clear, see also text.

In Figure 3.2, we show the colour-coded value of $\log|A_{\text{in}}/A_{\text{out}}|$ in the first quadrant of the complex plane with a resolution of $\Delta\omega M = 0.002$ in both directions; red encodes positive values, blue encodes negative values and the darker the colour the larger the magnitude of the value; hence, we are most interested in dark blue spots which indicate eigenmodes of the system. We can spot two dark red dots and eight dark blue dots—seven of which seem to lie on a curved line starting approximately at $\omega M \approx 0.4 + 0.0I$. These dots correspond to the w-modes found by KS92 and our values coincide well with their published values; we list them in Table 3.3. In Figures 3.3 and 3.4, we show the eigenfunctions of H_1 and W for the first six of these w-modes; they agree visually well with the eigenfunctions published in Leins et al. [22]. The amplitude of the eigenfunctions is largest in the centre of the star and the number of nodes in radial direction increases with frequency by one per mode. This is as expected for w-modes which are essentially vibrations of the space-time and hardly excite fluid motion; we find that at the surface of the star, the amplitude of the displacement W is roughly one order of magnitude smaller than the amplitude of the metric perturbation H_1.

We determine the zeros of the function $|A_{\text{in}}/A_{\text{out}}|$ using the method of Muller [80]; this method needs three initial values and then assumes that these three points are part of a complex-valued parabola. The zero of the function is then approximated by the

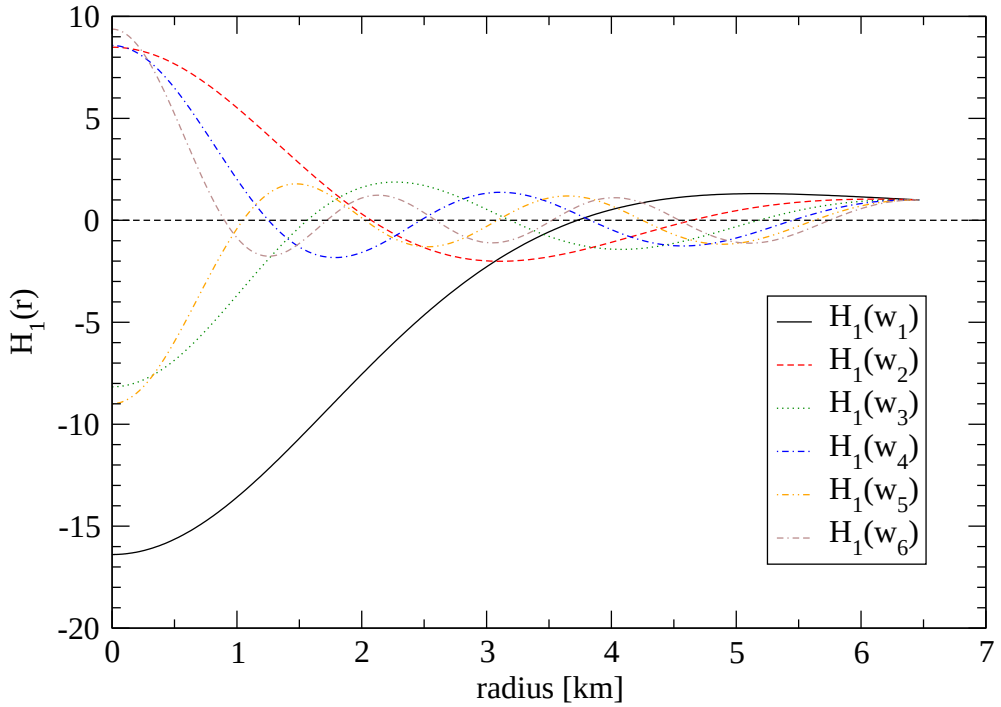

Figure 3.3: Eigenfunctions of H_1 of the w-modes inside the star; we have normalised them to $H_1(R) = 1$.

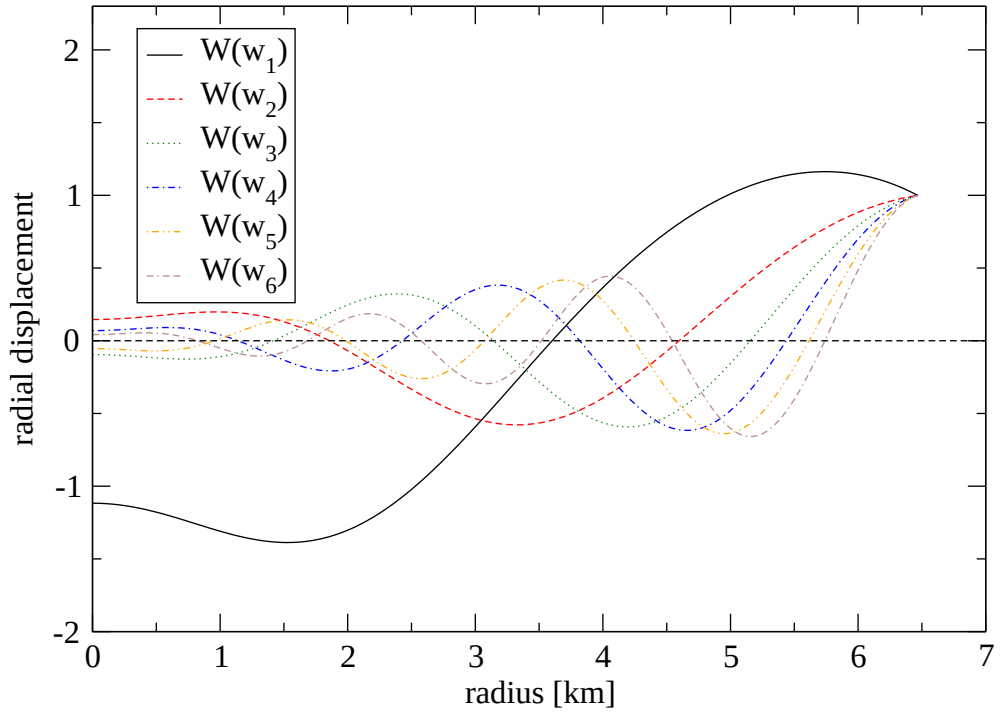

Figure 3.4: Eigenfunctions of W of the w-modes inside the star; we have normalised them to $W(R) = 1$.

zero of the parabola which is closer to the previous approximation. When searching for w-modes, this method turns out to be very reliable and fast; after only a few iterations the method converges with high accuracy. The w-modes form an infinite class of modes for which the frequency increases with higher order; with our code, we can easily find the first hundred of these modes, provided that we carefully increase the grid resolution in order to resolve every single node accurately.

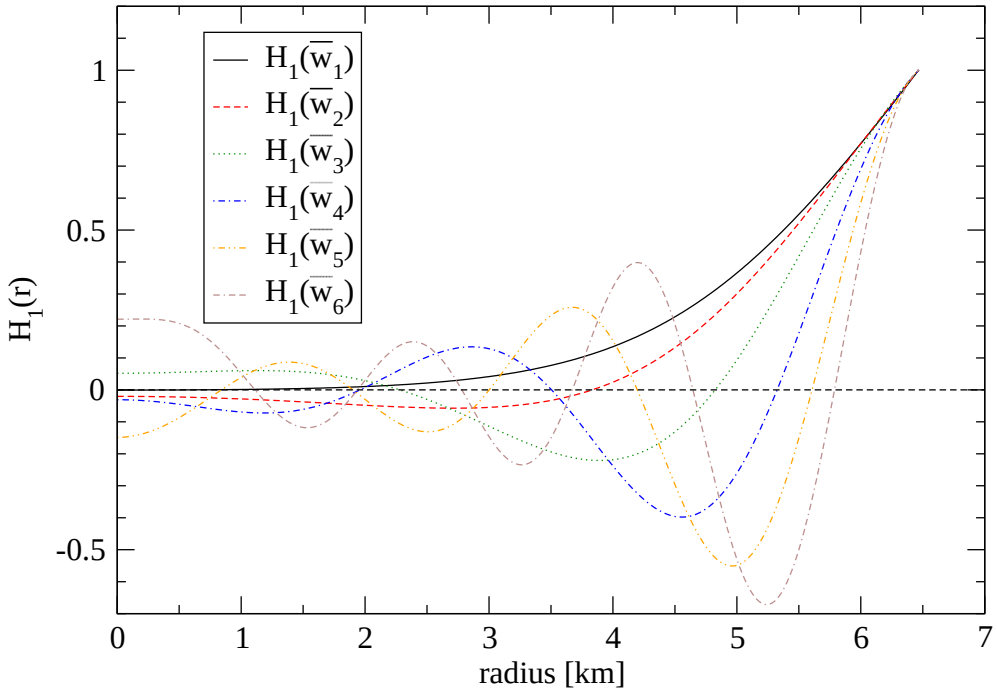

Figure 3.5: Same as Figure 3.3 but here for the w-modes with $\mathrm{Im}(\omega M) \approx 0.6$.

Besides the w-modes discussed, we find more zeros (the blue dots) in the complex plane in Figure 3.2. Quite prominently lies a series of blue dots on a nearly straight line with imaginary part $\mathrm{Im}(\omega M) \approx 0.6$. Our code converges quickly to any of these points to very high accuracy. However, neither have any authors identified these modes before (e.g. [21, 22, 61]) nor did we expect to find modes there for any physical reason. We show the eigenfunction of H_1 in Figure 3.5 and their frequencies in Table 3.2; we call them $\bar{w}$-modes in order to distinguish them from the known branch of w-modes; however, we retain the letter w for them due to their similarity to the w-modes, see below. From the graphs it becomes apparent that one of their characteristics is the small amplitude of H_1 and W at the centre of the star compared to at the surface; this effect is very strong for W. Again, the ratio $|H_1(R)/W(R)|$ reveals that the fluid motion is strongly suppressed which suggests that these modes are some sort of space-time modes, too. Whilst the discovery of a new branch of strongly damped modes is very exciting, we have to ask what the physical origin of these modes is. At present, we are unsure of the exact meaning of these modes. Are they physical? Why have they not been identified in previous studies? Could they possibly be an artefact of some

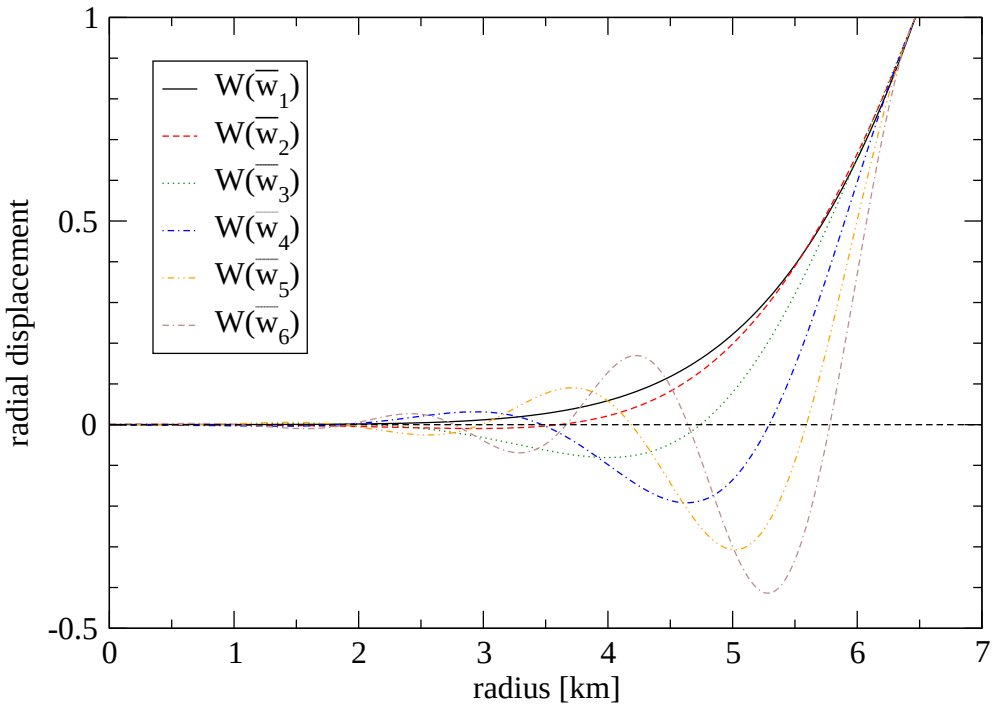

Figure 3.6: Same as Figure 3.4 but here for the w-modes with $\mathrm{Im}(\omega M) \approx 0.6$.

of the applied numerical methods? The latter two questions are not independent—we have implemented the same numerical methods as AKS95 (but with higher numerical accuracy), however, they did not identify these modes. One possible reason could be that the computational power which allowed us to quickly scan the entire rectangle $[0, 2] \times [0, 1] \subset \mathbb{C}$ (and even more than that) for modes was not available at that time. These modes deserve further consideration and a confirmation of their existence using different methods for the exterior solution would be very exciting. However, the aim of this study lies on the low frequency spectrum and a thorough investigation of the $\bar{w}$-modes would go well beyond the scope of this thesis.

Table 3.2: Eigenfrequencies of model 4 of KS92 of the modes with $\mathrm{Im}(\omega M) \approx 0.6$. Since these modes have not been identified yet, we call them $\bar{w}_n$ and start counting from the lowest frequency.

Mode	$\mathrm{Re}(\omega M)$	$\mathrm{Im}(\omega M)$
$\bar{w}_1$	0.1550	0.6580
$\bar{w}_2$	0.3750	0.6135
$\bar{w}_3$	0.6533	0.5894
$\bar{w}_4$	0.9737	0.5978
$\bar{w}_5$	1.318	0.5912
$\bar{w}_6$	1.692	0.5752

The one blue dot at $\omega M = 0.559 + 0.383I$ belongs to a (probably) different class of w-modes which has first been found by Leins et al. [22]. They have identified two further modes with even larger imaginary parts (at $\omega M = 0.353 + 0.838I$ and $0.142 + 1.286I$) which we are unable to find with our code (Leins et al. use a method for the exterior solution of the star that is based on a continued fraction). This is somewhat surprising as we implemented the identical procedure as AKS95 for the numerical solution of the problem and they did find the mode at $\omega M = 0.353 + 0.838I$. Furthermore, as computational power has considerably increased during the last 20 years, we would expect our code to be more accurate and able to find this mode.

To get a better idea of what is going on, we investigated the behaviour of the w-modes for large real parts. (We also extended the search for large imaginary parts but we were not able to identify any modes with $\mathrm{Im}(\omega M) > 1$.) We show the results in Figure 3.7; it becomes apparent that the two "branches" of w-modes are merging into each other at about $\mathrm{Re}(\omega M) \approx 4$. The merging is not perfect in the sense that the zeros in the complex plane are neither equidistant nor do they follow a different but simple pattern. Their imaginary parts $\mathrm{Im}(\omega M)$ vary between 0.4 and 0.5. The eigenfunctions, too, give no further insight into the problem. This is somewhat unsatisfactory and leaves space for further research. However, our results for the already identified modes are in excellent agreement with published results (less than 0.3 % discrepancy). We are unable to clarify the situation at this time and strongly encourage more thorough studies of these issues.

Convergence Test on w-modes

A numerical study can be comprehensive only if it features convergence tests which show that the accuracy of the solution is increased when the calculation is carried out on a finer grid. In our study, convergence tests come with a few caveats and feature a few peculiarities.

Firstly, the determination of the incoming wave amplitude, A_{in}, as a function of a prescribed frequency, ω, requires the solution of three fundamentally different sets of ODEs with different boundary conditions: After constructing the stationary background model using the TOV equations (2.7), the perturbation equations have to be solved in the interior of the star (DL85 and similar depending on the nature of the matter); finally, the exterior solution has to be determined (the non-linear ODE (3.157) derived from the Regge-Wheeler equation). For the solution of all these differential equations, we use a Runge-Kutta solver of order eight with adaptive mesh refinement (DOPRI); in our simulations, we demand an accuracy of 10^{-10}.

A difficulty of the convergence test stems from the fact that we integrate two different sets of differential equations over the same domain (the background and the interior solution) for which in general very different step sizes are necessary in order to achieve the same accuracy. This issue becomes manifest already in the background configura-

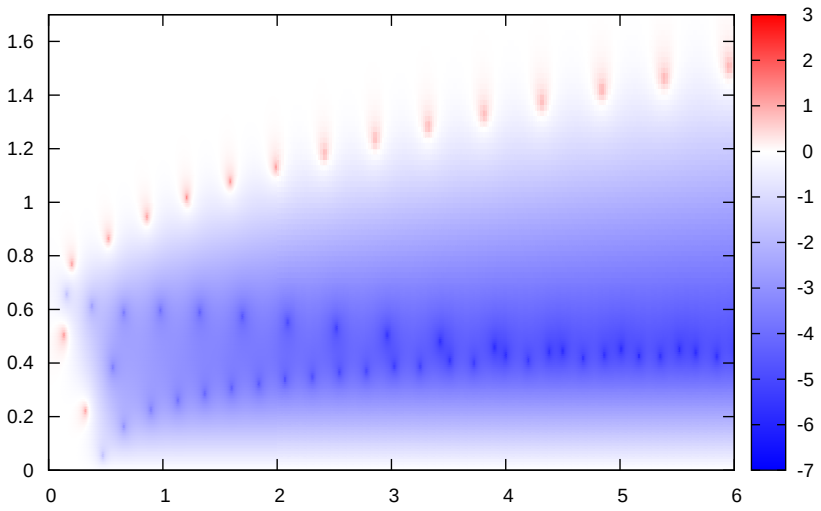

Figure 3.7: As Figure 3.2 but for a larger region of the complex plane. Due to the large area covered, we have decreased the resolution in the upper right corner slightly, compared to the rest of the graph ($\Delta\omega M = 0.02$ for $\mathrm{Re}(\omega M) > 2$ and $\mathrm{Im}(\omega M) > 0.6$. Besides the $\bar{w}$-modes with $\mathrm{Im}(\omega M) \approx 0.6$, we find an array of peaks (the red dots) at larger imaginary parts. The graph indicates a link between these $\bar{w}$-modes and these peaks.

tion, which we have to store on some grid since we need its values for the perturbation problem. It turns out that the step sizes chosen by the integrator in order to achieve an accuracy of 10^{-10} vary over several orders of magnitude from a few centimetres close to the surface and the centre of the star to several hundred metres in the middle of the computational domain. With such large steps we cannot expect to reliably interpolate background quantities for the calculation of the perturbations at the same accuracy; we need to (and do) enforce a maximum step size on the background. In return, this essentially results in the background configuration being more accurate than demanded, making a convergence test somewhat difficult. This peculiarity has to be taken into account when interpreting the results of the performed convergence tests.

A convergence test is supposed to demonstrate the convergence of a numerically determined quantity to the exact solution with increasing accuracy of the calculation. In our case, we obviously do not have the exact solution at hand, and a standard solution to this issue is to take the result of a high resolution run as the exact solution and investigate the convergence of the code towards this solution.

For brevity, we will not show detailed results regarding the convergence of the background solution, but simply state that an increased accuracy results in a more accurate

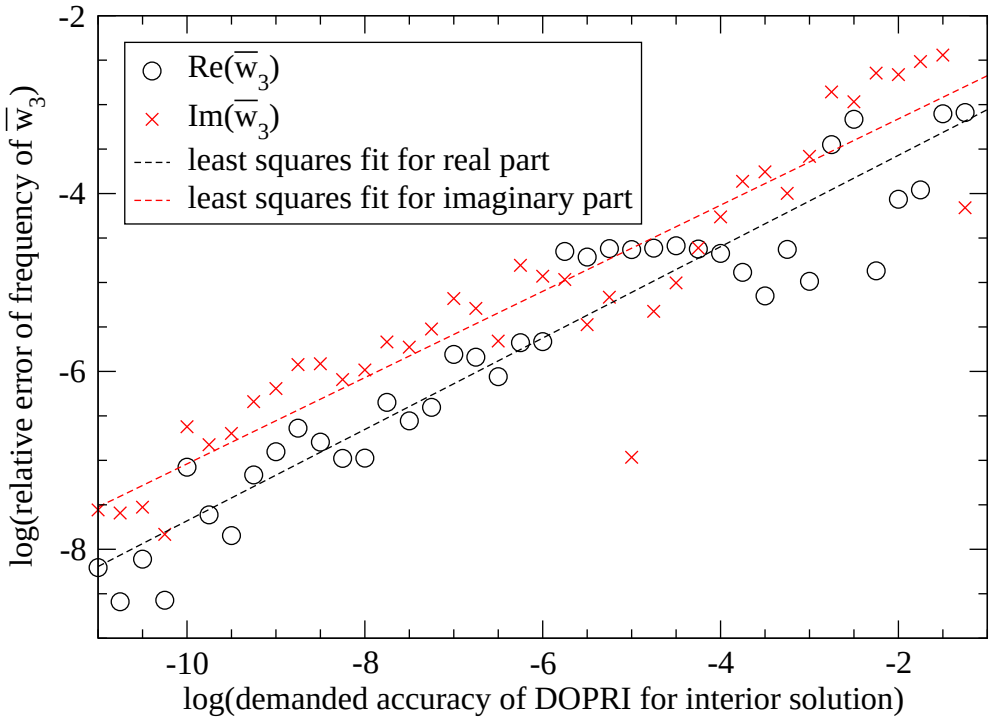

Figure 3.8: The convergence test for the $\bar{w}_3$-mode. We show the relative error of both the real and imaginary part of the frequency of this mode and plot it against the demanded accuracy of the DOPRI solver. The solution of the problem clearly converges with increased accuracy of the integration; the straight, dashed lines are least squares fits to the respective data points.

background model. Much more interesting is the convergence of the frequencies of the oscillation modes to a fixed value. We show this exemplary for the mode $\bar{w}_3$, which is the third of the modes which we deem spurious; in some cases, a convergence test can identify numerical artefacts in which case the solution will not converge to some value when the accuracy of the calculation is increased. We show the convergence test for this mode in Figure 3.8; we plot the relative error of the frequency of this mode (as compared to a high resolution simulation) against the demanded accuracy of the DOPRI solver. In order to simplify the convergence test, we keep the accuracy of the TOV integration fixed at 10^{-12} and vary only the accuracy of the integration of the perturbation equations over several orders of magnitude. The graph clearly shows convergence of the frequency of the $\bar{w}_3$-mode; we fit a straight line of the form

$$\log_{10} \text{“relative error”} = a \log_{10} \text{“accuracy of integration”} + b \tag{3.186}$$

to the real and imaginary parts of the solution by means of a least squares fit. We find

for the two parameters a and b the values

$$\left.\begin{aligned} a &= 0.5138 \pm 0.0254 \\ b &= -2.542 \pm 0.170 \end{aligned}\right\} \quad \text{for the real part,} \tag{3.187}$$

$$\left.\begin{aligned} a &= 0.4850 \pm 0.0311 \\ b &= -2.190 \pm 0.208 \end{aligned}\right\} \quad \text{for the imaginary part.} \tag{3.188}$$

We also see that the data points do not lie on a straight line but oscillate rather wildly around it; this is owing to the fact that, as explained earlier, the integrations both for the background and the perturbations will in general be subject to fundamentally different step sizes. The overall behaviour of the data points, however, shows a clear convergence to the result of the high resolution simulation. A convergence test, in this case, cannot rule out the physical reality of the new branch of w-modes (we find similar results for all other w-modes, too).

Fundamental and Pressure Modes

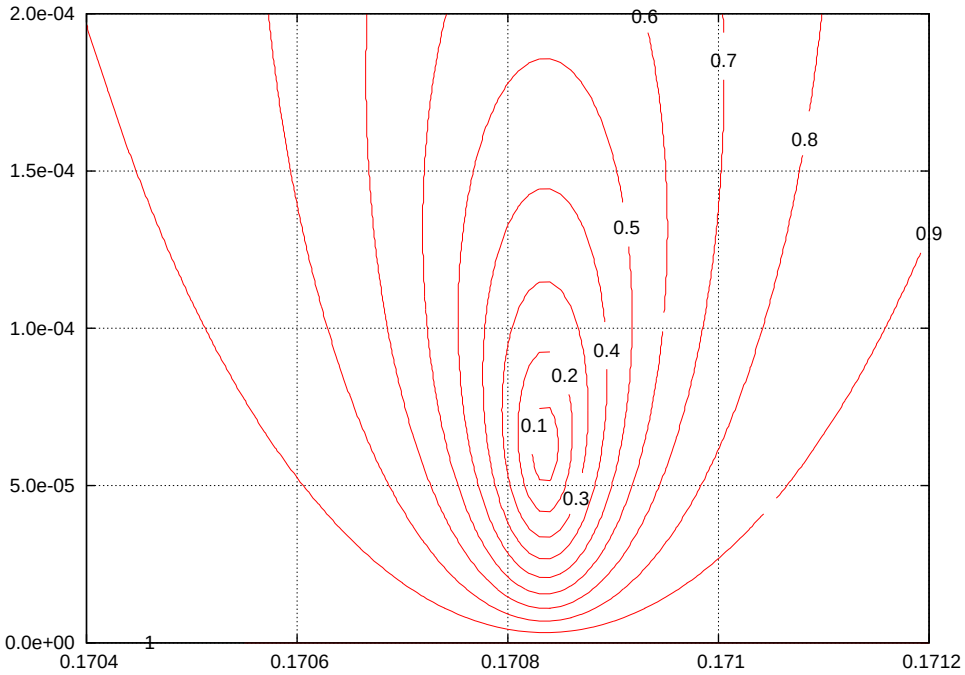

Figure 3.9: Contour lines of $|A_{\text{in}}/A_{\text{out}}|$ for the f-mode. The contour lines are equidistant with a difference of 0.1. The map of $|A_{\text{in}}/A_{\text{out}}|$ was produced with a resolution of $\Delta\text{Re}(\omega M) = 10^{-5}$ and $\Delta\text{Im}(\omega M) = 10^{-6}$. The contour lines are well defined and demonstrate the high accuracy of our code.

In theory, we should also find blue spots for the slowly damped f- and p-modes, very close to the real axis. However, there is no sign of any mode in this graph. The reason

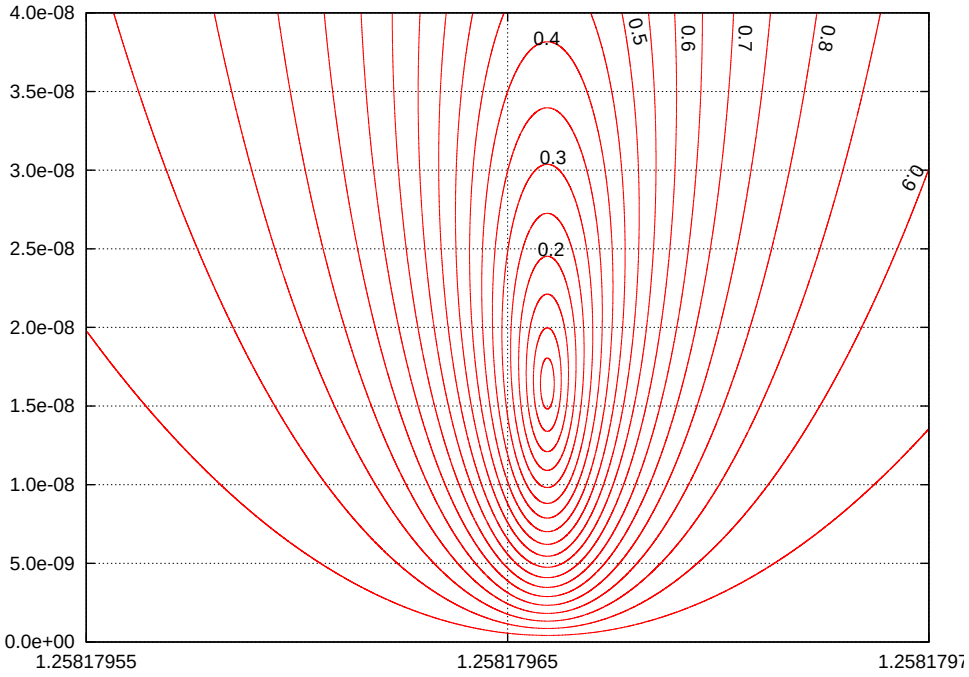

Figure 3.10: As Figure 3.9 but for the mode p_7. The resolution of the data are $\Delta\mathrm{Re}(\omega M) = 5 \cdot 10^{-10}$ and $\Delta\mathrm{Im}(\omega M) = 2 \cdot 10^{-10}$.

is simple: they do not appear in this figure because they cause very narrow singularities for which there is no hope that these could be resolved in Figure 3.2 at the resolution of $\Delta\omega M = 0.002$. We show contour lines for the fundamental mode and a high order pressure mode in Figs. 3.9 and 3.10 (we will explain in the following paragraph how we found them). These graphs clearly indicate a pronounced singularity for either mode. We chose to show contour lines for $|A_{\mathrm{in}}/A_{\mathrm{out}}|$ instead of its logarithm; since the singularities are *very* narrow, this makes the graphs clearer. The lowest contour line we show is for $|A_{\mathrm{in}}/A_{\mathrm{out}}| = 0.05$ but we point out that we are able to find ωM such that the magnitude of this ratio is less than 10^{-7}; this is our threshold for locating zeros (or more precisely: minima). The imaginary parts of ω are tiny compared to their real parts; they differ by 5 and 8 orders of magnitude for the two mentioned modes, respectively. These graphs have been produced using a resolution of $\Delta\omega M = 1 \cdot 10^{-6}$ for the f-mode and $\Delta\omega M = 2 \cdot 10^{-10}$ for the p_7-mode.

Similar to the w-modes, we expect to find the slowly damped modes by iterating using Muller's method. The main difficulty is that the slowly damped modes cause much narrower singularities than the w-modes. This means that in order for Muller's method to converge, we need three initial values which are already pretty close to the mode's frequency. If the three initial values are not within close vicinity of the singularity, we find that this method is prone to doing large jumps in different, unpredictable directions, finally converging to some w-mode in most of the cases. We can understand this as follows: if we have only a rough approximation for a mode, say, we choose the

three real parts are 1.70, 1.72 and 1.74 and $\mathrm{Im}(\omega M) = 5 \cdot 10^{-5}$ as a first approximation for the f-mode. We can see from Figure 3.9 that with these three values, we are well beyond the 0.9 contour line which gives us very similar values (somewhere between 0.9 and 1) for the ratio at these three points in the complex plane. Thus, the zeros of a parabola containing these three points will be far away and Muller's method will start with a huge jump which destroys any hope to find the f-mode using these initial values. We need a different tool to approximate the frequencies of slowly damped modes.

The idea, which has frequently been used [81, 61, 35], relies on the fact that the modes correspond to zeros of the asymptotic amplitude A_{in}. If such a mode is located close to the real axis, it might be possible to approximate the mode by plotting $\log |A_{\mathrm{in}}|$ for real values of ω and *not* normalise for the outgoing amplitude A_{out}. This approach works very well as we can see in Figure 3.11. Narrow singularities and spikes (at their negative end) in this graph correspond to slowly damped eigenmodes of the neutron star. This graph has a resolution of $\Delta\omega M = 0.005$ and can be quickly produced. It allows a precise determination of a mode's frequency (but not its damping time). Using these values as initial values, we can apply the bisection method to achieve even higher precision. In nearly all cases (apart from modes with very high order), we can easily push the value of $\log |A_{\mathrm{in}}|$ below -6. We find that the relative difference between the real part of the actual (complex-valued) zero of an oscillation mode and the value we approximated on the real axis is usually less than 10^{-4}. Hence, we assume that we can determine the frequencies of the slowly damped modes to sufficient accuracy from purely real-valued calculations.

The first singularity in Figure 3.11 at $\mathrm{Re}(\omega M) = 0.171$ belongs to the fundamental or f-mode, the following spikes (15 of them are visible in this graph) are the pressure restored p-modes. We show the frequencies of the f-mode, the first ten p-modes and the first eleven w-modes in Table 3.3; their values are in excellent agreement (the discrepancy is less than 0.3 %) with the values of AKS95 (they did not provide values for the higher order p-modes).

Once we have determined the real value of the frequency to good precision, we can start iterating for the imaginary part. We find that even with a precise knowledge of the real part of ω, Muller's method is prone to large jumps (as explained above) and does not converge to the desired zero. There are a number of methods which we potentially could use to solve our problem, $A_{\mathrm{in}} = 0$. However, every method comes with certain conditions that must be fulfilled for a successful application. These make several of the methods impracticable for our problem. The Newton-Raphson method, for example, requires the knowledge of the first derivative $\frac{\partial A_{\mathrm{in}}}{\partial \omega}$, which we can only approximate by finite differences and even this would be computationally very expensive. The multi-dimensional bisection method (Lehmer-Schur algorithm) would require us to specify an area within which the zero is definitely to be found and is considerably more complicated than the one-dimensional bisection method. This raises the problem as to how big an

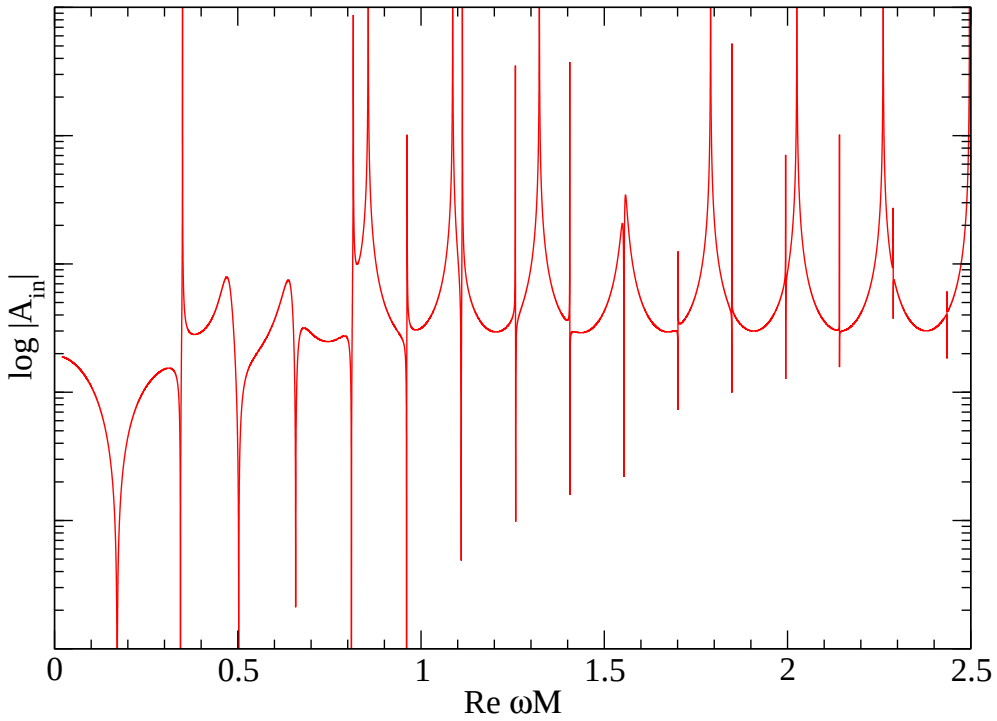

Figure 3.11: The incoming amplitude as a function of purely real frequencies ωM; the resolution is $\Delta\omega M = 0.0005$. A narrow singularity corresponds to a slowly damped mode. The f-mode and the first 15 p-modes are easy to distinguish.

area we should specify as initial conditions. Furthermore, any method that tries to find zeros of real-valued function is ruled out since A_{in} is complex-valued. By means of the magnitude we can turn our root-finding problem $A_{\text{in}}(\omega) = 0$ into the a problem of finding a root of the positive definite, real-valued function $|A_{\text{in}}(\omega)|$. However, due to finite computer precision, we cannot expect that our code will ever return precisely $|A_{\text{in}}(\omega)| = 0$ for some value of ω. We rather have to *minimise* the function $|A_{\text{in}}/A_{\text{out}}|$. We have effectively turned our problem into an optimisation problem. In the end we opt for the "Downhill Simplex" method [80] which is an optimisation method for non-linear functions. The basic idea is to place a small triangle in the close vicinity of the minimum and the value of the function is determined at the three vertices. The algorithm then replaces the worst (largest) of these values by a better one; this is found by reflecting, expanding or shrinking the triangle according to certain rules. The convergence rate of this method is fairly slow if applied to our problem but we take this expense in favour of reliability and robustness.

In practice, we determine the real part of ω to four to five digits precision. We then choose a small triangle in the complex plane. Its actual size and location are not very important—e.g. for the f-mode, it should be located somewhere within the graph in Figure 3.9 but it may also be a bit outside. The length of any side should not exceed 10^{-4} which is of the order of magnitude of the imaginary part of the expected frequency

(and accordingly smaller if even smaller imaginary parts are expected). If in doubt, it is essentially impossible to make the triangle too small. The algorithm will automatically expand the triangle. We appreciate this freedom in the initial conditions given by the Downhill Simplex algorithm and it is fairly easy to determine the imaginary part of an eigenmode. We show them for the first ten pressure modes in Table 3.3 (second pair of columns). Compared to AKS95, we are able to accurately calculate the damping times even for higher order p-modes and our results agree well for the lower order p-modes (we do not observe discrepancies in the real parts of the frequencies and the imaginary parts differ no more than 2 % for the f- and p_2-mode—due to the limited numerical accuracy of AKS95, the discrepancy is considerably larger for the imaginary parts of the other p-modes, 10 % and more). This is due to the fact that we integrate the differential equations to higher accuracy than AKS95; we use a Runge-Kutta solver of order eight with adaptive mesh refinement (DOPRI) and enforce accuracy of 10^{-10} for the background as well as the perturbations. We can infer that our calculated damping times are accurate even though they are ten orders of magnitude smaller than the real parts. However, depending on the threshold we impose for having "determined" an eigenmode, our code reaches its limit at the 10th p-mode. For higher order modes, we still see the iteration converging to a well-defined point in the complex plane, however, it becomes harder and sometimes impossible to achieve $\log|A_{\rm in}/A_{\rm out}| < -7$ (which has been our previous threshold).

We show the eigenfunctions of the displacement for the f-mode and the first four p-modes in Figure 3.12; we have normalised them again to $W(R) = 1$. It is clear that the largest amplitude of these modes is close to the surface. The number of nodes in radial directions is zero for the f-mode and it increases by one per mode. Similar to the w-modes, we have also calculated the fraction H_1/W at the surface of the star. In contrast to the w-modes where we found H_1 to be approximately one order of magnitude larger than W, it is about two orders of magnitude smaller for the f-mode and decreases quickly with the order of the p-modes. This indicates that these modes are essentially oscillations of the fluid that are weakly coupled to space-time.

Additional Features of the Spectra

Coming back to the graph in Figure 3.11, we point out that the graph features a number of peaks. Their presence is somewhat unclear. We find that they are somehow linked to the w-modes. In order to make this clearer, we plotted merely the incoming amplitude $|A_{\rm in}|$ in Figure 3.13 rather than the ratio. The graph is very similar to the graph in Figure 3.2; the blue and red spots from this graph are still present. However, we get a number of new red dots along the real axis as well as one blue spot. The blue spot corresponds to the f-mode. We should also find one blue spot for every p-mode, however, their singularities are again too narrow in order to be resolved. Instead, we find an array of red dots, and they seem to be well correlated to the w-modes which are

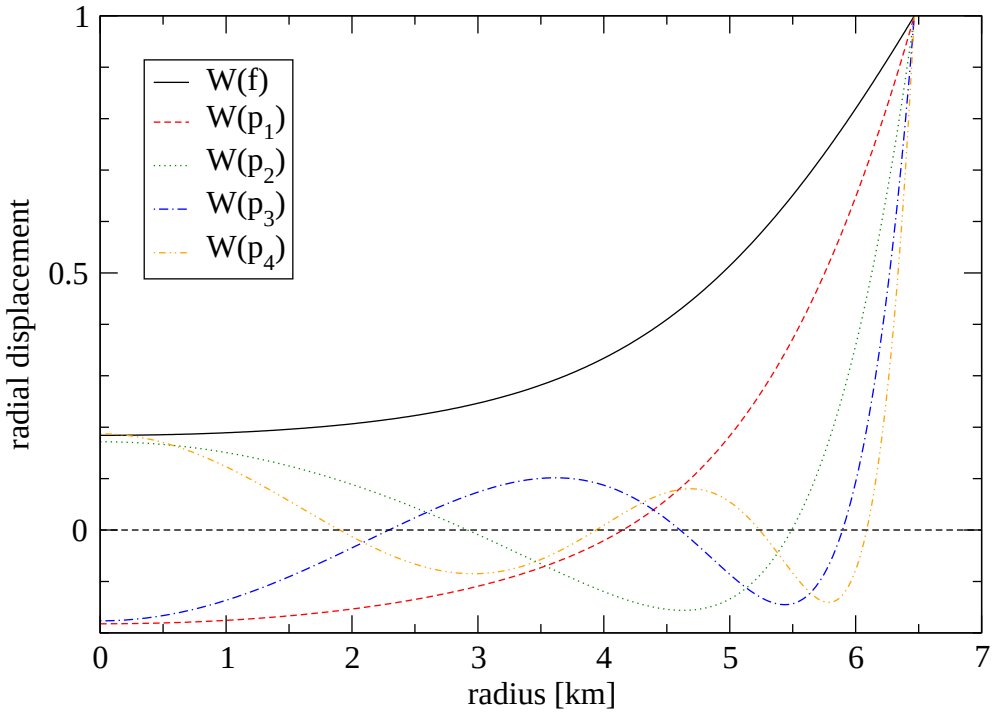

Figure 3.12: Eigenfunctions of W of the f- and first four p-modes of model 4 of KS92. The functions are normalised to $W(R) = 1$. The largest displacement is in the outer layers of the star and it is apparent that the number of nodes increases by one per mode.

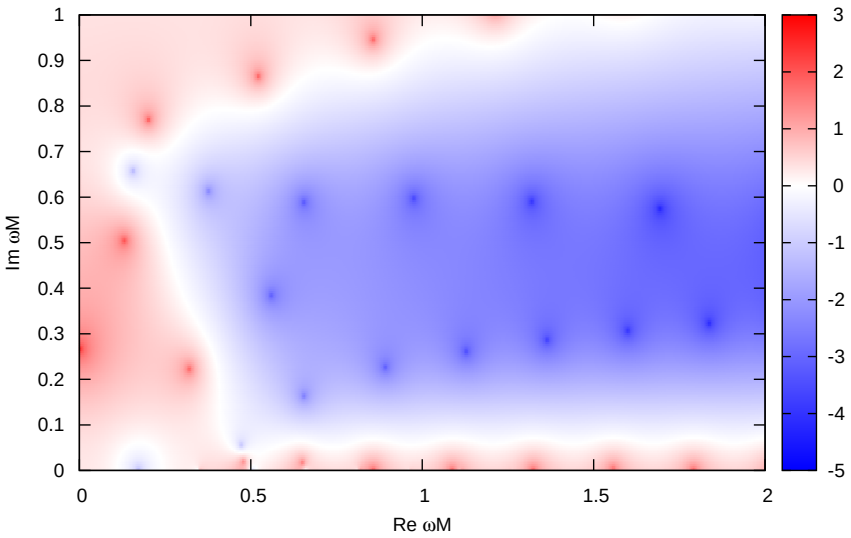

Figure 3.13: As Figure 3.2 but here we have plotted $\log|A_{\text{in}}|$ instead of $\log|A_{\text{in}}/A_{\text{out}}|$. The main difference are the singularities appearing close to the real axis which seem to be linked to the w-modes.

Table 3.3: Some eigenfrequencies of model 4 of Kokkotas & Schutz [21]. The first two columns show the highly damped w-modes (not the $\bar{w}$-modes); their values are in excellent agreement with Andersson et al. [61]. The second pair of columns shows the frequencies and damping times of the fundamental (first row) and pressure modes (remaining rows); our results agree very well with AKS95 for the real part and the imaginary part of the lower order p-modes. For the higher order p-modes we find a discrepancy of up to factor 10 which most likely stems from the limited numerical accuracy of the code which AKS95 have used. The last pair of columns shows again the eigenfrequencies of the f- and p-modes, however, this time for the stratified model 4 where we artificially set $\gamma/\gamma_0 = 1.1$. We do not show the w-modes of the stratified star as they are identical to the ones of the barotropic star.

Highly damped modes (w)		Slowly damped modes (f, p)			
		Barotropic		Stratified ($\gamma/\gamma_0 = 1.1$)	
$\mathrm{Re}(\omega M)$	$\mathrm{Im}(\omega M)$	$\mathrm{Re}(\omega M)$	$\mathrm{Im}(\omega M)$	$\mathrm{Re}(\omega M)$	$\mathrm{Im}(\omega M)$
0.471	0.056	0.1708	$6.193 \cdot 10^{-5}$	0.1709	$6.204 \cdot 10^{-5}$
0.653	0.164	0.3436	$2.460 \cdot 10^{-6}$	0.3663	$2.521 \cdot 10^{-6}$
0.891	0.227	0.5025	$3.965 \cdot 10^{-5}$	0.5320	$2.172 \cdot 10^{-5}$
1.127	0.261	0.6578	$3.384 \cdot 10^{-6}$	0.6940	$2.084 \cdot 10^{-6}$
1.362	0.287	0.8101	$6.737 \cdot 10^{-7}$	0.8530	$3.846 \cdot 10^{-7}$
1.598	0.307	0.9605	$1.685 \cdot 10^{-7}$	1.010	$8.718 \cdot 10^{-8}$
1.835	0.324	1.110	$4.947 \cdot 10^{-8}$	1.166	$2.274 \cdot 10^{-8}$
2.072	0.339	1.258	$1.636 \cdot 10^{-8}$	1.322	$6.395 \cdot 10^{-9}$
2.309	0.351	1.406	$5.922 \cdot 10^{-9}$	1.477	$1.872 \cdot 10^{-9}$
2.546	0.363	1.554	$2.273 \cdot 10^{-9}$	1.631	$5.400 \cdot 10^{-10}$
2.782	0.374	1.701	$9.091 \cdot 10^{-10}$	1.786	$1.418 \cdot 10^{-10}$

located farther away from the real axis with a larger imaginary part. We note that these peaks do not lie precisely on the real axis but have small imaginary parts. The precise origin of these peaks remains unclear. We can provide another piece for this puzzle; the locations of these peaks depend on the chosen normalisation. Remembering that we deal with a linear problem, we realise that the interior solution is unique only up to an arbitrary amplitude, see Section 3.7.1. In our simulations, we choose $W(R) = 1$ as normalisation condition. This also leads to the clearly visible spikes in the spectrum for the following reason. If the incoming gravitational wave is in resonance with the star, in particular with a slowly damped mode which essentially is an oscillation mode of the fluid, then only a weak incoming wave (low A_{in}) is necessary in order to excite a strong response of the fluid (large W). Even an excitation at a frequency slightly different from the eigenmode leads to a response of the fluid—this causes the singularities to have a "width". If a resonance of the fluid couples strongly to space-time vibrations then it can lose energy quicker via the emission of gravitational waves. The other way

around, such a mode can be excited by gravitational waves whose frequency deviates from the resonance frequency.

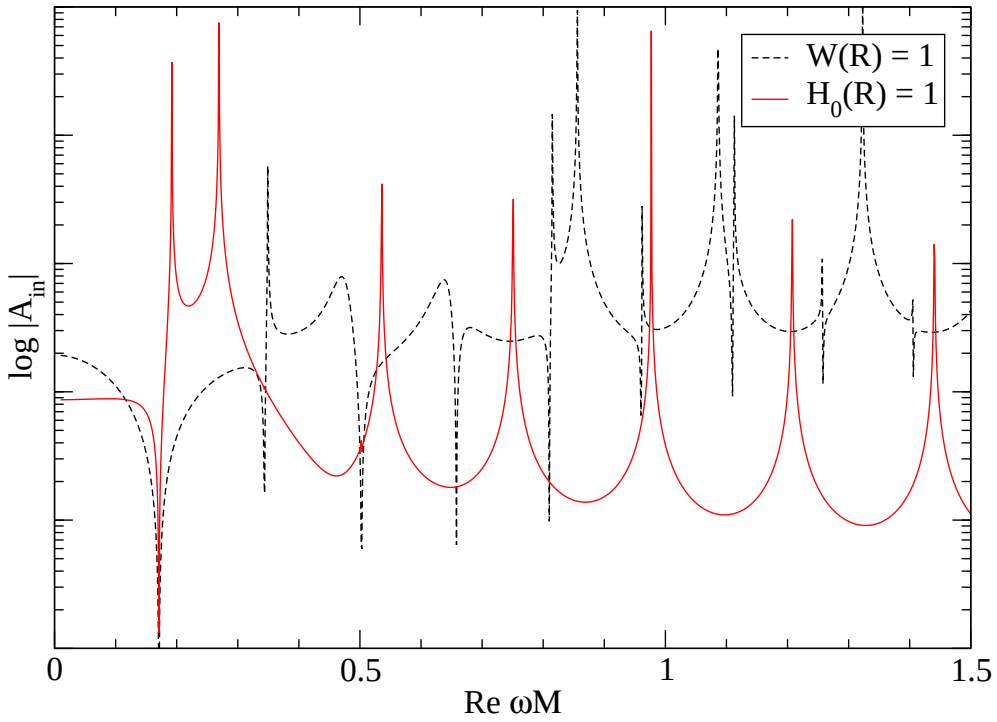

Figure 3.14: The spectrum as shown in graph as in Figure 3.11 compared to the spectrum when normalised with $H_0(R) = 1$. Both times we have used the resolution $\Delta\omega M = 0.001$. In the spectrum normalised with $H_0(R) = 1$, the p-modes are essentially indistinguishable—but they are there; they become visible when using a higher resolution. The peaks associated with w-modes are at different locations in both spectra.

If we, instead, enforce $H_0(R) = 1$, we are still able to locate the p-modes but it is incomparably harder; the spikes are even more narrow. This is because for slowly damped modes space-time and the fluid are not strongly coupled. The response of the fluid to deviations from the resonance frequency is less sensitive than the response of the space-time. We will, therefore, stick to the condition $W(R) = 1$. However, when using the normalisation condition $H_0(R) = 1$ then the broad peaks that seem to be connected to the w-modes have considerably shifted frequencies (but we still find one peak per w-mode). We show a comparison of both spectra in Figure 3.14. We have kept the resolution for both spectra at $\Delta\omega M = 0.001$ in order to demonstrate the severe difficulty in locating the p-modes when the normalisation $H_0(R) = 1$ is used.

The Effect of Stratification and Gravity Modes

We have now discussed the spectrum of a barotropic star. We successfully identified the w-modes as well as f- and p-modes and our results for model 4 of KS92 agree very well with published values; we were able to improve the accuracy of some results. As a next

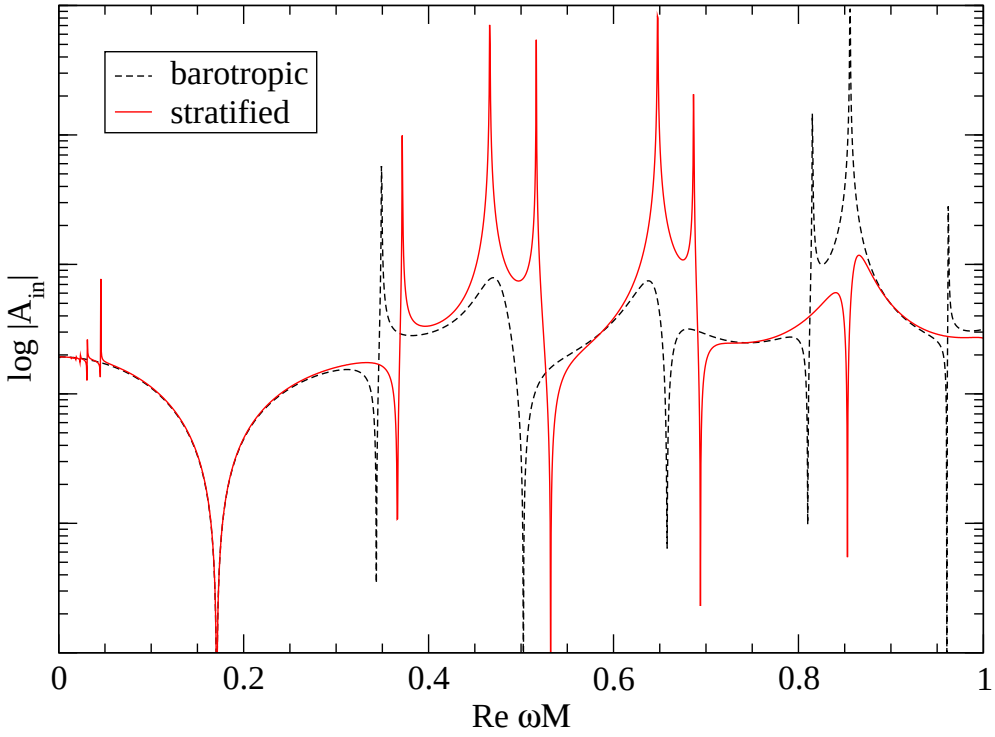

Figure 3.15: The spectra of the barotropic model 4 of KS92 as well as its stratified counterpart, where we artificially set $\gamma/\gamma_0 = 1.1$. In the stratified spectrum (solid line), we observe the appearance of g-modes in the low frequency part and that the p-modes are shifted to slightly higher frequencies.

step we will extend this basic model by introducing an artificial composition gradient. For this, we will simply increase the adiabatic index γ of the perturbed matter, so that $\gamma/\gamma_0 = 1.1$ throughout the star. This change strongly affects the gravity modes or g-modes which are all degenerate at zero frequency in a barotropic star [49]; these modes will populate the low frequency part of the spectrum at frequencies below the f-mode. Since the increased value of γ directly influences Δp, cf. equation (3.31), we also expect that the pressure modes are affected by this change.

We show the spectra of both the barotropic and stratified star in Figure 3.15. The f-mode is entirely unaffected by the stratification. To the right of the f-mode, we observe that the p-modes have slightly increased in frequency. The effect is stronger the higher the order of the p-mode is. We also find that the damping times (not visible in this graph) are increased compared to the barotropic star; we show them also in Table 3.3. For a clearer picture, we plot the complex frequencies of the f- and p-modes in Figure 3.16. We find the same surprising behaviour as AKS95; the damping time of the p_1-mode is considerably longer than that of the p_2-mode. If we leave the first p-mode out then the data indicate that the damping times grow approximately exponentially with the order of the p-mode. Apart from a small increase, the damping times of these modes are barely affected by stratification.

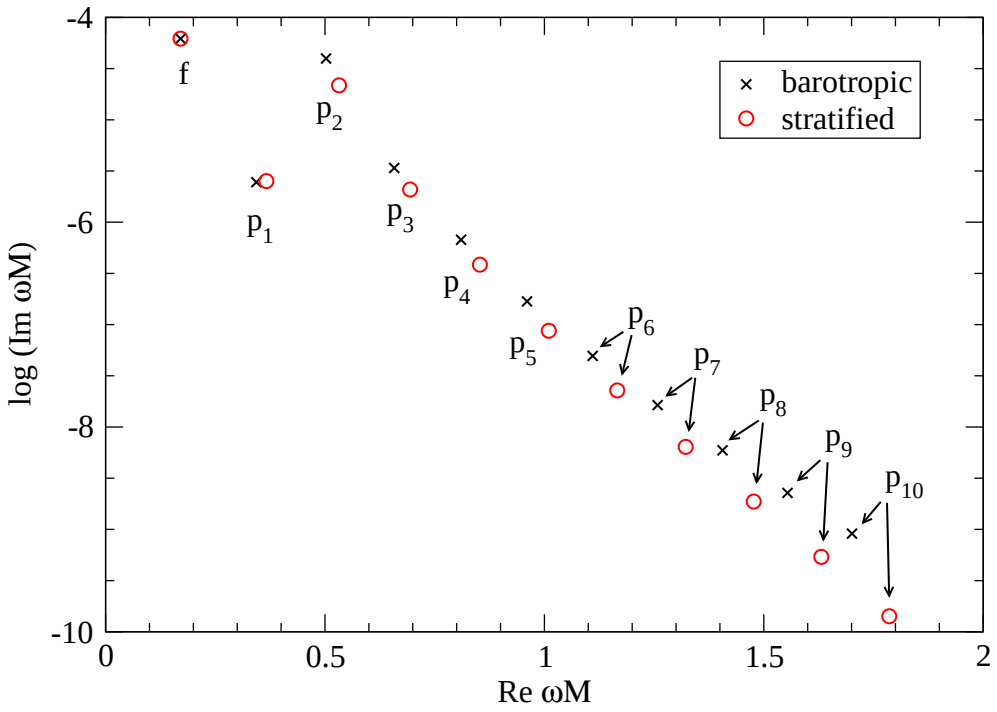

Figure 3.16: The complex frequencies of the slowly damped modes of model 4 of KS92. The crosses are for modes of the barotropic star whereas circles denote the frequencies of the stratified counterpart. The f-mode is entirely unaffected by stratification, the first p-mode is only slightly affected. Stratification slightly increases the frequency as well as the damping time of the higher order p-modes.

To the left of the f-mode in Figure 3.15, we observe a few small spikes. These are the gravity modes or g-modes. The g-mode with the highest frequency is located at $\mathrm{Re}(\omega M) = 0.0454$ and it is the g-mode of lowest order; this is a generic result proved by Andersson & Comer [82] who have reformulated the eigenmode problem as a Sturm-Liouville problem which has an infinite set of eigenfuntions as solution. In the case of the g-modes the lowest order mode has the highest frequency and with increasing order of the mode, the number of nodes in the radial direction increases and their frequency decreases and finally converges to zero. This means that the frequency difference between higher order g-modes gets smaller and smaller. We show a zoom-in in Figure 3.17 at very low frequencies which as been produced with a resolution of $\Delta\omega M = 10^{-6}$ and shows 37 g-modes. It is obvious that the modes move closer together at low frequencies. While oscillation modes of this high order are astrophysically most likely irrelevant, this graph clearly demonstrates the high accuracy of our code; at the lower end we can clearly distinguish modes which are only $\Delta\omega M = 4.2 \cdot 10^{-6}$ apart. We show the eigenfunction of the first five g-modes in Figure 3.18; it is apparent that, in contrast to the p-modes, these modes have their largest amplitude at the centre of the star. Similarly, we see that the number of nodes in radial direction increases by one per node with the lowest order mode having one radial node very close to the surface

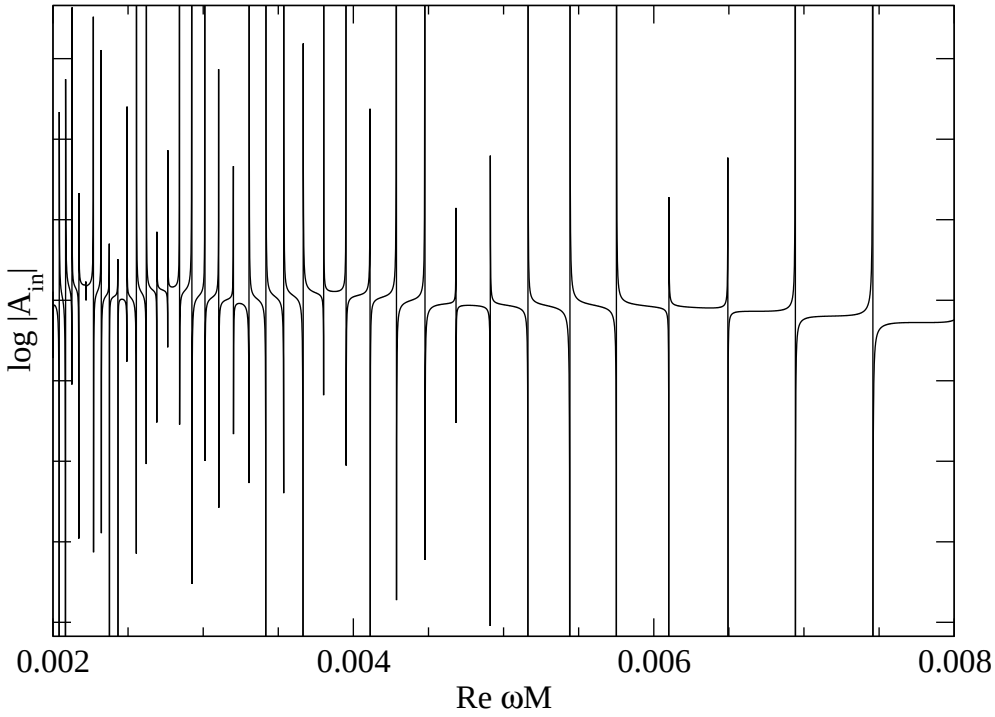

Figure 3.17: A zoom-in into the low frequency domain of the spectrum shown in Figure 3.16. This graph indicates 37 g-modes which at lower frequencies move closer to each other. This graph proves the accuracy of our code; we are able to distinguish modes that are $\Delta\omega M = 4.2 \cdot 10^{-6}$ apart.

of the star.

We also attempt to determine the damping time of the lowest order g-modes. This proves to be challenging and we are able to determine damping times for the three lowest g-modes; we show them in Table 3.4. The real value of ω can easily be determined to high accuracy. However, the damping times in these cases are very small—the imaginary part of ω is 10 or more orders of magnitude smaller than the real part which definitely scratches the limits of our numerical accuracy. While we are confident that the damping time for g_0 is somewhat accurate, we quote the damping times for g_1 and g_2 with care and they should be used only as a guideline. However, it is clear that g-modes are very long lived modes and the damping time seems to increase even faster than for p-modes when going to higher order.

All eigenmodes of neutron stars, apart from the w-modes, have quite long damping times which makes their determination within the framework we use here difficult. Therefore, we will quote damping times only in a few cases where we can determine them to acceptable accuracy and more for academic reasons; we are mainly interested in the frequencies of the oscillation modes in this study. We point out that the frequencies of high order modes can generally be accurately determined within the Cowling approximation in which oscillations of the space-time are neglected; in this framework, the equations are simpler (due to the neglected degree of freedom) and their solution

computationally less expensive. This approach works the better the smaller the damping due to gravitational wave emission is, that is, the higher the order of the modes.

Table 3.4: Eigenfrequencies of the three lowest g-modes of model 4 of Kokkotas & Schutz [21] to which we have added stratification ($\gamma/\gamma_0 = 1.1$). The real value of ω can easily be determined to high accuracy. The damping times in brackets should be taken with care as we do not fully trust these results due to limited numerical accuracy. For the modes g_3 and g_4, we did not attempt to calculate the damping times.

Mode	$\mathrm{Re}(\omega M)$	$\mathrm{Im}(\omega M)$
g_0	$4.535 \cdot 10^{-2}$	$1.41 \cdot 10^{-12}$
g_1	$3.070 \cdot 10^{-2}$	$(1.1 \cdot 10^{-13})$
g_2	$2.323 \cdot 10^{-2}$	$(8 \cdot 10^{-16})$
g_3	$1.871 \cdot 10^{-2}$	-
g_4	$1.570 \cdot 10^{-2}$	-

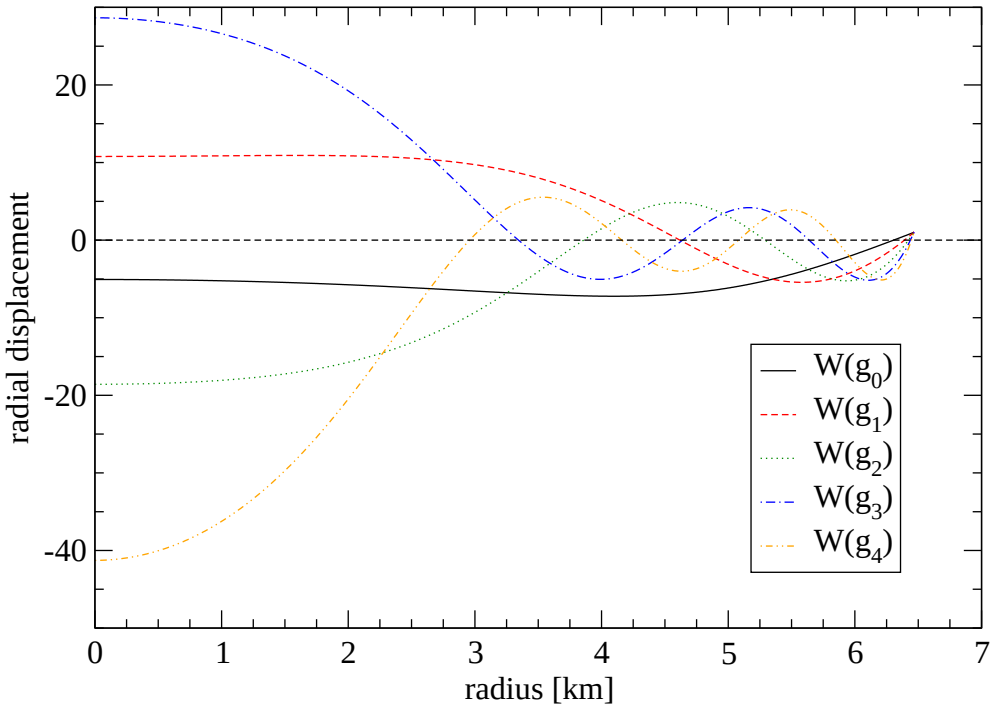

Figure 3.18: Eigenfunctions of W of first five g-modes of model 4 of KS92 (including stratification, $\gamma/\gamma_0 = 1.1$. The functions are normalised to $W(R) = 1$. The largest displacement is at the centre of the star and it is apparent that the number of nodes increases by one per mode.

3.10.2 Brief Summary on the Test Cases

Along with the comparison to established knowledge from literature, we have discussed the spectrum of a polytropic neutron star and built an understanding what to look for

and how to find it; we identified all mode classes expected for such a star, which are the f-, p-, g- and w-modes.

The w-modes are strongly damped which means their complex frequency has a comparatively large imaginary part and they are quite easy to find using Muller's method. Our code reproduces literature values with excellent agreement.

The complex frequencies of slowly damped modes, i.e. f-, p- and g-modes, have very small imaginary parts and are most efficiently determined by approximating them purely on the real axis. In many cases, the imaginary part of the latter cannot reliably be determined due to limited numerical accuracy. Our calculated values for the f- and p-modes agree well with literature values, while the results for the g-modes serve as qualitative evidence for the correct implementation of the physics.

When we put more physics into our neutron star model, we will encounter more classes of oscillation modes, all of which have very long damping times. This means that we will mainly focus on logarithmic plots of $|A_{\text{in}}|$ along the real axis in order to quantify the frequency spectrum of our model neutron star; the w-modes will always be present, of course, but they are a feature of the space-time rather than the neutron star itself and they will not be affected when we alter the physics of the neutron star model (but not its matter distribution). The slowly damped modes of a realistic neutron star will be the subject of the following sections.

3.10.3 Towards Reality: Perturbations of a Realistic Neutron Star Model

In the following, we will focus on a more realistic neutron star model. This model will be built using the EoS we have explained in Section 2.2. As before, we will, for a better understanding, put in more physics into our model step by step. After the investigation of the polytropic model in the previous section, we have a good understanding of the spectrum of a stratified, perfect fluid star. We will, therefore, take a stratified star as our starting point for the investigation of the more realistic model. However, owing to the EoS, we cannot omit the presence of density discontinuities—they are built into the EoS. This does not pose a serious problem since the corresponding interface modes (or i-modes) are easy to distinguish by their eigenfunction and there is exactly one mode per discontinuity (in contrast to the other classes of modes which normally consist of an infinite set of modes).

Our model neutron star which we will thoroughly study, has a central energy density of $\rho_c = 1 \cdot 10^{15}\,\mathrm{g\,cm^{-3}}$. This leads to a mass of $M = 1.447\,M_\odot$ and a circumferential radius of $R = 11.77\,\mathrm{km}$. The EoS consists of the (tabulated) SLy4 force in the core and the DH EoS for the crust (cf. Section 2.2).

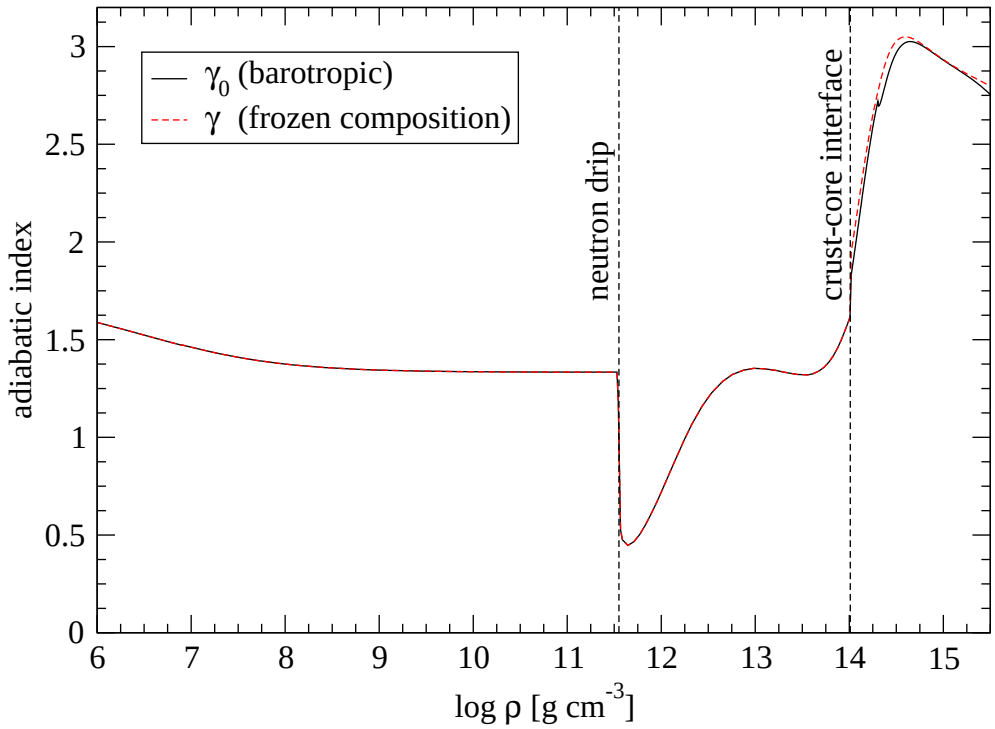

Figure 3.19: The adiabatic indices of our EoS. The solid line depicts the background adiabatic index γ_0, whereas the dashed line depicts the adiabatic index of the perturbed matter, γ. For clarity, we have marked with dashed lines the density at which the neutron drip occurs and the density of the crust-core interface.

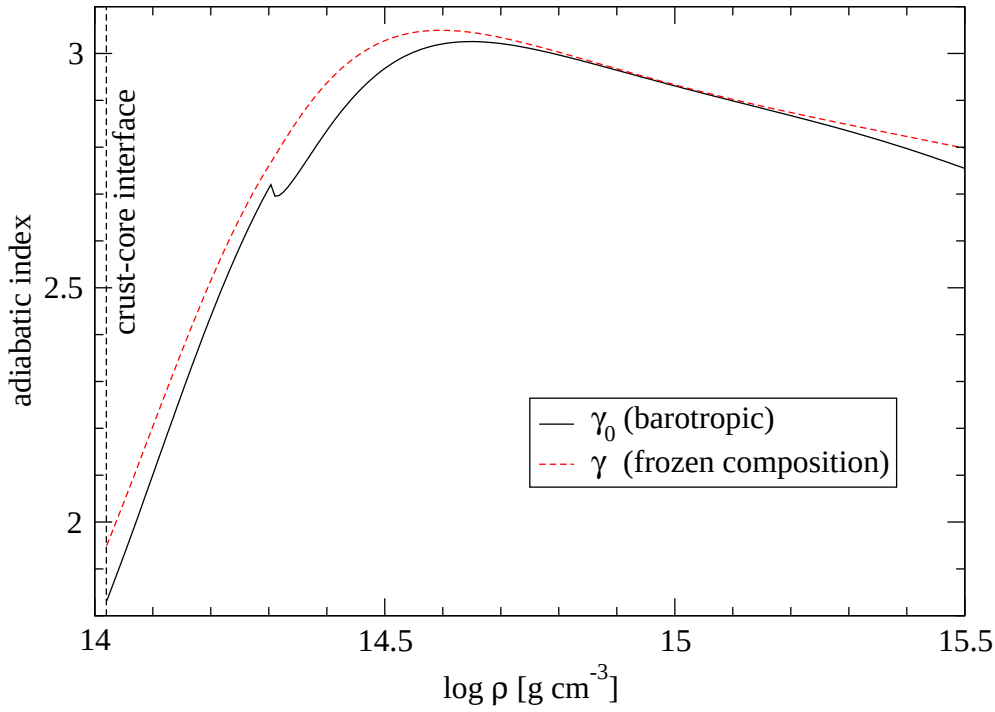

Figure 3.20: As Figure 3.19 but zoomed into the core region. These are essentially the adiabatic indices of the SLy4 force.

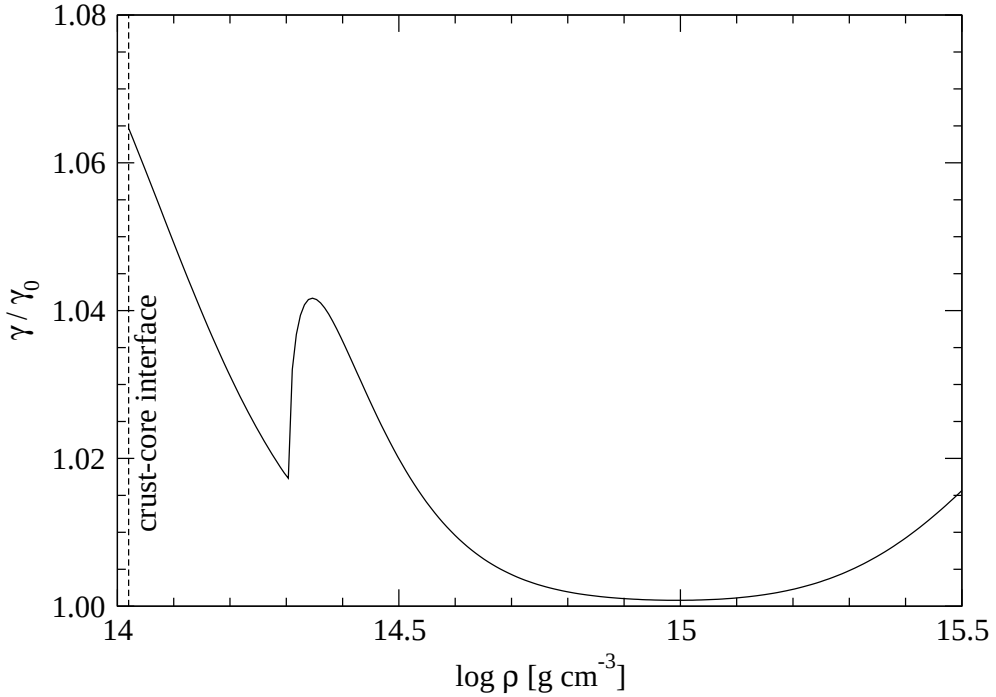

Figure 3.21: The ratio γ/γ_0 of adiabatic indices from our EoS in the core. We do not show the crustal region since we have $\gamma = \gamma_0$ there. The ratio increases nearly discontinuously at about $\log \rho \approx 14.3$ which is where the muons appear.

Composition Gradient

At first, we look at the pressure modes (and obviously the fundamental mode). We compare the spectrum for the barotropic model with the spectrum where we account for stratification in Figure 3.22. We find a prominent singularity for the f-mode at 1.938 kHz, and seven more singularities for the p-modes p_1 to p_7; we show their frequencies including damping times (where our code converged) in Table 3.5. It is apparent that the difference between the barotropic and the stratified spectrum is only marginal. This is due to the rather small difference between γ and γ_0, cf. Figure 3.21; the ratio γ/γ_0 never reaches 1.07 and quickly decreases towards the centre of the star. In fact, the ratio stays below 1.02 for large parts of the core. When we studied the polytropic case, we artificially employed a ratio of $\gamma/\gamma_0 = 1.1$ throughout the star in order to perturb the g-modes away from zero frequency; this fraction is much larger than the fraction as calculated from the EoS we use. This leads to a smaller correction of the pressure perturbation and hence a less pronounced shift in frequency of the p-modes.

As in the polytropic case, an accurate determination of the real part does not pose a problem; we can easily iterate and achieve several digits precision (given that our background model has the same precision). However, we find it very hard to calculate the damping times. For the modes f and p_1, our code converges relatively quickly to a reasonable result; 186 ms and 4062 ms, respectively. For higher order p-modes,

Table 3.5: Eigenfrequencies of the f-mode and the seven lowest p-modes of our barotropic neutron star model. The damping times in brackets should be taken as guideline only; for the modes p_5 to p_7, our code did not converge when iterating for the damping times.

Mode	Frequency [kHz]	Damping time [ms]
f	1.938	186
p_1	6.281	4063
p_2	9.410	$(2 \cdot 10^6)$
p_3	11.10	$(2 \cdot 10^6)$
p_4	12.46	$(6 \cdot 10^6)$
p_5	14.43	-
p_6	16.87	-
p_7	18.29	-

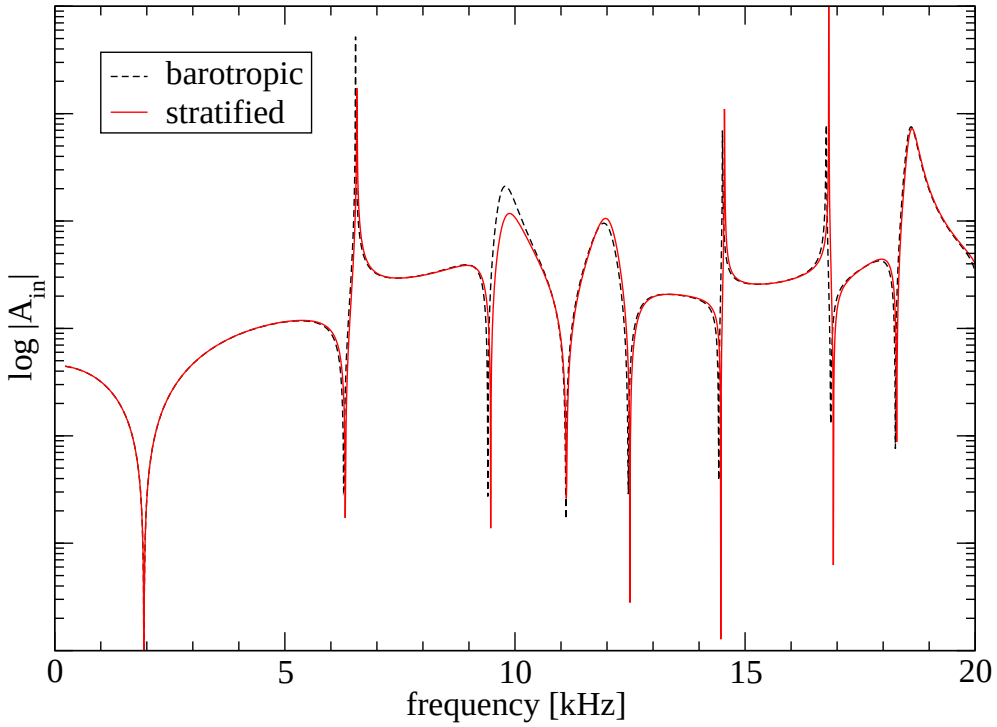

Figure 3.22: The spectra of our realistic model. The dashed line is for the barotropic star, the solid line shows the spectrum when accounting for stratification.

the iterations take much longer and we cannot push $\log|A_{\rm in}/A_{\rm out}|$ below about -4 (the minimum we can achieve depends on the mode, of course); firstly, this is a few orders of magnitude above our desired threshold of -7, secondly, a high resolution run at the estimated location of the eigenmode does not result in a neat ("pointy") singularity as in the polytropic case but rather in a depression with a ("flat") minimum. We quote the damping times for the modes p_2, p_3 and p_4 but note that they should be taken with care. While we cannot determine the damping time accurately, we still feel confident to say that the p_2-mode has a considerably longer damping time than the p_1-mode—in contrast to the polytropic case where the p_2-mode had an about 10 times shorter damping time. Iterating for the damping times of the mode p_5 or higher p-modes is entirely unsuccessful.

We will now turn to the low frequency part of the spectrum. As discussed earlier, we will inevitably find interface modes in the spectrum due to the phase transitions in the crust and also at the neutron drip and due to the artificial matching of the crust and core EoS. When we "switch on" stratification, we will also find g-modes. We show the low frequency domain up to 200 Hz as well as a zoom in at the lower the lower end of the frequency window for our neutron star model with zero temperature and without solid crust in Figures 3.23 and 3.24. In order to resolve all different modes, we have to choose a rather high frequency resolution, in particular for the lower end of the spectrum. For example, it turns out that the spike at roughly 30 Hz in Figure 3.24 actually consists of two separate singularities (cf. Table 3.6). We choose $\Delta\omega M = 5\cdot 10^{-8}$ for the lowest frequencies and find that a much coarser grid with $\Delta\omega M = 4\cdot 10^{-6}$ is enough in order to identify the modes above 80 Hz. It is imperative to select a potentially too high resolution to begin with since some of the singularities are incredibly narrow and can easily be overlooked if the resolution is too low.

The frequency range shown in Figure 3.23 contains all (slowly damped) low frequency modes that are present in the model below the f-mode. We note that our code is not able to produce reasonable results for very low frequencies; below 18 Hz, the spectrum gets quickly spoilt by noise which makes an eigenmode determination impossible. For comparison we show the spectrum for both the unstratified star (solid line) and the corresponding stratified star (dashed line). All low-frequency modes in an unstratified star are i-modes due to density discontinuities and there is precisely one interface mode associated with each density discontinuity. We order them by frequency and label them as i_n ($n \geq 1$), where i_1 is the interface mode with the highest frequency.

It turns out that the association with interface modes and specific density discontinuities is not unambiguous. The rule that the radial displacement of an interface mode has its peak amplitude exactly at the phase transition does not hold in our case [29]. The eigenfunctions have their maximum at a phase transition but we find that several interface modes would belong to the same phase transition according to this procedure. Likewise, there are discontinuities at which none of the i-modes have a maximum.

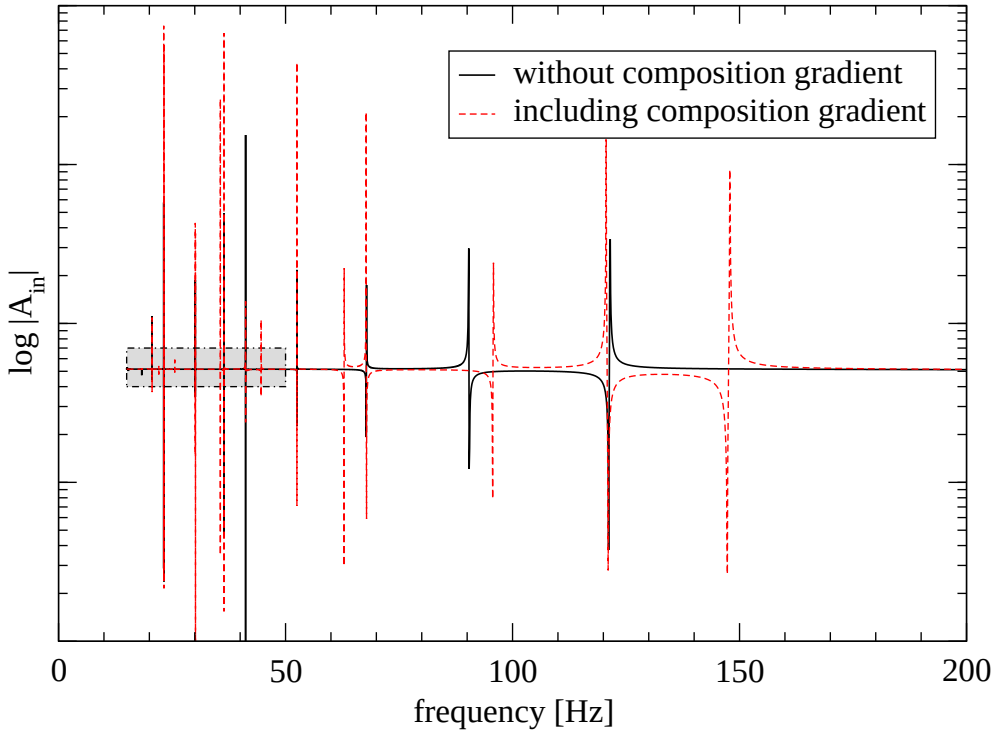

Figure 3.23: The low frequency spectrum of our neutron star at zero temperature and without a solid crust. Figure 3.24 shows a magnification of the dash-dotted box. The resolution varies between $\Delta\omega M = 5 \cdot 10^{-8}$ at lower end of the spectrum and $\Delta\omega M = 4 \cdot 10^{-6}$ at the upper end. The solid line shows the spectrum of the pure perfect fluid star, while the dashed line includes composition gradients. All spikes in the solid spectrum are interface modes as there is no composition gradient present; for each of these modes, there is also a mode present in the spectrum of the stratified star (with the exception of the mode at 90.4 Hz; see text). The "new" modes in the dashed spectrum are composition g-modes.

This is the result of the presence of several discontinuities in close vicinity which affect each other. We show the eigenfunctions of five interface modes in Figure 3.25, where the kinks at the phase transitions are clearly visible. The modes i_4 and i_5 have their strongest peak at the same transition. However, the i_1 mode has its highest amplitude at a transition where no other interface mode has its strongest peak. This *suggests* that this mode is associated with the transition $^{80}\mathrm{Zn} \rightarrow {}^{78}\mathrm{Ni}$. The i_2-mode apparently has its most prominent peak much deeper in the star and is associated with the artificial discontinuity at the crust-core interface due to the matching of the EoS.

Finn [27] provides a simple formula to give an estimate for the frequency of an i-mode; his calculations show that—in an idealised situation—the frequency of the interface mode is proportional to the relative jump in density, $\Delta\rho/\rho_+$, and the distance, Δr, of the associated phase transition from the surface of the star. Even though our results qualitatively agree, the formula is, unfortunately, not accurate enough for our purposes to make the exact association. As mentioned above, we find that the mode

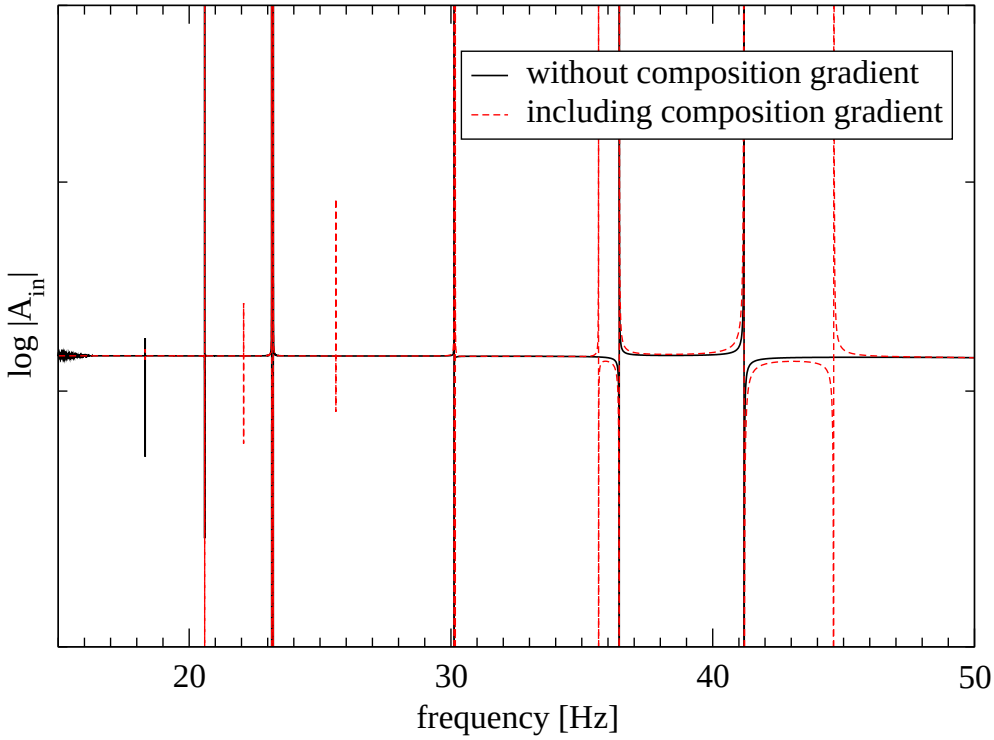

Figure 3.24: Magnification of the dash-dotted box in Figure 3.23.

i_1, which has the highest frequency amongst the interface modes in our star, is most likely due to the transition $^{80}\mathrm{Zn} \rightarrow {}^{78}\mathrm{Ni}$. This transition has the largest relative jump in density of $\Delta\rho/\rho_+ \approx 4.3\,\%$ and is located rather deep in the star when compared to the other phase transitions.

All interface modes (except for the one at 90.4 Hz; see below) are still present in the stratified star. However, we find a set of new modes appearing in the spectrum; these are the composition g-modes due to the stratification of the core (composition variations in the crust distinguish different layers and so only lead to interface modes associated with transitions from layer to layer). g-modes and i-modes are easy to distinguish if one examines their eigenfunctions. While the g-modes are mainly confined to the core and have their largest amplitude usually close to the centre of the star, the radial displacement of the i-modes nearly vanishes in the core and exhibit kinks at the phase transitions where they also have their peak amplitudes (cf. Figure 3.25). In contrast to the i-modes, the set of g-modes is infinite and we label them as g_n, where g_0 is the g-mode with the highest frequency and n will correspond to the number of nodes of the radial displacement *in the core*—we have to make this distinction here because we account for stratification only in the core region; in the crust the g-modes are still somewhat affected by the phase transitions.

We show the eigenfunctions of the first six g-modes in Figures 3.26 and 3.27 for the core and the crust, respectively; as the physics of the core and crust are very distinct the

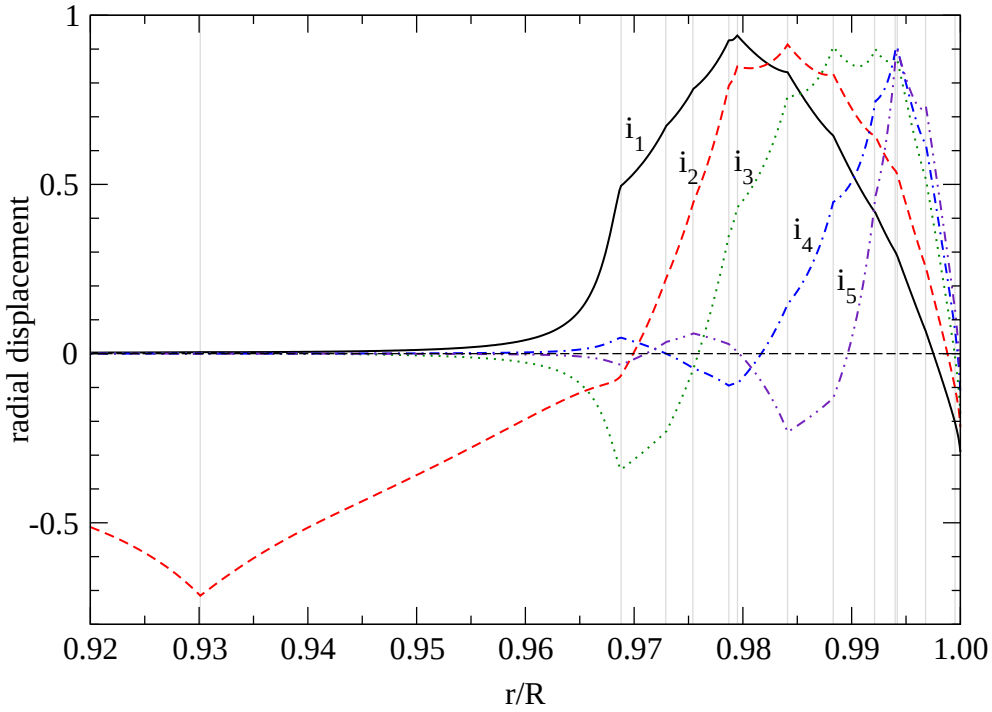

Figure 3.25: The radial displacement, ξ^r, for five i-modes of the unstratified star. The vertical, grey lines show the location of the different density discontinuities within the star; the interface at $r/R \approx 93\,\%$ is the crust-core interface. The amplitudes of the different modes are scaled so that they are of comparable size. The kinks at the phase transitions are clearly visible and the displacement nearly vanishes in the core (with the exception of the i_2-mode which is associated with the crust-core transition). The eigenfunctions are largely unaffected if stratification is switched on (again with the exception of the i_2-mode which turns into a g-mode, see text).

separation allows to scale both parts differently. The distinct g-mode pattern becomes apparent in Figure 3.26: the amplitude is largest at the centre of the star and the number of nodes in radial direction increases as the mode number increases. In the crust, the g-modes exhibit some kinks similar to the i-modes but their amplitude is smaller than in the core.

Let us have a brief look at the modes g_5 and i_6 which have very similar frequencies: 30.17 Hz and 30.12 Hz, respectively. We want to point out that our code has no problem to distinguish these modes from each other; their two singularities in the spectrum are well separated given that $\Delta\omega M$ is chosen small enough. Furthermore, their eigenfunctions are clearly different and perfectly show the distinct characteristics of the respective mode classes. The i_6-mode has its largest amplitude in the crust and its displacement essentially vanishes throughout the core whereas the g_5 has a large displacement throughout the core. However, both modes also bear striking similarities. If one looks at the core or the crustal region separately, one finds that their eigenfunctions are (apart from a proportionality constant) basically identical; the two constants

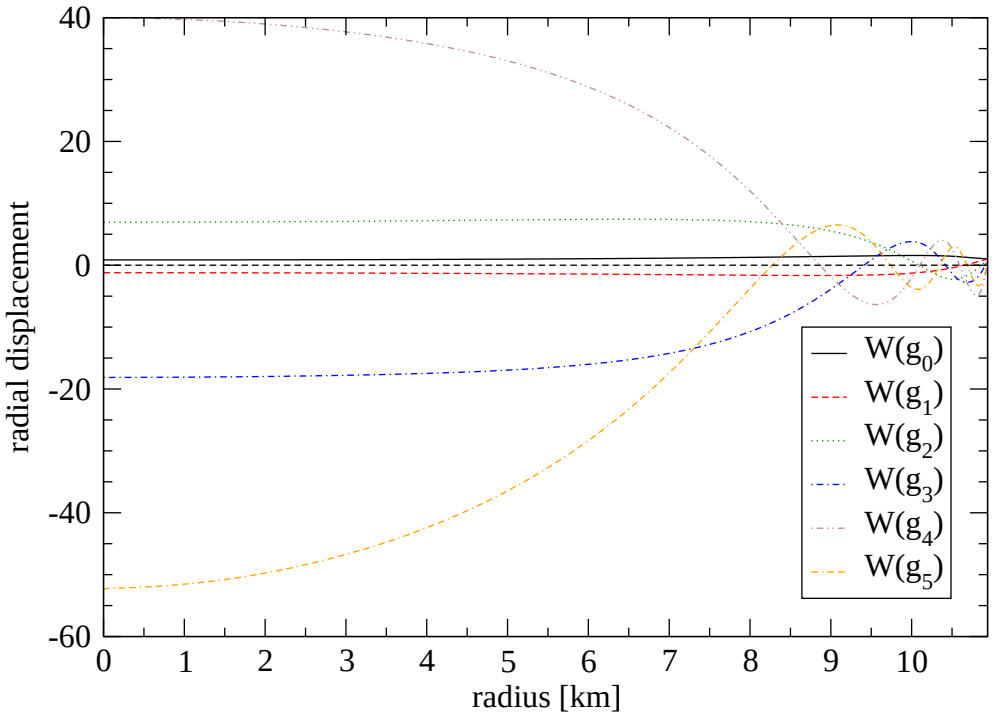

Figure 3.26: The eigenfunctions of the first six g-modes of our model neutron star. We show only the core region here (see Figure 3.27 for the crustal region) and we have normalised the functions to $W(R_{\rm cc}) = 1$. It is apparent the number of radial nodes increases as the mode number increases and the amplitude is largest at the centre of the star.

for crust and core differ considerably. We find

$$W(g_5)\big|_{\rm core} \approx c_1\, W(i_6)\big|_{\rm core}\,, \tag{3.189}$$

$$W(g_5)\big|_{\rm crust} \approx c_2\, W(i_6)\big|_{\rm crust}\,, \tag{3.190}$$

where $c_1/c_2 \approx -4000$. This number means that if the eigenfunctions of g_5 and i_6 have the same amplitude, say, in the core, then they differ by a factor of -4000 in the crust.

Starting from the surface of the star, the 13th jump in density, which is due to the manual matching of the EoS at the crust-core interface, deserves a few more comments since no associated interface mode can be found in the stratified star. When the star is barotropic (not stratified), we find an i-mode at 90.4 Hz associated with this density discontinuity. This discontinuity lies within (or at least at the edge of) the region where we account for stratification and an interface mode can be understood as a special kind of composition g-mode in the following way: a sudden change in density indicates a phase transition and as a result, a perturbed fluid element crossing this interface will experience buoyancy due to the different composition. This motivates that this i-mode loses its character and turns into the g-mode of lowest order when the star is stratified. To verify this, we ran a series of separate simulations in which we slowly

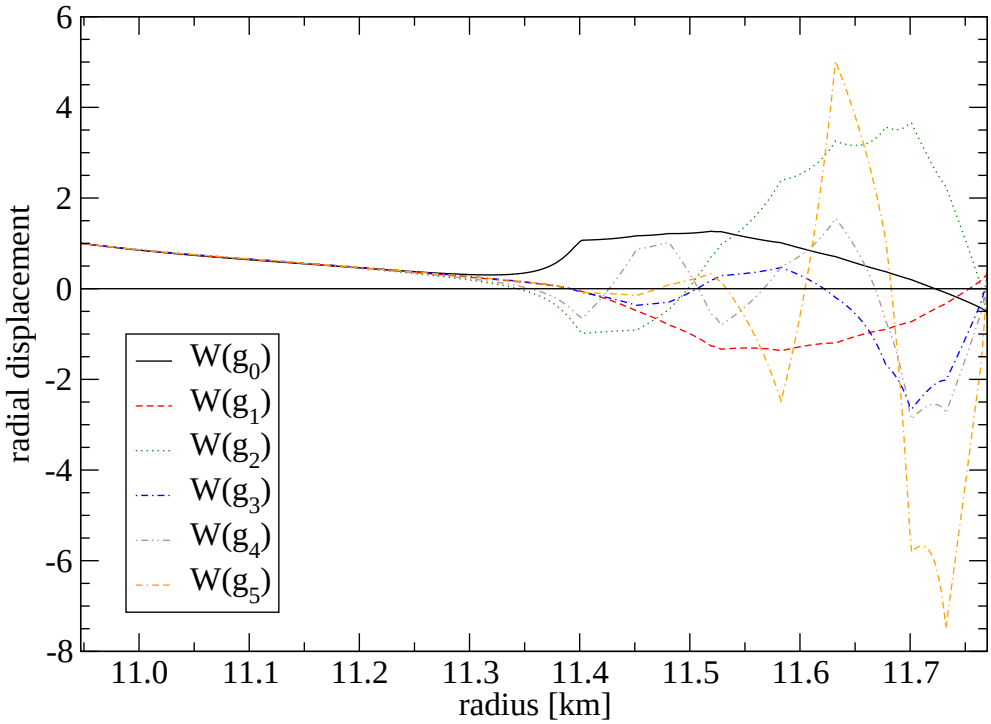

Figure 3.27: Same graph as in Figure 3.26 but here for the crust only. The g-modes are to some extent influenced by the phase transitions in the crust—they exhibit the same kinks as the i-modes.

Table 3.6: Frequencies of the i-modes and composition g-modes in the stratified, cold star.

Mode	Frequency [Hz]	Mode	Frequency [Hz]
g_0	147.3	g_5	30.2
i_1	121.1	i_6	30.1
g_1	95.6	g_6	25.6
i_2	67.8	i_7	23.2
g_2	62.8	i_8	23.1
i_3	52.5	g_7	22.1
g_3	44.6	i_9	20.6
i_4	41.2	g_8	19.6
i_5	36.4	i_{10}	18.3
g_4	35.6		

increased the composition gradient via the adiabatic index γ from "no stratification" up to "full stratification" (as given in the EoS). The interface mode accordingly increased in frequency and its eigenfunction changed, turning into the g_0 mode of the stratified star. This example illustrates the close relationship between these two classes of modes.

We list the low frequency modes of the stratified star in Table 3.6. The spectrum of the barotropic star can be easily extracted from this table by the following procedure: Remove all g-modes from this table and add one i-mode at 90.4 Hz. The frequencies of the i-modes are barely affected by stratification (they vary only by a few tenths of a hertz).

3.10.4 Accounting for Finite Temperature

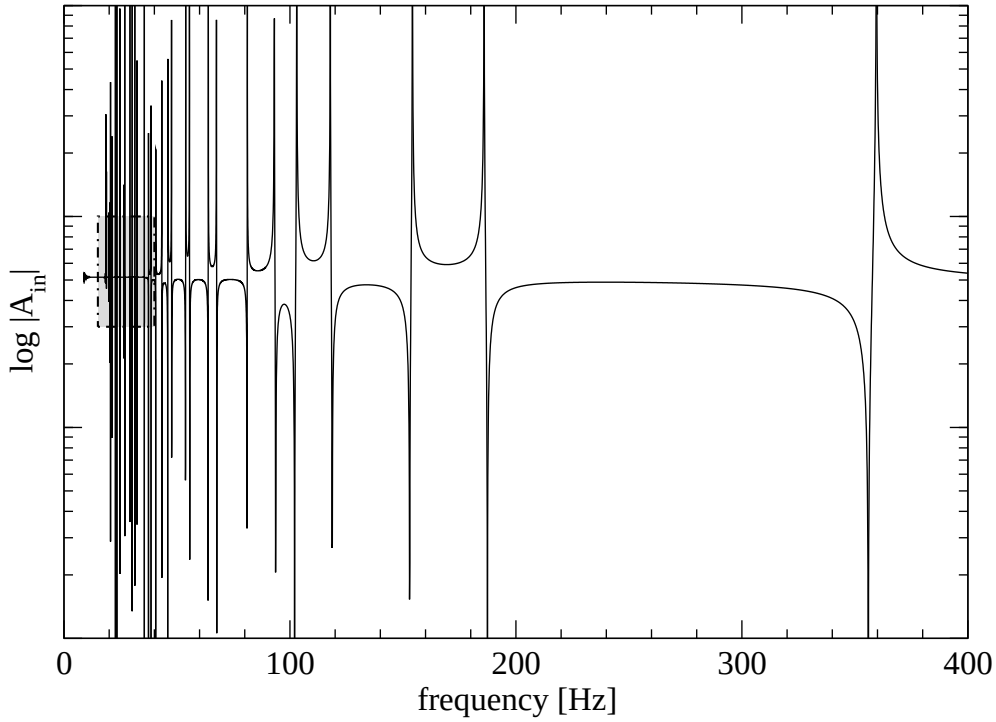

Figure 3.28: The low frequency spectrum when the star is 3 seconds old; including thermal pressure but without solid crust. Figure 3.29 shows a magnification of the dash-dotted box in the upper panel. The resolution varies between $\Delta\omega M = 5 \cdot 10^{-8}$ at low frequencies and $\Delta\omega M = 4 \cdot 10^{-6}$ at high frequencies.

The next step is to move away from the assumption that the neutron star is cold. As we have already described, we account for the thermal pressure by adding it to the static pressure of the cold equation of state used to determine the background. This leads to the results shown in Figure 3.28, which shows the low frequency spectrum of an isothermal neutron star with temperature $Te^{\nu} = 10^{10}$ K (our initial configuration). In comparison to the result at zero temperature (cf. Figure 3.23), we find a vastly enriched spectrum. A careful investigation reveals that all composition g-modes found

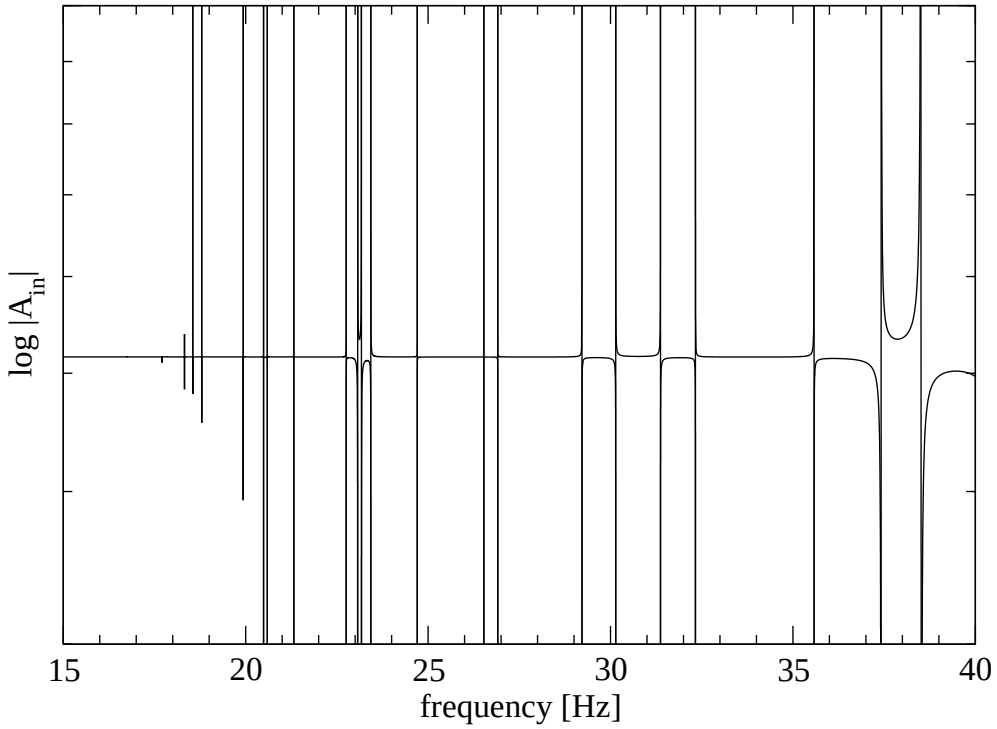

Figure 3.29: Magnification of the dash-dotted box in Figure 3.28.

in the cold, stratified star are still present in the hot star at only marginally altered frequencies (the difference is generally less than 0.1%, only the high frequency g-modes are shifted by up to 4%); likewise their eigenfunctions are unaltered. This is as expected since the composition g-modes in our model originate from the composition gradient in the core. The thermal pressure, however, is negligible in the core and hence does not affect the g-modes.

For the i-modes the situation is somewhat different. We find all interface modes in the hot star, too; however, while the low frequency interface modes maintain their frequency throughout the thermal evolution of the star, four interface modes with high frequencies (i_1, i_2, i_4 and i_5) have their oscillation period decreased. We are unable to provide a reason as to why this behaviour is observed for precisely these interface modes but not others.

In order to track the evolution of the spectrum as the star ages, we produced a time evolution of the low frequency modes in the following way: we start with the isothermal star at $Te^{\nu} = 10^{10}$ K, for which the spectrum is that shown in Figure 3.28, and extract temperature profiles at 120 time steps uniformly distributed on a logarithmic timescale up to the age of one million years. After extracting the mode frequencies for each of these temperature profiles, we are able to trace the evolution of the oscillation modes over time. This leads to the results shown in Figure 3.30. All modes exhibit avoided crossings which are easily visible in the high frequency part of the graph; they are also present in the low frequency part, where a higher resolution is necessary to resolve the

different modes.

We now find a set of new modes spread over the entire spectrum; these are the thermal g-modes. Their frequency decreases as the star cools and after about 100 years nearly all the thermal g-modes have frequencies of 18 Hz or less (below our noise cut-off). This is when the temperature has decreased so far that the thermal pressure is almost negligible and does not affect the frequencies of the g- and i-modes anymore.

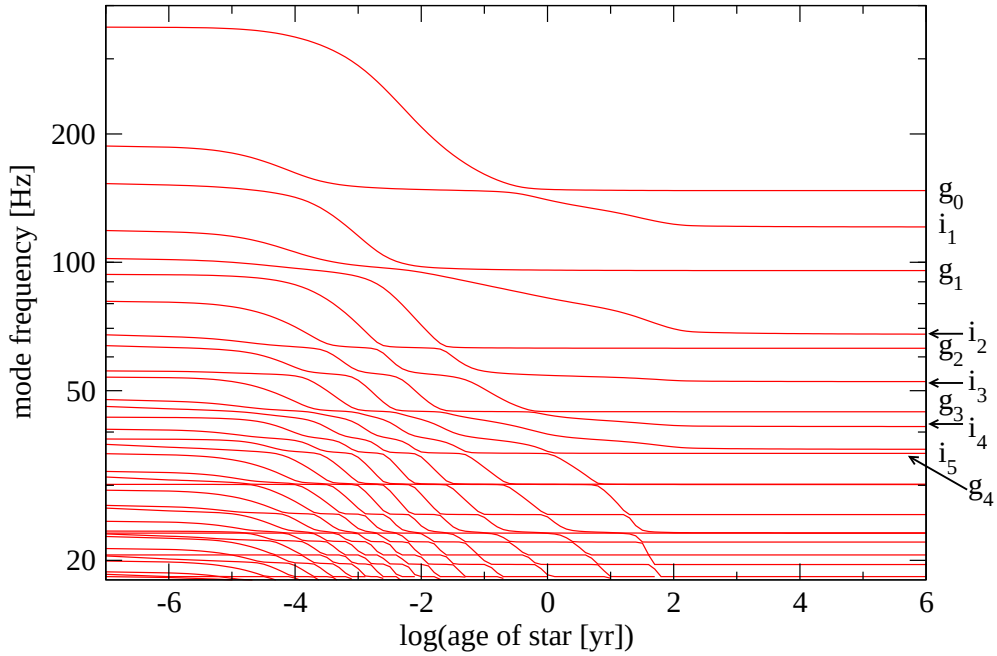

Figure 3.30: The star's low-frequency spectrum as the star cools. The thermal g-modes quickly decrease in frequency and are below 18 Hz after about 100 years. Four of the high frequency interface modes are affected by the thermal pressure (i_1, i_2, i_4 and i_5). All modes clearly exhibit avoided crossings.

For completeness, we considered the impact of thermal pressure on the fundamental and pressure modes. As an illustration of the results, we show the star's spectrum after 10 seconds, one month and 100 years in Figure 3.31. Since the f-mode is mainly due to the surface of the star and depends on the average density, it does not change (especially since we do not account for thermal pressure in the background model). The p-modes, however, should be affected since the thermal pressure contributes to the restoring force acting on sound waves. In our simulations we observe a slight increase in frequency by up to roughly 10 %, but only for p-modes of higher order and only in young, hot neutron stars. As is apparent from Figure 3.31, after just one month the frequencies of the p-modes are only slightly affected by the thermal pressure.

3.10.5 The Evolution of the Spectrum of a Star with Elastic Crust

Finally, we add the elastic crust to the model. As explained in Section 3.5.1, we define the region in which the crust is solid via the condition $\Gamma > 173$ for the Coulomb

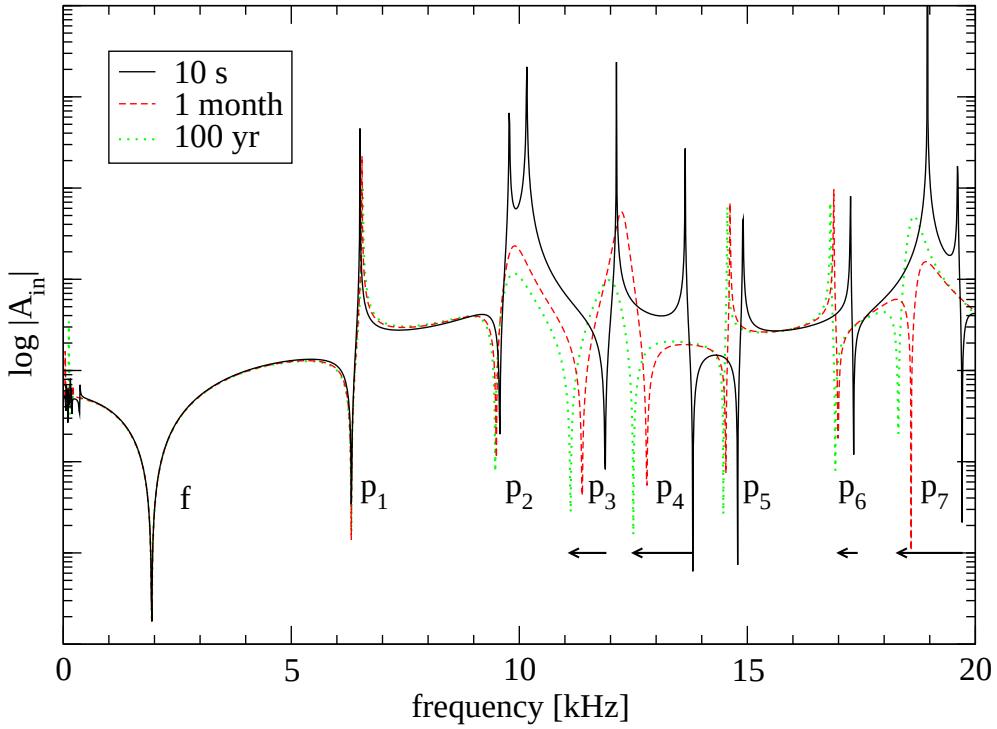

Figure 3.31: The stellar spectrum up to 20 kHz for three different temperature profiles. Clearly visible are the f-mode and first seven p-modes. Where the frequency of a p-mode varies visibly over time, an arrow indicates this change.

coupling parameter. As in the previous section, we start from an isothermal star with $Te^{\nu} = 10^{10}$ K. At this point, the crust is above its melting temperature and hence liquid; after approximately 1.1 days, the crust starts to crystallise (cf. Figure 3.1). In Figure 3.32 we show the spectrum up to 8 kHz for the neutron star at an age of 100 years, including the thermal pressure and composition gradients. Figure 3.33 provides a zoom-in at low frequencies. The two most prominent oscillation modes at 1.938 kHz and 6.315 kHz are the f-mode and the first p-mode, respectively; see also Figure 3.31. As expected, they are unaffected by the presence of the solid crust.

We want to comment on how we produced the graph in Figure 3.32. Apart from the relatively easy to identify f- and p-modes, we have, firstly, the gravity modes at low frequencies, but, secondly, we also find new modes with very thin spikes across the entire spectrum; these are the shear modes associated with the elastic crust (see below for discussion). They cause very narrow spikes which are nearly impossible to identify at the resolution of $\Delta\omega M = 5 \cdot 10^{-4}$ which we normally use to find pressure modes. We have therefore produced the spectrum using two different approaches; firstly, we have increased the overall resolution which at least reveals a few of the shear modes with lower frequencies. Due to their nature, the shear modes will appear approximately equidistantly spaced in the spectrum—this gives us a hint where to run the search again with higher resolution. The higher the frequency (or the order of the shear mode) the

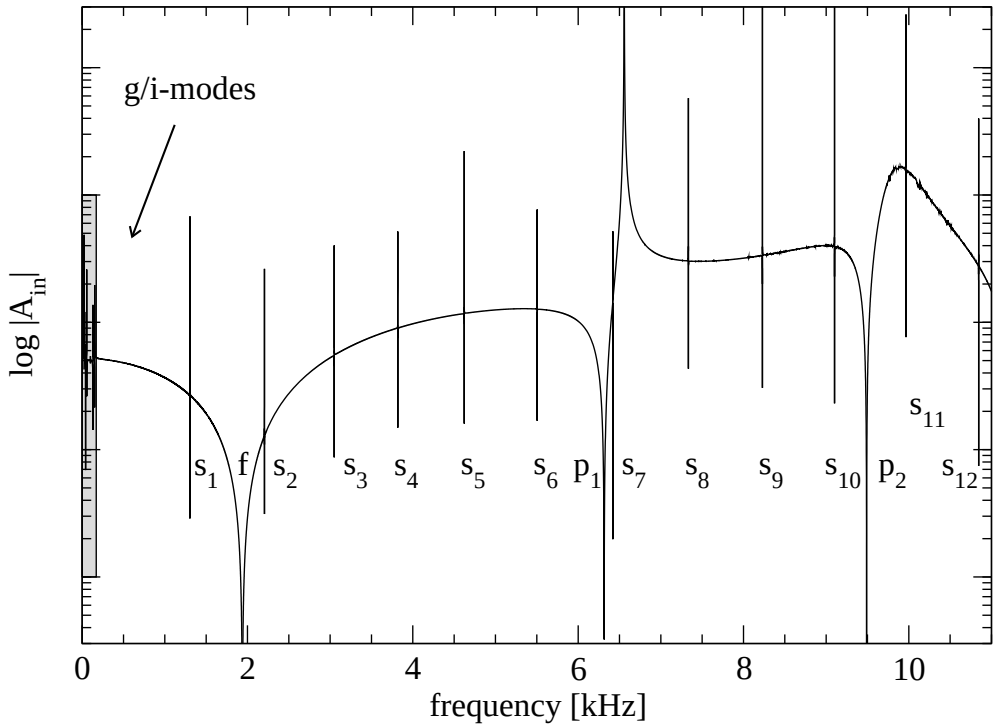

Figure 3.32: The spectrum of our model star including thermal pressure and an elastic crust, after hundred years of the star's life. This figure shows the high frequency domain, while Figure 3.33 zooms in at low frequencies to resolve the g- and i-modes.

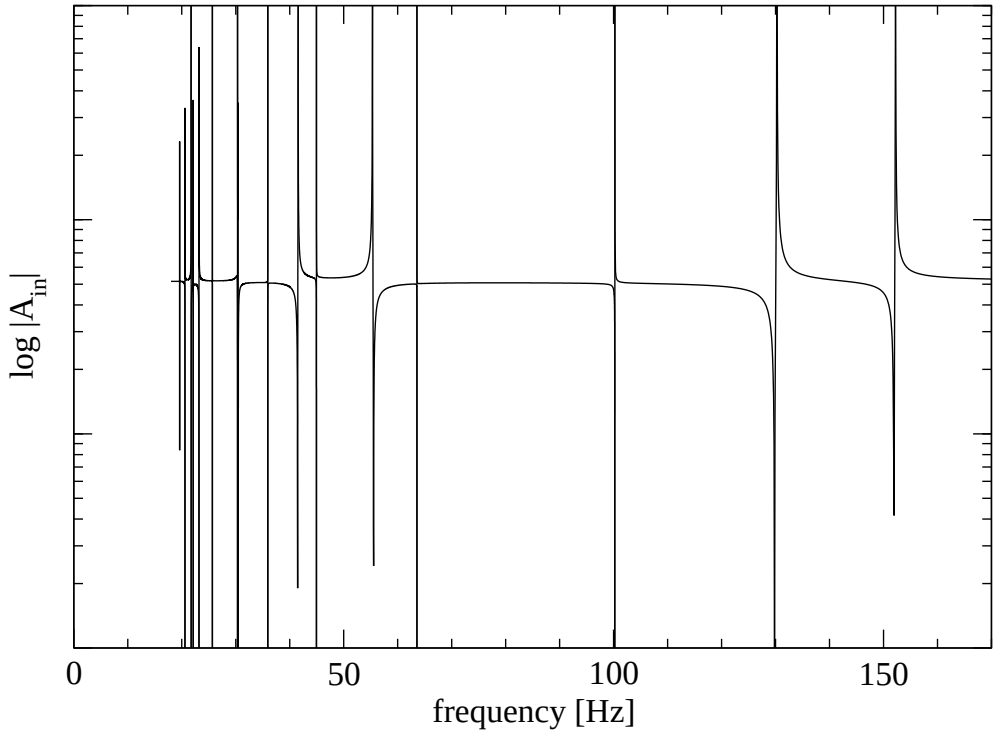

Figure 3.33: Magnification of the low frequency domain in Figure 3.32 in order to resolve the g- and i-modes.

harder it becomes to find it in the spectrum. Once we have revealed a shear mode in the spectrum, we resolve its close environment with a resolution of $\Delta\omega M = 10^{-8}$ which yields the clear spikes visible in Figure 3.32. The low frequency domain which covers the gravity modes is obviously also covered with a high frequency resolution; we have used the same approach as earlier and increased resolution as we get to lower frequencies. The highest resolution used for this part of the spectrum is $\Delta\omega M = 5 \cdot 10^{-8}$.

The low frequency domain again shows evidence for a large set of oscillation modes. However, only very few modes have maintained their frequency compared to the perfect fluid star. This is not surprising as we have changed the physics of the crust considerably and all the interface modes stem from phase transitions within the crust. We show the evolution of the low frequency spectrum of the star with elastic crust in Figure 3.34; for comparison we include the evolution of the star without elastic crust (the dash-dotted lines). Since the crust crystallises only after about 1.1 days (or $\log(t/\mathrm{yr}) \approx -2.56$), both evolutions coincide in the very early stages of the star's life. As soon as the crust exhibits elastic parts, the spectra start to diverge from each other. The modes at higher frequencies tend to slightly increase in frequency, whereas the modes at lower frequencies are shifted to lower frequencies.

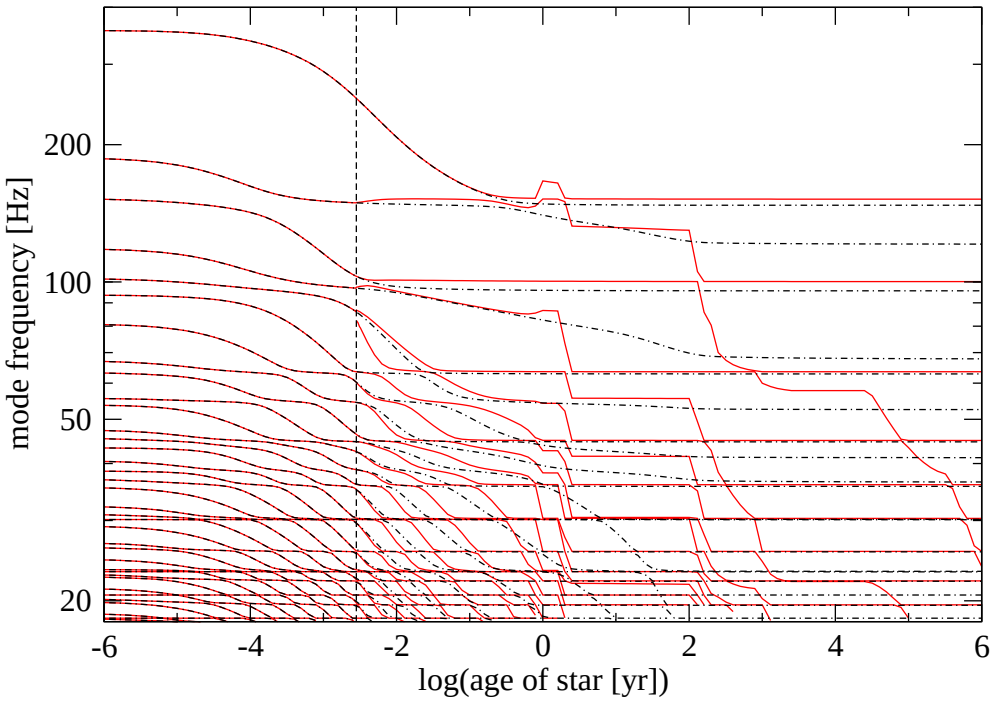

Figure 3.34: A zoom-in of Figure 3.41 at low frequencies in order to resolve the numerous g-modes and interface modes. We include the evolution of the low frequency spectrum of the star without elastic crust (dash-dotted lines) for comparison. As the crust of our model star is fluid during its very early stages, the evolutions coincide for about 1.1 days until the crust starts to crystallise. Then the evolution of the low frequency modes is affected by the solid crust, leading to partially higher mode frequencies. The vertical dashed line indicates the time at which the crust starts to crystallise.

The threshold between these to different characteristics is the mode at 86.2 Hz; as soon as the crust starts to solidify, this mode gets shifted up to 86.7 Hz and a new mode appears in close vicinity at 82.3 Hz which cannot be directly linked to any other oscillation mode present in the star that previously had no solid crust. We show in Figure 3.37 that we trace the two adjacent modes at 86.7 Hz and 63.5 Hz correctly. In Figure 3.38, we compare the eigenfunction of the mode at 86.7 Hz with the eigenfunction of the newly emerged mode at 82.2 Hz. Both modes bear resemblance to each other both in the core and the outer crust, whereas they differ within the inner crust. These modes are clearly different and we cannot find a mode in the fluid star that could be linked to the new mode. However, we are unable to find a physical reason as to why this mode appears as the crust solidifies. It is clearly not a shear mode—eigenfunction as well as frequency easily annihilate this suggestion, see discussion below. This is the only new mode appearing in the spectrum (which is accessible to us, i.e. down to ≈ 18 Hz).

Another interesting feature is the disappearance of interface modes in the ageing star. As can be seen from Figure 3.34, the number of modes in the low frequency spectrum of the star with elastic crust is smaller than if the star was a perfect fluid. The eigenfunctions of the present modes, which we show in Figure 3.35, reveal that the elasticity of the crust prevents the for interface modes characteristically large radial displacement at the phase transitions: the few interface modes we can find all have their maximum radial displacement in the thin fluid ocean, whereas their amplitude is considerably smaller within the elastic crust. For the last model of our cooling sequence at an age of one million years, we are able to identify only one interface mode at a frequency of 26.4 Hz; we show its eigenfunction in Figure 3.35. In this graph it becomes obvious that its amplitude is strongly confined to the surface of the star. Its peak is located at $r = 11.745$ km which, firstly, is the location of the second phase transition (as counted from the surface from the star), and secondly, is just outside the solid crust. The fact that this interface mode has its peak at the second phase transition suggests that there is one more interface mode present. However, we are not able to locate it and we suspect that it has a frequency of less than 18 Hz which is below the noise cut-off of our code.

As a test, we artificially extended the elastic crust close to the surface of the star (using the temperature profile of our star at the age of 10^6 years and keeping it fixed) so that only one phase transition would lie within the fluid ocean. In the low frequency spectrum (down to our numerical limit of about 13 Hz; this is lower than in our other simulations as we chose to increase the resolution for this test), we identified the first 13 g-modes and one i-mode at about 16.9 Hz whose radial displacement is largely confined to the fluid ocean. We gradually increased the thickness of the elastic crust but the spectrum did not change significantly as long as the phase transition stayed within the fluid ocean. As soon as the phase transition got "swallowed" by the elastic crust, the

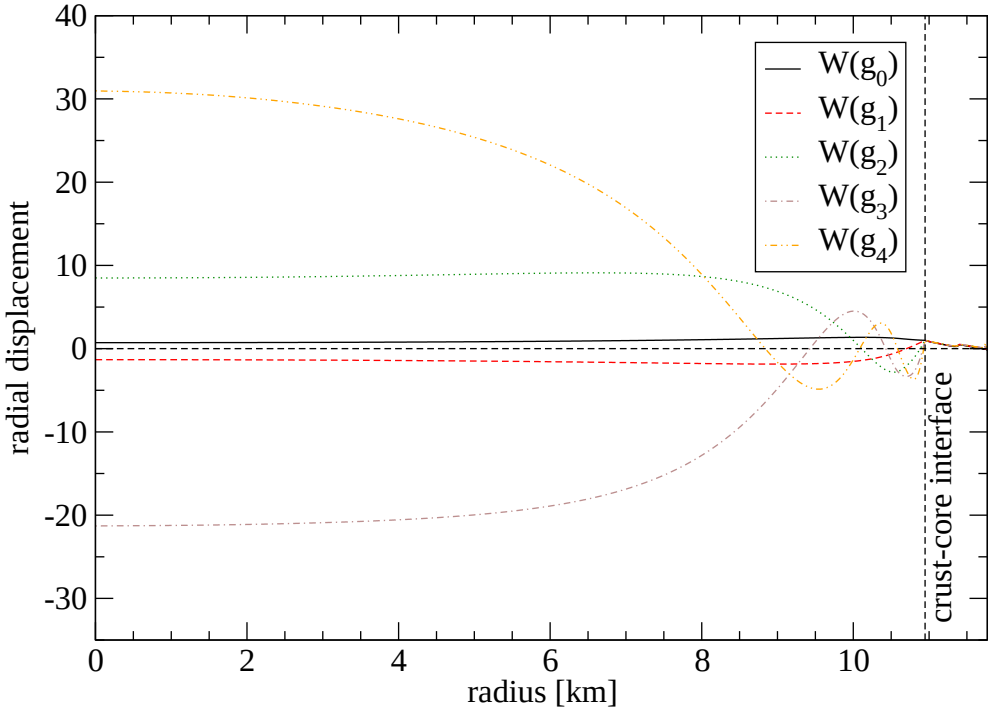

Figure 3.35: The eigenfunctions of the remaining oscillations modes of our model neutron star with solid crust at an age of one million years. We have normalised them to $W(R_{\rm cc}) = 1$, where $R_{\rm cc}$ is the location of the crust-core interface. All modes display the characteristics of g-modes.

corresponding i-mode quickly decreased in frequency as the crust thickens. We conclude that the crust elasticity effectively suppresses interface modes. However, the numerical instabilities in the low frequency region prevent us from quantitatively investigating at what frequencies interface modes, which are caused by phase transitions within the elastic crust, can be found. As the interface modes are still present in the spectrum even shortly after the phase transition has been absorbed into the elastic region, we assume that their frequencies quickly approach zero but in fact do not reach it as we cannot reasonably argue that the interface modes should become degenerate suddenly whilst the star's parameters (in particular the temperature and hence the thickness of the crust) vary smoothly without reaching a boundary of their domain.

When we consider higher frequencies, we find several narrow spikes in the spectrum. These belong to the shear modes associated with the solid crust. We list the frequencies of the twelve lowest shear modes when the star is 100 years old in Table 3.7. In Figures 3.39 and 3.40, we show the radial and transverse displacement of the second shear modes s_2 and s_5, respectively (for our neutron star at the age of three months); we order the shear modes by frequency and denote the n-th shear modes by s_n where s_1 has the lowest frequency. Note that we have scaled the transverse displacement, represented by the variable V, by a factor of 0.02 for s_2 and by 0.05 for s_5. That is, the displacement is predominantly transverse. Furthermore, the displacement is strongly

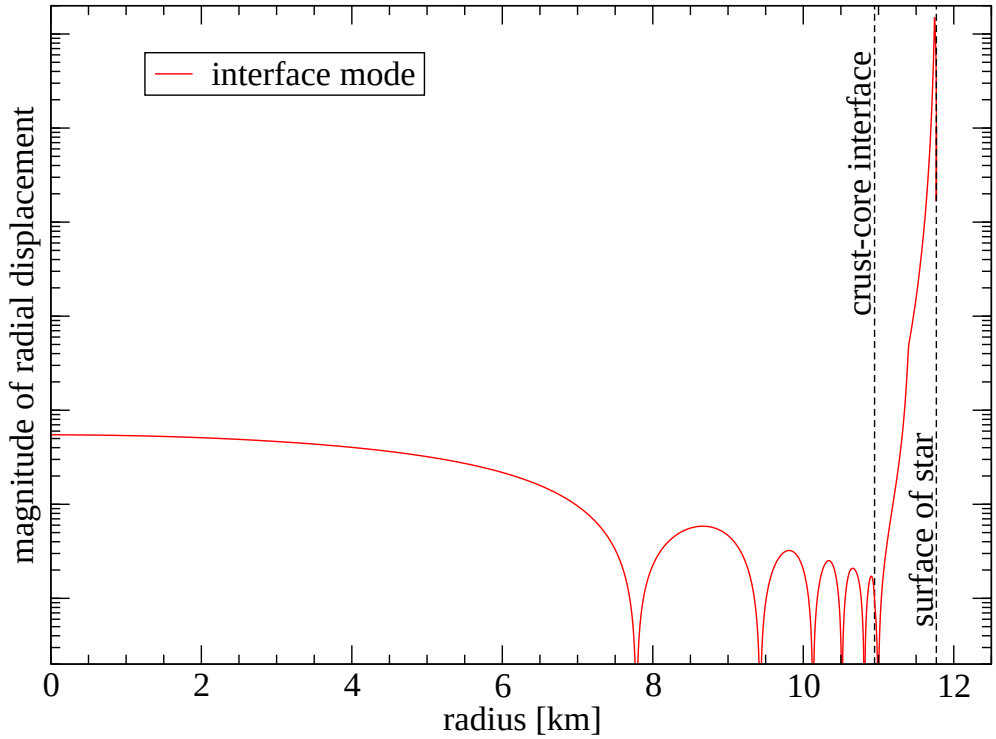

Figure 3.36: The eigenfunction of the only interface mode which we are able to identify in the old star. The amplitude is strongly confined to the surface of the star. We depict the crust-core interface as well as the surface of the star, however, we cannot depict the outer edge of the crust (the crust-ocean interface) as it is so close to the surface that it could not be resolved in this graph (the ocean has a depth of only 24 m at this stage).

confined to the crust (apart from a small, almost constant, radial displacement in the fluid ocean). Both displacement variables exhibit one oscillation to very good precision; however, they are out of phase by approximately $\pi/4$ which indicates an ellipsoidal motion (rather than circular due to the dominance of the transverse displacement) of the "fluid elements" in the crust. The eigenfunctions for the other shear modes show a similar behaviour; higher order shear modes exhibit more oscillations, in particular, the number of oscillations increases by one half per order. This feature is well visible for the two shear modes we show in Figures 3.39 and 3.40 which to good approximation exhibit two and five half oscillations, respectively.

The frequency of the shear waves deserves a further comment. For reasons that will become more clear later, we again consider our neutron star at the age of three months. It has a solid crust in the region from $R_{\rm cc} = 10.947\,\mathrm{km}$ (**c**ore-**c**rust interface) to $R_{\rm co} = 11.292\,\mathrm{km}$ (**c**rust-**o**cean interface). As is apparent from Figure 3.39, the s_2 mode essentially fits one oscillation into this region, suggesting a wavelength of $\lambda \approx 345\,\mathrm{m}$. This is the same behaviour as observed for axial shear modes [7]. Together with the frequency of 2.673 kHz we infer a wave speed of $c = \lambda f \approx 0.922{\cdot}10^8$ cm/s. This is in good agreement with the shear velocity $c_t = \sqrt{\tilde{\mu}/\rho}$, which varies between $0.98 - 1.4{\cdot}10^8$ cm/s

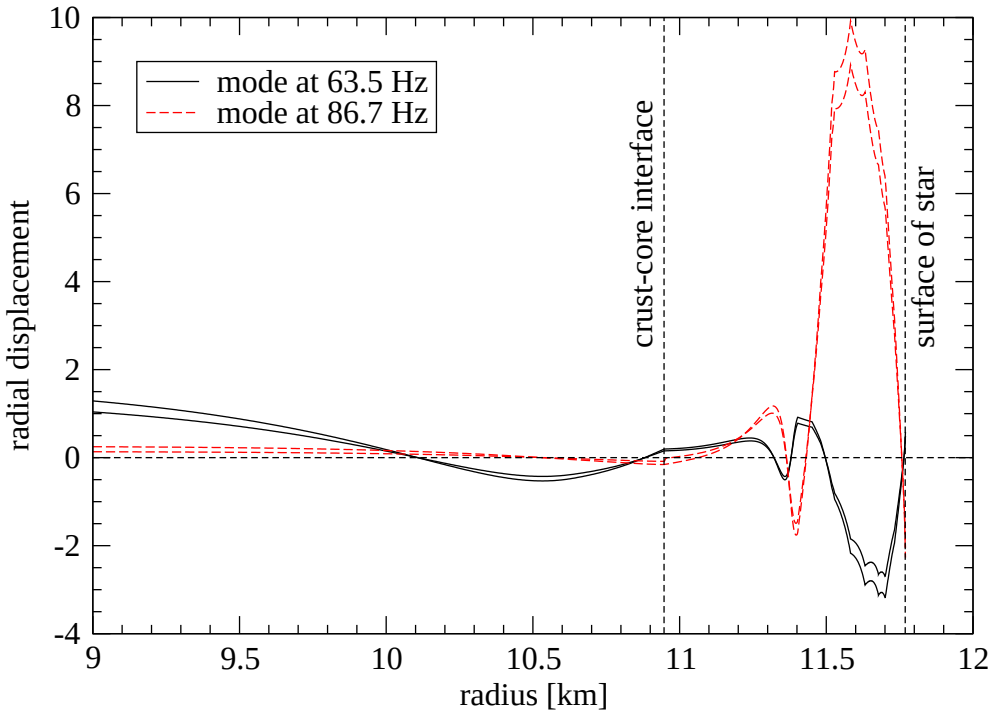

Figure 3.37: The eigenfunctions of the two modes adjacent to the newly emerging mode. For each mode we show two eigenfunctions: one of them while the crust is still fluid (at the time $\log(t/\mathrm{yr}) = -2.559$), the other one just after the first bits of matter have solidified (at the time $\log(t/\mathrm{yr}) = -2.548$). The two eigenfunctions of the same mode at different times are in very good agreement which undoubtedly proves that we trace the modes correctly. (We show the eigenfunction only for the outer parts of the star; the eigenfunctions continue basically constant throughout the core and agree well there, too.

Table 3.7: Frequencies of the high frequency modes for the neutron star model at the age of hundred years (as shown in Figure 3.32).

Mode	Frequency [kHz]	Mode	Frequency [kHz]
s_1	1.304	s_7	6.417
f	1.938	s_8	7.333
s_2	2.205	s_9	8.229
s_3	3.049	s_{10}	9.101
s_4	3.818	p_2	9.489
s_5	4.622	s_{11}	9.966
s_6	5.504	s_{12}	10.844
p_1	6.315		

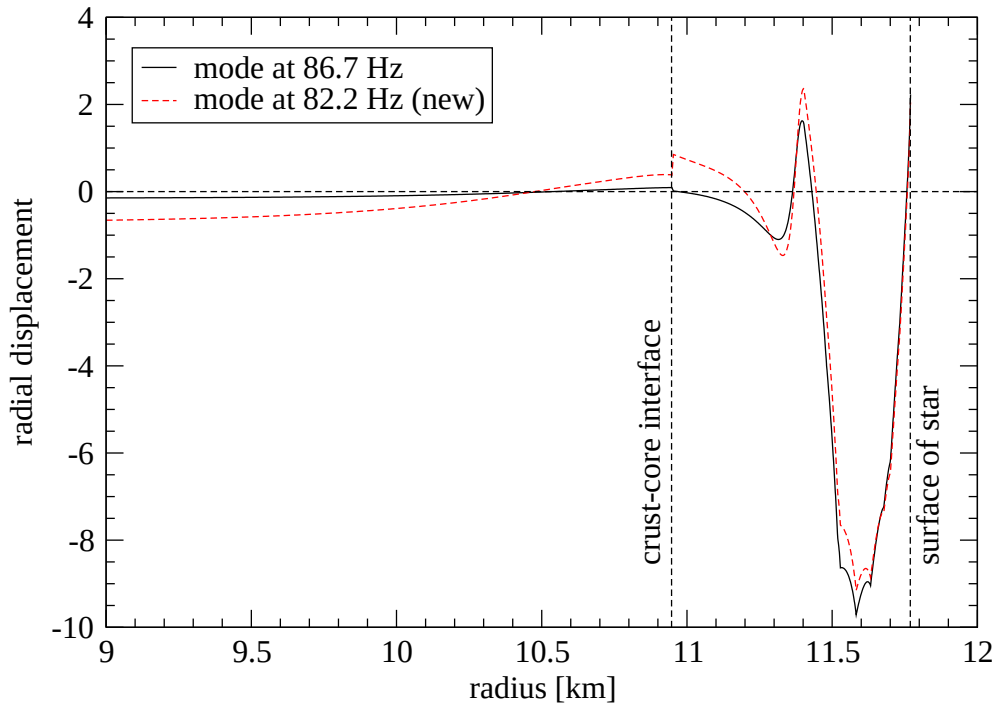

Figure 3.38: We compare the eigenfunction of the mode at 86.7 Hz with the eigenfunction of the newly emerged mode at 82.2 Hz. They coincide well in the very outer parts of the star for $r \gtrsim 11.3\,\mathrm{km}$ but then start to deviate from each other as we go deeper into the star down to the crust-core interface. Within the core, both eigenfunctions are again approximately identical (apart from a proportionality constant).

in the elastic region (as calculated from values provided by the DH EoS). The slight disagreement stems from the fact that the s_2-mode does not exactly exhibit a full oscillation period but slightly less; its associated wavelength is, hence, a bit longer than 360 m which also increases the wave speed closer to the expected interval. A similar behaviour can of course be observed in older stars, too. However, as the elastic crust spans a wider region in older stars, the shear speed begins to significantly vary with depth which effectively distorts the neat sinusoidal shape of the eigenfunctions.

In Figure 3.41 we show how the high frequency part of the spectrum changes with time. We can identify the two frequencies, 1.938 kHz and 6.315 kHz, which are eigenfrequencies of the star during its entire lifetime (apart from very short periods when a shear mode crosses over and the two modes in question exhibit an avoided crossing); these are the f-mode and the first p-mode, respectively. Since the crust does not form until the star is about 1.1 days old, we do not expect to see other modes in the spectrum. As discussed above, we expect the frequency of the shear modes to be determined roughly by the shear speed and the thickness of the elastic crust; when the crust starts to crystallise, the shear modes will have very high frequencies to begin with. Since the crystallised region grows as the star cools, while the shear speed is subject to only small variations, we expect the shear mode frequencies to decrease with time.

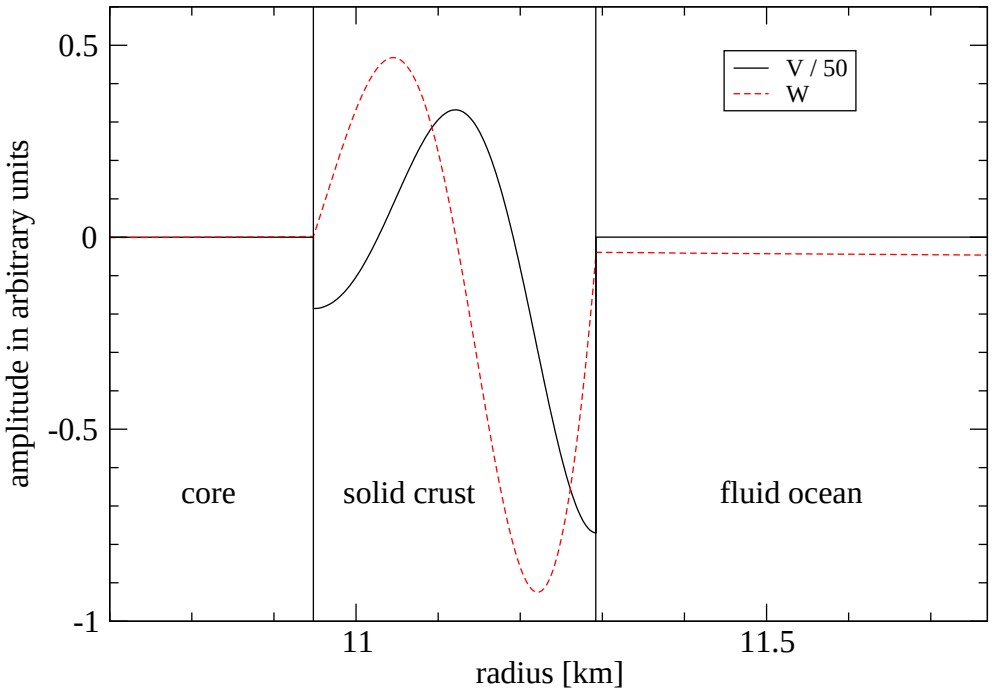

Figure 3.39: The displacement associated with the second shear mode, s_2. The star is three months old and its s_2-mode has a frequency of 2.673 kHz. Within the crust, the amplitude of the eigenfunction exhibits to good approximation one full oscillation in the radial direction.

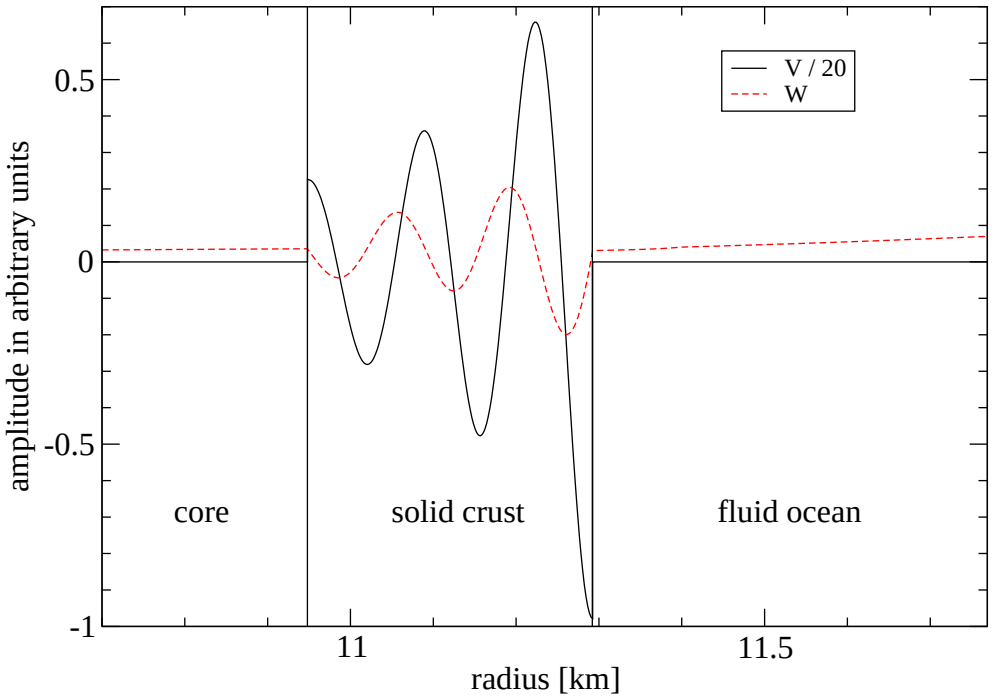

Figure 3.40: The displacement associated with the fifth shear mode, s_5. The star is three months old and its s_5-mode has a frequency of 6.459 kHz. Within the crust, the amplitude of the eigenfunction exhibits to good approximation two and a half oscillations in the radial direction.

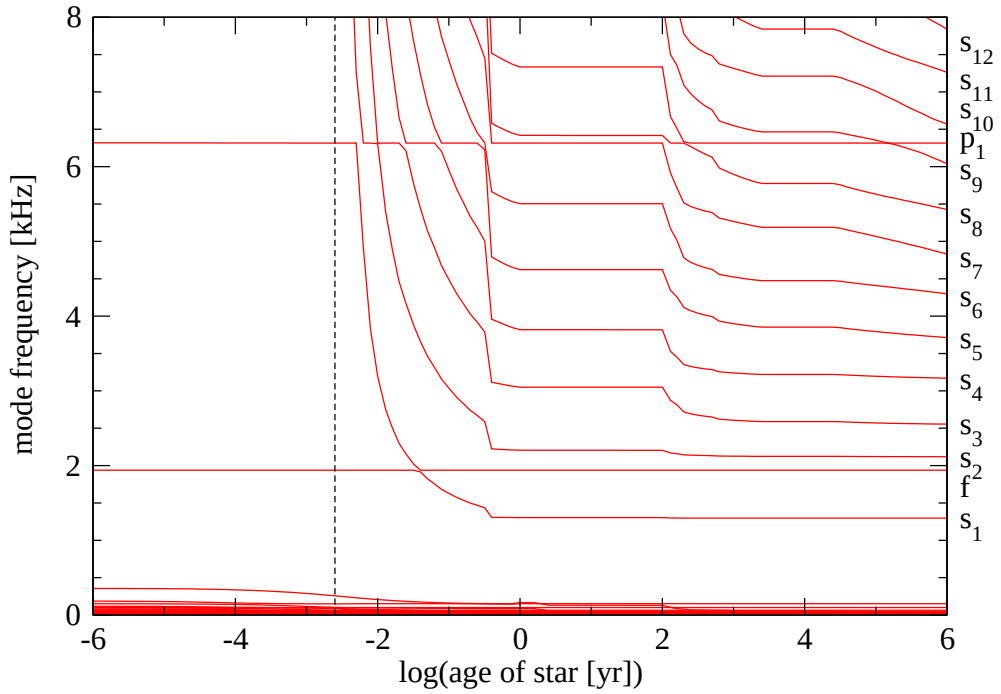

Figure 3.41: The graph shows how the mode frequencies of the star with elastic crust change as the star cools. As Figure 3.30 but this time for the high frequency part of the spectrum, where our model star accounts for the elastic crust. The two modes at constant frequencies, 1.938 kHz and 6.315 kHz, are the f-mode and first p-mode, respectively, whose frequencies remain unaffected. The shear modes appear at the top end of the spectrum after about 1.1 days when the crust starts to crystallise (indicated by the vertical dashed line). At the bottom of the graph the low frequency g-modes and interface modes are visible.

The described behaviour is clearly visible in Figure 3.41: the shear modes occur at the top end of the spectrum after about 1.1 days and quickly decrease in frequency until the crust reaches a "plateau" after about 1 year. For the next hundred years or so, the crust does not significantly increase in width (cf. Figure 3.1) and hence the shear modes remain largely unaffected. After this phase the crust gains in width quickly, causing the shear mode frequencies to drop almost discontinuously. After roughly 1000 years, the solid crust has almost reached its final thickness. Thus, the shear modes do not experience a significant change in frequency later.

Our findings for stratified stars with an elastic crust are in agreement with results from McDermott et al. [83] who considered a star with an elastic crust in Newtonian theory. Qualitatively, our numerical calculations confirm their spectra; we find the same sets of mode, that is f-, p-, g-, i- and s-modes. However, while McDermott et al. find two different sets of g-modes which they label surface g-modes and core g-modes, according to the region to which they are mainly confined, our simulations do not reproduce these findings as we do not have a detailed ocean model here. Furthermore, the frequencies for the g-modes which McDermott et al. find are much lower (below

3 Hz) than in our simulations. This is due to the rather low temperature (10^7 K) used in their calculations. At these temperatures we would expect similar frequencies in our simulations but the numerical procedure does not allow us to investigate the spectrum at these low values. Nevertheless, our results agree qualitatively with the results of McDermott et al. [83].

3.11 Summary of Single Fluid Calculations

The main aim of this project was to build technology which enables us to study quasi-normal modes of compact stars in full general relativity. We have started with the widely used perfect fluid formalism as described by Detweiler & Lindblom [19], including suggested improvements on the numerical solution of the problem (see Andersson et al. [61]); we extended it to account for stratification as well as thermal pressure due to neutrons and protons in the core which is accomplished by only small modifications. We derived a new set of equations which governs perturbations in the solid crust. We also revisited the junction condition problem which examines the behaviour of the perturbation variables across interfaces; we encountered mathematically contradictory results when considering the continuity of the extrinsic curvature when there is a phase transition in the background matter. We were able to find a satisfactory set of junction conditions without the need for the use of the second fundamental form. However, the implications of its continuity need further investigation.

A fundamental ingredient for the study of oscillations of realistic neutron stars is obviously the model of a realistic neutron star. In Chapter 2, we lay out how we constructed one particular background model which served amongst more simplified models for test cases as the main model on which we test our code. We choose a tabulated equation of state for the crustal region of the star and a recent analytical representation of the SLy4 force for the core region which accounts for npeμ-matter and provides us with all necessary coefficients to describe the dynamics of two-fluid systems. In constructing the background model, we accounted explicitly for density discontinuities due to phase transitions in the crustal region as well as due to the artificial matching of the core and crustal EoS. These discontinuities which appear solely in the background but not in the perturbation equations caused interface modes to appear in our calculated spectra.

We started our calculations by comparing the results of our code to published results; we find excellent agreement with the results published by Andersson et al. [61]. The increase of computational power during the past two decades allowed us to perform a comprehensive search for w-modes covering a large area of the complex plane with high resolution. Similar to [61], we were not able to identify the different branch of w-modes that has been found by Leins et al. [22] (who have used a different method for the exterior solution), but our simulations uncovered a new set of w-modes with

slightly shorter damping times than the w-modes known so far. This new set of w-modes appears to consist of eigenmodes with slowly increasing damping time as the oscillation frequency increases. After a few tens of modes, this new branch and the known branch of w-modes appear to "merge" into each other. We have not expected to find this kind of fast damped modes in our simulations and we also cannot physically reason their existence. It could be the case that these modes are an artefact of the exterior solution of the perturbation problem; this part of the solution relies on certain approximations and is peppered with numerical challenges. Further research is strongly encouraged to be undertaken in this direction in order to gain insight into this issue.

We then turn to the low frequency part of the spectrum and find it to be populated by g-modes as soon as we take stratification into account. Test simulations for polytropic neutron star models with an artificially set ratio of $\gamma/\gamma_0 = 1.1$ prove the high numerical accuracy of our code; we are able to distinguish modes that are only $\Delta\omega M = 4.2 \cdot 10^{-6}$ apart. The only limitation is numerical noise that emerges for very low frequencies and prevents us from investigating the spectrum at frequencies below roughly 10 - 20 Hz. Thus, we derived a new set of equations for the low frequency domain in order to circumvent a numerical cancellation. This new set of equations allows us to investigate the spectrum at lower frequencies; however, there is still a limit below which the noise is not eliminated. This issue needs to be studied in further detail.

After the tests of our code against literature values, we turn to investigating a realistic neutron star model. The EoS we use to construct this neutron star consists of the DH EoS for the crust and an analytical representation of the SLy4 force for the core. Our model star has a radius of $R = 11.77\,\mathrm{km}$ and a mass of $M = 1.447\,M_\odot$. It turns out that the low frequency spectrum is populated mainly by interface modes, the ones with the highest frequencies being the interface modes due to the artificially introduced density gap at the core-crust interface and on the other hand, as a second order phase transition, the appearance of muons in the core. Accounting for composition gradients in the core only shifts the frequencies of these two interface modes to slightly higher frequencies, whereas the interface modes due to the phase transitions in the crust are unaffected.

When we account for thermal pressure due to neutrons and protons in the core, we find that several thermal g-modes enter in the low frequency part of the spectrum. Some of the higher frequency interface modes experience an increase in frequency while most of the interface modes stay unaffected. Using the thermal evolution of the neutron star, we are able to investigate the change of frequencies of the different modes over time. After approximately 100 years, all thermal g-modes have dropped below 18 Hz in frequency (the noise cut-off in our simulations) and the thermal effect on the interface modes has almost vanished. However, we have not accounted for thermal pressure in the crust yet, and since the thermal pressure will not negligible in comparison to the static pressure in the crust, we expect to observe significant changes in the spectrum

when we extend our study to include thermal pressure in the crust.

Finally, we took the crystallisation of the crust into consideration and investigated the according changes to the spectrum. From our thermal evolution, we approximately calculated the region in which the star is solid. For the low frequency domain we find that those interface modes which existed due to phase transitions inside the now solid crust, have vanished or have been lowered in frequency. On the other hand, the spectrum is enriched by the shear modes which have a very long damping time (or very small imaginary part) and therefore appear as tiny spikes in the spectrum only. The shear modes show an oscillatory behaviour in the solid region and we confirmed that their frequencies are in good agreement with the shear speed. Our overall findings are in good agreement with results from previous studies, in particular [83].

We have demonstrated the first step towards a comprehensive computational technology to study quasinormal modes of single fluid compact stars. Subsequently in the second part of this project, we will extend this work to account for a multi-fluid core where we consider the neutrons to be superfluid and the protons to be superconducting. An important part of this study will be to include the equation of state proposed by Chamel [38] in which entrainment is considered.

Chapter 4

Perturbations of Multi-Fluid Stars

It is widely accepted that the core of neutron stars has a superfluid component. Similar to electrons forming Cooper pairs in a superconductor according to the BCS theory, neutrons as well as protons can form Cooper pairs in a neutron star core once the neutron star has cooled below a critical temperature. The onset of superfluidity, i.e. the critical temperature, strongly depends on the density and the quantum state of the nucleons. We will get back to this matter in more detail in Section 4.7; for the moment we focus on the important fact that neutrons and/or protons which are superfluid form a separate component within the neutron star core and are able to penetrate the non-superfluid component. Effectively, the neutron star core is a multi-fluid system consisting of several components which are able to flow freely; however, the strong interaction between protons and neutrons leads to a coupling between these components whereby their flow is not entirely independent; this is the so-called entrainment effect.

The difficulty now lies in the fact that the Einstein equations alone are not enough to determine the behaviour of the multi-fluid system. We need another set of equations of motion for the second fluid. Furthermore, as in the case of the elastic crust, we need to link regions of different nature to each other. We will tackle both these problems in this chapter.

4.1 The Variational Approach

The principle of stationary action has been proven very useful in all different fields of physics, starting from classical mechanics to modern quantum field theory. The fundamental idea is that the realised trajectory of a particle (or more general, the path of a system within a configuration space) is the one for which the so-called *action*, S, is stationary, $\delta S = 0$. The action is defined via an integral over the Lagrangian, L. The condition of stationary action then leads to the equations of motion—for trajectories

of particles in classical mechanics or for the fields in field theories.

As we deal with the gravitational field we will focus on the field theoretical version of this principle. In this case, the action, S, is defined as an integral of a Lagrangian density, $\mathcal{L}$, over the entire space-time:

$$S := \int \mathcal{L}\sqrt{-g}\,\mathrm{d}^4x, \tag{4.1}$$

where g is the determinant of the metric tensor. The Einstein-Hilbert action which yields the Einstein field equations through the principle of stationary action is obtained by setting

$$\mathcal{L}_{EH} = \frac{1}{16\pi}R, \tag{4.2}$$

where R is the Ricci scalar. As there are only geometric quantities involved in this Lagrangian, we will obtain the Einstein equations for a vacuum space-time. The presence of matter will be accounted for by adding the matter Lagrangian to the Einstein-Hilbert action,

$$S = \int \left(\frac{1}{16\pi}R + \mathcal{L}_{\mathrm{matter}}\right)\sqrt{-g}\,\mathrm{d}^4x. \tag{4.3}$$

4.1.1 The Matter Lagrangian for a Single Fluid

We will lay out the procedure first for a single fluid and later consider multi-fluids. The central quantity is the so-called master function, Λ, which is a function of the scalar $n^2 = -n_\mu n^\mu$ only, i.e. $\Lambda = \Lambda(n^2)$, where n^μ is the number density current associated with the flow of the fluid. By making this definition, we assume that the matter is locally isotropic. In the action principle, the master function serves as the Lagrangian density, i.e.

$$\mathcal{L}_{\mathrm{matter}} = \Lambda. \tag{4.4}$$

We will now calculate the variation of the master function as we will need it for the action principle. At first, since Λ is a function of n^2 only, we have

$$\delta\Lambda = \frac{\partial\Lambda}{\partial n^2}\delta n^2. \tag{4.5}$$

The variation of n^2 can be decomposed as

$$\delta n^2 = -\delta\left(g_{\mu\nu}n^\mu n^\nu\right) = -n^\mu n^\nu \delta g_{\mu\nu} - 2n_\mu \delta n^\mu. \tag{4.6}$$

Inserting this into the previous equation, we get

$$\delta\Lambda = -2\frac{\partial\Lambda}{\partial n^2}n_\mu\delta n^\mu - \frac{\partial\Lambda}{\partial n^2}n^\mu n^\nu \delta g_{\mu\nu} \tag{4.7}$$

$$= \mu_\nu \delta n^\nu + \frac{1}{2}n^\mu \mu^\nu \delta g_{\mu\nu}, \tag{4.8}$$

where we have made the definitions

$$\mu_\nu = \mathcal{B} n_\nu, \qquad \text{with} \quad \mathcal{B} := -2\frac{\partial \Lambda}{\partial n^2}. \tag{4.9}$$

μ_ν is the momentum covector and it is conjugate to n^ν; its magnitude can be understood to be the chemical potential of the particles in the corresponding fluid.

4.1.2 Derivation of the Equations of Motion

We can now derive the equations of motion from the principle of stationary action. Recalling that the action is given by

$$S = \int \left(\frac{1}{16\pi} R + \Lambda \right) \sqrt{-g}\, \mathrm{d}^4 x, \tag{4.10}$$

the action principle implying $\delta S = 0$, requires us to determine the variation of the integrand. For clarity, we consider the geometric part, the Einstein-Hilbert Lagrangian, and the matter part, separately. We start with the geometric part,

$$\delta\left(\sqrt{-g}\mathcal{L}_{EH}\right) = \delta\left(\sqrt{-g}\frac{1}{16\pi}R\right) = \frac{\sqrt{-g}}{16\pi}\left[\frac{\partial R}{\partial g^{\mu\nu}} + \frac{R}{\sqrt{-g}}\frac{\partial\sqrt{-g}}{\partial g^{\mu\nu}}\right]\delta g^{\mu\nu}. \tag{4.11}$$

Lengthy but straightforward calculations reveal the two identities (we do not show the actual derivation as they can easily be found in text books, e.g. [71])

$$\frac{\partial R}{\partial g^{\mu\nu}} = R_{\mu\nu} \quad \text{and} \quad \frac{1}{\sqrt{-g}}\frac{\partial\sqrt{-g}}{\partial g^{\mu\nu}} = -\frac{1}{2}g_{\mu\nu} \tag{4.12}$$

for the two terms in the square brackets. We see immediately that the term in the square brackets in (4.11) is nothing other than the Einstein tensor, $G_{\mu\nu} = R_{\mu\nu} - \frac{1}{2}Rg_{\mu\nu}$, i.e. we have

$$\delta\left(\sqrt{-g}\mathcal{L}_{EH}\right) = -\frac{\sqrt{-g}}{16\pi}G^{\mu\nu}\delta g_{\mu\nu}. \tag{4.13}$$

We will lay out the calculation of the variation of the matter Lagrangian, $\mathcal{L}_{\text{matter}} = \Lambda$, in more detail. Later, we will need the variation of the four current which is given in [84]

$$\delta n^\nu = -\mathcal{L}_\xi n^\nu - n^\nu\left(\nabla_\sigma \xi^\sigma + \frac{1}{2}g^{\sigma\rho}\delta g_{\sigma\rho}\right). \tag{4.14}$$

Here, ξ^μ is the Lagrangian displacement vector of the fluid. We have

$$\delta\left(\sqrt{-g}\Lambda\right) = \sqrt{-g}\delta\Lambda + \Lambda\delta\sqrt{-g}. \tag{4.15}$$

Using the identity $\delta\sqrt{-g} = -\frac{1}{2}\sqrt{-g}\left(g_{\mu\nu}\delta g^{\mu\nu}\right)$ and (4.8) yields

$$= \sqrt{-g}\left[\mu_\nu \delta n^\nu + \frac{1}{2}n^\mu\mu^\nu\delta g_{\mu\nu} - \frac{1}{2}\Lambda g_{\mu\nu}\delta g^{\mu\nu}\right] \tag{4.16}$$

$$= \sqrt{-g}\left[\mu_\nu \delta n^\nu + \frac{1}{2}\left(n^\mu \mu^\nu + \Lambda g^{\mu\nu}\right)\delta g_{\mu\nu}\right] \tag{4.17}$$

$$= \sqrt{-g}\left[-\mu_\nu \mathcal{L}_\xi n^\nu - \mu_\nu n^\nu \nabla_\mu \xi^\mu + \frac{1}{2}\left(n^\mu \mu^\nu + \Lambda g^{\mu\nu} - \mu_\lambda n^\lambda g^{\mu\nu}\right)\delta g_{\mu\nu}\right], \tag{4.18}$$

where we have used (4.14) for the variation of the four-current. We continue by expanding the Lie derivative, $\mathcal{L}_\xi n^\nu = \xi^\mu \nabla_\mu n^\nu - n^\mu \nabla_\mu \xi^\nu$, and using the product rule to reformulate the existing terms as well as defining the generalised pressure as $\Psi := \Lambda - \mu_\lambda n^\lambda$,

$$= \sqrt{-g}\Bigg[- \xi^\mu \nabla_\mu \left(\mu_\nu n^\nu\right) + n^\mu \nabla_\mu \left(\mu_\nu \xi^\nu\right) - \mu_\nu n^\nu \nabla_\mu \xi^\mu \tag{4.19}$$

$$\underbrace{+ n^\mu \xi^\nu \nabla_\nu \mu_\mu - n^\mu \xi^\nu \nabla_\mu \mu_\nu}_{= n^\mu \xi^\nu \omega_{\nu\mu}} + \frac{1}{2}\left(n^\mu \mu^\nu + \Psi g^{\mu\nu}\right)\delta g_{\mu\nu}\Bigg], \tag{4.20}$$

where we have defined $\omega_{\nu\mu} := 2\nabla_{[\nu}\mu_{\mu]}$. The first and third term in the brackets can be combined to form a covariant derivative while the second one can be transformed into a covariant derivative by noting that $\nabla_\mu n^\mu = 0$ due to baryon number conservation. We also define the stress-energy tensor $T^{\mu\nu} := n^\mu \mu^\nu + \Psi g^{\mu\nu}$,

$$= \sqrt{-g}\nabla_\mu \left(n^\mu \mu_\nu \xi^\nu - \xi^\mu \mu_\nu n^\nu\right) + \sqrt{-g}\left[n^\mu \xi^\nu \omega_{\nu\mu} + \frac{1}{2} T^{\mu\nu}\delta g_{\mu\nu}\right]. \tag{4.21}$$

Via the relation $\sqrt{-g}\nabla_\mu A^\mu = \partial_\mu(\sqrt{-g}A^\mu)$, which can easily be proven by expanding the covariant derivative in Christoffel symbols, the first term can be transformed into a total derivative,

$$= \partial_\mu\left[\sqrt{-g}\left(n^\mu \mu_\nu \xi^\nu - \xi^\mu \mu_\nu n^\nu\right)\right] + \sqrt{-g}\left[-\xi^\nu f_\nu + \frac{1}{2} T^{\mu\nu}\delta g_{\mu\nu}\right], \tag{4.22}$$

where we have also introduced the force density, $f_\nu := n^\mu \omega_{\mu\nu}$. Via Stokes' theorem, the total derivative contributes to the action integral only through surface terms which are irrelevant for the deduction of the equations of motion.

We can now combine the variations of the Einstein-Hilbert Lagrangian and the matter Lagrangian, and we arrive at

$$\delta\left[\sqrt{-g}\left(\mathcal{L}_{EH} + \mathcal{L}_{\text{matter}}\right)\right] = \sqrt{-g}\left[-\frac{1}{16\pi} G^{\mu\nu} + \frac{1}{2} T^{\mu\nu}\right]\delta g_{\mu\nu} - \sqrt{-g} f_\nu \xi^\nu \tag{4.23}$$

$$+ \text{“boundary terms”}. \tag{4.24}$$

As the variations of the metric, $\delta g_{\mu\nu}$, and the displacement vector, ξ^ν, are arbitrary, the action principle demands that both their coefficients must vanish. This leads to

the equations of motion

$$\boxed{G_{\mu\nu} = 8\pi T_{\mu\nu},} \tag{4.25a}$$

$$\boxed{f_\nu = 0.} \tag{4.25b}$$

We note that if the complete set of equations of motion (4.25) is satisfied, it is automatically true that the divergence of the stress-energy tensor vanishes (as we consider only one species of particle here, its four-current must be conserved, $\nabla_\mu n^\mu = 0$):

$$\nabla_\mu T^\mu_\nu = \nabla_\mu \left(\Psi \delta^\mu_\nu + n^\mu \mu_\nu\right) \tag{4.26}$$

$$= \nabla_\nu \left(\Lambda - n^\lambda \mu_\lambda\right) + n^\mu \nabla_\mu \mu_\nu + \mu_\nu \underbrace{\nabla_\mu n^\mu}_{=0} \tag{4.27}$$

$$= \nabla_\nu \Lambda - \mu_\lambda \nabla_\nu n^\lambda + f_\nu. \tag{4.28}$$

By virtue of the definition of the momentum covector μ_ν as given in (4.9), we have $\nabla_\nu \Lambda = \frac{\partial \Lambda}{\partial n^2} \nabla_\nu n^2 = \mu_\lambda \nabla_\nu n^\lambda$, and hence

$$\nabla_\mu T^\mu_\nu = 0. \tag{4.29}$$

This result, together with the above derived equations of motion, demonstrates that we have chosen meaningful Lagrangian densities for our problem.

In using this approach, we have changed our description of the star from using quantities that describe the fluid as a whole, namely the energy density, ρ, and the pressure, p, to using quantities which are intrinsic to an individual fluid, i.e. its number density current, n^ν, and momentum covector, μ_ν. This ansatz will make it much easier to model multi-fluid systems in which several dynamically independent fluids penetrate each other. The analysis of the equations of motion for such system will be subject of the following section.

4.1.3 The Matter Lagrangian for a Multi-Fluid

We will now take an important step and generalise the previous model for a single fluid to a model for a multi-fluid in which the interpenetrating fluids can move relative to each other. This step is necessary as it is generally accepted that the outer core of a neutron star contains superfluid neutrons, superconducting protons as well as a highly degenerate gas of electrons and the inner crust will be permeated by a neutron superfluid.

In order to distinguish between quantities assigned to the different fluids, we will introduce *constituent indices* x and y which range over the constituents under consideration; amongst the more obvious particles like neutrons (n), protons (p), electrons (e) or muons (μ), we could also consider the entropy (s) as a fluid or take the possibility of more exotic quark matter in the deep core into account. In our study, we will restrict

ourselves to the former four particle species, n, p, e and μ.

In order to avoid cluttering of the indices, we will place the constituent indices liberally upstairs or downstairs; furthermore, the Einstein sum convention will *not* apply to constituent indices. A sum like this, $\sum_{\mathrm{x}}$, means that x runs over all present constituents; we keep the set of constituent indices variable as in the core of a neutron star, we will certainly find a mixture of neutrons, protons and electrons, i.e. the constituent index will run over $\{\mathrm{n},\mathrm{p},\mathrm{e}\}$, however, above a certain threshold density, muons will start to appear and the index will run over the set $\{\mathrm{n},\mathrm{p},\mathrm{e},\mu\}$.

We will assume that the different species are separately conserved, i.e. their number density four-currents, n^{μ}_{x}, are divergence-free,

$$\nabla_{\mu} n^{\mu}_{\mathrm{x}} = 0. \tag{4.30}$$

As in the single fluid case, the central quantity will be the "master" function, Λ, which in this case is a function of all scalar combinations of the four-currents, n^{μ}_{x}. Aside the scalars $n^2_{\mathrm{x}} = -g_{\mu\nu} n^{\mu}_{\mathrm{x}} n^{\nu}_{\mathrm{x}}$, we also have mixed scalars

$$n^2_{\mathrm{xy}} = -g_{\mu\nu} n^{\mu}_{\mathrm{x}} n^{\nu}_{\mathrm{y}} \quad \text{for} \quad \mathrm{x} \neq \mathrm{y}. \tag{4.31}$$

The variation of the master function, $\Lambda = \Lambda(n^2_{\mathrm{x}}, n^2_{\mathrm{xy}}, n^2_{\mathrm{y}}, \ldots)$, is, in analogy to the previous section,

$$\delta\Lambda = \sum_{\mathrm{x}} \mu^{\mathrm{x}}_{\nu} \delta n^{\nu}_{\mathrm{x}} + \frac{1}{2} g^{\nu\lambda} \left(\sum_{\mathrm{x}} n^{\mu}_{\mathrm{x}} \mu^{\mathrm{x}}_{\lambda} \right) \delta g_{\mu\nu}, \tag{4.32}$$

where we have defined

$$\mu^{\mathrm{x}}_{\mu} := \mathcal{B}^{\mathrm{x}} n^{\mathrm{x}}_{\mu} + \sum_{\mathrm{y}\neq\mathrm{x}} \mathcal{A}^{\mathrm{xy}} n^{\mathrm{y}}_{\mu}, \tag{4.33}$$

$$\mathcal{B}^{\mathrm{x}} := -2 \frac{\partial\Lambda}{\partial n^2_{\mathrm{x}}}, \tag{4.34}$$

$$\mathcal{A}^{\mathrm{xy}} := -\frac{\partial\Lambda}{\partial n^2_{\mathrm{xy}}}, \quad \text{for} \quad \mathrm{x} \neq \mathrm{y}. \tag{4.35}$$

The $\mathcal{A}^{\mathrm{xy}}$ are the so-called *entrainment coefficients* and they are by definition symmetric in their constituent indices, $\mathcal{A}^{\mathrm{xy}} = \mathcal{A}^{\mathrm{yx}}$. Apparently, these coefficients are responsible for the fact that the momentum of a particular fluid does not need to be parallel to its current. Furthermore, these coefficients make no distinction between entrainment for a superfluid-superfluid system and a superfluid-normal fluid system; the current understanding is that the entrainment does not depend (to leading order) on the nature of the individual interpenetrating fluids. This can be understood by noting that both entrainment as well as Cooper pairing are due to the strong force, and hence the exchange of virtual gluons, which should be independent of whether or not the nucleons

participating in the gluon exchange are Cooper paired to another nucleon.

A calculation analogous to the single fluid case, yields for the variation of the Lagrangian

$$\delta\left(\sqrt{-g}\Lambda\right) = \frac{1}{2}\sqrt{-g}\left[\Psi g^{\mu\nu} + \sum_{\mathrm{x}} n^{\mu}_{\mathrm{x}}\mu^{\nu}_{\mathrm{x}}\right]\delta g_{\mu\nu} - \sqrt{-g}\sum_{\mathrm{x}} f^{\mathrm{x}}_{\nu}\xi^{\nu}_{\mathrm{x}} \tag{4.36}$$

$$+ \text{“boundary terms”}, \tag{4.37}$$

where we now have the definitions

$$\Psi := \Lambda - \sum_{\mathrm{x}} n^{\nu}_{\mathrm{x}}\mu^{\mathrm{x}}_{\nu}, \tag{4.38}$$

$$f^{\mathrm{x}}_{\nu} := n^{\mu}_{\mathrm{x}}\omega^{\mathrm{x}}_{\mu\nu}, \quad \text{with} \quad \omega^{\mathrm{x}}_{\mu\nu} := 2\nabla_{[\mu}\mu^{\mathrm{x}}_{\nu]}. \tag{4.39}$$

Note that we necessarily have introduced separate displacement vectors, ξ^{ν}_{x}, for each fluid; our underlying motivation was to account for several individual fluids that penetrate each other but may flow independent of each other.

Turning to the equations of motion obtained from the action principle, we obviously need to add the Einstein-Hilbert term (4.13) first. Since the displacement vectors, ξ^{ν}_{x}, are independent variations, their individual coefficients must vanish, i.e. we have

$$\boxed{\begin{aligned} G^{\mu\nu} &= 8\pi T^{\mu\nu}, && \text{(4.40a)}\\ f^{\mathrm{x}}_{\nu} &= 0 \quad \text{for each present constituent x}, && \text{(4.40b)}\end{aligned}}$$

plus the conservation conditions (4.30). The stress-energy tensor is given by

$$T^{\mu\nu} = \Psi g^{\mu\nu} + \sum_{\mathrm{x}} n^{\mu}_{\mathrm{x}}\mu^{\nu}_{\mathrm{x}}, \tag{4.41}$$

and by virtue of the number density conservation conditions as well as (4.40b), we will again find $\nabla_{\mu}T^{\mu\nu} = 0$, as desired.

We see that, in general, our set of equations of motion consists of 10 equations from the Einstein equations plus 4 equations for each independent fluid. In our study, the actual number of non-vanishing and independent equations is significantly lower due to the several symmetries of non-rotating stars.

At last, we will comment on a particular case which will be very important for this project. We will assume that the electrons and muons (if present) are electromagnetically locked to the protons and thereby do not have an independent displacement vector, i.e.

$$\xi^{\nu}_{\mathrm{p}} = \xi^{\nu}_{\mathrm{e}} = \xi^{\nu}_{\mu}. \tag{4.42}$$

We can apply this condition directly to the Lagrangian in (4.36), whereby it takes the

form

$$\delta\left(\sqrt{-g}\Lambda\right) = \frac{1}{2}\sqrt{-g}\left[\Psi g^{\mu\nu} + \sum_{\mathrm{x}} n_{\mathrm{x}}^{\mu}\mu_{\mathrm{x}}^{\nu}\right]\delta g_{\mu\nu} - \sqrt{-g}f_{\nu}^{\mathrm{n}}\xi_{\mathrm{n}}^{\nu} - \sqrt{-g}\left(\sum_{\mathrm{x}\in\mathrm{P}} f_{\nu}^{\mathrm{x}}\right)\xi_{\mathrm{p}}^{\nu} + \text{“boundary terms”}. \tag{4.43}$$

We have introduced and denoted by P the set of constituents locked to each other in the proton fluid. In the above equation, we have $P = \{\mathrm{p}, \mathrm{e}, \mu\}$; however, the same calculation holds also for the case where muons are absent, i.e. $P = \{\mathrm{p}, \mathrm{e}\}$, for example in the outer core below the density at which muons appear. The essential difference is the last term in which only the proton displacement ξ_{p}^{ν} appears instead of the displacement vectors for protons, electrons and muons.

The resulting four equations of motion (4.40b) for the individual fluids, are replaced by two equations: one for the neutron fluid and one for the fluid composed of protons, electrons and muons. For simplicity, we will refer to the latter as the *proton fluid*. The equations of motion are

$$\boxed{\begin{aligned} G^{\mu\nu} &= 8\pi T^{\mu\nu}, && \text{(4.44a)}\\ f_{\nu}^{\mathrm{n}} &= 0, && \text{(4.44b)}\\ f_{\nu}^{\mathrm{p}} + f_{\nu}^{\mathrm{e}} + f_{\nu}^{\mu} &= 0. && \text{(4.44c)} \end{aligned}}$$

Of course, as before, the last equation has to be replaced by $f_{\nu}^{\mathrm{p}} + f_{\nu}^{\mathrm{e}} = 0$ if we are below the threshold for the appearance of muons (or if we want to neglect their presence for academic reasons).

While this set of equations contains all necessary information to describe the dynamics of a multi-fluid star, we are not constrained to using exactly these equations. As we said before, the divergence of the stress-energy tensor vanishes, $\nabla_{\mu}T^{\mu\nu} = 0$, and we may as well include this equation into the set of equations of motion. This equation does not give us new input but may provide the available information in a different way which could make it easier to derive the preferred set of perturbation equations. In practice, we will perturb all available equations of motion, expand them into the fundamental perturbations quantities and then pick those equations which are most suitable for numerical implementation.

4.2 A Two-fluid Model for Superfluid Neutron Star Cores

If we want to make use of the multi-fluid formalism, we need to have an equation of state given in terms of the master function, Λ, rather than tabulated. The upside is that for such an EoS, we will be able to calculate all necessary quantities analytically as well as unambiguously accurate to our desired precision. This is preferable over a tabulated

EoS where the interpolation between different points is subject to ambiguities in the choice of method. However, the other side of the coin is that a unique description of the real EoS of neutron star matter, spanning the entire density range of a neutron star from the atmosphere at about $\rho \approx 10^6\,\mathrm{g\,cm^{-3}}$ up to the star's core at several times the nuclear saturation density, $\rho \approx 2 \cdot 10^{15}\,\mathrm{g\,cm^{-3}}$, is most likely not possible (at least not in an analytically handsome way) due to the very different physics governing different regions of the star. Several separate EoSs will need to be matched at certain interfaces between the different layers.

The first studies on oscillations of superfluid neutron stars by Comer et al. [35] and Andersson et al. [36] have employed relativistic polytropes for the different fluids (the polytropic parameters were allowed to vary between the fluids), where the latter introduced a simple entrainment model. Lin et al. [37] have implemented a more sophisticated EoS, the so-called "PAL" EoS [85] whilst using an independently provided entrainment model (Comer & Joynt [86]). Only briefly after their work was completed, Chamel [38] provided the first ever consistent EoS model including entrainment. This EoS is valid in the outer core: The composition under consideration is a uniform mixture of neutrons, protons, electrons and muons that is expected to be found at densities above the crust-core transition density, $\rho_{\mathrm{cc}} \approx 1.4 \cdot 10^{14}\,\mathrm{g\,cm^{-3}}$, and below $\lesssim 2 - 3\rho_{\mathrm{nuc}}$, where $\rho_{\mathrm{nuc}} \approx 2.8 \cdot 10^{14}\,\mathrm{g\,cm^{-3}}$ is the nuclear saturation density. Despite the upper limit on the considered composition, we will assume the same composition for higher densities, too; once for simplicity and second due to the lack of accurate knowledge about the actual composition of neutron star cores.

In the following we will summarise the formalism laid out in the paper by Chamel [38]. As we are going to deal with non-rotating stars in this study opposed to rotating equilibrium configurations, many of the relations given by Chamel will simplify. In equilibrium, the four-velocities for all fluids will be the same and given by $u^\mu = (e^{-\nu/2}, 0, 0, 0)$; the number density currents are $n_{\mathrm{x}}^\mu = n_{\mathrm{x}} u^\mu$. In this case, the master function, Λ, coincides with the negative of the internal energy density, $\Lambda = -U_{\mathrm{ins}}$. The static pressure reads

$$\Psi = \sum_{\mathrm{x}} n_{\mathrm{x}} \mu_{\mathrm{x}} - U_{\mathrm{ins}}, \tag{4.45}$$

where μ_{x} is the chemical potential of species x, defined by

$$\mu_{\mathrm{x}} := \frac{\partial U_{\mathrm{ins}}}{\partial n_{\mathrm{x}}}. \tag{4.46}$$

4.2.1 The Equilibrium Composition of the Neutron Star Core

The rates of electroweak processes, which transform particles of different species into each other, determine the composition of the neutron star core. As an axiomatic

condition from particle physics, the baryon number is always conserved,

$$\nabla_\mu n_b^\mu = 0, \tag{4.47}$$

where $n_b^\mu := n_{\rm n}^\mu + n_{\rm p}^\mu$ is the baryon number density current. Neutrons and protons can be transformed into each other by means of the direct Urca process

$$n \to p + \ell + \bar{\nu}_\ell, \tag{4.48a}$$

$$p + \ell \to n + \nu_\ell, \tag{4.48b}$$

where ℓ is electron or muon. This process is allowed at sufficiently high energy densities; should the densities be lower than a certain threshold, similar reactions are allowed to occur, i.e. the modified Urca processes

$$n + N \to p + N + \ell + \bar{\nu}_\ell, \tag{4.49a}$$

$$p + N + \ell \to n + N + \nu_\ell, \tag{4.49b}$$

which involve an additional spectator nucleon N (neutron or proton) and are therefore considerably slower. Regarding the leptonic part, electrons and muons can be transformed into each other via the lepton-modified Urca processes

$$e^- + X \to \mu^- + X + \bar{\nu}_\mu + \nu_e, \tag{4.50a}$$

$$\mu^- + X \to e^- + X + \bar{\nu}_e + \nu_\mu, \tag{4.50b}$$

where X is a nucleon or lepton.

An analysis of the reaction rates [87, 88] reveals that the relaxation times of these β-processes (neglecting nucleon superfluidity) are approximately given by $\tau^{(D)} \sim 20\, T_9^{-4}\,\mathrm{s}$ for the direct and $\tau^{(M)} \sim T_9^{-6}$ months for the modified Urca process, respectively (T_9 is the temperature in units of $10^9\,\mathrm{K}$). Very high temperatures of the order of $\sim 10^{11}\,\mathrm{K}$ as found in proto-neutron stars result in equilibrating the core matter within microseconds, justifying the background model assumed to be in β-equilibrium. After about 1 yr, the star has cooled down to approximately $10^9\,\mathrm{K}$ (cf. Figure 2.4), which results in relaxation times of 20 s for the direct Urca and several months for the modified Urca process; the relaxation times grow even more rapidly once the temperature has dropped below the threshold for the onset of superfluidity. Consequently, during the short time-scales of $\sim 0.1 - 100$ milliseconds relevant for the oscillations under consideration in this study, the composition of the fluid elements remains essentially frozen in stars which are older than one year. For younger stars, relaxation times can be as low as 2 ms for the direct Urca process at the beginning of the cooling sequence and the perturbed matter cannot be well approximated by either of the two extremes, frozen composition or steady β-equilibrium; for simplicity, we will assume a frozen com-

position in young stars, too, but emphasise the need for a more elaborate approach in future studies. Thus, for our study, we will assume that the constituents are separately conserved

$$\nabla_\mu n^\mu_{\rm p} = 0, \quad \nabla_\mu n^\mu_{\rm e} = 0. \tag{4.51}$$

The very short time-scale of the comparably (to the electroweak interaction) strong electromagnetic interaction leads to electroneutrality of neutron star matter, thus

$$n_{\rm p} = n_{\rm e} + n_\mu. \tag{4.52}$$

This condition and baryon number conservation in conjunction with (4.51) leads to the conservation of the other currents, too, $\nabla_\mu n^\mu_{\rm n} = 0$ and $\nabla_\mu n^\mu_\mu = 0$.

Chamel further argues that, under the assumption that neutron stars become transparent to neutrinos already a few seconds after their birth, both the direct and modified Urca processes can be translated into conditions for the chemical potentials of the particles involved. In particular, we have

$$\boxed{\begin{aligned} \mu_{\rm n} &= \mu_{\rm p} + \mu_e, && \text{(4.53a)}\\ \mu_e &= \mu_\mu, && \text{(4.53b)}\\ n_{\rm p} &= n_{\rm e} + n_\mu, && \text{(4.53c)} \end{aligned}}$$

where we, for completeness, have repeated the condition (4.52) for electroneutrality. These three equations determine the composition of the core once, e.g. the neutron number density or the baryon number density, is given.

If matter is in equilibrium, the static pressure as given in (4.45), can be reduced to

$$\Psi = \mu_{\rm n} n_b - U_{\rm ins} \tag{4.54}$$

by means of the equilibrium conditions (4.53).

4.2.2 The Internal Static Energy

The internal static energy, $U_{\rm ins}$, can be decomposed into several contributions

$$U_{\rm ins}(n_{\rm n}, n_{\rm p}, n_{\rm e}, n_\mu) = U_N(n_{\rm n}, n_{\rm p}) + U_{\rm Coul}(n_{\rm p}) + U_L(n_{\rm e}) + U_L(n_\mu), \tag{4.55}$$

where U_N is the nucleon part, $U_{\rm Coul}$ is the Coulomb part and U_L is the lepton part. The proton Coulomb energy can be approximated to

$$U_{\rm Coul}(n_{\rm p}) = -\frac{3}{4} e^2 \left(\frac{3}{\pi}\right)^{1/3} n_{\rm p}^{4/3}. \tag{4.56}$$

The leptons behave like an ideal relativistic Fermi gas and hence their kinetic energy is given by

$$U_L(n_\ell) = \frac{\hbar c}{8\pi^2 \lambda_\ell^4}\left[x_\ell(2x_\ell^2+1)\sqrt{x_\ell^2+1} - \ln\left(x_\ell + \sqrt{x_\ell^2+1}\right)\right], \tag{4.57}$$

where $\lambda_\ell = \hbar/m_\ell c$ is the Compton wavelength and the dimensionless parameter x_ℓ is defined by

$$x_\ell := \lambda_\ell k_{\mathrm{F}\ell}, \tag{4.58}$$

with $k_{\mathrm{F}\ell}$ the Fermi wave number given by

$$k_{\mathrm{F}\ell} = \left(3\pi^2 n_\ell\right)^{1/3}. \tag{4.59}$$

The Fermi momentum is defined to be $p_{\mathrm{F}\ell} := \hbar k_{\mathrm{F}\ell}$. We neglect the electron mass in our calculations, thus the electron energy density is obtained by taking the limit $m_\mathrm{e} \to 0$ of (4.57), yielding

$$\bar{U}_L(n_\mathrm{e}) := \lim_{m_\mathrm{e}\to 0} U_L(n_\mathrm{e}) = \frac{p_{\mathrm{Fe}} c^4}{4\pi^2(\hbar c)^3}. \tag{4.60}$$

The nucleon energy density is assumed to be

$$U_N(n_\mathrm{n}, n_\mathrm{p}) = n_b m c^2 + \frac{\hbar^2}{2m}\tau_b + B_1 n_b^2 + B_2\left(n_\mathrm{n}^2 + n_\mathrm{p}^2\right) + B_3 n_b \tau_b \tag{4.61}$$

$$+ B_4\left(n_\mathrm{n}\tau_\mathrm{n} + n_\mathrm{p}\tau_\mathrm{p}\right) + B_5 n_b^{2+\alpha} + B_6 n_b^\alpha\left(n_\mathrm{n}^2 + n_\mathrm{p}^2\right), \tag{4.62}$$

where we have defined the kinetic energy densities of the nucleons

$$\tau_\mathrm{x} := \frac{3}{5}\left(3\pi^2\right)^{2/3} n_\mathrm{x}^{5/3} \quad \text{for} \quad \mathrm{x} = \mathrm{n}, \mathrm{p}, \tag{4.63}$$

in units of $\hbar^2/2m$, and $\tau_b := \tau_\mathrm{n} + \tau_\mathrm{p}$. The coefficients B_n can be used to approximate different tabulated EoSs; see the following Section 4.2.3 for more details.

4.2.3 The Core EoS Quantitatively

In the previous section, we have introduced a two-fluid model for a neutron star core and the different contributions to the master function. For our study, we will use the parametrisation given in Tab. 4.1 which is an approximation to the SLy4 force. Chamel [38] provides two more parametrisations, however, as our study is of quantitative character and wants to provide technology rather than precise results, we can pick one of the provided sets of values. We opt for the SLy4 force as it comes with the advantage that we can easily match it at the crust-core interface to the DH EoS (see Section 2.2) which we use for the crust.

As explained above, given a number density, we can use (4.53) in order to calculate

Table 4.1: Parameters of the chosen SLy4 force. The units of energy and length are MeV and fm, respectively.

	B_1	B_2	B_3	B_4	B_5	B_6	α
SLy4	-1763.39	1660.1	32.473	49.3128	1925.34	-2128.55	1/6

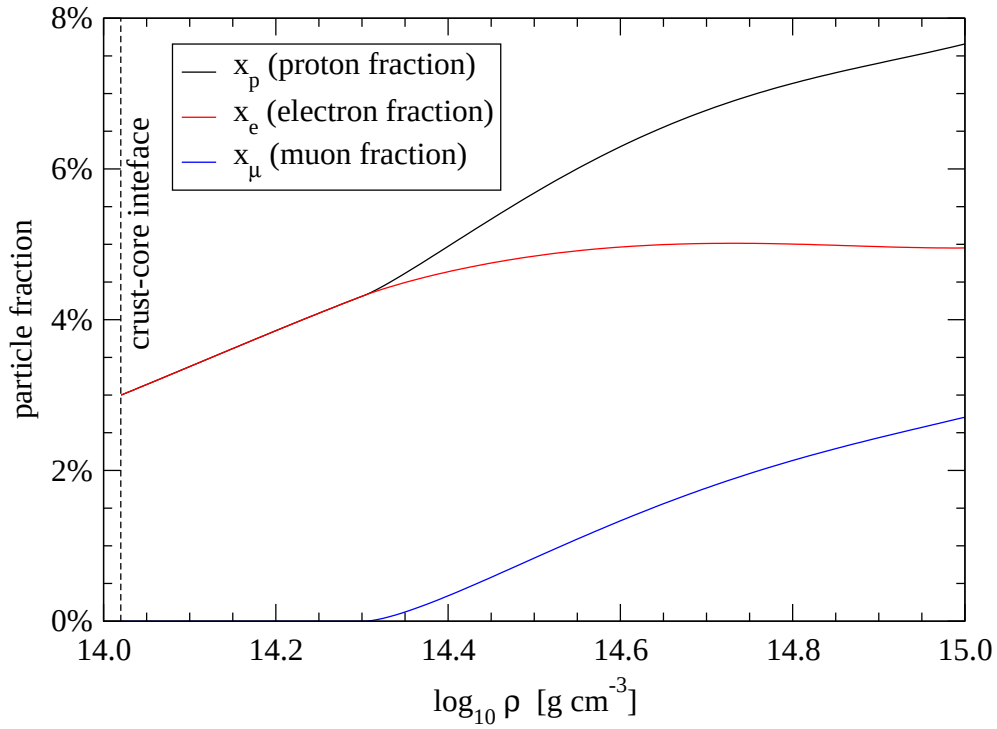

Figure 4.1: Particle fraction of protons, electrons and muons in the core.

the remaining number densities of the other species and hence the matter composition of the core. We show the electron fraction, $x_\mathrm{e} = n_\mathrm{e}/n_b$, the muon fraction, $x_\mu = n_\mu/n_b$ and the proton fraction, $x_\mathrm{p} = n_\mathrm{p}/n_b$ in Fig. 4.1. The neutron fraction can easily be obtained from $n_\mathrm{n} = 1 - n_\mathrm{p}$. Due to electroneutrality, we obviously have $x_\mathrm{p} = x_\mathrm{e} + x_\mu$. As we can see from Fig. 4.1, muons start to appear at about $\rho \approx 2 \cdot 10^{14}\,\mathrm{g\,cm^{-3}}$ in this particular parametrisation. Assuming that $\rho \approx m n_b$ at these densities, the equivalent baryon number density at which muons start to appear is roughly $n_b \approx 0.12\,\mathrm{fm}^{-3}$. While the exact value for n_b depends on the chosen parametrisation (the B_n values), we can easily calculate the proton number density at which muons appear. From the equations (4.53) for β-equilibrium we know that $\mu_\mathrm{e} = \mu_\mu$. For the electron chemical potential, we find

$$\mu_\mathrm{e} = \frac{\partial U_\mathrm{ins}}{\partial n_\mathrm{e}} = \frac{\partial \bar{U}_L(n_\mathrm{e})}{\partial n_\mathrm{e}} = \hbar c k_\mathrm{Fe} = p_\mathrm{Fe} c, \tag{4.64}$$

which is the Fermi energy of a massless particle. After a tedious but straightforward

calculation, we find for the muon chemical potential the fairly simple expression

$$\mu_\mu = \frac{\partial U_{\rm ins}}{\partial n_\mu} = \frac{\partial U_L(n_\mu)}{\partial n_\mu} = \hbar c \frac{\sqrt{x_\mu^2 + 1}}{\lambda_\mu}. \tag{4.65}$$

Again, simple algebraic manipulations reveal the relativistic energy of a particle with mass

$$\mu_\mu = \sqrt{p_{{\rm F}\mu}^2 c^2 + m_\mu^2 c^4}, \tag{4.66}$$

as expected. Equalising these two chemical potentials and setting the muon number density $n_\mu = 0$ (implying $x_\mu = 0$), yields

$$k_{\rm Fe} = \lambda_\mu^{-1} \quad \Rightarrow \quad n_{\rm p} = n_{\rm e} = \frac{1}{3\pi^2}\left(\frac{m_\mu c}{\hbar}\right)^3 \approx 0.005185\,{\rm fm}^{-3}, \tag{4.67}$$

for the proton number density at which muons appear. As the proton fraction is approximately 4 % at this density also for the other proposed parametrisations given by Chamel, the baryon number density for the transition is roughly $n_b \approx 0.12\,{\rm fm}^{-3}$.

For a better understanding of the core EoS, we have calculated the adiabatic indices for matter in β-equilibrium as well as for perturbed matter in frozen composition as defined in (3.30) and (3.54).

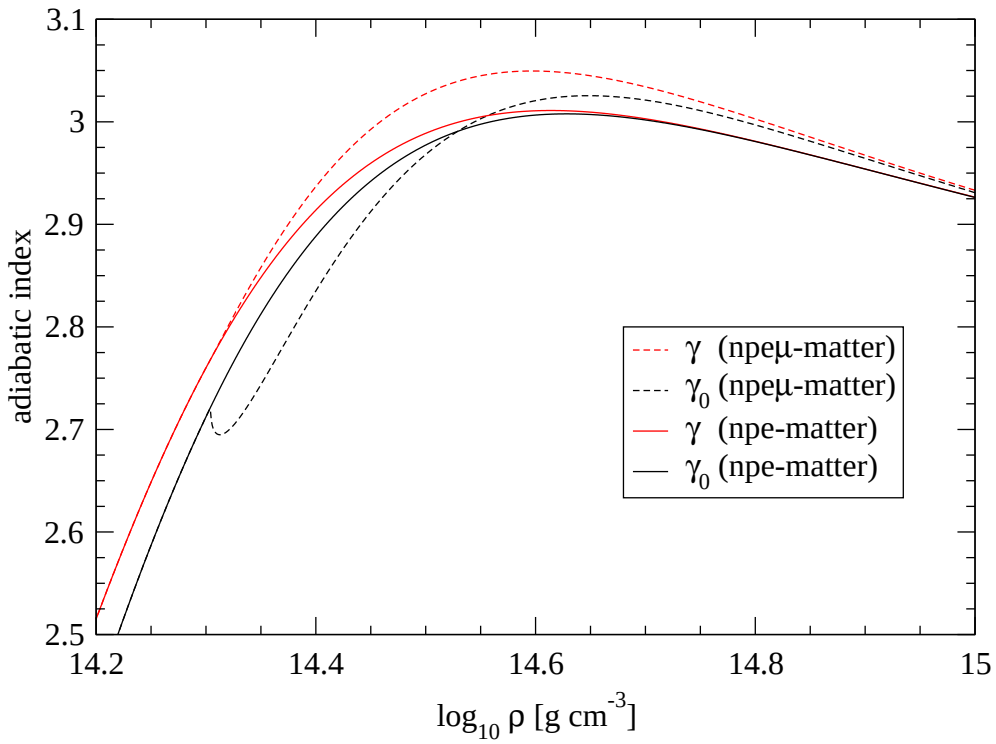

Figure 4.2: The adiabatic indices for matter in β-equilibrium and frozen composition. The dashed lines are for npeμ-matter whereas the solid lines depict the indices of muon-free matter.

The adiabatic indices, γ_0 and γ, are plotted for the core region of the star for matter with and without muons in Figure 4.2 for comparison. The graph for γ_0 for npeμ-matter exhibits a kink at about $\log\rho \approx 14.3$ which is where muons start to appear. The appearance of a new particle species softens the core matter slightly. In contrast, the kink in γ_0 does not appear anymore when we remove the muons.

As can be seen from the graphs, the value for γ is larger than γ_0 throughout the core; for npeμ-matter as well as matter without muons. According to the analysis of the Schwarzschild discriminant as defined in (3.55), pulsations of our model neutron star are stable against convection.

The quantity γ/γ_0 appears in the Schwarzschild discriminant and has been taken to be constant for simplicity in previous, qualitative studies on g-modes [24, 25]. In Figure 4.3, we show this ratio both for an npeμ-core and an npe-core. At first, we observe that the ratio is strictly below 1.07 throughout the core. The appearance of muons at $\log\rho \approx 14.3$ is clearly visible by a nearly discontinuous increase after which the ratio again drops. In both cases, the ratio continues to decrease as the density increases and it reaches values close to 1.0. We therefore expect composition g-modes to have a larger amplitude closer to the crust-core interface compared to the centre of the star.

4.2.4 Constructing a Multi-Fluid Background

We have now all necessary ingredients to construct a multi-fluid equilibrium model. We have several different possibilities on how to construct such a model; this new freedom stems from the larger number of quantities that we now associate with the individual fluids. Apart from the bulk properties of the fluid like pressure p and energy density ρ, we also have individual chemical potentials μ_{x} and number densities n_{x} for the different components.

The master function as described in the previous Section 4.2.3 provides us with one-to-one relations between these. Hence, we can choose between different equivalent formulations; we will present two of them here. This freedom concerns only the matter part of the equations; the metric potentials ν and λ will always be described by the two equations

$$\lambda' = \frac{1-e^{\lambda}}{r} - 8\pi r e^{\lambda}\Lambda, \tag{4.68}$$

$$\nu' = \frac{e^{\lambda}-1}{r} + 8\pi r e^{\lambda}\Psi, \tag{4.69}$$

which follow directly from the Einstein equations, $G_{\mu\nu} = 8\pi T_{\mu\nu}$. We have substituted the pressure p and the energy density ρ by the generalised pressure Ψ and the master function $-\Lambda$, respectively.

The most straightforward approach for the matter distribution would be to simply

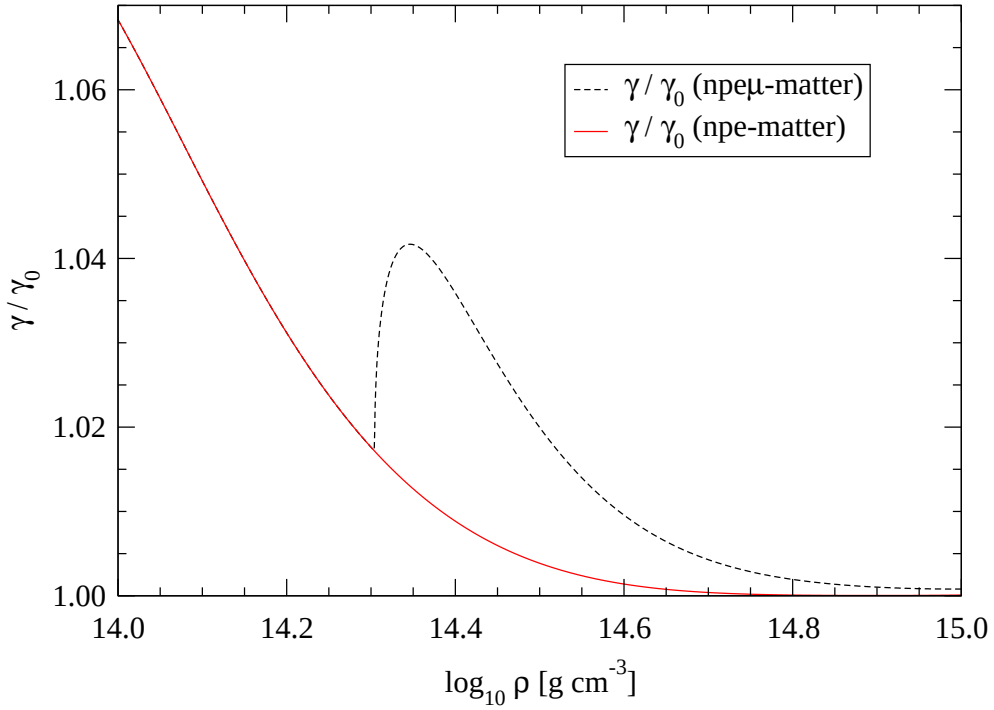

Figure 4.3: The ratio of the two adiabatic indices, γ/γ_0. In the outer layers of the core the ratio varies between 1.02 and 1.065 and since muons never appear there, the ratio does not depend on whether we account for the presence of muons in the EoS or not. If we account for muons then the ratio increases nearly discontinuously at $\log\rho \approx 14.3$ up to a value of 1.04 and then quickly drops towards higher densities; it takes values below 1.01 when $\log\rho \gtrsim 14.6$. If we neglect the presence of muons, the ratio continues to decrease monotonically throughout the core and takes values very close to 1.0; for densities with $\log\rho \in [14.7, 15.0]$ the ratio is below 1.0004.

continue using the complete set of TOV equations, i.e.

$$\Psi' = -\frac{1}{2}\nu'(\Psi - \Lambda), \tag{4.70}$$

along with the two equations for the metric potentials above. Assuming β-equilibrium, a given value of Ψ can uniquely be translated into four (or three) number densities for neutrons, protons, electrons and (possibly) muons from which all other necessary quantities can be calculated.

Another approach would be to make use of the equations of motion which we have derived from the variation principle. In particular, we will use $f^{\rm n}_\nu = 0$. We note that in a non-rotating star, the number density currents take the simple form

$$n^\mu_{\rm x} = n_{\rm x} u^\mu, \tag{4.71}$$

and the same holds true for the momentum covectors,

$$\mu^{\mu}_{\mathrm{x}} = \mu_{\mathrm{x}} u^{\mu}, \tag{4.72}$$

where μ_x is the chemical potential of species x and u^μ is the four-velocity of the equilibrium configuration. It is, of course, identical to the single fluid velocity and we repeat it here for completeness, $u^\mu = (e^{-\nu/2}, 0, 0, 0)$. We can now expand the equation of motion for the neutron fluid

$$0 = f^{\mathrm{n}}_{\nu} \tag{4.73}$$

$$= n^{\mu}_{\mathrm{n}} \left(\nabla_\mu \mu^{\mathrm{n}}_{\nu} - \nabla_\nu \mu^{\mathrm{n}}_{\mu} \right). \tag{4.74}$$

The covariant derivatives turn into partial derivatives since the Christoffel symbols are symmetric in their two lower indices. Using the fact that the matter in the equilibrium configuration is at rest yields

$$= n_{\mathrm{n}} u^t \left(\partial_t \mu^{\mathrm{n}}_{\nu} - \partial_\nu \mu^{\mathrm{n}}_{t} \right). \tag{4.75}$$

The temporal derivative vanishes since the equilibrium is not time-dependant and we are left with (only the r-component of this equation does not vanish)

$$0 = \partial_r \left(\mu_{\mathrm{n}} e^{\nu/2} \right) \tag{4.76}$$

or equivalently

$$\mu'_{\mathrm{n}} = -\frac{1}{2} \nu' \mu_{\mathrm{n}}. \tag{4.77}$$

This equation complements the two equations for the metric potentials, (4.68) and (4.69). In order to find a background solution, we need to specify a central chemical potential for the neutrons. In practice, we will prescribe a central neutron number density and then calculate the corresponding chemical potential (in β-equilibrium).

After every step on the radial grid, we have to calculate the composition in β-equilibrium from the chemical potential in order to determine pressure and energy density—computationally, there is no real advantage in using (4.77) compared to (4.70). In the case of a non-rotating star, this is a matter of personal choice; we use (4.77).

In order to avoid any doubts, we will show that equations (4.77) and (4.70) are physically equivalent. Multiply the former equation with n_b and remember that in β-equilibrium the simple relation $\Psi - \Lambda = \mu_{\mathrm{n}} n_b$ holds (cf. equation (4.45)). We arrive at

$$\Psi' - \Lambda' - \mu_{\mathrm{n}} n'_b = -\frac{1}{2} \nu' (\Psi - \Lambda). \tag{4.78}$$

We will (again!) make use of β-equilibrium which allows us to treat the energy density of

the background configuration as a function of n_b only; hence we can write $\Lambda' = \frac{\partial \Lambda}{\partial n_b} n_b' = -\mu_{\mathrm{n}} n_b'$ which proves our statement. Furthermore, it is now obvious that, even though μ_{n} depends on the entrainment $\mathcal{A}^{\mathrm{np}}$, our background will be entirely independent of the entrainment effect.

In order to construct the equilibrium configuration, we do not necessarily need to use the equation of motion (4.44c) for the proton fluid. However, we will need it when we derive the perturbation equations which is why we give it brief consideration now. As for the neutron fluid, we expand the equation

$$0 = \sum_{\mathrm{x} \in P} f_\nu^{\mathrm{x}} = 2 \sum_{\mathrm{x} \in P} n_{\mathrm{x}}^\mu \nabla_{[\mu} \mu_{\nu]}^{\mathrm{x}}. \tag{4.79}$$

We make use of the symmetry of the Christoffel symbols and the fact that the configuration is time-independent, which yields

$$= - \sum_{\mathrm{x} \in P} n_{\mathrm{x}} u^\mu \partial_\nu \mu_\mu^{\mathrm{x}}. \tag{4.80}$$

Furthermore, the star is at rest and the momenta depend only on r, which means that only the component with $\nu = r$ of the previous equation does not vanish; we obtain,

$$0 = \sum_{\mathrm{x} \in P} n_{\mathrm{x}} \left(\mu_t^{\mathrm{x}}\right)' . \tag{4.81}$$

In β-equilibrium, this equation is equivalent to the equation of motion (4.77) for the neutron fluid, and hence does not contain new information. This can easily be proven by remembering that $\mu_t^{\mathrm{x}} = -e^{\nu/2} \mu_{\mathrm{x}}$ from (4.72) and repeatedly applying equations (4.53) for β-equilibrium.

4.3 Entrainment and the Low-Velocity Expansion

A bit earlier, when we discussed the multi-fluid Lagrangian, we have seen that the momentum (4.33) of a fluid does not necessarily need to be proportional to the velocity of that fluid. This is due to the entrainment effect which becomes manifest in the coefficients $\mathcal{A}^{\mathrm{xy}}$. Physically this means that the individual fluids are not entirely independent but are influenced by each others presence and motion; this is the case when there is a coupling between two interpenetrating fluids.

In our four-constituent star, we account for two of these couplings. Firstly, even if neutrons are superfluid and can permeate the proton fluid, the strong interaction between the nucleons couples both fluids. This effect will be reflected in a non-vanishing $\mathcal{A}^{\mathrm{np}}$. Secondly, the electromagnetic interaction couples electrons and muons to the proton fluid. Due to the comparatively low mass of electrons and muons, we have assumed that all charged particles are fully locked to each other. Rather than having

$\mathcal{A}^{\mathrm{pe}} \neq 0$ or $\mathcal{A}^{\mathrm{p}\mu} \neq 0$, we account for the electromagnetic coupling by enforcing that their displacement vectors are identical, $\xi^\nu_{\mathrm{p}} = \xi^\nu_{\mathrm{e}} = \xi^\nu_\mu$. This assumption simplifies our equations as we now have $\mathcal{A}^{\mathrm{pe}} = \mathcal{A}^{\mathrm{p}\mu} = 0$. In fact, the only non-vanishing coefficient is $\mathcal{A}^{\mathrm{np}}$ (there is no entrainment between neutrons and leptons).

We want to shed light onto these coefficients from a different angle. For this we will closely follow the analysis of Andersson et al. [36]. The key quantity for the entrainment is the variable $n^2_{\mathrm{xy}} = -n^\mu_{\mathrm{x}} n^{\mathrm{y}}_\mu$. We can write the four-currents in the form

$$n^\mu_{\mathrm{x}} = n_{\mathrm{x}} u^\mu_{\mathrm{x}}, \tag{4.82}$$

where u^μ_{x} denotes the total velocity of fluid x and is normalised by $u^\mu_{\mathrm{x}} u^{\mathrm{x}}_\mu = -1$. Let τ_{x} denote the proper time of the fluid elements of fluid x, then the world line of a fluid element is given by

$$x^\mu_{\mathrm{x}}(\tau_{\mathrm{x}}) = \left(t(\tau_{\mathrm{x}}), x^i_{\mathrm{x}}(\tau_{\mathrm{x}})\right), \tag{4.83}$$

and its four-velocity by

$$u^\mu_{\mathrm{x}} = \frac{\mathrm{d}x^\mu_{\mathrm{x}}}{\mathrm{d}\tau_{\mathrm{x}}}. \tag{4.84}$$

Let us consider a small region within the fluid across which the gravitational field does not considerably change. To a good approximation, this region has Minkowski geometry and the metric can be written like the flat metric,

$$\mathrm{d}s^2 = -\,\mathrm{d}(ct)^2 + \delta_{ij}\,\mathrm{d}x^i\,\mathrm{d}x^j. \tag{4.85}$$

We can define the 3-velocity of the fluid elements as usual in Euclidean space by

$$u^i_{\mathrm{x}} = \frac{\mathrm{d}x^i_{\mathrm{x}}}{\mathrm{d}t}, \tag{4.86}$$

and its magnitude u_{x} is given by $u^2_{\mathrm{x}} = \delta_{ij} u^i_{\mathrm{x}} u^j_{\mathrm{x}}$. With these prerequisites, it can be shown that the 4-velocity can be written as

$$u^0_{\mathrm{x}} = \frac{1}{\sqrt{1-u^2_{\mathrm{x}}}} \quad \text{and} \quad u^i_{\mathrm{x}} = \frac{u^i_{\mathrm{x}}}{\sqrt{1-u^2_{\mathrm{x}}}}. \tag{4.87}$$

Using these relations, we can calculate the entrainment variable,

$$n^2_{\mathrm{xy}} = -n_{\mathrm{x}} u^\mu_{\mathrm{x}} n_{\mathrm{y}} u^{\mathrm{y}}_\mu \tag{4.88}$$

$$= -n_{\mathrm{x}} n_{\mathrm{y}} \left(u^0_{\mathrm{x}} u^{\mathrm{y}}_0 - u^i_{\mathrm{x}} u^{\mathrm{y}}_i\right) \tag{4.89}$$

$$= n_{\mathrm{x}} n_{\mathrm{y}} \left(\frac{1 - \delta_{ij} u_{\mathrm{x}}^i u_{\mathrm{y}}^j}{\sqrt{1 - u_{\mathrm{x}}^2}\sqrt{1 - u_{\mathrm{y}}^2}} \right). \tag{4.90}$$

When we consider neutron star oscillations, then the individual 3-velocities of the fluid elements will be very small compared to the speed of light, i.e.

$$\left| u_{\mathrm{x}}^i \right| \ll 1, \tag{4.91}$$

and then obviously $\left| u_{\mathrm{x}}^2 \right| \ll 1$, too. This implies that we have $n_{\mathrm{xy}}^2 \approx n_{\mathrm{x}} n_{\mathrm{y}}$ to a good approximation; alternatively, the quantity $n_{\mathrm{xy}} - n_{\mathrm{x}} n_{\mathrm{y}}$ is very small and is well-suited as an expansion variable in a Taylor series.

While the previous discussion is true for any combination of fluids x and y, we will restrict ourselves for simplicity to the neutron and proton fluid only. This means that our equation of state (the master function) is given by

$$\Lambda = \Lambda(n_{\mathrm{x}}^2, n_{\mathrm{y}}^2, n_{\mathrm{xy}}^2) \tag{4.92}$$

$$= \Lambda(n_{\mathrm{n}}^2, n_{\mathrm{np}}^2, n_{\mathrm{p}}^2, n_{\mathrm{e}}^2, n_{\mu}^2). \tag{4.93}$$

The fact that the leptons do not take part in any entrainment allows us to separate them off into individual pieces, e.g.

$$\Lambda = \Lambda^{\mathrm{np}}(n_{\mathrm{n}}^2, n_{\mathrm{np}}^2, n_{\mathrm{p}}^2) + \Lambda^{\mathrm{e}}(n_{\mathrm{e}}^2) + \Lambda^{\mu}(n_{\mu}^2). \tag{4.94}$$

In general, we would need one (part-) master function for each pair of fluids that is mutually entrained; as explained above, we consider merely the neutron-proton entrainment due to the strong interaction. For the baryon part, Λ^{np}, we will now make use of the fact that the velocities are small and expand this function like

$$\Lambda^{\mathrm{np}}(n_{\mathrm{n}}^2, n_{\mathrm{p}}^2, n_{\mathrm{np}}^2) = \sum_{k=0}^{\infty} \lambda_k^{\mathrm{np}} \left(n_{\mathrm{n}}^2, n_{\mathrm{p}}^2\right) \left(n_{\mathrm{np}}^2 - n_{\mathrm{n}} n_{\mathrm{p}}\right)^k, \tag{4.95}$$

where the λ_k^{np} are the Taylor coefficients whose meaning we are going to explain below. Given this expansion, we can calculate the coefficients

$$\mathcal{A}^{\mathrm{np}} = -\frac{\partial \Lambda}{\partial n_{\mathrm{np}}^2} = -\sum_{k=1}^{\infty} k \lambda_k^{\mathrm{np}} \left(n_{\mathrm{n}}^2, n_{\mathrm{p}}^2\right) \left(n_{\mathrm{np}}^2 - n_{\mathrm{n}} n_{\mathrm{p}}\right)^{k-1}, \tag{4.96}$$

$$\mathcal{B}^{\mathrm{n}} = -2\frac{\partial \Lambda}{\partial n_{\mathrm{n}}^2} = -\frac{1}{n_{\mathrm{n}}} \frac{\partial \Lambda}{\partial n_{\mathrm{n}}} \tag{4.97}$$

$$= -\frac{1}{n_{\mathrm{n}}} \left[\frac{\partial \lambda_0^{\mathrm{np}}}{\partial n_{\mathrm{n}}} + n_{\mathrm{p}} A^{\mathrm{np}} + \sum_{k=1}^{\infty} \frac{\partial \lambda_k}{\partial n_{\mathrm{n}}} \left(n_{\mathrm{np}}^2 - n_{\mathrm{n}} n_{\mathrm{p}}\right)^k \right], \tag{4.98}$$

and

$$\mathcal{B}^{\mathrm{p}} = -2\frac{\partial\Lambda}{\partial n_{\mathrm{p}}^2} = -\frac{1}{n_{\mathrm{p}}}\left[\frac{\partial\lambda_0^{\mathrm{np}}}{\partial n_{\mathrm{p}}} + n_{\mathrm{n}}A^{\mathrm{np}} + \sum_{k=1}^{\infty}\frac{\partial\lambda_k}{\partial n_{\mathrm{n}}}\left(n_{\mathrm{np}}^2 - n_{\mathrm{n}}n_{\mathrm{p}}\right)^k\right]. \tag{4.99}$$

For a complete and convenient description, we need three other quantities, the relevance of which will become clear later and we denote them by $\mathcal{B}^{\mathrm{n}0}_{\ 0}$, $\mathcal{B}^{\mathrm{p}0}_{\ 0}$ and $\mathcal{A}^{\mathrm{np}0}_{\ 0}$. The expressions for them are lengthy and given in Appendix A; there we also show that they are closely linked to the partial derivatives of the chemical potentials. In the low-velocity expansion, they take the form

$$\frac{\partial\mu_{\mathrm{n}}}{\partial n_{\mathrm{n}}} = \mathcal{B}^{\mathrm{n}0}_{\ 0} = -\frac{\partial^2\lambda_0^{\mathrm{np}}}{(\partial n_{\mathrm{n}})^2} - \sum_{k=1}^{\infty}\frac{\partial^2\lambda_k^{\mathrm{np}}}{(\partial n_{\mathrm{n}})^2}\left(n_{\mathrm{np}}^2 - n_{\mathrm{n}}n_{\mathrm{p}}\right)^k, \tag{4.100}$$

$$\frac{\partial\mu_{\mathrm{p}}}{\partial n_{\mathrm{p}}} = \mathcal{B}^{\mathrm{p}0}_{\ 0} = -\frac{\partial^2\lambda_0^{\mathrm{np}}}{(\partial n_{\mathrm{p}})^2} - \sum_{k=1}^{\infty}\frac{\partial^2\lambda_k^{\mathrm{np}}}{(\partial n_{\mathrm{p}})^2}\left(n_{\mathrm{np}}^2 - n_{\mathrm{n}}n_{\mathrm{p}}\right)^k, \tag{4.101}$$

and

$$\frac{\partial\mu_{\mathrm{n}}}{\partial n_{\mathrm{p}}} = \frac{\partial\mu_{\mathrm{p}}}{\partial n_{\mathrm{n}}} = \mathcal{A}^{\mathrm{np}0}_{\ 0} = -\frac{\partial^2\lambda_0^{\mathrm{np}}}{\partial n_{\mathrm{p}}\partial n_{\mathrm{n}}} - \sum_{k=1}^{\infty}\frac{\partial^2\lambda_k^{\mathrm{np}}}{\partial n_{\mathrm{p}}\partial n_{\mathrm{n}}}\left(n_{\mathrm{np}}^2 - n_{\mathrm{n}}n_{\mathrm{p}}\right)^k. \tag{4.102}$$

The magic of this currently rather messy looking expansion becomes apparent when we evaluate the different quantities on the background where we have $n_{\mathrm{np}} = n_{\mathrm{n}}n_{\mathrm{p}}$; the infinite sums collapse and only the two coefficients λ_0^{np} and λ_1^{np} remain. We can immediately grasp their physical relevance; on the background, we have

$$\Lambda^{\mathrm{np}} = \lambda_0^{\mathrm{np}} \qquad \text{or} \qquad \Lambda = \lambda_0^{\mathrm{np}} + \Lambda^{\mathrm{e}} + \Lambda^{\mu}, \tag{4.103}$$

which tells us that λ_0^{np} is the (negative) internal energy density of the baryonic component. Furthermore, the other coefficient encodes the entrainment effect since

$$\mathcal{A}^{\mathrm{np}} = -\lambda_1^{\mathrm{np}}. \tag{4.104}$$

This decomposition enables us to specify the equation of state and the entrainment separately.

We use the entrainment provided by Chamel [38] in conjunction with the analytic representation of the SLy4 force; the entrainment coefficient is

$$\lambda_1^{\mathrm{np}} = -m\frac{\beta_3}{1+\beta_3 n_b} \quad \text{with} \quad \beta_3 = \frac{2m}{\hbar^2}B_3, \tag{4.105}$$

where B_3 is the parameter given in Table 4.1.

4.4 Prerequisites for the Derivation of the Perturbation Equations

We have determined the equations of motion for a multi-fluid star (see equations (4.40) or (4.44)), we now need to populate them with ansätze for different quantities which stem from the specific properties of our problem in order to find the perturbation equations which govern small perturbations of a multi-fluid star. These ansätze will not differ very much from those for the single fluid problem which we have described to great detail in Section 3.2. The main difference is that we will now have one displacement vector for each individual fluid.

Our ansatz for the metric perturbation for even perturbations is identical to the one in the single fluid problem (cf. equation (3.13)), but we will repeat it here for completeness,

$$\delta g_{\mu\nu} = -r^l \begin{pmatrix} e^\nu H_0 & i\omega r H_1 & 0 & 0 \\ i\omega r H_1 & e^\lambda H_2 & 0 & 0 \\ 0 & 0 & r^2 K & 0 \\ 0 & 0 & 0 & r^2 \sin^2\theta K \end{pmatrix} P_l(\cos\theta) e^{i\omega t}, \tag{4.106}$$

where $P_l(\cos\theta)$ is the Legendre polynomial of degree l. The definition of the displacement vectors differs only by the constituent index which we will assign to each quantity that is specific to an individual fluid. We have

$$\xi^t_{\mathrm{x}} = 0, \tag{4.107}$$

$$\xi^r_{\mathrm{x}} = r^l e^{-\lambda/2} \frac{W_{\mathrm{x}}}{r} P_l e^{i\omega t}, \tag{4.108}$$

$$\xi^\theta_{\mathrm{x}} = -r^l \frac{V_{\mathrm{x}}}{r^2} \frac{\mathrm{d}P_l}{\mathrm{d}\theta} e^{i\omega t}, \tag{4.109}$$

$$\xi^\phi_{\mathrm{x}} = 0, \tag{4.110}$$

where x runs over all constituent indices of the individual fluids; V_{x} and W_{x} are the tangential and radial displacement of the respective fluid.

In our case, the constituents are (essentially) n for the neutron fluid and p for the proton fluid. We point out that this is a simplified statement as we actually consider a 4-constituent fluid, consisting of npeμ-matter, where we assume that the electrons and muons are electromagnetically locked to the protons and hence their displacement vectors coincide (see equation (4.42)). However, while the displacement vectors of these three constituents are indistinguishable, other quantities associated with the different species, like their number density, n_{x} or their chemical potentials, μ_{x}, will surely have different values for each species. We, therefore, cannot simply assume that the electrons and muons are lumped together with the protons and forget about their presence; in

several occasions, starting from the equations of motion (4.44), associated quantities will inevitably appear in our equations.

As a next step, we will have a look at the equations of motion. In foresight of the application to our specific problem—a 4-constituent star with two individual fluids—we will investigate the more specialised set of equations (4.44), but we emphasise that a generalisation to a differently composed neutron star is possible without much effort.

4.4.1 The Perturbed Einstein Equations

Even though we consider a multi-constituent star now, several perturbation equations will still stem from the Einstein equations—as in the single fluid case. We have to solve

$$\delta G_{\mu\nu} = 8\pi \delta T_{\mu\nu}, \tag{4.111}$$

where $\delta G_{\mu\nu}$ is given in (3.15). The perturbed stress-energy tensor will take a slightly different form since we have expressed it in quantities different from the ones we used to describe the single fluid. We will give the complete expression in Section 4.4.4.

4.4.2 The Euler-type Equation for the Neutrons

The second equation of motion is the one for the neutron fluid (or more general, the equation of motion for one individual fluid; the constituent index n can be exchanged for the general index x without any problems). We have

$$0 = 2f^{\mathrm{n}}_{\nu} = 2n^{\mu}_{\mathrm{n}} \nabla_{[\mu} \mu^{\mathrm{n}}_{\nu]} = 2n^{\mu}_{\mathrm{n}} \partial_{[\mu} \mu^{\mathrm{n}}_{\nu]}, \tag{4.112}$$

where we have achieved the last equality by using that the Christoffel symbols are symmetric in their lower indices. Decomposing the "full" quantities into their background part and Eulerian perturbation, we find

$$0 = 2\left(n^{\mu}_{\mathrm{n}} + \delta n^{\mu}_{\mathrm{n}}\right) \partial_{[\mu} \left(\mu^{\mathrm{n}}_{\nu]} + \delta \mu^{\mathrm{n}}_{\nu]}\right). \tag{4.113}$$

Since the unperturbed part, $n^{\mu}_{\mathrm{n}} \partial_{[\mu} \mu^{\mathrm{n}}_{\nu]} = 0$, must be fulfilled for the background, too, we have

$$= n^{\mu}_{\mathrm{n}} \left(\partial_{\mu} \delta\mu^{\mathrm{n}}_{\nu} - \partial_{\nu} \delta\mu^{\mathrm{n}}_{\mu}\right) + \delta n^{\mu}_{\mathrm{n}} \left(\partial_{\mu} \mu^{\mathrm{n}}_{\nu} - \partial_{\nu} \mu^{\mathrm{n}}_{\mu}\right) \tag{4.114}$$

after linearisation. We will focus on the second term in this expression now and show that it vanishes. In the cases $\nu = \theta$ and $\nu = \phi$, this term vanishes since, first, $\mu^{\mathrm{n}}_{\theta} =$

$\mu^{\mathrm{n}}_{\phi} = 0$ and, second, μ^{n}_{μ} does not depend on θ or ϕ. If $\nu = t$, we have

$$\delta n^{\mu}_{\mathrm{n}} \left(\partial_{\mu}\mu^{\mathrm{n}}_{t} - \underbrace{\partial_{t}\mu^{\mathrm{n}}_{\mu}}_{=0} \right) = \delta n^{\mu}_{\mathrm{n}} \partial_{\mu}\mu^{\mathrm{n}}_{t} = \delta n^{r}_{\mathrm{n}} \partial_{r}\mu^{\mathrm{n}}_{t} = 0 \tag{4.115}$$

where the second equality is due to the fact that μ^{n}_{t} is a function of r only and the last one is due to the background equation, $\partial_{r}\mu^{\mathrm{n}}_{t} = 0$. The last case, in which $\nu = r$, yields

$$\delta n^{\mu}_{\mathrm{n}} \left(\partial_{\mu} \underbrace{\mu^{\mathrm{n}}_{r}}_{=0} - \partial_{r}\mu^{\mathrm{n}}_{\mu} \right) = -\delta n^{t}_{\mathrm{n}} \partial_{r}\mu^{\mathrm{n}}_{t} = 0, \tag{4.116}$$

which vanishes due to fact that μ^{n}_{μ} differs from zero only for $\mu = t$ and again the background equation, $\partial_{r}\mu^{\mathrm{n}}_{t} = 0$. Altogether, the second term in (4.114) vanishes and we are left with

$$0 = n^{t}_{\mathrm{n}} \left(\partial_{t}\delta\mu^{\mathrm{n}}_{\nu} - \partial_{\nu}\delta\mu^{\mathrm{n}}_{t} \right), \tag{4.117}$$

where we have used that $n^{\mu}_{\mathrm{n}} \neq 0$ only for $\mu = t$. Thus, we have

$$\partial_{t}\delta\mu^{\mathrm{n}}_{\nu} = \partial_{\nu}\delta\mu^{\mathrm{n}}_{t}. \tag{4.118}$$

4.4.3 The Euler-type Equations for the Proton Fluid

The remaining equations of motion will be due to (4.44c),

$$f^{\mathrm{p}}_{\nu} + f^{\mathrm{e}}_{\nu} + f^{\mu}_{\nu} = \sum_{\mathrm{x}\in P} f^{\mathrm{x}}_{\nu} = 0. \tag{4.119}$$

In contrast to the previous equations of motion, this one is obviously specific to our problem as it concerns an individual fluid consisting of three constituents. When muons are absent, f^{μ}_{ν} obviously vanishes from this equation.

Starting in a similar fashion to the previous section, we expand the terms in (4.119) and decompose them into their background and perturbation parts. After making use of the background equation (4.81) and linearisation, we arrive at

$$\sum_{\mathrm{x}\in P} \left[n^{\mu}_{\mathrm{x}} \left(\partial_{\mu}\delta\mu^{\mathrm{x}}_{\nu} - \partial_{\nu}\delta\mu^{\mathrm{x}}_{\mu} \right) + \delta n^{\mu}_{\mathrm{x}} \left(\partial_{\mu}\mu^{\mathrm{x}}_{\nu} - \partial_{\nu}\mu^{\mathrm{x}}_{\mu} \right) \right] = 0. \tag{4.120}$$

Again, we will show that the second term (which we abbreviate with Ξ_{ν}) identically vanishes. Due to the three constituents involved, this requires a bit more effort.

We want to show that

$$\Xi_{\nu} := \sum_{\mathrm{x}\in P} \delta n^{\mu}_{\mathrm{x}} \left(\partial_{\mu}\mu^{\mathrm{x}}_{\nu} - \partial_{\nu}\mu^{\mathrm{x}}_{\mu} \right) = 0. \tag{4.121}$$

As an abbreviation, we define $\zeta_{\mathrm{x}} := \partial_r \mu_t^{\mathrm{x}}$ and we note that the background equation (4.81) can be written as $\sum_{\mathrm{x}} n_{\mathrm{x}} \zeta_{\mathrm{x}} = 0$ using this definition. As before, the cases $\nu = \theta$ and $\nu = \phi$ are trivial. Let us turn to the case $\nu = t$:

$$\Xi_t = \sum_{\mathrm{x}\in P} \delta n_{\mathrm{x}}^{\mu} \left(\partial_\mu \mu_t^{\mathrm{x}} - \partial_t \mu_\mu^{\mathrm{x}} \right) = \sum_{\mathrm{x}\in P} \delta n_{\mathrm{x}}^{\mu} \partial_\mu \mu_t^{\mathrm{x}} = \sum_{\mathrm{x}\in P} \delta n_{\mathrm{x}}^{r} \zeta_{\mathrm{x}}, \tag{4.122}$$

where we have used $\mu_\mu^{\mathrm{x}} = \mu_\mu^{\mathrm{x}}(r)$ in the last equality. The Eulerian perturbation, δn_{x}^r, can be written as

$$\delta n_{\mathrm{x}}^r = n_{\mathrm{x}} \delta u_{\mathrm{x}}^r + \underbrace{u_{\mathrm{x}}^r}_{=0} \delta n_{\mathrm{x}} = n_{\mathrm{x}} \delta u_{\mathrm{x}}^r. \tag{4.123}$$

The perturbed velocities are identical in this case since we consider the constituents of the proton fluid which are locked together. Thus,

$$\Xi_t = \sum_{\mathrm{x}\in P} \delta n_{\mathrm{x}}^r \zeta_{\mathrm{x}} = \delta u_{\mathrm{p}}^r \underbrace{\sum_{\mathrm{x}\in P} n_{\mathrm{x}} \zeta_x}_{=0} = 0, \tag{4.124}$$

by means of (4.81). Last but not least, $\nu = r$:

$$\Xi_r = \sum_{\mathrm{x}\in P} \delta n_{\mathrm{x}}^{\mu} \left(\partial_\mu \mu_r^{\mathrm{x}} - \partial_r \mu_\mu^{\mathrm{x}} \right) \tag{4.125}$$

$$= -\sum_{\mathrm{x}\in P} \delta n_{\mathrm{x}}^{\mu} \partial_r \mu_\mu^{\mathrm{x}} \qquad \mu_\mu^{\mathrm{x}} \neq 0 \text{ only for } \mu = t \tag{4.126}$$

$$= -\sum_{\mathrm{x}\in P} \delta n_{\mathrm{x}}^{t} \zeta_{\mathrm{x}} \tag{4.127}$$

with $\delta n_{\mathrm{x}}^t = u^t \delta n_{\mathrm{x}}$ due to $\delta u^t = 0$, we find

$$= -u^t \sum_{\mathrm{x}\in P} \delta n_{\mathrm{x}} \zeta_{\mathrm{x}}. \tag{4.128}$$

The relation between Eulerian and Lagrangian perturbations yields

$$= -u^t \sum_{\mathrm{x}\in P} \left(\Delta n_{\mathrm{x}} - n_{\mathrm{x}}' e^{-\lambda/2} r^{l-1} W_{\mathrm{x}} \right) \zeta_{\mathrm{x}} \tag{4.129}$$

$$= -u^t \sum_{\mathrm{x}\in P} n_{\mathrm{x}} \frac{\Delta n_{\mathrm{x}}}{n_{\mathrm{x}}} \zeta_{\mathrm{x}} + u^t e^{-\lambda/2} r^{l-1} \sum_{\mathrm{x}\in P} n_{\mathrm{x}}' W_{\mathrm{x}} \zeta_{\mathrm{x}}. \tag{4.130}$$

We can now use the fact that the displacement vectors are identical, $W_{\mathrm{p}} = W_{\mathrm{e}} = W_\mu$, and that hence the fractions $\Delta n_{\mathrm{x}}/n_{\mathrm{x}}$ are independent of the species, too,

$$= -u^t \frac{\Delta n_{\mathrm{p}}}{n_{\mathrm{p}}} \underbrace{\sum_{\mathrm{x}\in P} n_{\mathrm{x}} \zeta_{\mathrm{x}}}_{=0} + u^t e^{-\lambda/2} r^{l-1} W_{\mathrm{p}} \underbrace{\sum_{\mathrm{x}\in P} n_{\mathrm{x}}' \zeta_{\mathrm{x}}}_{=0} = 0. \tag{4.131}$$

We are left with the proof that the last sum actually vanishes. For this, we will make use of the equations (4.53) for β-equilibrium. First, we note that $\mu_{\mathrm{e}} = \mu_\mu$ implies $\zeta_{\mathrm{e}} = \zeta_\mu$. Starting from (4.81), we have

$$0 = \sum_{\mathrm{x}\in P} n_{\mathrm{x}}\zeta_{\mathrm{x}} = n_{\mathrm{p}}\zeta_{\mathrm{p}} + n_{\mathrm{e}}\zeta_{\mathrm{e}} + n_\mu\zeta_\mu = n_{\mathrm{p}}\zeta_{\mathrm{p}} + \underbrace{(n_{\mathrm{e}} + n_\mu)}_{=n_{\mathrm{p}}}\zeta_{\mathrm{e}} = n_{\mathrm{p}}(\zeta_{\mathrm{p}} + \zeta_{\mathrm{e}}), \tag{4.132}$$

which implies $\zeta_{\mathrm{p}} + \zeta_{\mathrm{e}} = 0$. Hence, reversing this calculation yields

$$0 = n'_{\mathrm{p}}(\zeta_{\mathrm{p}} + \zeta_{\mathrm{e}}) = n'_{\mathrm{p}}\zeta_{\mathrm{p}} + \underbrace{(n'_{\mathrm{e}} + n'_\mu)}_{=n'_{\mathrm{p}}}\zeta_{\mathrm{e}} = n'_{\mathrm{p}}\zeta_{\mathrm{p}} + n'_{\mathrm{e}}\zeta_{\mathrm{e}} + n'_\mu\zeta_\mu = \sum_{\mathrm{x}\in P} n'_{\mathrm{x}}\zeta_{\mathrm{x}}, \tag{4.133}$$

as desired.

We have shown that $\Xi_\nu = 0$ and therefore the equations of motion reduce to

$$0 = \sum_{\mathrm{x}\in P} n^\mu_{\mathrm{x}} \left(\partial_\mu\delta\mu^{\mathrm{x}}_\nu - \partial_\nu\delta\mu^{\mathrm{x}}_\mu\right) \tag{4.134}$$

$$= \sum_{\mathrm{x}\in P} n_{\mathrm{x}} u^t \left(\partial_t\delta\mu^{\mathrm{x}}_\nu - \partial_\nu\delta\mu^{\mathrm{x}}_t\right), \tag{4.135}$$

where we have used that $u^r = u^\theta = u^\phi = 0$. Finally, we have

$$0 = \sum_{\mathrm{x}\in P} n_{\mathrm{x}} \left(\partial_t\delta\mu^{\mathrm{x}}_\nu - \partial_\nu\delta\mu^{\mathrm{x}}_t\right), \tag{4.136}$$

which is a bit more complicated than the equation (4.118) for the single constituent fluid because we have to account for the three constituents in this case.

We point out that the result is identical if muons are absent, i.e. if $P = \{\mathrm{p}, \mathrm{e}\}$. Only the derivation of $\sum_{\mathrm{x}} n'_{\mathrm{x}}\zeta_{\mathrm{x}} = 0$ cannot be used "literally" (as in symbol by symbol) but the necessary modifications are obvious.

4.4.4 The Perturbations of μ^{x}_ν, $G^{\mu\nu}$ and $T^{\mu\nu}$

We are now a big step closer to deriving the perturbation equations for our four-constituent two-fluid neutron star. We have to solve

$$\delta G^{\mu\nu} = 8\pi\delta T^{\mu\nu}, \tag{4.137a}$$

$$\partial_t\delta\mu^{\mathrm{n}}_\nu = \partial_\nu\delta\mu^{\mathrm{n}}_t, \tag{4.137b}$$

$$0 = \sum_{\mathrm{x}\in P} n_{\mathrm{x}} \left(\partial_t\delta\mu^{\mathrm{x}}_\nu - \partial_\nu\delta\mu^{\mathrm{x}}_t\right), \tag{4.137c}$$

where the set of constituent indices, P, can be $P = \{\mathrm{p}, \mathrm{e}\}$ or $P = \{\mathrm{p}, \mathrm{e}, \mu\}$. We have already calculated the perturbed Einstein tensor $\delta G^{\mu\nu}$ in equation (3.15) and we do

not repeat the result here. The perturbation of the stress-energy tensor (4.41) is

$$\delta T^{\nu}_{\mu} = \delta\Psi\delta^{\nu}_{\mu} + \sum_{\mathrm{x}} \left(\mu^{\mathrm{x}}_{\mu}\delta n^{\nu}_{\mathrm{x}} + \delta\mu^{\mathrm{x}}_{\mu} n^{\nu}_{\mathrm{x}}\right), \tag{4.138}$$

for which we need the perturbation of the generalised pressure, $\Psi = \Lambda - \sum_{\mathrm{x}} n^{\nu}_{\mathrm{x}}\mu^{\mathrm{x}}_{\nu}$, and the perturbation of the momentum covectors, $\delta\mu^{\mathrm{x}}_{\nu}$. For the calculation of $\delta\Psi$, we use (4.32),

$$\delta\Psi = \delta\Lambda - \sum_{\mathrm{x}} \left(\delta\mu^{\mathrm{x}}_{\nu} n^{\nu}_{\mathrm{x}} + \mu^{\mathrm{x}}_{\nu}\delta n^{\nu}_{\mathrm{x}}\right) \tag{4.139}$$

$$= \frac{1}{2} g^{\nu\lambda} \left(\sum_{\mathrm{x}} n^{\mu}_{\mathrm{x}}\mu^{\mathrm{x}}_{\lambda}\right) \delta g_{\mu\nu} - \sum_{\mathrm{x}} \delta\mu^{\mathrm{x}}_{\nu} n^{\nu}_{\mathrm{x}}. \tag{4.140}$$

The variations of the momentum covectors μ^{x}_{ν} as given in (4.33) are

$$\delta\mu^{\mathrm{x}}_{\nu} = \delta\mathcal{B}^{\mathrm{x}} n^{\mathrm{x}}_{\nu} + \mathcal{B}^{\mathrm{x}}\delta n^{\mathrm{x}}_{\nu} + \sum_{\mathrm{y}\neq\mathrm{x}} \left(\delta\mathcal{A}^{\mathrm{xy}} n^{\mathrm{y}}_{\nu} + \mathcal{A}^{\mathrm{xy}}\delta n^{\mathrm{y}}_{\nu}\right). \tag{4.141}$$

Our aim is to have $\delta\mu^{\mathrm{x}}_{\nu}$ expressed solely in the variations $\delta n^{\mathrm{x}}_{\nu}$ and $\delta g_{\mu\nu}$ since we know how to express these in terms of the displacement vectors and the metric perturbations. We rewrite the variations $\delta\mathcal{B}^{\mathrm{x}}$ and $\delta\mathcal{A}^{\mathrm{xy}}$ as

$$\delta\mathcal{B}^{\mathrm{x}} = \sum_{\mathrm{z}_1} \frac{\partial\mathcal{B}^{\mathrm{x}}}{\partial n^2_{\mathrm{z}_1}}\delta n^2_{\mathrm{z}_1} + \sum_{\mathrm{z}_1}\sum_{\mathrm{z}_2\neq\mathrm{z}_1} \frac{\partial\mathcal{B}^{\mathrm{x}}}{\partial n^2_{\mathrm{z}_1\mathrm{z}_2}}\delta n^2_{\mathrm{z}_1\mathrm{z}_2}, \tag{4.142}$$

$$\delta\mathcal{A}^{\mathrm{xy}} = \sum_{\mathrm{z}_1} \frac{\partial\mathcal{A}^{\mathrm{xy}}}{\partial n^2_{\mathrm{z}_1}}\delta n^2_{\mathrm{z}_1} + \sum_{\mathrm{z}_1}\sum_{\mathrm{z}_2\neq\mathrm{z}_1} \frac{\partial\mathcal{A}^{\mathrm{xy}}}{\partial n^2_{\mathrm{z}_1\mathrm{z}_2}}\delta n^2_{\mathrm{z}_1\mathrm{z}_2}. \tag{4.143}$$

In general, we have to account for all partial derivatives of $\mathcal{B}^{\mathrm{x}}$ and $\mathcal{A}^{\mathrm{xy}}$ with respect to the number density currents $n^2_{\mathrm{z}_1}$ as well as the mixed currents $n^2_{\mathrm{z}_1\mathrm{z}_2}$. We give a more detailed insight into the lengthy calculation in Appendix A. In our special case, fortunately, a great amount of these partial derivatives vanishes, leading to much simpler expression. We account for entrainment only between neutrons and protons, which implies $A^{\mathrm{xy}} \neq 0$ only for $(\mathrm{x},\mathrm{y}) = (\mathrm{n},\mathrm{p})$ (or $(\mathrm{x},\mathrm{y}) = (\mathrm{p},\mathrm{n})$ of course); furthermore, the partial derivatives $\frac{\partial\mathcal{B}^{\mathrm{x}}}{\partial n^2_{\mathrm{y}}}$ vanish if $\mathrm{x} \neq \mathrm{y}$, the only exception being again $(\mathrm{x},\mathrm{y}) = (\mathrm{n},\mathrm{p})$ (or reversed). We also use the two identities

$$\delta n^2_{\mathrm{x}} = -\delta\left(n^{\mathrm{x}}_{\mu} n^{\mathrm{x}}_{\nu} g^{\mu\nu}\right) \tag{4.144}$$

$$= -2n^{\mu}_{\mathrm{x}}\delta n^{\mathrm{x}}_{\mu} + n^{\mu}_{\mathrm{x}} n^{\nu}_{\mathrm{x}}\delta g_{\mu\nu} \tag{4.145}$$

and

$$\delta n^2_{\mathrm{xy}} = -n^{\mu}_{\mathrm{x}}\delta n^{\mathrm{y}}_{\mu} - n^{\mu}_{\mathrm{y}}\delta n^{\mathrm{x}}_{\mu} + n^{\mu}_{\mathrm{x}} n^{\nu}_{\mathrm{y}}\delta g_{\mu\nu}, \tag{4.146}$$

for which we have used the identity $\delta g^{\mu\nu} = -g^{\mu\lambda}g^{\nu\sigma}\delta g_{\lambda\sigma}$. Finally, we need to resolve $\delta n^{\rm x}_\mu$ for which we consider the temporal and spatial parts separately. The temporal part yields

$$\delta n^{\rm x}_t = \delta(n_{\rm x}u^{\rm x}_t) = u_t\delta n_{\rm x} + n_{\rm x}\delta u^{\rm x}_t \tag{4.147}$$

$$= u_t\delta n_{\rm x} + \frac{1}{2}n_{\rm x}u^t\delta g_{tt} \tag{4.148}$$

where we have used that all background velocities are identical, $u^{\rm x}_\mu = u_\mu$, and

$$\delta u^{\rm x}_t = g_{tt}\delta u^t_{\rm x} + \delta g_{tt}u^t \tag{4.149}$$

$$= \frac{1}{2}\underbrace{g_{tt}u^tu^t}_{=-1}u^t\delta g_{tt} + \delta g_{tt}u^t \tag{4.150}$$

$$= \frac{1}{2}u^t\delta g_{tt}. \tag{4.151}$$

The spatial part of the number density current yields

$$\delta n^{\rm x}_i = n_{\rm x}\delta u^{\rm x}_i, \tag{4.152}$$

since $u_i = 0$.

We insert these expressions into (4.141), and arrive at

$$\delta\mu^{\rm x}_t = -e^{\nu/2}\left[\frac{\partial\mu_{\rm x}}{\partial n_{\rm x}}\delta n_{\rm x} + \sum_{\rm y\neq x}\frac{\partial\mu_{\rm x}}{\partial n_{\rm y}}\delta n_{\rm y} - \frac{1}{2}\mu_{\rm x}e^{-\nu}\delta g_{tt}\right], \tag{4.153}$$

$$\delta\mu^{\rm x}_i = \mathcal{B}^{\rm x}n_{\rm x}\delta u^{\rm x}_i + \sum_{\rm y\neq x}\mathcal{A}^{\rm xy}n_{\rm y}\delta u^{\rm y}_i. \tag{4.154}$$

In the expression for the temporal component of $\delta\mu^{\rm x}_\nu$, we have used the partial derivatives of the chemical potentials. That this makes sense becomes clear if we write

$$\delta\mu^{\rm x}_t = \mu_x\delta u^{\rm x}_t + u_t\delta\mu_{\rm x}, \tag{4.155}$$

and use this in (4.153); we arrive at

$$\delta\mu_{\rm x} = \frac{\partial\mu_{\rm x}}{\partial n_{\rm x}}\delta n_{\rm x} + \sum_{\rm y\neq x}\frac{\partial\mu_{\rm x}}{\partial n_{\rm y}}\delta n_{\rm y}, \tag{4.156}$$

which is as it should be. This should not obscure the fact that we have arrived at (4.153) via the rather lengthy calculation as explained above; the coefficients of $\delta n_{\rm x}$ and $\delta n_{\rm y}$ in this equation are given in Appendix A where we call them $\mathcal{B}^{\rm x}{}_0^0$ and $\mathcal{A}^{\rm xy}{}_0^0$, respectively. Their expressions are lengthy; by comparison with (4.153), it turns out

that they are simply the partial derivatives of the chemical potentials

$$\mathcal{B}^{\mathrm{x}0}{}_0 = \frac{\partial \mu_{\mathrm{x}}}{\partial n_{\mathrm{x}}}, \tag{4.157}$$

$$\mathcal{A}^{\mathrm{xy}0}{}_0 = \frac{\partial \mu_{\mathrm{x}}}{\partial n_{\mathrm{y}}} = \frac{\partial \mu_{\mathrm{y}}}{\partial n_{\mathrm{x}}}, \tag{4.158}$$

which are easier to grasp.

As for the spatial components (4.154), we see that the approach via the lengthy calculation was essential in order to see that the variation of the momentum of one species depends on the perturbed velocities of other species via the entrainment. We could not have arrived at the concise expression (4.154) without the comprehensive calculation.

4.5 The Equations Governing Perturbations of a Multi-Fluid

We have everything we need to plug into the equations of motion (4.40). In a similar fashion to previous studies [19, 35], we define variables, X_{x}, which are related to the Lagrangian pressure variation, one for each species,

$$\begin{aligned} X_{\mathrm{n}} = {} & \frac{1}{2}\mu_{\mathrm{n}} n_{\mathrm{n}} e^{\nu/2} H_0 + \omega^2 e^{-\nu/2} n_{\mathrm{n}} \left(\mathcal{B}^{\mathrm{n}} n_{\mathrm{n}} V_{\mathrm{n}} + \mathcal{A}^{\mathrm{np}} n_{\mathrm{p}} V_{\mathrm{p}}\right) \\ & - e^{(\nu-\lambda)/2} \frac{n_{\mathrm{n}}'}{r} \left(\mathcal{B}^{\mathrm{n}0}{}_0 n_{\mathrm{n}} W_{\mathrm{n}} + \mathcal{A}^{\mathrm{np}0}{}_0 n_{\mathrm{p}} W_{\mathrm{p}}\right), \end{aligned} \tag{4.159a}$$

$$\begin{aligned} X_{\mathrm{p}} = {} & \frac{1}{2}\mu_{\mathrm{p}} n_{\mathrm{p}} e^{\nu/2} H_0 + \omega^2 e^{-\nu/2} n_{\mathrm{p}} \left(\mathcal{B}^{\mathrm{p}} n_{\mathrm{p}} V_{\mathrm{p}} + \mathcal{A}^{\mathrm{np}} n_{\mathrm{n}} V_{\mathrm{n}}\right) \\ & - e^{(\nu-\lambda)/2} \frac{n_{\mathrm{p}}'}{r} \left(\mathcal{B}^{\mathrm{p}0}{}_0 n_{\mathrm{p}} W_{\mathrm{p}} + \mathcal{A}^{\mathrm{np}0}{}_0 n_{\mathrm{n}} W_{\mathrm{n}}\right), \end{aligned} \tag{4.159b}$$

$$\begin{aligned} X_{\mathrm{e}} = {} & \frac{1}{2}\mu_{\mathrm{e}} n_{\mathrm{e}} e^{\nu/2} H_0 + \omega^2 e^{-\nu/2} n_{\mathrm{e}} \left(\mathcal{B}^{\mathrm{e}} n_{\mathrm{e}} V_{\mathrm{e}}\right) \\ & - e^{(\nu-\lambda)/2} \frac{n_{\mathrm{e}}'}{r} \left(\mathcal{B}^{\mathrm{e}0}{}_0 n_{\mathrm{e}} W_{\mathrm{e}}\right), \end{aligned} \tag{4.159c}$$

$$\begin{aligned} X_{\mu} = {} & \frac{1}{2}\mu_{\mu} n_{\mu} e^{\nu/2} H_0 + \omega^2 e^{-\nu/2} n_{\mu} \left(\mathcal{B}^{\mu} n_{\mu} V_{\mu}\right) \\ & - e^{(\nu-\lambda)/2} \frac{n_{\mu}'}{r} \left(\mathcal{B}^{\mu 0}{}_0 n_{\mu} W_{\mu}\right). \end{aligned} \tag{4.159d}$$

Note that we have left the electron and muon displacements explicitly in these definitions for the sake of generality. However, in the following, we will immediately apply $W_{\mathrm{p}} = W_{\mathrm{e}} = W_{\mu}$ and $V_{\mathrm{p}} = V_{\mathrm{e}} = V_{\mu}$ for simplicity. As an abbreviation, we also define

$$\mathcal{E}^0_0 = -n_{\mathrm{p}}^2 \mathcal{A}^{\mathrm{np}0}{}_0{}^2 + n_{\mathrm{p}}^2 \mathcal{B}^{p0}{}_0 \mathcal{B}^{\mathrm{n}0}{}_0 + n_{\mathrm{e}}^2 \mathcal{B}^{e0}{}_0 \mathcal{B}^{\mathrm{n}0}{}_0 + n_{\mu}^2 \mathcal{B}^{\mu 0}{}_0 \mathcal{B}^{\mathrm{n}0}{}_0. \tag{4.160}$$

By inspection of the equations, it turns out that the combination

$$X_{\mathrm{P}} := \sum_{\mathrm{x}\in P} X_{\mathrm{x}} = X_{\mathrm{p}} + X_{\mathrm{e}} + X_{\mu} \qquad \text{for} \quad \mathrm{npe}\mu\text{-matter} \tag{4.161}$$

or

$$X_{\mathrm{P}} := \sum_{\mathrm{x}\in P} X_{\mathrm{x}} = X_{\mathrm{p}} + X_{\mathrm{e}} \qquad \text{for} \quad \mathrm{npe\text{-}matter}, \tag{4.162}$$

serves as a useful perturbation variable. The reason for this is that we consider electrons and muons electromagnetically locked to the protons; from a physical point of view it is intuitively clear that the variation of the partial pressure of the whole proton fluid (described by the new variable X_{P}) plays a more important role than the variations of the partial pressures of the individual species. We intentionally use the capitalised index P opposed to the similar looking lower case p which we use for protons only, as it reflects the fact that this quantity is assigned to the "proton fluid" which also includes the electrons and (perhaps) muons. The final perturbation equations then are

$$H_1' = \left[\frac{1}{2}\left(\lambda' - \nu'\right) - \frac{l+1}{r}\right] H_1 + \frac{e^{\lambda}}{r}\left[H_0 + K - 16\pi(\mu_{\mathrm{n}} n_{\mathrm{n}} V_{\mathrm{n}} + \mu_{\mathrm{n}} n_{\mathrm{p}} V_{\mathrm{p}})\right], \tag{4.163a}$$

$$K' = \frac{1}{r}H_0 + \frac{n+1}{r}H_1 + \left[\frac{1}{2}\nu' - \frac{l+1}{r}\right] K - \frac{8\pi e^{\lambda/2}}{r}\left[\mu_{\mathrm{n}} n_{\mathrm{n}} W_{\mathrm{n}} + \mu_{\mathrm{n}} n_{\mathrm{p}} W_{\mathrm{p}}\right], \tag{4.163b}$$

$$\begin{aligned} W_{\mathrm{n}}' = {} & e^{\lambda/2}\left[\frac{r}{2}H_0 + rK - \frac{l(l+1)}{r}V_{\mathrm{n}}\right] - \frac{l+1}{r}W_{\mathrm{n}} \\ & + \frac{n_{\mathrm{p}}}{n_{\mathrm{n}}}\frac{\mathcal{A}^{\mathrm{np}0}_{\ 0}}{\mathcal{E}^0_0}\left[\frac{n_{\mathrm{n}}'}{n_{\mathrm{n}}} - \frac{n_{\mathrm{p}}'}{n_{\mathrm{p}}}\right]\left[\mathcal{B}^{\mathrm{p}0}_{\ 0} n_{\mathrm{p}}^2 W_{\mathrm{p}} + \mathcal{A}^{\mathrm{np}0}_{\ 0} n_{\mathrm{n}} n_{\mathrm{p}} W_{\mathrm{n}} + \mathcal{B}^{\mathrm{e}0}_{\ 0} n_{\mathrm{e}}^2 W_{\mathrm{p}} + \mathcal{B}^{\mu 0}_{\ 0} n_{\mu}^2 W_{\mathrm{p}}\right] \\ & + \frac{\mathcal{B}^{\mathrm{p}0}_{\ 0} n_{\mathrm{p}}^2 + \mathcal{B}^{\mathrm{e}0}_{\ 0} n_{\mathrm{e}}^2 + \mathcal{B}^{\mu 0}_{\ 0} n_{\mu}^2}{n_{\mathrm{n}}^2 \mathcal{E}^0_0} e^{(\lambda-\nu)/2} r X_{\mathrm{n}} - \frac{n_{\mathrm{p}}}{n_{\mathrm{n}}}\frac{\mathcal{A}^{\mathrm{np}0}_{\ 0}}{\mathcal{E}^0_0} e^{(\lambda-\nu)/2} r X_{\mathrm{P}}, \end{aligned} \tag{4.163c}$$

$$\begin{aligned} W_{\mathrm{p}}' = {} & e^{\lambda/2}\left[\frac{r}{2}H_0 + rK - \frac{l(l+1)}{r}V_{\mathrm{p}}\right] - \frac{l+1}{r}W_{\mathrm{p}} \\ & + \frac{\mathcal{A}^{\mathrm{np}0}_{\ 0}}{\mathcal{E}^0_0}\left[\frac{n_{\mathrm{p}}'}{n_{\mathrm{p}}} - \frac{n_{\mathrm{n}}'}{n_{\mathrm{n}}}\right]\left[\mathcal{B}^{\mathrm{n}0}_{\ 0} n_{\mathrm{n}} n_{\mathrm{p}} W_{\mathrm{n}} + \mathcal{A}^{\mathrm{np}0}_{\ 0} n_{\mathrm{p}}^2 W_{\mathrm{p}}\right] \\ & + \frac{\mathcal{B}^{\mathrm{n}0}_{\ 0}}{\mathcal{E}^0_0} e^{(\lambda-\nu)/2} r X_{\mathrm{P}} - \frac{n_{\mathrm{p}}}{n_{\mathrm{n}}}\frac{\mathcal{A}^{\mathrm{np}0}_{\ 0}}{\mathcal{E}^0_0} e^{(\lambda-\nu)/2} r X_{\mathrm{n}}, \end{aligned} \tag{4.163d}$$

$$\begin{aligned} X_{\mathrm{n}}' = {} & -\frac{l}{r}X_{\mathrm{n}} + \frac{1}{2}e^{\nu/2}\left[\mu_{\mathrm{n}} n_{\mathrm{n}}\left(\frac{1}{r} - \nu'\right) - \mu_{\mathrm{n}}' n_{\mathrm{n}} + \mathcal{A}^{\mathrm{np}0}_{\ 0}\left(n_{\mathrm{p}}' n_{\mathrm{n}} - n_{\mathrm{n}}' n_{\mathrm{p}}\right)\right] H_0 \\ & + \mu_{\mathrm{n}} n_{\mathrm{n}}\left[\frac{1}{2}e^{\nu/2}\frac{n+1}{r} + \frac{1}{2}\omega^2 r e^{-\nu/2}\right] H_1 \\ & + e^{\nu/2}\left[\mu_{\mathrm{n}} n_{\mathrm{n}}\left(\frac{\nu'}{4} - \frac{1}{2r}\right) - \mu_{\mathrm{n}}' n_{\mathrm{n}} + \mathcal{A}^{\mathrm{np}0}_{\ 0}\left(n_{\mathrm{p}}' n_{\mathrm{n}} - n_{\mathrm{n}}' n_{\mathrm{p}}\right)\right] K \\ & + \frac{l(l+1)}{r^2}e^{\nu/2}\left(\mu_{\mathrm{n}}' n_{\mathrm{n}} V_{\mathrm{n}} - n_{\mathrm{p}}' \mathcal{A}^{\mathrm{np}0}_{\ 0} n_{\mathrm{n}} V_{\mathrm{n}} + n_{\mathrm{n}}' \mathcal{A}^{\mathrm{np}0}_{\ 0} n_{\mathrm{p}} V_{\mathrm{p}}\right) \end{aligned}$$

$$
\begin{aligned}
&- e^{\frac{\lambda-\nu}{2}}\frac{\omega^2}{r}\left(\mu_{\mathrm{n}}n_{\mathrm{n}}W_{\mathrm{n}} - \mathcal{A}^{\mathrm{np}}n_{\mathrm{n}}n_{\mathrm{p}}W_{\mathrm{n}} + \mathcal{A}^{\mathrm{np}}n_{\mathrm{n}}n_{\mathrm{p}}W_{\mathrm{p}}\right)\\
&- 4\pi e^{\frac{\lambda+\nu}{2}}\frac{\mu_{\mathrm{n}}n_{\mathrm{n}}}{r}\left(\mu_{\mathrm{n}}n_{\mathrm{n}}W_{\mathrm{n}} + \mu_{\mathrm{n}}n_{\mathrm{p}}W_{\mathrm{p}}\right)\\
&+ e^{\frac{\nu-\lambda}{2}}\frac{1}{r}\left[\left((n_{\mathrm{p}}'\mathcal{A}^{\mathrm{np}0}{}_0)'n_{\mathrm{n}}W_{\mathrm{n}} - (n_{\mathrm{n}}'\mathcal{A}^{\mathrm{np}0}{}_0)'n_{\mathrm{p}}W_{\mathrm{p}}\right) - \mu_{\mathrm{n}}''n_{\mathrm{n}}W_{\mathrm{n}}\right.\\
&\qquad\left. + \left(\frac{2}{r} + \frac{\lambda'-\nu'}{2}\right)\left(\mu_{\mathrm{n}}'n_{\mathrm{n}}W_{\mathrm{n}} - n_{\mathrm{p}}'\mathcal{A}^{\mathrm{np}0}{}_0n_{\mathrm{n}}W_{\mathrm{n}} + n_{\mathrm{n}}'\mathcal{A}^{\mathrm{np}0}{}_0n_{\mathrm{p}}W_{\mathrm{p}}\right)\right],
\end{aligned}
\tag{4.163e}
$$

$$
\begin{aligned}
X_{\mathrm{P}}' = &-\frac{l}{r}X_{\mathrm{P}} + \frac{1}{2}e^{\nu/2}\left[\mu_{\mathrm{n}}n_{\mathrm{p}}\left(\frac{1}{r} - \nu'\right) - \mu_{\mathrm{n}}'n_{\mathrm{p}} - \mathcal{A}^{\mathrm{np}0}{}_0\left(n_{\mathrm{p}}'n_{\mathrm{n}} - n_{\mathrm{n}}'n_{\mathrm{p}}\right)\right]H_0\\
&+ \mu_{\mathrm{n}}n_{\mathrm{p}}\left[\frac{1}{2}e^{\nu/2}\frac{n+1}{r} + \frac{1}{2}\omega^2 re^{-\nu/2}\right]H_1\\
&+ e^{\nu/2}\left[\mu_{\mathrm{n}}n_{\mathrm{p}}\left(\frac{\nu'}{4} - \frac{1}{2r}\right) - \mu_{\mathrm{n}}'n_{\mathrm{p}} - \mathcal{A}^{\mathrm{np}0}{}_0\left(n_{\mathrm{p}}'n_{\mathrm{n}} - n_{\mathrm{n}}'n_{\mathrm{p}}\right)\right]K\\
&+ \frac{l(l+1)}{r^2}e^{\nu/2}\left(n_{\mathrm{p}}'\mathcal{A}^{\mathrm{np}0}{}_0n_{\mathrm{n}}V_{\mathrm{n}} - n_{\mathrm{n}}'\mathcal{A}^{\mathrm{np}0}{}_0n_{\mathrm{p}}V_{\mathrm{p}} + \mu_{\mathrm{n}}'n_{\mathrm{p}}V_{\mathrm{p}}\right)\\
&- e^{\frac{\lambda-\nu}{2}}\frac{\omega^2}{r}\left(\mathcal{A}^{\mathrm{np}}n_{\mathrm{n}}n_{\mathrm{p}}W_{\mathrm{n}} - \mathcal{A}^{\mathrm{np}}n_{\mathrm{n}}n_{\mathrm{p}}W_{\mathrm{p}} + \mu_{\mathrm{n}}n_{\mathrm{p}}W_{\mathrm{p}}\right)\\
&- 4\pi e^{\frac{\lambda+\nu}{2}}\frac{\mu_{\mathrm{n}}n_{\mathrm{p}}}{r}\left(\mu_{\mathrm{n}}n_{\mathrm{n}}W_{\mathrm{n}} + \mu_{\mathrm{n}}n_{\mathrm{p}}W_{\mathrm{p}}\right)\\
&+ e^{\frac{\nu-\lambda}{2}}\frac{1}{r}\left[\left(-(n_{\mathrm{p}}'\mathcal{A}^{\mathrm{np}0}{}_0)'n_{\mathrm{n}}W_{\mathrm{n}} + (n_{\mathrm{n}}'\mathcal{A}^{\mathrm{np}0}{}_0)'n_{\mathrm{p}}W_{\mathrm{p}}\right) - \mu_{\mathrm{n}}''n_{\mathrm{p}}W_{\mathrm{p}}\right.\\
&\qquad\left. + \left(\frac{2}{r} + \frac{\lambda'-\nu'}{2}\right)\left(n_{\mathrm{p}}'\mathcal{A}^{\mathrm{np}0}{}_0n_{\mathrm{n}}W_{\mathrm{n}} - n_{\mathrm{n}}'\mathcal{A}^{\mathrm{np}0}{}_0n_{\mathrm{p}}W_{\mathrm{p}} + \mu_{\mathrm{n}}'n_{\mathrm{p}}W_{\mathrm{p}}\right)\right].
\end{aligned}
\tag{4.163f}
$$

These six differential equations are complemented by three algebraic equations

$$
\begin{aligned}
X_{\mathrm{n}} = &\frac{1}{2}\mu_{\mathrm{n}}n_{\mathrm{n}}e^{\nu/2}H_0 + \omega^2 e^{-\nu/2}n_{\mathrm{n}}\left(\mathcal{B}_{\mathrm{n}}n_{\mathrm{n}}V_{\mathrm{n}} + A_{\mathrm{np}}n_{\mathrm{p}}V_{\mathrm{p}}\right)\\
&- e^{\frac{\nu-\lambda}{2}}\frac{n_{\mathrm{n}}'}{r}(\mathcal{B}^{\mathrm{n}0}{}_0n_{\mathrm{n}}W_{\mathrm{n}} + \mathcal{A}^{\mathrm{np}0}{}_0n_{\mathrm{p}}W_{\mathrm{p}}),
\end{aligned}
\tag{4.164a}
$$

$$
\begin{aligned}
X_{\mathrm{P}} = &\frac{1}{2}\mu_{\mathrm{n}}n_{\mathrm{p}}e^{\nu/2}H_0 + \omega^2 e^{-\nu/2}\left(A_{\mathrm{np}}n_{\mathrm{n}}n_{\mathrm{p}}V_{\mathrm{n}} - A_{\mathrm{np}}n_{\mathrm{n}}n_{\mathrm{p}}V_{\mathrm{p}} + \mu_{\mathrm{n}}n_{\mathrm{p}}V_{\mathrm{p}}\right)\\
&- e^{\frac{\nu-\lambda}{2}}\left(\frac{n_{\mathrm{p}}'}{r}\mathcal{A}^{\mathrm{np}0}{}_0n_{\mathrm{n}}W_{\mathrm{n}} - \frac{n_{\mathrm{n}}'}{r}\mathcal{A}^{\mathrm{np}0}{}_0n_{\mathrm{p}}W_{\mathrm{p}} + \frac{\mu_{\mathrm{n}}'}{r}n_{\mathrm{p}}W_{\mathrm{p}}\right),
\end{aligned}
\tag{4.164b}
$$

$$
\begin{aligned}
\left[\frac{1}{2}e^{-\lambda}r(r\nu'-2) + (n+1)r\right]H_0 = &\, e^{-\lambda}r^2\left[\omega^2 re^{-\nu} - \frac{n+1}{2}\nu'\right]H_1\\
&+ \left[nr - \omega^2 r^3 e^{-\nu} - \frac{1}{4}r^2e^{-\lambda}\nu'(r\nu'-2)\right]K + 8\pi r^3 e^{-\nu/2}(X_{\mathrm{n}} + X_{\mathrm{P}}).
\end{aligned}
\tag{4.164c}
$$

The origin of these equations are (for brevity, we denote the components of the Einstein equations with $[\mu\nu]$ as a shortcut for $G_{\mu\nu} = 8\pi T_{\mu\nu}$): Equations (4.163a) and (4.163b)

are $[t\theta]$ and $[tr]$, respectively; (4.163c) and (4.163d) are $f^{\mathrm{n}}_{\theta} = 0$ and $\sum_{\mathrm{x}\in P} f^{\mathrm{x}}_{\theta} = 0$; (4.163e) and (4.163f) are $f^{\mathrm{n}}_{r} = 0$ and $\sum_{\mathrm{x}\in P} f^{\mathrm{x}}_{r} = 0$; (4.164a) and (4.164b) are due to the definitions of X_{n} and X_{P}; (4.164c) is $[rr]$.

Throughout these equations, we have already applied the simple identity $H_2 = H_0$ which holds in the fluid case. The last equation (4.164c) can be used to calculate H_0 from the other quantities, while the first two algebraic equations (4.164a) and (4.164b), can be simultaneously inverted to find V_{n} and V_{p}.

We also make extensive use of the relations (4.53) for β-equilibrium, which allows us to remove, to the greatest possible extent, quantities which are directly associated with the muons and also the ones associated with the electrons. This shortens several equations drastically. We also chose to use the relations for the chemical potentials and their radial derivatives in order to replace, firstly, the coefficients $\mathcal{B}^{\mathrm{x}}$ by μ_{x} and $\mathcal{A}^{\mathrm{xy}}$ and, secondly, the coefficients $\mathcal{B}^{\mathrm{x}}{}_{0}^{0}$ by μ'_{x} and $\mathcal{A}^{\mathrm{xy}}{}_{0}^{0}$.

Most of the equations are now entirely void of quantities referring to electrons or muons—the only two equations containing electron or muon quantities are the differential equations for W_{n} (explicitly) and W_{p} (only via the abbreviation $\mathcal{E}^0_0$). This makes it very easy to find the equations for npe-matter (without muons) or if we are interested in the two-constituent case with neutrons and protons only: In order to "remove" one species from the equations, we have to set the according number density to zero, $n_\mu = 0$ or $n_{\mathrm{e}} = 0$ (or both). This removes two terms (per species) in the equation for W'_{n} and it shortens the definition of $\mathcal{E}^0_0$ (if we remove both electrons and muons from our equations, it is easy to show that they are equivalent to the equations for a pure neutron-proton conglomerate presented by Comer et al. [35]). Of course, we must not forget to remove the correspondent terms from our master function as well (or equivalently, the internal static energy as given in (4.55)).

4.5.1 The Taylor Expansion at the Centre of the Star

As in the previous cases, we need the Taylor expansion of the equations (4.163) at the centre of the star $r = 0$. The entire procedure is completely identical to the one given in Section 3.2.1; we will state only the results of the calculation here.

Since the coefficients of the Taylor expansion are lengthy, we will use an overbar and an overhat to designate zeroth and second order, respectively. We have

$$\overline{q} = q_0, \qquad \hat{q} = \frac{1}{2} q_2, \qquad \overline{ab} = a_0 b_0, \qquad \widehat{ab} = \frac{1}{2}\left(a_0 b_2 + a_2 b_0\right). \tag{4.165}$$

The zeroth order constraints are

$$\begin{aligned} X_{\mathrm{n}}(0) = \frac{1}{2} e^{\nu_0/2} \overline{\mu_{\mathrm{n}} n_{\mathrm{n}}} K(0) - \left[e^{\nu_0/2} \widehat{n}_{\mathrm{n}} \overline{\mathcal{B}^{\mathrm{n}}{}_{0}^{0} n_{\mathrm{n}}} + \frac{\omega^2}{l} e^{-\nu_0/2} \overline{\mathcal{B}^{\mathrm{n}} n_{\mathrm{n}}^2} \right] W_{\mathrm{n}}(0) \\ - \left[e^{\nu_0/2} \widehat{n}_{\mathrm{n}} \overline{\mathcal{A}^{\mathrm{np}}{}_{0}^{0} n_{\mathrm{p}}} + \frac{\omega^2}{l} e^{-\nu_0/2} \overline{\mathcal{A}^{\mathrm{np}} n_{\mathrm{n}} n_{\mathrm{p}}} \right] W_{\mathrm{p}}(0), \end{aligned} \tag{4.166a}$$

$$X_{\mathrm{P}}(0) = \frac{1}{2}e^{\nu_0/2}\overline{\mu_{\mathrm{n}} n_{\mathrm{p}}}K(0) - \left[e^{\nu_0/2}\widehat{n}_{\mathrm{p}}\overline{\mathcal{A}^{\mathrm{np}}{}_0^0 n_{\mathrm{n}}} + \frac{\omega^2}{l}e^{-\nu_0/2}\overline{\mathcal{A}^{\mathrm{np}} n_{\mathrm{n}} n_{\mathrm{p}}}\right] W_{\mathrm{n}}(0)$$
$$- \left[e^{\nu_0/2} n_0^{\mathrm{p}}\left(\widehat{\mu}_{\mathrm{n}} - \overline{\mathcal{A}^{\mathrm{np}}{}_0^0}\widehat{n}_{\mathrm{n}}\right) + \frac{\omega^2}{l}e^{-\nu_0/2} n_0^{\mathrm{p}}\left(\overline{\mu_{\mathrm{n}}} - \overline{\mathcal{A}^{\mathrm{np}} n_{\mathrm{n}}}\right)\right] W_{\mathrm{p}}(0), \quad (4.166b)$$

$$H_1(0) = \frac{lK(0) + 8\pi(\overline{\mu_{\mathrm{n}} n_{\mathrm{n}}}W_{\mathrm{n}}(0) + \overline{\mu_{\mathrm{n}} n_{\mathrm{p}}}W_{\mathrm{p}}(0))}{n+1}, \quad (4.166c)$$

as well as the simpler equalities

$$H_0(0) = K(0), \qquad V_{\mathrm{n}}(0) = -\frac{W_{\mathrm{n}}(0)}{l}, \qquad V_{\mathrm{p}}(0) = -\frac{W_{\mathrm{p}}(0)}{l}. \quad (4.167)$$

This completes the zeroth order. Similar to the single fluid case, the specification of the three perturbations $K(0)$, $W_{\mathrm{n}}(0)$ and $W_{\mathrm{p}}(0)$ is sufficient to determine the remaining perturbation quantities at the origin.

For the computation of the second order coefficients of the perturbation variables, we also need the Taylor coefficients of the background variables. The background equations imply

$$\lambda_2 = -\frac{16\pi}{3}\Lambda_0, \quad (4.168a)$$
$$\nu_2 = \frac{8\pi}{3}(3\Psi_0 - \Lambda_0), \quad (4.168b)$$
$$n_2^{\mathrm{n}} = \frac{1}{2\mathcal{D}}\nu_2\mu_0^{\mathrm{n}}\left(\mathcal{A}^{\mathrm{np}}{}_0^0\mathcal{B}^{\mathrm{e}}{}_0^0 + \mathcal{A}^{\mathrm{np}}\mathcal{B}^{\mu}{}_0^0 - \mathcal{B}^{\mathrm{p}}{}_0^0\mathcal{B}^{\mathrm{e}}{}_0^0 - \mathcal{B}^{\mathrm{p}}{}_0^0\mathcal{B}^{\mu}{}_0^0 - \mathcal{B}^{\mathrm{e}}{}_0^0\mathcal{B}^{\mu}{}_0^0\right), \quad (4.168c)$$
$$n_2^{\mathrm{p}} = \frac{1}{2\mathcal{D}}\nu_2\mu_0^{\mathrm{n}}\left(\mathcal{A}^{\mathrm{np}}{}_0^0 - \mathcal{B}^{\mathrm{n}}{}_0^0\right)\left(\mathcal{B}^{\mathrm{e}}{}_0^0 + \mathcal{B}^{\mu}{}_0^0\right), \quad (4.168d)$$
$$n_2^{\mathrm{e}} = \frac{1}{2\mathcal{D}}\nu_2\mu_0^{\mathrm{n}}\left(\mathcal{A}^{\mathrm{np}} - \mathcal{B}^{\mathrm{n}}{}_0^0\right)\mathcal{B}^{\mu}{}_0^0, \quad (4.168e)$$
$$n_2^{\mu} = \frac{1}{2\mathcal{D}}\nu_2\mu_0^{\mathrm{n}}\left(\mathcal{A}^{\mathrm{np}} - \mathcal{B}^{\mathrm{n}}{}_0^0\right)\mathcal{B}^{\mathrm{e}}{}_0^0, \quad (4.168f)$$
$$\Lambda_2 = -\mu_0^{\mathrm{n}}(n_2^{\mathrm{n}} + n_2^{\mathrm{p}}), \quad (4.168g)$$
$$\Psi_2 = -\frac{1}{2}\mu_0^{\mathrm{n}}(n_0^{\mathrm{n}} + n_0^{\mathrm{p}})\nu_2, \quad (4.168h)$$
$$\mu_2^{\mathrm{n}} = -\frac{1}{2}\mu_0^{\mathrm{n}}\nu_2, \quad (4.168i)$$
$$\lambda_4 = -\frac{16\pi}{5}\Lambda_2 + \frac{1}{2}\lambda_2^2, \quad (4.168j)$$
$$\nu_4 = \frac{1}{4}\lambda_4 + \frac{1}{8}\nu_2(\lambda_2 - \nu_2) + 2\pi(\Psi_0\lambda_2 + \Psi_2), \quad (4.168k)$$
$$\mu_4^{\mathrm{n}} = -\frac{1}{2}\nu_4\mu_0^{\mathrm{n}} - \frac{1}{4}\nu_2\mu_2^{\mathrm{n}}, \quad (4.168l)$$
$$n_4^{\mathrm{n}} = \frac{n_2^{\mathrm{n}}}{\mathcal{D}}\left(\widehat{\mathcal{A}^{\mathrm{np}}{}_0^0{}^2\mathcal{B}^{\mathrm{e}}{}_0^0} + \widehat{\mathcal{A}^{\mathrm{np}}{}_0^0{}^2\mathcal{B}^{\mu}{}_0^0} - \mathcal{B}^{\mathrm{n}}{}_0^0\widehat{\mathcal{B}^{\mathrm{p}}{}_0^0\mathcal{B}^{\mathrm{e}}{}_0^0} - \mathcal{B}^{\mathrm{n}}{}_0^0\widehat{\mathcal{B}^{\mathrm{p}}{}_0^0\mathcal{B}^{\mu}{}_0^0} - \mathcal{B}^{\mathrm{n}}{}_0^0\widehat{\mathcal{B}^{\mathrm{e}}{}_0^0\mathcal{B}^{\mu}{}_0^0}\right)$$
$$- \frac{\mu_2^{\mathrm{n}}}{\mathcal{D}}\left(\widehat{\mathcal{A}^{\mathrm{np}}{}_0^0\mathcal{B}^{\mathrm{e}}{}_0^0} + \widehat{\mathcal{A}^{\mathrm{np}}{}_0^0\mathcal{B}^{\mu}{}_0^0} - \widehat{\mathcal{B}^{\mathrm{p}}{}_0^0\mathcal{B}^{\mathrm{e}}{}_0^0} - \widehat{\mathcal{B}^{\mathrm{p}}{}_0^0\mathcal{B}^{\mu}{}_0^0} - \widehat{\mathcal{B}^{\mathrm{e}}{}_0^0\mathcal{B}^{\mu}{}_0^0}\right) - \frac{2\mu_4^{\mathrm{n}} n_2^{\mathrm{n}}}{\nu_2\mu_0^{\mathrm{n}}}, \quad (4.168m)$$
$$n_4^{\mathrm{p}} = \frac{n_2^{\mathrm{p}}}{\mathcal{D}}\left(\widehat{\mathcal{A}^{\mathrm{np}}{}_0^0{}^2\mathcal{B}^{\mathrm{e}}{}_0^0} + \widehat{\mathcal{A}^{\mathrm{np}}{}_0^0{}^2\mathcal{B}^{\mu}{}_0^0} - \mathcal{B}^{\mathrm{n}}{}_0^0\widehat{\mathcal{B}^{\mathrm{p}}{}_0^0\mathcal{B}^{\mathrm{e}}{}_0^0} - \mathcal{B}^{\mathrm{n}}{}_0^0\widehat{\mathcal{B}^{\mathrm{p}}{}_0^0\mathcal{B}^{\mu}{}_0^0} - \mathcal{B}^{\mathrm{n}}{}_0^0\widehat{\mathcal{B}^{\mathrm{e}}{}_0^0\mathcal{B}^{\mu}{}_0^0}\right)$$

$$- \frac{\mu_2^{\rm n}}{\mathcal{D}} \left(\widehat{\mathcal{A}^{\rm np}{}_0^0 \mathcal{B}^{\rm e}{}_0^0} + \widehat{\mathcal{A}^{\rm np}{}_0^0 \mathcal{B}^{\mu}{}_0^0} - \widehat{\mathcal{B}^{\rm n}{}_0^0 \mathcal{B}^{\rm e}{}_0^0} - \widehat{\mathcal{B}^{\rm n}{}_0^0 \mathcal{B}^{\mu}{}_0^0} \right) - \frac{2\mu_4^{\rm n} n_2^{\rm p}}{\nu_2 \mu_0^{\rm n}}, \tag{4.168n}$$

where $\mathcal{D}$ is given by the determinant

$$\mathcal{D} = \begin{vmatrix} \mathcal{B}^{\rm n}{}_0^0 & \mathcal{A}^{\rm np}{}_0^0 & 0 & 0 \\ \mathcal{A}^{\rm np}{}_0^0 & \mathcal{B}^{\rm p}{}_0^0 & \mathcal{B}^{\rm e}{}_0^0 & 0 \\ \mathcal{A}^{\rm np}{}_0^0 & \mathcal{B}^{\rm p}{}_0^0 & 0 & \mathcal{B}^{\mu}{}_0^0 \\ 0 & 1 & -1 & -1 \end{vmatrix}. \tag{4.169}$$

It proves useful to define the three auxiliary variables Q_0, $Q_{\rm n}$ and $Q_{\rm p}$ so that

$$H_0''(0) = K''(0) + Q_0, \tag{4.170}$$

$$V_{\rm n}''(0) = Q_{\rm n} - \frac{l+3}{l(l+1)} W_{\rm n}''(0), \tag{4.171}$$

$$V_{\rm p}''(0) = Q_{\rm p} - \frac{l+3}{l(l+1)} W_{\rm p}''(0). \tag{4.172}$$

These three variables are then given by

$$\begin{aligned} Q_0 = \frac{2}{n} \Bigg[& \left(\omega^2 e^{-\nu_0} - \frac{n+1}{2} \nu_2 \right) H_1(0) - \left(\frac{1}{2}\lambda_2 + \omega^2 e^{-\nu_0} \right) K(0) \\ & + 8\pi e^{-\nu_0/2} \left(X_{\rm n}(0) + X_{\rm P}(0) \right) \Bigg], \end{aligned} \tag{4.173a}$$

$$\begin{aligned} Q_{\rm n} = \frac{1}{n+1} \Bigg[& \frac{3}{2} K_0 + \left(\frac{l+1}{4}\lambda_2 - (n_0^{\rm n} n_2^{\rm p} - n_2^{\rm n} n_0^{\rm p}) \overline{\left(\frac{n_{\rm p}}{n_{\rm n}} \frac{\mathcal{A}^{\rm np}{}_0^{0\,2}}{\mathcal{E}_0^0} \right)} \right) W_{\rm n}(0) \\ & - (n_0^{\rm n} n_2^{\rm p} - n_2^{\rm n} n_0^{\rm p}) \overline{\left(\frac{\mathcal{A}^{\rm np}{}_0^0 (n_{\rm p}^2 \mathcal{B}^{\rm p}{}_0^0 + n_{\rm e}^2 \mathcal{B}^{\rm e}{}_0^0 + n_\mu^2 \mathcal{B}^{\mu}{}_0^0)}{n_{\rm n}^2 \mathcal{E}_0^0} \right)} W_{\rm p}(0) \\ & + e^{-\nu_0/2} \overline{\left(\frac{n_{\rm p}^2 \mathcal{B}^{\rm p}{}_0^0 + n_{\rm e}^2 \mathcal{B}^{\rm e}{}_0^0 + n_\mu^2 \mathcal{B}^{\mu}{}_0^0}{n_{\rm n}^2 \mathcal{E}_0^0} \right)} X_{\rm n}(0) - e^{-\nu_0/2} \overline{\left(\frac{n_{\rm p}}{n_{\rm n}} \frac{\mathcal{A}^{\rm np}{}_0^0}{\mathcal{E}_0^0} \right)} X_{\rm P}(0) \Bigg], \end{aligned} \tag{4.173b}$$

$$\begin{aligned} Q_{\rm p} = \frac{1}{n+1} \Bigg[& \frac{3}{2} K_0 + (n_0^{\rm n} n_2^{\rm p} - n_2^{\rm n} n_0^{\rm p}) \overline{\left(\frac{\mathcal{A}^{\rm np}{}_0^0 \mathcal{B}^{\rm n}{}_0^0}{\mathcal{E}_0^0} \right)} W_{\rm n}(0) \\ & + \left(\frac{l+1}{4}\lambda_2 + (n_0^{\rm n} n_2^{\rm p} - n_2^{\rm n} n_0^{\rm p}) \overline{\left(\frac{n_{\rm p}}{n_{\rm n}} \frac{\mathcal{A}^{\rm np}{}_0^{0\,2}}{\mathcal{E}_0^0} \right)} \right) W_{\rm p}(0) \\ & - e^{-\nu_0/2} \overline{\left(\frac{n_{\rm p}}{n_{\rm n}} \frac{\mathcal{A}^{\rm np}{}_0^0}{\mathcal{E}_0^0} \right)} X_{\rm n}(0) + e^{-\nu_0/2} \overline{\left(\frac{\mathcal{B}^{\rm n}{}_0^0}{\mathcal{E}_0^0} \right)} X_{\rm P}(0) \Bigg]. \end{aligned} \tag{4.173c}$$

The second order coefficients can then be obtained by solving the following linear

system:

$$
\begin{aligned}
&-\frac{1}{2}\overline{\mu_{\rm n} n_{\rm n}}K''(0)+\left(\overline{\mathcal{B}^{\rm n}{}^{0}_{0} n_{\rm n}}n_2^{\rm n}+e^{-\nu_0}\overline{\mathcal{B}^{\rm n} n_{\rm n}^2}\frac{\omega^2(l+3)}{l(l+1)}\right)W_{\rm n}''(0)+\left(\overline{\mathcal{A}^{\rm np}{}^{0}_{0} n_{\rm p}}n_2^{\rm n}\right.\\
&\qquad\left.+e^{-\nu_0}\overline{\mathcal{A}^{\rm np} n_{\rm n} n_{\rm p}}\frac{\omega^2(l+3)}{l(l+1)}\right)W_{\rm p}''(0)+e^{-\nu_0/2}X_{\rm n}''(0)\\
&\quad=\widehat{\mu_{\rm n} n_{\rm n}}K(0)-\left[2n_2^{\rm n}\widehat{\mathcal{B}^{\rm n}{}^{0}_{0} n_{\rm n}}+\overline{\mathcal{B}^{\rm n}{}^{0}_{0} n_{\rm n}}\left(2n_4^{\rm n}-\frac{1}{2}\lambda_2 n_2^{\rm n}\right)\right.\\
&\qquad\left.+\frac{\omega^2}{le^{\nu_0}}\left(2\widehat{\mathcal{B}^{\rm n} n_{\rm n}^2}-\nu_2\overline{\mathcal{B}^{\rm n} n_{\rm n}^2}\right)\right]W_{\rm n}(0)-\left[2n_2^{\rm n}\widehat{\mathcal{A}^{\rm np}{}^{0}_{0} n_{\rm p}}+\overline{\mathcal{A}^{\rm np}{}^{0}_{0} n_{\rm p}}\left(2n_4^{\rm n}-\frac{1}{2}\lambda_2 n_2^{\rm n}\right)\right.\\
&\qquad\left.+\frac{\omega^2}{le^{\nu_0}}\left(2\widehat{\mathcal{A}^{\rm np} n_{\rm n} n_{\rm p}}-\nu_2\overline{\mathcal{A}^{\rm np} n_{\rm n} n_{\rm p}}\right)\right]W_{\rm p}(0)+\frac{1}{2}e^{-\nu_0/2}\nu_2 X_{\rm n}(0)+\frac{1}{2}\overline{\mu_{\rm n} n_{\rm n}}Q_0\\
&\qquad+e^{-\nu_0}\omega^2\overline{\mathcal{B}^{\rm n} n_{\rm n}^2}Q_{\rm n}+e^{-\nu_0}\omega^2\overline{\mathcal{A}^{\rm np} n_{\rm n} n_{\rm p}}Q_{\rm p},
\end{aligned}
\tag{4.174a}
$$

$$
\begin{aligned}
&-\frac{1}{2}\overline{\mu_{\rm n} n_{\rm p}}K''(0)+\left(\overline{\mathcal{A}^{\rm np}{}^{0}_{0} n_{\rm n}}n_2^{\rm p}+e^{-\nu_0}\overline{\mathcal{A}^{\rm np} n_{\rm n} n_{\rm p}}\frac{\omega^2(l+3)}{l(l+1)}\right)W_{\rm n}''(0)+\left(\mu_2^{\rm n}n_0^{\rm p}-\overline{\mathcal{A}^{\rm np}{}^{0}_{0} n_{\rm p}}n_2^{\rm n}\right.\\
&\qquad\left.+e^{-\nu_0}\overline{(\mu_{\rm n}-\mathcal{A}^{\rm np} n_{\rm n})n_{\rm p}}\frac{\omega^2(l+3)}{l(l+1)}\right)W_{\rm p}''(0)+e^{-\nu_0/2}X_{\rm P}''(0)\\
&\quad=\widehat{\mu_{\rm n} n_{\rm p}}K(0)-\left[2n_2^{\rm p}\widehat{\mathcal{A}^{\rm np}{}^{0}_{0} n_{\rm n}}+\overline{\mathcal{A}^{\rm np}{}^{0}_{0} n_{\rm n}}\left(2n_4^{\rm p}-\frac{1}{2}\lambda_2 n_2^{\rm p}\right)\right.\\
&\qquad\left.+\frac{\omega^2}{le^{\nu_0}}\left(2\widehat{\mathcal{A}^{\rm np} n_{\rm n} n_{\rm p}}-\nu_2\overline{\mathcal{A}^{\rm np} n_{\rm n} n_{\rm p}}\right)\right]W_{\rm n}(0)-\left[2n_2^{\rm n}\widehat{\mathcal{A}^{\rm np}{}^{0}_{0} n_{\rm p}}-2\mu_4^{\rm n}n_0^{\rm p}-\mu_2^{\rm n}n_2^{\rm p}\right.\\
&\qquad+\frac{\omega^2}{le^{\nu_0}}\left(2\left(\widehat{\mathcal{A}^{\rm np} n_{\rm n} n_{\rm p}}-\widehat{\mu_{\rm n} n_{\rm p}}\right)-\nu_2\left(\overline{\mathcal{A}^{\rm np} n_{\rm n} n_{\rm p}}-\overline{\mu_{\rm n} n_{\rm p}}\right)\right)+\frac{1}{2}\lambda_2\mu_2^{\rm n}n_0^{\rm p}\\
&\qquad\left.+\overline{\mathcal{A}^{\rm np}{}^{0}_{0} n_{\rm p}}\left(2n_4^{\rm n}-\frac{1}{2}\lambda_2 n_2^{\rm n}\right)\right]W_{\rm p}(0)+\frac{1}{2}e^{-\nu_0/2}\nu_2 X_{\rm P}(0)+\frac{1}{2}\overline{\mu_{\rm n} n_{\rm p}}Q_0\\
&\qquad+e^{-\nu_0}\omega^2\overline{\mathcal{A}^{\rm np} n_{\rm n} n_{\rm p}}Q_{\rm n}+e^{-\nu_0}\omega^2\overline{(\mu_{\rm n}-\mathcal{A}^{\rm np} n_{\rm n})n_{\rm p}}Q_{\rm p},
\end{aligned}
\tag{4.174b}
$$

$$
\begin{aligned}
&-(n+1)H_1''(0)+(l+2)K''(0)+8\pi\overline{\mu_{\rm n} n_{\rm n}}W_{\rm n}''(0)+8\pi\overline{\mu_{\rm n} n_{\rm p}}W_{\rm p}''(0)\\
&\quad=\nu_2 K(0)-8\pi\left(2\widehat{\mu_{\rm n} n_{\rm n}}+\frac{1}{2}\lambda_2\overline{\mu_{\rm n} n_{\rm n}}\right)W_{\rm n}(0)-8\pi\left(2\widehat{\mu_{\rm n} n_{\rm p}}+\frac{1}{2}\lambda_2\overline{\mu_{\rm n} n_{\rm p}}\right)W_{\rm p}(0)\\
&\qquad+Q_0,
\end{aligned}
\tag{4.174c}
$$

$$
\begin{aligned}
&\frac{l+3}{2}H_1''(0)-K''(0)-4\pi\overline{\mu_{\rm n} n_{\rm n}}\frac{l+3}{n+1}W_{\rm n}''(0)-4\pi\overline{\mu_{\rm n} n_{\rm p}}\frac{l+3}{n+1}W_{\rm p}''(0)\\
&\quad=\frac{1}{2}\left((l+2)\lambda_2-\nu_2\right)H_1(0)+\frac{16\pi}{l}\widehat{\mu_{\rm n} n_{\rm n}}W_{\rm n}(0)+\frac{16\pi}{l}\widehat{\mu_{\rm n} n_{\rm p}}W_{\rm p}(0)+\frac{1}{2}Q_0\\
&\qquad-8\pi\overline{\mu_{\rm n} n_{\rm n}}Q_{\rm n}-8\pi\overline{\mu_{\rm n} n_{\rm p}}Q_{\rm p},
\end{aligned}
\tag{4.174d}
$$

$$
\begin{aligned}
&-\frac{n+1}{4}e^{\nu_0/2}\overline{\mu_{\rm n}n_{\rm n}}H_1''(0)+e^{\nu_0/2}\left(\frac{l+2}{2}n_2^{\rm n}\overline{\mathcal{B}^{\rm n}{}_0^0 n_{\rm n}}+2\pi\overline{\mu_{\rm n}n_{\rm n}}^2+\frac{\omega^2}{2}e^{-\nu_0}\overline{\mathcal{B}^{\rm n}n_{\rm n}^2}\right)W_{\rm n}''(0)\\
&\quad+e^{\nu_0/2}\left(\frac{l+2}{2}n_2^{\rm n}\overline{\mathcal{A}^{\rm np}{}_0^0 n_{\rm p}}+2\pi\overline{\mu_{\rm n}n_{\rm n}\mu_{\rm n}n_{\rm p}}+\frac{\omega^2}{2}e^{-\nu_0}\overline{\mathcal{A}^{\rm np}n_{\rm n}n_{\rm p}}\right)W_{\rm p}''(0)\\
&\quad+\frac{l+2}{2}X_{\rm n}''(0)\\
&=+\frac{\omega^2}{2}e^{-\nu_0/2}\overline{\mu_{\rm n}n_{\rm n}}H_1(0)-\frac{1}{2}e^{\nu_0/2}\left(\frac{1}{2}\nu_2\overline{\mu_{\rm n}n_{\rm n}}+3n_2^{\rm n}\left(\overline{\mathcal{B}^{\rm n}{}_0^0 n_{\rm n}}+\overline{\mathcal{A}^{\rm np}{}_0^0 n_{\rm p}}\right)\right)K(0)\\
&\quad+e^{\nu_0/2}\left[-4\pi\overline{\mu_{\rm n}n_{\rm n}}\widehat{\mu_{\rm n}n_{\rm n}}-\frac{l+2}{2}\left(\mathcal{B}^{\rm n}{}_0^0\right)_2 n_0^{\rm n}n_2^{\rm n}-\pi\lambda_2\overline{\mu_{\rm n}n_{\rm n}}^2\right.\\
&\quad+\left(\frac{1}{4}n_2^{\rm n}(\lambda_2-(l+2)\nu_2)-(l+2)n_4^{\rm n}\right)\overline{\mathcal{B}^{\rm n}{}_0^0 n_{\rm n}}\\
&\quad\left.+\omega^2e^{-\nu_0}n_0^{\rm n}\left(\frac{1}{4}(\nu_2-\lambda_2)\overline{\mathcal{B}^{\rm n}n_{\rm n}}-\widehat{\mathcal{B}^{\rm n}n_{\rm n}}\right)\right]W_{\rm n}(0)+e^{\nu_0/2}\left[-4\pi\overline{\mu_{\rm n}n_{\rm n}}\widehat{\mu_{\rm n}n_{\rm p}}\right.\\
&\quad-\frac{l+2}{2}\left(\mathcal{A}^{\rm np}{}_0^0\right)_2 n_0^{\rm p}n_2^{\rm n}-\pi\lambda_2\overline{\mu_{\rm n}n_{\rm n}\mu_{\rm n}n_{\rm p}}+\frac{l}{2}\left(\mathcal{A}^{\rm np}{}_0^0\right)_0 n_2^{\rm n}\left(\frac{n_0^{\rm p}}{n_0^{\rm n}}n_2^{\rm n}-n_2^{\rm p}\right)\\
&\quad+\left(\frac{1}{4}n_2^{\rm n}(\lambda_2-(l+2)\nu_2)-(l+2)n_4^{\rm n}\right)\overline{\mathcal{A}^{\rm np}{}_0^0 n_{\rm p}}\\
&\quad\left.+\omega^2e^{-\nu_0}n_0^{\rm n}\left(\frac{1}{4}(\nu_2-\lambda_2)\overline{\mathcal{A}^{\rm np}n_{\rm p}}-\widehat{\mathcal{A}^{\rm np}n_{\rm p}}\right)\right]W_{\rm p}(0)+\left[\frac{\widehat{\mu_{\rm n}n_{\rm n}}}{\overline{\mu_{\rm n}n_{\rm n}}}+\frac{1}{4}\nu_2\right]lX_{\rm n}(0)\\
&\quad+\frac{1}{4}e^{\nu_0/2}\overline{\mu_{\rm n}n_{\rm n}}Q_0+(n+1)e^{\nu_0/2}n_2^{\rm n}\left(\overline{\mathcal{B}^{\rm n}{}_0^0 n_{\rm n}}Q_{\rm n}+\overline{\mathcal{A}^{\rm np}{}_0^0 n_{\rm p}}Q_{\rm p}\right),
\end{aligned}
\tag{4.174e}
$$

$$
\begin{aligned}
&-\frac{n+1}{4}e^{\nu_0/2}\overline{\mu_{\rm n}n_{\rm p}}H_1''(0)+e^{\nu_0/2}\left[\frac{l+2}{2}n_2^{\rm p}\overline{\mathcal{A}^{\rm np}{}_0^0 n_{\rm n}}+2\pi\overline{\mu_{\rm n}n_{\rm n}\mu_{\rm n}n_{\rm p}}\right.\\
&\quad\left.+\frac{\omega^2}{2}e^{-\nu_0}\overline{\mathcal{A}^{\rm np}n_{\rm n}n_{\rm p}}\right]W_{\rm n}''(0)-e^{\nu_0/2}\left[\frac{l+2}{2}n_2^{\rm n}\overline{\mathcal{A}^{\rm np}{}_0^0 n_{\rm p}}+\frac{l+2}{4}\nu_2\overline{\mu_{\rm n}n_{\rm p}}-2\pi\overline{\mu_{\rm n}n_{\rm p}}^2\right.\\
&\quad\left.+\frac{\omega^2}{2}e^{-\nu_0}\left(\overline{\mathcal{A}^{\rm np}n_{\rm n}n_{\rm p}}-\overline{\mu_{\rm n}n_{\rm p}}\right)\right]W_{\rm p}''(0)+\frac{l+2}{2}X_{\rm p}''(0)\\
&=+\frac{\omega^2}{2}e^{-\nu_0/2}\overline{\mu_{\rm n}n_{\rm p}}H_1(0)+\frac{1}{2}e^{\nu_0/2}\left[\nu_2\overline{\mu_{\rm n}n_{\rm p}}+3\left(\mathcal{A}^{\rm np}{}_0^0\right)_0\left(n_2^{\rm n}n_0^{\rm p}-n_0^{\rm n}n_2^{\rm p}\right)\right]K(0)\\
&\quad+e^{\nu_0/2}\left[-4\pi\overline{\mu_{\rm n}n_{\rm p}}\widehat{\mu_{\rm n}n_{\rm n}}-\frac{l+2}{2}\left(\mathcal{A}^{\rm np}{}_0^0\right)_2 n_0^{\rm n}n_2^{\rm p}-\pi\lambda_2\overline{\mu_{\rm n}n_{\rm n}\mu_{\rm n}n_{\rm p}}\right.\\
&\quad+\frac{l}{2}\left(\mathcal{A}^{\rm np}{}_0^0\right)_0 n_2^{\rm p}\left(\frac{n_0^{\rm n}}{n_0^{\rm p}}n_2^{\rm p}-n_2^{\rm n}\right)+\left(\frac{1}{4}n_2^{\rm p}(\lambda_2-(l+2)\nu_2)-(l+2)n_4^{\rm p}\right)\overline{\mathcal{A}^{\rm np}{}_0^0 n_{\rm n}}\\
&\quad\left.+\omega^2e^{-\nu_0}n_0^{\rm p}\left(\frac{1}{4}(\nu_2-\lambda_2)\overline{\mathcal{A}^{\rm np}n_{\rm n}}-\widehat{\mathcal{A}^{\rm np}n_{\rm n}}\right)\right]W_{\rm n}(0)+e^{\nu_0/2}\left[-4\pi\overline{\mu_{\rm n}n_{\rm p}}\widehat{\mu_{\rm n}n_{\rm p}}\right.\\
&\quad-\frac{l+2}{2}\left(\mathcal{A}^{\rm np}{}_0^0\right)_2 n_2^{\rm n}n_0^{\rm p}-\pi\lambda_2\overline{\mu_{\rm n}n_{\rm p}}^2-\frac{1}{8}\overline{\mu_{\rm n}n_{\rm p}}\nu_2\left(\lambda_2-(l+2)\nu_2\right)-(l+2)\mu_4^{\rm n}n_0^{\rm p}\\
&\quad-\left(\frac{1}{4}n_2^{\rm n}(\lambda_2-(l+2)\nu_2)-(l+2)n_4^{\rm n}\right)\overline{\mathcal{A}^{\rm np}{}_0^0 n_{\rm p}}-\omega^2e^{-\nu_0}n_0^{\rm p}\left(\frac{1}{4}(\nu_2-\lambda_2)\overline{\mathcal{A}^{\rm np}n_{\rm n}}\right.\\
&\quad\left.\left.-\widehat{\mathcal{A}^{\rm np}n_{\rm n}}-\frac{1}{4}(2\nu_2-\lambda_2)\mu_0^{\rm n}\right)\right]W_{\rm p}(0)+\left[\frac{\widehat{\mu_{\rm n}n_{\rm p}}}{\overline{\mu_{\rm n}n_{\rm p}}}+\frac{1}{4}\nu_2\right]lX_{\rm p}(0)+\frac{1}{4}e^{\nu_0/2}\overline{\mu_{\rm n}n_{\rm p}}Q_0
\end{aligned}
$$

$$+ (n+1)e^{\nu_0/2}\overline{\mathcal{A}^{\mathrm{np}0}_{\ 0}n_{\mathrm{n}}}n_2^{\mathrm{p}}Q_{\mathrm{n}} + (n+1)e^{\nu_0/2}\left(\mu_2^{\mathrm{n}} - \left(\mathcal{A}^{\mathrm{np}0}_{\ 0}\right)_0 n_2^{\mathrm{n}}\right)n_0^{\mathrm{p}}Q_{\mathrm{p}}, \quad (4.174\mathrm{f})$$

We point out that—similar to the differential equations (4.163)—we decided to remove the explicit appearance of quantities assigned to electrons or muons to greatest possible extent. The only place where such quantities appear explicitly are the variables Q_{n} and Q_{p} as given in equations (4.173b) and (4.173c), respectively. Again, as in the previous case, the equations valid for npe-matter or a simple neutron-proton fluid can be obtained by removing the electron or muon quantities from the equations.

4.6 The Single Fluid Limit

We have derived the equations governing perturbations of a multi-fluid, consisting of two individual fluids (where the proton fluid has three constituents). When the star is very young and hot, none of the components will be in the superfluid state yet; all four constituents will be locked together and the neutron star core will behave like a single fluid. We therefore have to specialise our equations for the single fluid case. In contrast to Andersson et al. [36] who considered this limit by letting the number density of one of the constituents vanish, we will choose a different approach: similar to how we locked the charged particles together, we will now lock all four constituents together by assuming that their displacement vectors are identical,

$$W := W_{\mathrm{n}} = W_{\mathrm{p}} = W_{\mathrm{e}} = W_{\mu}, \quad (4.175)$$

$$V := V_{\mathrm{n}} = V_{\mathrm{p}} = V_{\mathrm{e}} = V_{\mu}. \quad (4.176)$$

This will simplify the perturbation equations (4.163) somewhat and more importantly reduce the number of differential equations by two; we will have only one wave degree of freedom for the fluid.

In order to have a consistent description, we will again define the variables X_{x} for each species as in (4.159a). However, the variable which is relevant for the numerical solution will be the *total* Lagrangian pressure variation

$$X := \sum_{\mathrm{x}} X_{\mathrm{x}} = X_{\mathrm{n}} + X_{\mathrm{p}} + X_{\mathrm{e}} + X_{\mu}. \quad (4.177)$$

This is similar to the multi-fluid case in the sense that we have precisely one variable for the Lagrangian pressure per individual fluid; we had two of them for the two-fluid case (X_{n} for the neutron fluid and X_{P} for the proton fluid), whereas now we have only one X valid for the entire fluid.

Also, the definition of the variable $\mathcal{E}_0^0$ changes. As it takes a different form, we call it $\mathcal{F}_0^0$ now. We have

$$\mathcal{F}_0^0 = \mathcal{B}^{\mathrm{n}0}_{\ 0}n_{\mathrm{n}}^2 + 2\mathcal{A}^{\mathrm{np}0}_{\ 0}n_{\mathrm{n}}n_{\mathrm{p}} + \mathcal{B}^{\mathrm{p}0}_{\ 0}n_{\mathrm{p}}^2 + \mathcal{B}^{\mathrm{e}0}_{\ 0}n_{\mathrm{e}}^2 + \mathcal{B}^{\mu 0}_{\ 0}n_{\mu}^2. \quad (4.178)$$

How can we understand the particular form of this variable (and of $\mathcal{E}_0^0$)? These two variables appear only in the differential equations for the radial displacements, W_{x}. These equations are generally arrived at by defining the variables X_{x} as above and then solving a linear system simultaneously for all independent W'_{x}-s. The linear system in general consists of the equations $f_\theta^{\mathrm{x}} = 0$ where x runs over all constituents (which means we get one equation per constituent); it turns out that one of the terms in f_θ^{x} is proportional to

$$\mathcal{B}^{\mathrm{x}0}{}_0 n_{\mathrm{x}}^2 W'_{\mathrm{x}} + \sum_{\mathrm{y}\neq\mathrm{x}} \mathcal{A}^{\mathrm{xy}0}{}_0 n_{\mathrm{x}} n_{\mathrm{y}} W'_{\mathrm{y}}. \tag{4.179}$$

Solving for the individual W'_{x}-s is essentially equivalent to inverting the matrix of the coefficients of the W'_{x}-s which introduces its determinant to the equations; the variables $\mathcal{F}_0^0$ and $\mathcal{E}_0^0$ are precisely these determinants.

The matrix has as many dimensions as we have individual fluids; locking several species together "removes" some of the W_{x} from the problem. In the two-fluid case discussed above, we assumed $W_{\mathrm{p}} = W_{\mathrm{e}} = W_\mu$. Hence, we find

$$\begin{pmatrix} f_\theta^{\mathrm{n}} \\ f_\theta^{\mathrm{p}} + f_\theta^{\mathrm{e}} + f_\theta^{\mu} \end{pmatrix} = 0 \Leftrightarrow \underbrace{\begin{pmatrix} \mathcal{B}^{\mathrm{n}0}{}_0 n_{\mathrm{n}}^2 & \mathcal{A}^{\mathrm{np}0}{}_0 n_{\mathrm{n}} n_{\mathrm{p}} \\ \mathcal{A}^{\mathrm{np}0}{}_0 n_{\mathrm{n}} n_{\mathrm{p}} & \mathcal{B}^{\mathrm{p}0}{}_0 n_{\mathrm{p}}^2 + \mathcal{B}^{\mathrm{e}0}{}_0 n_{\mathrm{e}}^2 + \mathcal{B}^{\mu 0}{}_0 n_\mu^2 \end{pmatrix}}_{=:E} \begin{pmatrix} W'_{\mathrm{n}} \\ W'_{\mathrm{p}} \end{pmatrix} = \begin{pmatrix} R_{\mathrm{n}} \\ R_{\mathrm{pe}\mu} \end{pmatrix}, \tag{4.180}$$

where R_{n} and $R_{\mathrm{pe}\mu}$ denote the remaining terms of the equations of motion. It is easy to see that the determinant of the matrix E is closely linked to $\mathcal{E}_0^0$,

$$\mathcal{E}_0^0 = n_{\mathrm{n}}^2 \det E. \tag{4.181}$$

If we lock all four constituents together, $W := W_{\mathrm{n}} = W_{\mathrm{p}} = W_{\mathrm{e}} = W_\mu$, we find that $\mathcal{F}_0^0$ is proportional to the coefficient of W'.

The perturbation equations for a four-constituent single fluid then are;

$$H_1' = \left[\frac{1}{2}\left(\lambda' - \nu'\right) - \frac{l+1}{r}\right] H_1 + \frac{e^\lambda}{r}\left(H_0 + K - 16\pi\mu_{\mathrm{n}} n_{\mathrm{b}} V\right), \tag{4.182a}$$

$$K' = \frac{1}{r}H_0 + \frac{n+1}{r}H_1 + \left[\frac{1}{2}\nu' - \frac{l+1}{r}\right] K - \frac{8\pi e^{\lambda/2}}{r}\mu_{\mathrm{n}} n_{\mathrm{b}} W, \tag{4.182b}$$

$$W' = -\frac{l+1}{r}W + r e^{\lambda/2}\left[\frac{e^{-\nu/2}}{\mathcal{F}_0^0}X - \frac{l(l+1)}{r^2}V + \frac{1}{2}H_0 + K\right], \tag{4.182c}$$

$$\begin{aligned} X' = {} & -\frac{l}{r}X + \frac{1}{2}e^{\nu/2}\mu_{\mathrm{n}} n_b \left\{\left[\frac{1}{r} - \frac{\nu'}{2}\right] H_0 + \left[\omega^2 r e^{-\nu} + \frac{n+1}{r}\right] H_1 \right. \\ & \left. + \left[\frac{3\nu'}{2} - \frac{1}{r}\right] K - \nu' \frac{l(l+1)}{r^2} V - \frac{1}{r}\left[8\pi\mu_{\mathrm{n}} n_b e^{\lambda/2} - 2\omega^2 e^{\lambda/2-\nu}\right] W \right\} \end{aligned}$$

$$+ e^{(\nu-\lambda)/2}\frac{1}{r}\left[\left(\frac{2}{r}+\frac{\lambda'-\nu'}{2}\right)\mu_{\rm n}' - \mu_{\rm n}''\right] n_b W, \tag{4.182d}$$

where $n_b = n_{\rm n} + n_{\rm p}$. We also have two algebraic constraints

$$X = \frac{1}{2}\mu_{\rm n} n_b e^{\nu/2} H_0 + \omega^2 e^{-\nu/2}\mu_{\rm n} n_b V - e^{(\nu-\lambda)/2}\frac{\mu_{\rm n}' n_b}{r} W, \tag{4.183a}$$

and

$$\left[\frac{1}{2}e^{-\lambda}r(r\nu'-2) + (n+1)r\right] H_0 = e^{-\lambda}r^2\left[\omega^2 r e^{-\nu} - \frac{n+1}{2}\nu'\right] H_1 + \left[nr - \omega^2 r^3 e^{-\nu} - \frac{1}{4}r^2 e^{-\lambda}\nu'(r\nu'-2)\right] K + 8\pi r^3 e^{-\nu/2} X. \tag{4.183b}$$

The origin of these equations is essentially the same as for the two-fluid equations (4.163); we will not repeat the derivation here.

We want to point out the similarity to the DL85 formulation (see equations (3.33)) which we used at the beginning of the project for a perfect fluid star. The most obvious substitution is $\mu_{\rm n} n_b = \rho + p$ which is the Euler relation. The last coefficient of W in the equation for X' is not so obvious but straightforward to prove when using the background equation $\mu_{\rm n}' = -\frac{1}{2}\nu'\mu_{\rm n}$. The remaining necessary substitution takes place in the differential equation for W'. By comparison, we find

$$\mathcal{F}_0^0 = \gamma p. \tag{4.184}$$

That we indeed have γp on the right-hand side of this equation and not $\gamma_0 p$ (the background term), can be seen as follows. We start from the right-hand side and use the definition of γ, equation (3.54),

$$\gamma p = (\rho + p)\left(\frac{\partial p}{\partial \rho}\right)_n, \tag{4.185}$$

where the partial derivative has to be evaluated at constant (frozen) composition. If we take the neutron number density $n_{\rm n}$ as reference (this is no restriction, we could as well start with the number density of any other species), then assuming a frozen composition means mathematically

$$0 = {\rm d}\left(\frac{n_{\rm n}}{n_{\rm x}}\right) \quad \text{or equivalently} \quad {\rm d}n_{\rm x} = \frac{n_{\rm x}}{n_{\rm n}}\,{\rm d}n_{\rm n}. \tag{4.186}$$

We use this relation to express ${\rm d}\rho$ solely in terms of the neutron number density,

$$ {\rm d}\rho = \left[\mu_{\rm n} + \sum_{{\rm y}\neq{\rm n}} \mu_{\rm y}\frac{n_{\rm y}}{n_{\rm n}}\right] {\rm d}n_{\rm n} = (\rho+p)\frac{1}{n_{\rm n}}\,{\rm d}n_{\rm n}. \tag{4.187}$$

where we have used $\mu_{\mathrm{x}} = \frac{\partial \rho}{\partial n_{\mathrm{x}}}$ and the Euler relation. In the same way we consider the pressure to be a function of the number densities and we find for its differential,

$$\mathrm{d}p = \left[\frac{\partial p}{\partial n_{\mathrm{n}}} + \sum_{\mathrm{y} \neq \mathrm{n}} \frac{\partial p}{\partial n_{\mathrm{y}}} \frac{n_{\mathrm{y}}}{n_{\mathrm{n}}} \right] \mathrm{d}n_{\mathrm{n}}. \tag{4.188}$$

We can also calculate $\mathrm{d}p$ starting from the Euler relation,

$$p = \sum_{\mathrm{x}} \mu_{\mathrm{x}} n_{\mathrm{x}} - \rho, \tag{4.189}$$

which implies

$$\mathrm{d}p = \sum_{\mathrm{x}} \left(\mu_{\mathrm{x}} \, \mathrm{d}n_{\mathrm{x}} + n_{\mathrm{x}} \, \mathrm{d}\mu_{\mathrm{x}} \right) - \sum_{\mathrm{x}} \mu_{\mathrm{x}} \, \mathrm{d}n_{\mathrm{x}} \tag{4.190}$$

$$= \sum_{\mathrm{x}} n_{\mathrm{x}} \sum_{\mathrm{y}} \frac{\partial \mu_{\mathrm{x}}}{\partial n_{\mathrm{y}}} \, \mathrm{d}n_{\mathrm{y}}. \tag{4.191}$$

We identify the partial derivatives

$$\frac{\partial p}{\partial n_{\mathrm{y}}} = \sum_{\mathrm{x}} n_{\mathrm{x}} \frac{\partial \mu_{\mathrm{x}}}{\partial n_{\mathrm{y}}} \tag{4.192}$$

and plug them into (4.188),

$$\mathrm{d}p = \left[\sum_{\mathrm{x}} n_{\mathrm{x}} \frac{\partial \mu_{\mathrm{x}}}{\partial n_{\mathrm{n}}} + \sum_{\mathrm{y} \neq \mathrm{n}} \sum_{\mathrm{x}} n_{\mathrm{x}} \frac{\partial \mu_{\mathrm{x}}}{\partial n_{\mathrm{y}}} \frac{n_{\mathrm{y}}}{n_{\mathrm{n}}} \right] \mathrm{d}n_{\mathrm{n}} \tag{4.193}$$

$$= \left[\sum_{\mathrm{x}} n_{\mathrm{x}}^2 \mathcal{B}^{\mathrm{x}0}{}_0 + \sum_{\mathrm{x}} \sum_{\mathrm{y} \neq \mathrm{x}} n_{\mathrm{x}} n_{\mathrm{y}} \mathcal{A}^{\mathrm{xy}0}{}_0 \right] \frac{1}{n_{\mathrm{n}}} \, \mathrm{d}n_{\mathrm{n}}, \tag{4.194}$$

where we have replaced the partial derivatives of the chemical potentials using

$$\mathcal{B}^{\mathrm{x}0}{}_0 = \frac{\partial \mu_{\mathrm{x}}}{\partial n_{\mathrm{x}}} \quad \text{and} \quad \mathcal{A}^{\mathrm{xy}0}{}_0 = \frac{\partial \mu_{\mathrm{x}}}{\partial n_{\mathrm{y}}}, \tag{4.195}$$

and we have rearranged the sums. Note that the relations for $\mathrm{d}p$ and $\mathrm{d}\rho$ have been derived under the assumption of frozen composition.

We can now focus on our specific four-constituent fluid, where only neutrons and protons are entrained, i.e. only $\mathcal{A}^{\mathrm{np}} \neq 0$. This immediately shows that

$$\mathrm{d}p = \mathcal{F}^0_0 \frac{1}{n_{\mathrm{n}}} \, \mathrm{d}n_{\mathrm{n}}. \tag{4.196}$$

In conjunction with (4.187) and (4.185), we find

$$\mathcal{F}_0^0 = \gamma p, \tag{4.197}$$

as we have claimed above. This shows that the variational approach automatically assumes a frozen composition.

As in the two-fluid case, the presence of different particle species is almost entirely hidden; only the coefficient $\mathcal{F}_0^0$ witnesses their existence. If we want to specialise to a system without muons and maybe also without electrons, this can easily be done by removing the corresponding terms from $\mathcal{F}_0^0$. No other changes are necessary.

4.6.1 The Taylor Expansion at the Centre of the Star

As in the previous cases, we need the Taylor expansion of the equations (4.182) at the centre of the star $r = 0$. In the early stages of a neutron star's life, its core temperature will certainly exceed the critical temperature for the onset of superfluidity and hence the matter will appropriately be described by a single fluid. We will calculate the Taylor expansion consistent with the other cases. Hence, we will state the results only and refer to Section 3.2.1 for the precise meaning of the variables used here. We also use the abbreviations (4.165) as introduced in Section 4.5.1.

The zeroth order constraints are

$$X(0) = e^{\nu_0/2}\overline{\mu_{\mathrm{n}} n_b}\left(\frac{1}{2}K(0) + \left[\frac{1}{2}\nu_2 - \frac{\omega^2}{l}e^{-\nu_0}\right]W(0)\right), \tag{4.198a}$$

$$H_1(0) = \frac{lK(0) + 8\pi\overline{\mu_{\mathrm{n}} n_b}W(0)}{n+1}, \tag{4.198b}$$

$$H_0(0) = K(0), \tag{4.198c}$$

$$V(0) = -\frac{W(0)}{l}, \tag{4.198d}$$

All second order coefficients for the background, which appear in the linear system below, are identical to the ones given in Section 4.5.1.

We again define the two auxiliary variables Q_0 and Q_1 so that

$$H_0''(0) = K''(0) + Q_0, \tag{4.199}$$

$$V''(0) = Q_1 - \frac{l+3}{l(l+1)}W''(0). \tag{4.200}$$

These two variables are then given by

$$Q_0 = \frac{2}{n}\left[\left[\omega^2 e^{-\nu_0} - \frac{n+1}{2}\nu_2\right]H_1(0) - \left[\frac{1}{2}\lambda_2 + \omega^2 e^{-\nu_0}\right]K(0) + 8\pi e^{-\nu_0/2}X(0)\right], \tag{4.201a}$$

$$Q_1 = \frac{1}{n+1}\left[\frac{3}{2}K_0 + \frac{l+1}{4}\lambda_2 W(0) + e^{-\nu_0/2}\overline{\left(\frac{1}{\mathcal{F}_0^0}\right)}X_{\mathrm{P}}(0)\right]. \tag{4.201b}$$

The second order coefficients can then be obtained by solving the following linear system:

$$\begin{aligned}
&-\frac{1}{2}\overline{\mu_{\mathrm{n}} n_b}K''(0) + \overline{\mu_{\mathrm{n}} n_b}\left[-\frac{1}{2}\nu_2 + \frac{\omega^2(l+3)}{l(l+1)}e^{-\nu_0}\right] + e^{-\nu_0/2}X''(0)\\
&\quad = \widehat{\mu_{\mathrm{n}} n_b}K(0) - \left[-\frac{1}{2}\mu_0^{\mathrm{n}} n_2^b \nu_2 + \overline{n_b}\left(2\mu_4^{\mathrm{n}} - \frac{1}{2}\lambda_2\mu_2^{\mathrm{n}}\right) + \frac{\omega^2}{l e^{\nu_0}}\left(2\widehat{\mu_{\mathrm{n}} n_b} - \nu_2\overline{\mu_{\mathrm{n}} n_b}\right)\right]W(0)\\
&\qquad + \frac{1}{2}e^{-\nu_0/2}\nu_2 X(0) + \frac{1}{2}\overline{\mu_{\mathrm{n}} n_b}Q_0 + e^{-\nu_0}\omega^2\overline{\mu_{\mathrm{n}} n_b}Q_1,
\end{aligned} \tag{4.202a}$$

$$\begin{aligned}
&-(n+1)H_1''(0) + (l+2)K''(0) + 8\pi\overline{\mu_{\mathrm{n}} n_b}W''(0)\\
&\qquad = \nu_2 K(0) - 8\pi\left(2\widehat{\mu_{\mathrm{n}} n_b} + \frac{1}{2}\lambda_2\overline{\mu_{\mathrm{n}} n_b}\right)W(0) + Q_0,
\end{aligned} \tag{4.202b}$$

$$\begin{aligned}
&\frac{l+3}{2}H_1''(0) - K''(0) - 4\pi\overline{\mu_{\mathrm{n}} n_b}\frac{l+3}{n+1}W''(0)\\
&\qquad = \frac{1}{2}\left((l+2)\lambda_2 - \nu_2\right)H_1(0) + \frac{16\pi}{l}\widehat{\mu_{\mathrm{n}} n_b}W(0) + \frac{1}{2}Q_0 - 8\pi\overline{\mu_{\mathrm{n}} n_b}Q_1,
\end{aligned} \tag{4.202c}$$

$$\begin{aligned}
&-\frac{n+1}{4}e^{\nu_0/2}\overline{\mu_{\mathrm{n}} n_b}H_1''(0) + e^{\nu_0/2}\left[-\frac{l+2}{4}\nu_2\overline{\mu_{\mathrm{n}} n_b} + 2\pi\overline{\mu_{\mathrm{n}} n_b}^2 + \frac{\omega^2}{2}e^{-\nu_0}\overline{\mu_{\mathrm{n}} n_b}\right]W''(0)\\
&\qquad + \frac{l+2}{2}X''(0)\\
&\quad = +\frac{\omega^2}{2}e^{-\nu_0/2}\overline{\mu_{\mathrm{n}} n_b}H_1(0) + \frac{1}{2}e^{\nu_0/2}\nu_2\overline{\mu_{\mathrm{n}} n_b}K(0) + e^{\nu_0/2}\left[-4\pi\overline{\mu_{\mathrm{n}} n_b}\widehat{\mu_{\mathrm{n}} n_b}\right.\\
&\qquad -\pi\lambda_2\overline{\mu_{\mathrm{n}} n_b}^2 + \frac{1}{4}\mu_2^{\mathrm{n}}(\lambda_2 - \nu_2)n_0^b - \mu_4^{\mathrm{n}} n_0^b + \frac{l+1}{2}\nu_4\overline{\mu_{\mathrm{n}} n_b}\\
&\qquad \left.+\frac{\omega^2}{4}e^{-\nu_0}(2\nu_2 - \lambda_2)\overline{\mu_{\mathrm{n}} n_b}\right]W(0) + \left[\frac{\widehat{\mu_{\mathrm{n}} n_b}}{\overline{\mu_{\mathrm{n}} n_b}} + \frac{1}{4}\nu_2\right]lX(0)\\
&\qquad + \frac{1}{4}e^{\nu_0/2}\overline{\mu_{\mathrm{n}} n_b}Q_0 - \frac{n+1}{2}e^{\nu_0/2}\nu_2\overline{\mu_{\mathrm{n}} n_b}Q_1.
\end{aligned} \tag{4.202d}$$

This linear system determines the second order coefficients of the perturbations variables.

4.7 The Superfluid Gap

The knowledge of the equations governing perturbations of a multi-fluid system alone is, of course, not enough. We need a criterion that helps us decide in which parts of the star we will actually find a superfluid component, i.e. we need a *critical temperature* T_c

for the onset of superfluidity below which (parts of) the neutron star matter behaves as a superfluid. We will lay out the fundamental concept and how the critical temperature is modelled as found in [89, 90, 60].

When we say that the neutron star matter behaves as a superfluid, we actually mean that one (or more) of the present species undergo Cooper pairing according to BCS theory for classic superconductors. The bosonic Cooper pairs are formed of two fermions and can assume different states depending on the spin alignment of the constituents. More precisely, we distinguish in principle between three different possible pairings as suggested by Ho et al. [60]: neutrons will undergo singlet-state Cooper pairing in the crust and triplet-state pairing in the core, while protons undergo single-state pairing in the core. For every type of Cooper pair, there is a specific model for the superfluid energy gap $\Delta(k_F)$ on the Fermi surface. This quantity is key in the description of nucelon superfluidity; it corresponds to half the energy required to break up a Cooper pair. The critical temperature is closely related to this quantity by

$$kT_c \approx 0.5669\Delta(k_{F\mathrm{x}}) \quad \text{for singlets and} \tag{4.203}$$

$$kT_c \approx 0.8418\Delta(k_{F\mathrm{x}}) \quad \text{for triplets,} \tag{4.204}$$

where k is the Boltzmann constant. It is customary to use the following parametrisation of the energy gap

$$\Delta(k_{F\mathrm{x}}) = \Delta_0 \frac{(k_{F\mathrm{x}} - k_0)^2}{(k_{F\mathrm{x}} - k_0)^2 + k_1} \frac{(k_{F\mathrm{x}} - k_2)^2}{(k_{F\mathrm{x}} - k_2)^2 + k_3} \quad \text{for} \quad k_0 \leq k_{F\mathrm{x}} \leq k_2, \tag{4.205}$$

where $p_{F\mathrm{x}} = \hbar k_{F\mathrm{x}}$ is the Fermi momentum of species x and Δ_0, k_0, k_1, k_2, and k_3 are parameters specific to the gap model; they are given in Table 4.2 for the three cases mentioned above (we provide two different models for the neutron triplet). If the Fermi momentum lies outside the range $[\hbar k_0, \hbar k_2]$, then the energy gap is taken to be zero.

Table 4.2: Phenomenological parameters for superfluid energy gap as provided by [60].

	Proton singlet	Neutron singlet	Shallow neutron triplet	Deep neutron triplet
Δ_0 [MeV]	120	68	0.068	0.15
k_0 [fm^{-1}]	0	0.1	1.28	2
k_1 [fm^{-1}]	9	4	0.1	0.1
k_2 [fm^{-1}]	1.3	1.7	2.37	3.1
k_3 [fm^{-1}]	1.8	4	0.02	0.02

In Figure 4.4, we show the different critical temperatures according to the listed models for our model neutron star. In our simulations, we will, for simplicity, only

check whether any of the species is superfluid but not account for separate superfluid components. The models for the neutron triplets are, thus, irrelevant for our study since the protons are superfluid anyway whenever neutrons could form triplet states. The crustal region becomes permeated by a neutron superfluid at fairly high temperatures, however, we will not account for superfluidity in the crust yet; this will be future work. However, a small portion of the neutrons close to the core-crust boundary become superfluid before the protons start forming singlets. This will lead to two separate superfluid regions in our star for a short time period during our cooling sequence. See the results Section 4.10.4 for more details.

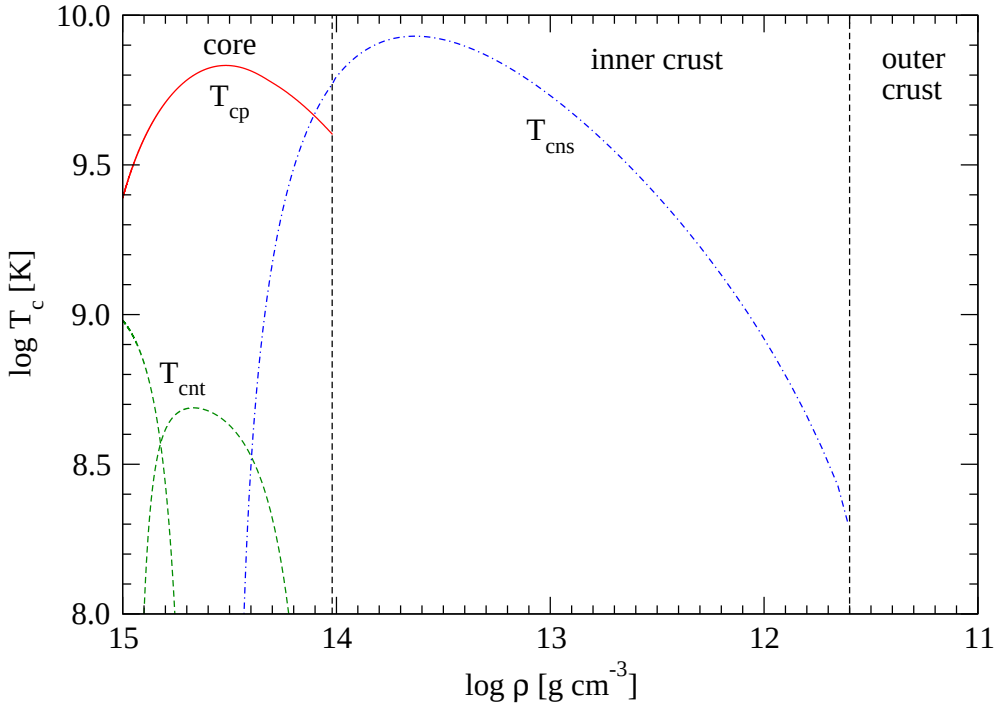

Figure 4.4: The superfluid critical temperatures as a function of density for our particular EoS. The solid line depicts the critical temperature for proton singlets, the dash-dotted line depicts neutron singlets, and the dashed lines depict neutron triplets (depending on model). The protons become superfluid in the core at high temperatures, i.e. very soon into the neutron star's life; the same is true for the neutrons in the crust, however, we do not account for this possibility here. The neutron triplets form only at comparably low temperatures.

The Superfluid Critical Velocity

We have modelled the superfluid energy gap as a function that depends on the temperature as well as the density of the matter. In reality, the energy gap also depends on the relative motion of the superfluid and normal liquid components, as Gusakov & Kantor [91] have argued recently; a relative motion between these two components results in a modified critical temperature for the onset of superfluidity and above a

certain relative velocity, the *superfluid critical velocity*, the formation of Cooper pairs and thus superfluidity is completely suppressed. This effect will influence neutron star dynamics considerably but its implementation is in no way straightforward; whether the superfluid critical velocity is exceeded in a lifelike neutron star highly depends on to what extent particular oscillation modes are excited and what their corresponding velocity amplitude is. In this study, we will disregard the existence of this threshold and assume for simplicity that the superfluid energy gaps are independent of the relative motion of the fluids.

4.8 Crust Elasticity Revisited

The inner crust of a neutron star surrounds the neutron star core. Unlike the core, we still find atomic structures in this region; more precisely, we encounter highly neutron-rich nuclei. The outer boundary of the inner crust is defined to be the neutron drip; this is the density above which neutrons are so abundant that they start to drip out of the nuclei and form a neutron fluid. In a mature neutron star that has cooled sufficiently, the neutron-rich nuclei form an elastic lattice. We have described the perturbations of the solid crust (which may extend also into the outer crust) in Section 3.5.

As we just explained, we also find a neutron fluid within the inner crust. In sufficiently cold neutron stars, these neutrons will be superfluid and flow relative to the elastic crust. The dynamics of this system are relevant for a range of problem from pulsar glitches to oscillation modes and gravitational wave emission. An appropriate modelling of this region as a multi-fluid system is therefore compulsory; in this section, we will derive the perturbation equations for an elastic crust permeated by a neutron superfluid.

A comprehensive description of elastic matter in the framework of general relativity, which is sometimes referred to as *relasticity*, is very involved and goes beyond the scope of this thesis. We will, therefore, not show the derivation of the relevant quantities, but motivate the key results as derived by Karlovini & Samuelsson [92] and Andersson et al. [93].

An appropriate start for the derivation of the relevant equation is, as in the multi-fluid case which we have described in Section 4.1, the Lagrangian density of the system. The solid (elastic) contribution to the matter Lagrangian is

$$\Lambda_{\mathrm{sol}} = -\check{\mu} s^2, \tag{4.206}$$

where $\check{\mu}$ is the shear modulus and s^2 is the shear scalar. The entire matter Lagrangian then is

$$\Lambda_{\mathrm{matter}} = \Lambda_{\mathrm{liq}} + \Lambda_{\mathrm{sol}}, \tag{4.207}$$

where Λ_{liq} is the Lagrangian density of the liquid as described in Section 4.1.1.

In order to keep things simple, we will consider a single fluid now, $\Lambda = \Lambda(n^2)$. We apply the action principle to our system described by the Lagrangian $\Lambda = \Lambda_{\mathrm{EH}} + \Lambda_{\mathrm{liq}} + \Lambda_{\mathrm{sol}}$; the presence of the shear scalar leads to an additional term in the stress-energy tensor,

$$T_{\mu\nu} = (\Lambda - n^\lambda \mu_\lambda) g_{\mu\nu} + n_\mu \mu_\nu + \pi_{\mu\nu}, \tag{4.208}$$

where the new term $\pi_{\mu\nu}$ encodes the anisotropic pressure, cf. (4.41). Since we will deal only with perturbations on an unstrained background, $s^2 = 0$ and $\pi_{\mu\nu} = 0$, we will not state the precise expressions for these quantities here. The Einstein equations imply that the divergence of the stress-energy tensor vanishes, $\nabla_\mu T^{\mu\nu} = 0$. Given number

density conservation $\nabla_\mu n^\mu = 0$, it is easy to show that

$$2n^\nu \nabla_{[\nu}\mu_{\lambda]} + \nabla^\nu \pi_{\nu\lambda} = 0 \qquad \text{(for elastic matter)}. \tag{4.209}$$

It is instructive to compare this result to the perfect fluid case; there we have

$$2n^\nu \nabla_{[\nu}\mu_{\lambda]} = 0 \qquad \text{(for a perfect fluid)}. \tag{4.210}$$

The elastic force of the solid matter is represented by the divergence of the anisotropic pressure tensor.

We can now turn to the multi-fluid case, or more precisely, to our specific case in which a solid crust is permeated by a neutron superfluid. This means that we have to account for two (possibly coupled) fluxes. Within the crust, we have the two fluxes $n_{\rm c}^\nu$ and $n_{\rm f}^\nu$, where the constituent indices c and f distinguish the *confined* baryons in the lattice from the *free* neutrons (which may be superfluid depending on the temperature). A distinction by species, i.e. in protons and neutrons, does physically not make sense in this case; the confined baryons, described by $n_{\rm c}^\nu$, have contributions from both species. Note that we do not account for the presence of electrons (which are necessary for charge neutrality) explicitly here. The solid component of the master function, $\Lambda_{\rm sol}$, is the same as before (see equation (4.206)) but associated solely with the confined flux; i.e. the shear modulus is a function of $n_{\rm c}$ only, $\check{\mu} = \check{\mu}(n_{\rm c})$.

The liquid contribution will be analogous to the multi-fluid case; $\Lambda_{\rm liq}$ is now a function of the three scalars

$$n_{\rm f}^2 = -n_\mu^{\rm f} n_{\rm f}^\mu, \quad n_{\rm c}^2 = -n_\mu^{\rm c} n_{\rm c}^\mu \quad \text{and} \quad n_{\rm cf}^2 = -n_\mu^{\rm c} n_{\rm f}^\mu, \tag{4.211}$$

and we will continue to use the same notation as in the multi-fluid case. We have the canonically conjugate momenta

$$\mu_\nu^{\rm f} = \frac{\partial\Lambda}{\partial n_{\rm f}^{\rm n}} = \frac{\partial\Lambda_{\rm liq}}{\partial n_{\rm f}^{\rm n}} \quad \text{and} \quad \mu_\nu^{\rm c} = \frac{\partial\Lambda}{\partial n_{\rm c}^\nu}, \tag{4.212}$$

and we write formally

$$\mu_\nu^{\rm f} = \mathcal{B}^{\rm f} n_\nu^{\rm f} + \mathcal{A}^{\rm cf} n_\nu^{\rm c}, \tag{4.213}$$

$$\mu_\nu^{\rm c} = \mathcal{B}^{\rm c} n_\nu^{\rm c} + \mathcal{A}^{\rm cf} n_\nu^{\rm f}, \tag{4.214}$$

with the definitions

$$\mathcal{B}^{\rm f} = -2\frac{\partial\Lambda}{\partial n_{\rm f}^2}, \quad \mathcal{B}^{\rm c} = -2\frac{\partial\Lambda}{\partial n_{\rm c}^2} \quad \text{and} \quad \mathcal{A}^{\rm cf} = -2\frac{\partial\Lambda}{\partial n_{\rm cf}^2}. \tag{4.215}$$

The stress-energy tensor takes the form

$$T^{\mu}_{\nu} = \Psi\delta^{\mu}_{\nu} + \sum_{\mathrm{x=c,f}} n^{\mu}_{\mathrm{x}}\mu^{\mathrm{x}}_{\nu} + \pi^{\mu}_{\nu}, \tag{4.216}$$

with the generalised pressure

$$\Psi = \Lambda - \sum_{\mathrm{x=c,f}} n^{\mathrm{x}}_{\nu}\mu^{\nu}_{\mathrm{x}}. \tag{4.217}$$

These results are in full analogy to the multi-fluid case; the elasticity becomes manifest in the presence of π^{μ}_{ν} in the stress-energy tensor. We consider the two fluxes to be individually conserved, i.e. we assume that the time scales of the corresponding reactions are much slower than the dynamical time scale; we have

$$\nabla_{\nu} n^{\nu}_{\mathrm{c}} = \nabla_{\nu} n^{\nu}_{\mathrm{f}} = 0. \tag{4.218}$$

In this case, the equations of motion take the form

$$2n^{\nu}_{\mathrm{c}}\nabla_{[\nu}\mu^{\mathrm{c}}_{\lambda]} + \nabla^{\nu}\pi_{\nu\lambda} = 0, \tag{4.219a}$$

$$2n^{\nu}_{\mathrm{f}}\nabla_{[\nu}\mu^{\mathrm{f}}_{\lambda]} = 0, \tag{4.219b}$$

paired with the Einstein equations, of course. The shape of these equations is not surprising after we have discussed the single fluid case in the previous section. The free neutrons are governed by equation (4.219b), which is the equation of motion for a perfect fluid. The confined baryons, however, governed by equation (4.219a), are subject to an elastic force due to the anisotropic pressure.

The equations (4.219) are neither independent nor uncoupled. The entrainment coefficient $\mathcal{A}^{\mathrm{cf}}$ appearing in the momentum covectors couples the two fluxes to each other. Furthermore, both equations combined ensure the conservation of energy momentum, $\nabla_{\mu}T^{\mu}_{\nu} = 0$ which is already implied by the Einstein equations.

4.8.1 The Entrainment between the Crust and the Superfluid

For the superfluid entrainment in the crust, we will follow the approach by Samuelsson & Andersson [33]. They make use of the small velocity expansion for the liquid part of the Lagrangian which we described in Section 4.3 and write

$$\Lambda_{\mathrm{liq}} = -\rho + \Lambda_{\mathrm{ent}}, \tag{4.220}$$

where ρ denotes the velocity independent energy density (in the unstrained background) and Λ_{ent} encodes the effects of the relative current.

The entrainment Lagrangian can then be written as [92]

$$\Lambda_{\rm ent} = \frac{m_{\rm c}^{\rm f}}{n_{\rm c}} \left(n_{\rm cf}^2 - n_{\rm c} n_{\rm f} \right), \tag{4.221}$$

where $m_{\rm f}^*$ is the effective mass of the neutrons and m is the neutron mass.

When calculating the coefficients and in particular the occuring partial derivatives, we have to take care to accurately use the definitions of, e.g. the number density $n_{\rm x} = \sqrt{n_{\rm x}^2} = \sqrt{-n_{\rm x}^\mu n_\mu^{\rm x}}$, which is why we will show these calculations in more detail. Two of the coefficients are straightforward; we have

$$\mathcal{A}^{\rm cf} = -\frac{\partial \Lambda}{\partial n_{\rm cf}^2} = -\frac{m_{\rm c}^{\rm f}}{n_{\rm c}}, \tag{4.222}$$

and

$$\mathcal{B}^{\rm f} = -2\frac{\partial \Lambda}{\partial n_{\rm f}^2} = 2\frac{\partial \rho}{\partial n_{\rm f}^2} + \frac{m_{\rm c}^{\rm f}}{n_{\rm f}} = \frac{1}{n_{\rm f}} \left(\frac{\partial \rho}{\partial n_b} + m_{\rm c}^{\rm f} \right), \tag{4.223}$$

where we have used

$$\frac{\partial n_{\rm x}}{\partial n_{\rm x}^2} = \frac{\partial \sqrt{n_{\rm x}^2}}{\partial n_{\rm x}^2} = \frac{1}{2n_{\rm x}} \quad \text{and} \quad \frac{\partial n_b}{\partial n_{\rm x}} = 1. \tag{4.224}$$

For the coefficient of the confined baryons, we find

$$\begin{aligned} \mathcal{B}^{\rm c} &= -2\frac{\partial \Lambda}{\partial n_{\rm c}^2} && (4.225)\\ &= 2\frac{\partial \rho}{\partial n_{\rm c}^2} - 2\left[\frac{\partial}{\partial n_{\rm c}^2} \frac{1}{n_{\rm c}} \right] m_{\rm c}^{\rm f} \left(n_{\rm cf}^2 - n_{\rm c} n_{\rm f} \right) - 2\frac{m_{\rm c}^{\rm f}}{n_{\rm c}} \frac{\partial}{\partial n_{\rm c}^2} \left(n_{\rm cf}^2 - n_{\rm c} n_{\rm f} \right) && (4.226)\\ &= \frac{1}{n_{\rm c}} \frac{\partial \rho}{\partial n_b} + \frac{1}{n_{\rm c}^3} m_{\rm c}^{\rm f} \left(n_{\rm cf}^2 - n_{\rm c} n_{\rm f} \right) + \frac{m_{\rm c}^{\rm f}}{n_{\rm c}^2} n_{\rm f}. && (4.227) \end{aligned}$$

After we have taken the derivatives, we can now evaluate this expression on the background, i.e. $n_{\rm cf}^2 = n_{\rm c} n_{\rm f}$, which yields

$$= \frac{1}{n_{\rm c}} \left(\frac{\partial \rho}{\partial n_b} + \frac{n_{\rm f}}{n_{\rm c}} m_{\rm c}^{\rm f} \right). \tag{4.228}$$

The derivative $\frac{\partial \rho}{\partial n_b}$ can be easily evaluated by means of the fundamental law of thermodynamics (3.28); we find

$$\frac{\partial \rho}{\partial n_b} = \frac{\rho + p}{n_b}. \tag{4.229}$$

We must emphasise that in the derivation of the $\mathcal{B}^{\rm x}$ coefficients, we have made the assumption that the ρ is a function of the total number density n_b only. This leads to the relation

$$\mu_\nu^{\rm c} = \mu_\nu^f \tag{4.230}$$

on the background. However, this is true only for the equilibrium configuration; in general, ρ is a function of both $n_{\rm c}^2$ and $n_{\rm f}^2$ which is essential for the correct calculation of the coefficients

$$\mathcal{B}^{\rm c}{}_0^0 = \frac{\partial \mu_{\rm c}}{\partial n_{\rm c}}, \quad \mathcal{B}^{\rm f}{}_0^0 = \frac{\partial \mu_{\rm f}}{\partial n_{\rm f}}, \quad \text{and} \quad \mathcal{A}^{\rm cf}{}_0^0 = \frac{\partial \mu_{\rm c}}{\partial n_{\rm f}}, \tag{4.231}$$

i.e. the partial derivatives of the chemical potentials. When calculating these, it is imperative that *first* the derivative is taken and only *then* the result is evaluated in equilibrium.

4.8.2 The Perturbation Equations for an Elastic Crust Permeated by a Superfluid

Let us now turn to the Lagrangian perturbations of this system. We need to work with Lagrangian perturbations rather than Eulerian perturbations since the Lagrangian perturbations have the advantage that they commute with the covariant derivative. Having two distinct displacements ξ^ν_f and $\xi^\nu_{\rm c}$ naturally leads to introducing Lagrangian perturbations with respect to either of these; we define

$$\Delta_{\rm x} = \delta + \mathcal{L}_{\xi^{\rm x}}, \tag{4.232}$$

where δ is the Eulerian perturbation, $\mathcal{L}_{\xi^{\rm x}}$ the Lie-derivative along $\xi^{\rm x}$, and the constituent index x represents either f or c throughout this section. We have

$$\Delta_{\rm x} n^\nu_{\rm x} = -\frac{1}{2} n^\nu_{\rm x} g^{\sigma\lambda} \Delta_{\rm x} g_{\sigma\lambda}, \tag{4.233}$$

where

$$\Delta_{\rm x} g_{\mu\nu} = \delta g_{\mu\nu} + 2\nabla_{(\mu}\xi^{\rm x}_{\nu)}. \tag{4.234}$$

The perturbation equations which we have to solve stem from the perturbed equations of motion (4.219). We take the Lagrangian perturbation of these equations with respect to the corresponding displacement and arrive at

$$2n^\nu_{\rm c}\nabla_{[\nu}\Delta_{\rm c}\mu^{\rm c}_{\lambda]} + \nabla^\nu \Delta_{\rm c}\pi_{\nu\lambda} = 0, \tag{4.235}$$

$$2n^\nu_{\rm f}\nabla_{[\nu}\Delta_{\rm f}\mu^{\rm f}_{\lambda]} = 0. \tag{4.236}$$

We need to calculate the Lagrangian perturbations of the momenta. We take equations (4.213) and (4.214) as starting point. The calculation itself is lengthy and consists of algebraic manipulations only, hence, we do not show it here. After rearranging terms appropriately, we find

$$\Delta_{\rm x}\mu^{\rm x}_\mu = \left(\mathcal{B}^{\rm x}_{\mu\nu} + \mathcal{A}^{\rm xx}_{\mu\nu}\right)\Delta_{\rm x} n^\nu_{\rm x} + \left(\chi^{\rm xy}_{\mu\nu} + \mathcal{A}^{\rm xy}_{\mu\nu}\right)\Delta_{\rm x} n^\nu_{\rm y}$$

$$+\frac{1}{2}g^{\sigma\nu}\left[\delta^\lambda_\mu\mu^{\mathrm{x}}_\nu+\left(\mathcal{B}^{\mathrm{x}}_{\mu\nu}+\mathcal{A}^{\mathrm{xx}}_{\mu\nu}\right)n^\lambda_{\mathrm{x}}+\left(\chi^{\mathrm{xy}}_{\mu\nu}+\mathcal{A}^{\mathrm{xy}}_{\mu\nu}\right)n^\lambda_{\mathrm{y}}\right]\Delta_{\mathrm{x}}g_{\lambda\sigma}, \quad (4.237)$$

where we have $\mathrm{y}\neq\mathrm{x}$. We have defined

$$\mathcal{B}^{\mathrm{x}}_{\mu\nu}=\mathcal{B}^{\mathrm{x}}g_{\mu\nu}-2\frac{\partial\mathcal{B}^{\mathrm{x}}}{\partial n^2_{\mathrm{x}}}n^{\mathrm{x}}_\mu n^{\mathrm{x}}_\nu, \quad (4.238)$$

$$\chi^{\mathrm{xy}}_{\mu\nu}=-2\frac{\partial\mathcal{B}^{\mathrm{x}}}{\partial n^2_{\mathrm{y}}}n^{\mathrm{x}}_\mu n^{\mathrm{y}}_\nu, \quad (4.239)$$

$$\mathcal{A}^{\mathrm{xx}}_{\mu\nu}=-\frac{\partial\mathcal{B}^{\mathrm{x}}}{\partial n^2_{\mathrm{xy}}}\left(n^{\mathrm{x}}_\mu n^{\mathrm{y}}_\nu+n^{\mathrm{x}}_\nu n^{\mathrm{y}}_\mu\right)-\frac{\partial\mathcal{A}^{\mathrm{xy}}}{\partial n^2_{\mathrm{xy}}}n^{\mathrm{y}}_\mu n^{\mathrm{y}}_\nu, \quad (4.240)$$

$$\mathcal{A}^{\mathrm{xy}}_{\mu\nu}=\mathcal{A}^{\mathrm{xy}}g_{\mu\nu}-\frac{\partial\mathcal{B}^{\mathrm{x}}}{\partial n^2_{\mathrm{xy}}}n^{\mathrm{x}}_\mu n^{\mathrm{x}}_\nu-\frac{\partial\mathcal{B}^{\mathrm{y}}}{\partial n^2_{\mathrm{xy}}}n^{\mathrm{y}}_\mu n^{\mathrm{y}}_\nu-\frac{\partial\mathcal{A}^{\mathrm{xy}}}{\partial n^2_{\mathrm{xy}}}n^{\mathrm{y}}_\mu n^{\mathrm{x}}_\nu. \quad (4.241)$$

We obviously need a "mixed" Lagrangian variation of the number density, too, i.e. the Lagrangian variation of the free neutrons as seen from the confined baryons (which is $\Delta_{\mathrm{c}}n^\nu_{\mathrm{f}}$) and vice versa. Defining the difference vector

$$\psi^{\mathrm{xy}}_\mu:=\xi^{\mathrm{x}}_\mu-\xi^{\mathrm{y}}_\mu, \quad (4.242)$$

we find the simple relation

$$\Delta_{\mathrm{x}}n^\mu_{\mathrm{y}}=\Delta_{\mathrm{y}}n^\mu_{\mathrm{y}}+\psi^\nu_{\mathrm{xy}}\nabla_\nu n^\mu_{\mathrm{y}}-n^\nu_{\mathrm{y}}\nabla_\nu\psi^\mu_{\mathrm{xy}}, \quad (4.243)$$

which can easily be proven by appying the definition (4.232) of the Lagrangian variation and eliminating $\delta n^\mu_{\mathrm{y}}$ from $\Delta_{\mathrm{x}}n^\mu_{\mathrm{y}}$ and $\Delta_{\mathrm{y}}n^\mu_{\mathrm{y}}$. We have now all things together to derive the perturbation equations for an elastic lattice permeated by a neutron superfluid. Inspired by the derivation of the perturbation equations in the other cases, we again define in analogy two variables, X_{f} and X_{c}, by

$$\begin{aligned}X_{\mathrm{f}}=&\frac{1}{2}\mu_{\mathrm{f}}n_{\mathrm{f}}e^{\nu/2}H_0+\omega^2e^{-\nu/2}n_{\mathrm{f}}\left(\mathcal{B}_{\mathrm{f}}n_{\mathrm{f}}V_{\mathrm{f}}+\mathcal{A}^{\mathrm{cf}}n_{\mathrm{c}}V_{\mathrm{c}}\right)\\&-e^{(\nu-\lambda)/2}\frac{n'_{\mathrm{f}}}{r}(\mathcal{B}^{\mathrm{f}0}{}_0n_{\mathrm{f}}W_{\mathrm{f}}+\mathcal{A}^{\mathrm{cf}0}{}_0n_{\mathrm{c}}W_{\mathrm{c}}),\end{aligned} \quad (4.244a)$$

$$\begin{aligned}X_{\mathrm{c}}=&\frac{1}{2}\mu_{\mathrm{c}}n_{\mathrm{c}}e^{\nu/2}H_0+\omega^2e^{-\nu/2}\left(\mathcal{B}_{\mathrm{c}}n_{\mathrm{c}}V_{\mathrm{c}}+\mathcal{A}^{\mathrm{cf}}n_{\mathrm{f}}V_{\mathrm{f}}\right)\\&-e^{(\nu-\lambda)/2}\frac{n'_{\mathrm{c}}}{r}(\mathcal{B}^{\mathrm{c}0}{}_0n_{\mathrm{c}}W_{\mathrm{c}}+\mathcal{A}^{\mathrm{cf}0}{}_0n_{\mathrm{f}}W_{\mathrm{f}}),\end{aligned} \quad (4.244b)$$

And as an abbreviation, we define

$$\mathcal{E}^0_0=-n^2_{\mathrm{c}}\mathcal{A}^{\mathrm{cf}0^2}_0+n^2_{\mathrm{c}}\mathcal{B}^{c0}{}_0\mathcal{B}^{\mathrm{f}0}{}_0. \quad (4.245)$$

We could factor out $n_{\rm c}^2$ from this variable but we leave it in here for consistency with the other formulations. The final perturbation equations then are

$$H_1' = \left[\frac{1}{2}\left(\lambda' - \nu'\right) - \frac{l+1}{r}\right] H_1 + \frac{e^{\lambda}}{r}\left[H_0 + K - 16\pi(\mu_{\rm f} n_{\rm f} V_{\rm f} + \mu_{\rm c} n_{\rm c} V_{\rm c})\right], \tag{4.246a}$$

$$K' = \frac{1}{r}H_2 + \frac{n+1}{r}H_1 + \left[\frac{1}{2}\nu' - \frac{l+1}{r}\right] K - \frac{8\pi e^{\lambda/2}}{r}\left[\mu_{\rm f} n_{\rm f} W_{\rm f} + \mu_{\rm c} n_{\rm c} W_{\rm c}\right], \tag{4.246b}$$

$$H_0' = K' - r e^{-\nu}\omega^2 H_1 - \left[\frac{1}{2}\nu' + \frac{l-1}{r}\right] H_0 - \left[\frac{1}{2}\nu' + \frac{1}{r}\right] H_2 + \frac{l}{r}K - \frac{16\pi}{r}T_2, \tag{4.246c}$$

$$V_{\rm c}' = \frac{1}{2\breve{\mu} r}T_2 + \frac{e^{\lambda/2}}{r}W_{\rm c} + \frac{2-l}{r}V_{\rm c}, \tag{4.246d}$$

$$\begin{aligned} T_2' = &-\frac{1}{2}r e^{\lambda}\mu_{\rm c} n_{\rm c} H_0 + \left[\frac{4n e^{\lambda}\breve{\mu}}{r} - e^{\lambda-\nu} r\omega^2 \mathcal{B}^{\rm c} n_{\rm c}^2\right] V_{\rm c} \\ &- e^{\lambda-\nu} r\omega^2 A_{\rm fc} n_{\rm f} n_{\rm c} V_{\rm f} + e^{\lambda/2} n_{\rm c}' \left(\mathcal{B}^{\rm c0}_{\ 0} n_{\rm c} W_{\rm c} + \mathcal{A}^{\rm cf0}_{\ \ 0} n_{\rm f} W_{\rm f}\right) \\ &+ r e^{\lambda-\nu/2}\left(X_{\rm c} - \frac{1}{2r^2}e^{\nu/2}T_1\right) + \left[\frac{1}{2}(\lambda' - \nu') - \frac{l+1}{r}\right] T_2, \end{aligned} \tag{4.246e}$$

$$\begin{aligned} X_{\rm f}' = &-\frac{l}{r}X_{\rm f} + \frac{1}{4}e^{\nu/2}\mu_{\rm f} n_{\rm f}\left[\frac{2}{r} - \nu'\right] H_0 + \mu_{\rm f} n_{\rm f}\left[\frac{n+1}{2r}e^{\nu/2} + \frac{1}{2}\omega^2 r e^{-\nu/2}\right] H_1 \\ &- \frac{1}{4}e^{\nu/2}\left[\mu_{\rm f} n_{\rm f}\nu' + 2n_{\rm f}'\left(\mathcal{B}^{\rm f0}_{\ 0} n_{\rm f} + \mathcal{A}^{\rm cf0}_{\ \ 0} n_{\rm c}\right)\right] H_2 + e^{\nu/2}\left[\mu_{\rm f} n_{\rm f}\left(\frac{\nu'}{4} - \frac{1}{2r}\right)\right. \\ &\left. - n_{\rm f}'\left(\mathcal{B}^{\rm f0}_{\ 0} n_{\rm f} + \mathcal{A}^{\rm cf0}_{\ \ 0} n_{\rm c}\right)\right] K + \frac{l(l+1)}{r^2}e^{\nu/2} n_{\rm f}'\left(\mathcal{B}^{\rm f0}_{\ 0} n_{\rm f} V_{\rm f} + \mathcal{A}^{\rm cf0}_{\ \ 0} n_{\rm c} V_{\rm c}\right) \\ &- \frac{8\pi}{r}e^{\nu/2}\mu_{\rm f} n_{\rm f} T_2 + e^{(\nu-\lambda)/2}\frac{1}{r}\left[-n_{\rm f}'\left(\mathcal{B}^{\rm f0\prime}_{\ \ 0} n_{\rm f} W_{\rm f} + \mathcal{A}^{\rm cf0\prime}_{\ \ \ 0} n_{\rm c} W_{\rm c}\right)\right. \\ &\left. + \left(\frac{2n_{\rm f}'}{r} + \frac{\lambda' - \nu'}{2}n_{\rm f}' - n_{\rm f}''\right)\left(\mathcal{B}^{\rm f0}_{\ 0} n_{\rm f} W_{\rm f} + \mathcal{A}^{\rm cf0}_{\ \ 0} n_{\rm c} W_{\rm c}\right)\right] \\ &- 4\pi e^{(\lambda+\nu)/2}\frac{\mu_{\rm f} n_{\rm f}}{r}\left(\mu_{\rm f} n_{\rm f} W_{\rm f} + \mu_{\rm c} n_{\rm c} W_{\rm c}\right) \\ &- e^{(\lambda-\nu)/2}\frac{\omega^2}{r} n_{\rm f}\left(\mathcal{B}^{\rm f} n_{\rm f} W_{\rm f} + \mathcal{A}^{\rm cf} n_{\rm c} W_{\rm c}\right), \end{aligned} \tag{4.246f}$$

$$\begin{aligned} W_{\rm f}' = &\, e^{\lambda/2}\left[\frac{r}{2}H_2 + rK - \frac{l(l+1)}{r}V_{\rm f}\right] - \frac{l+1}{r}W_{\rm f} \\ &+ \frac{n_{\rm c}}{n_{\rm f}}\frac{\mathcal{A}^{\rm cf0}_{\ \ 0}}{\mathcal{E}^0_0}\left[\frac{n_{\rm f}'}{n_{\rm f}} - \frac{n_{\rm c}'}{n_{\rm c}}\right]\left(\mathcal{B}^{\rm c0}_{\ 0} n_{\rm c}^2 W_{\rm c} + \mathcal{A}^{\rm cf0}_{\ \ 0} n_{\rm f} n_{\rm c} W_{\rm f}\right) \\ &+ \frac{n_{\rm c}^2 \mathcal{B}^{\rm c0}_{\ 0}}{n_{\rm f}^2 \mathcal{E}^0_0}e^{(\lambda-\nu)/2} r X_{\rm f} - \frac{n_{\rm c}}{n_{\rm f}}\frac{\mathcal{A}^{\rm cf0}_{\ \ 0}}{\mathcal{E}^0_0}e^{(\lambda-\nu)/2} r X_{\rm c}, \end{aligned} \tag{4.246g}$$

$$\begin{aligned} W_{\rm c}' = &\, e^{\lambda/2}\left[\frac{r}{2}H_2 + rK - \frac{l(l+1)}{r}V_{\rm c}\right] - \frac{l+1}{r}W_{\rm c} \\ &+ \frac{\mathcal{A}^{\rm cf0}_{\ \ 0}}{\mathcal{E}^0_0}\left[\frac{n_{\rm c}'}{n_{\rm c}} - \frac{n_{\rm f}'}{n_{\rm f}}\right]\left(\mathcal{B}^{\rm f0}_{\ 0} n_{\rm f} n_{\rm c} W_{\rm f} + \mathcal{A}^{\rm cf0}_{\ \ 0} n_{\rm c}^2 W_{\rm c}\right) \\ &+ \frac{\mathcal{B}^{\rm f0}_{\ 0}}{\mathcal{E}^0_0}e^{(\lambda-\nu)/2} r X_{\rm p} - \frac{n_{\rm c}}{n_{\rm f}}\frac{\mathcal{A}^{\rm cf0}_{\ \ 0}}{\mathcal{E}^0_0}e^{(\lambda-\nu)/2} r X_{\rm f}. \end{aligned} \tag{4.246h}$$

These eight differential equations are complemented by four algebraic equations

$$H_2 = H_0 + 64\pi\check{\mu}V_{\mathrm{c}}, \tag{4.247a}$$

$$\begin{aligned}\omega^2\mathcal{B}_{\mathrm{f}}n_{\mathrm{f}}^2V_{\mathrm{f}} &= e^{\nu/2}X_{\mathrm{f}} - \frac{1}{2}e^{\nu}\mu_{\mathrm{f}}n_{\mathrm{f}}H_0 - \omega^2A_{\mathrm{fc}}n_{\mathrm{f}}n_{\mathrm{c}}V_{\mathrm{c}} \\ &\quad + \frac{1}{r}e^{\nu-\lambda/2}n_{\mathrm{f}}'\left(\mathcal{B}^{\mathrm{f}0}{}_0n_{\mathrm{f}}W_{\mathrm{f}} + \mathcal{A}^{\mathrm{cf}0}{}_0n_{\mathrm{c}}W_{\mathrm{c}}\right),\end{aligned} \tag{4.247b}$$

$$\begin{aligned}0 &= -\left[\frac{re^{-\lambda}}{2}(r\nu'-2) + (n+1)r\right]H_0 + r^2e^{-\lambda}\left[\omega^2re^{-\nu} - \frac{n+1}{2}\nu'\right]H_1 \\ &\quad + \left[nr - \omega^2r^3e^{-\nu} - \frac{1}{4}r^2e^{-\lambda}\nu'(r\nu'-2)\right]K \\ &\quad + 8\pi r^3e^{-\nu/2}(X_{\mathrm{f}}+X_{\mathrm{c}}) + 8\pi rT_1 - 16\pi re^{-\lambda}T_2,\end{aligned} \tag{4.247c}$$

$$\begin{aligned}0 &= \check{\mu}\frac{\mathcal{E}_0^0}{\mathcal{B}^{\mathrm{f}0}_0}\left(2e^{-\lambda/2}W_{\mathrm{c}} - r^2K + l(l+1)V_{\mathrm{c}}\right) + \frac{1}{4}\frac{\mathcal{E}_0^0}{\mathcal{B}^{\mathrm{f}0}_0}T_1 \\ &\quad - \frac{2}{3}e^{-\lambda/2}\check{\mu}rn_{\mathrm{c}}\frac{\mathcal{A}^{\mathrm{cf}0}_0}{\mathcal{B}^{\mathrm{f}0}_0}\left(\frac{n_{\mathrm{c}}'}{n_{\mathrm{c}}} - \frac{n_{\mathrm{f}}'}{n_{\mathrm{f}}}\right)\left(\mathcal{A}^{\mathrm{cf}0}{}_0n_{\mathrm{c}}W_{\mathrm{c}} + \mathcal{B}^{\mathrm{f}0}{}_0n_{\mathrm{f}}W_{\mathrm{f}}\right) \\ &\quad - \frac{2}{3}e^{-\nu/2}\check{\mu}r^2\left(X_{\mathrm{c}} - \frac{n_{\mathrm{c}}}{n_{\mathrm{f}}}\frac{\mathcal{A}^{\mathrm{cf}0}_0}{\mathcal{B}^{\mathrm{f}0}_0}X_{\mathrm{f}}\right).\end{aligned} \tag{4.247d}$$

The origin of these equations are (for brevity, we denote the components of the Einstein equations with $[\mu\nu]$ as a shortcut for $G_{\mu\nu} = 8\pi T_{\mu\nu}$): Equations (4.246a) (4.246b) and (4.246c) are $[t\theta]$, $[tr]$ and $[r\theta]$, respectively; (4.246d) is due to the definition of T_2; (4.246e) is due to $f_\theta^{\mathrm{c}} + \nabla^\mu\pi_{\mu\theta} = 0$; (4.246f) is due to $f_r^{\mathrm{f}} = 0$; (4.246g) and (4.246h) are due to the definitions of X_{c} and X_{f}; (4.247c) is $[rr]$; (4.247a) is $[\theta\theta] - [\phi\phi]$; (4.247b) is $f_\theta^{\mathrm{f}} = 0$; (4.247d) is obtained by eliminating W_{c}' and W_{f}' from the definitions of X_{c}, X_{f} and T_1.

Altogether, we describe the perturbation by the means of twelve variables; four for the metric perturbations, H_0, H_1, H_2 and K; four for the displacement of the two fluids, W_{c}, W_{f}, V_{c} and V_{f}; we defined two traction variables, T_1 and T_2; and we defined to variables related to the Lagrangian pressure variation, X_{c} an X_{f}. For these variables, we have eight ODEs (4.246) and four algebraic constraints (4.247). The problem is thereby completely determined; the equations can be solved by integrating the eight coupled ODEs, then use (4.247a) to determine H_2, then (4.247b) to determine V_{f} and finally solve (4.247c) and (4.247d) simultaneously for X_{c} and T_1.

In contrast to the multi-fluid case where we eliminated the appearance of quantities related to the leptons, we left all coefficients $\mathcal{B}^{\mathrm{x}}$ and $\mathcal{A}^{\mathrm{fc}}$ largely untouched. The fact that we find neutrons bound in the nuclei as well as freely flowing (above the neutron drip) makes it complicated to establish relations between the variables μ_{c} and μ_{f}. Formally, they are defined identically to the chemical potentials in the multi-fluid case; however, in the current situation we have difficulties to interpret them in this way. We can understand the problem if we try to put one more neutron into the inner crust; the

chemical potential would tell us how much energy we need in order to do that. The problem arises from the fact that we have two individual components (the elastic lattice as well as the neutron fluid) but we do not know a priori in which of these two "bins" the neutron will end up. Hence, neither μ_{f} nor μ_{c} can flawlessly be understood as some chemical potential. Both quantities serve rather as useful variables in the description of the problem.

4.9 The Junction Condition Matrix for Multi-Fluid Systems

As in the single fluid case, we have to take care about the different interfaces in our star. Simply due to the fact that we model our neutron star as a multi-fluid, we will have a number of new interfaces. One example is the boundary of a superfluid component; on the one side the matter is described by a single-fluid whereas we need the multi-fluid equations for the other side. We then need to match these two solutions using certain junction conditions. The analysis is fundamentally identical to the single-fluid case which we discussed in Section 3.6.1; we define hypersurfaces using some scalar quantity and then impose that the first and second fundamental form are continuous across these hypersurfaces.

However, as we have laid out, the analysis led to contradictions, in particular in the case of density discontinuities. For the multi-fluid problem, we will use the same temporary solution as in the single fluid case; mathematically pedantic calculations peppered with well-defined physical intuition will result in a comprehensive set of junction conditions for our multi-fluid problem. In particular, we will not make use of the continuity of $[K']_r = 0$ (cf. equation (3.112)) as derived for a purely fluid interface. If applied, we would, owing to (4.163b), arrive at the condition

$$(\mu_{\mathrm{n}} n_{\mathrm{n}} W_{\mathrm{n}} + \mu_{\mathrm{p}} n_{\mathrm{p}} W_{\mathrm{p}})\,|_{R^-} = ((\rho + p) W)\,|_{R^+} \tag{4.248}$$

at an interface between a multi-fluid and a single fluid, where R^- and R^+ denote evaluation on the respective sides of the boundary. If we were to impose a "lockstep" condition for the superfluid as has been done, e.g. by Lin et al. [37] (see below for discussion), i.e. $W_{\mathrm{n}}(R^-) = W_{\mathrm{p}}(R^-)$, we would then arrive at

$$((\rho + p) W_{\mathrm{p}})\,|_{R^-} = ((\rho + p) W)\,|_{R^+}, \tag{4.249}$$

where we have used the Euler relation $\mu_{\mathrm{n}} n_{\mathrm{n}} + \mu_{\mathrm{p}} n_{\mathrm{p}} = \rho + p$. A density discontinuity, $\rho(R^-) \neq \rho(R^+)$ then implies that $W_{\mathrm{p}}(R^-) \neq W(R^+)$ which (as in the single fluid case) corresponds to a gap in the perturbed matter. The contradiction is not as obvious as in the single fluid case and is based rather on physical arguments rather than on

mathematical ones but we are obviously not satisfied with this result. In order to circumvent these issues, we will consider the two components (fluid and superfluid or elastic matter and superfluid) separately and derive junction conditions using the approach based on the location of some interface within this component of the fluid.

Before we turn to this type of junction conditions, we want to discuss the boundaries of a superfluid layer first. That is, we consider a location within the star where its temperature is precisely the critical temperature for the onset of superfluidity. On one side of this location where the star is colder, we will find a superfluid component (for the following discussion we will assume that the neutrons are superfluid while the protons behave as a normal fluid) and we need to describe the perturbations there using the multi-fluid equations; on the other side, where the temperature is higher, we will find a single fluid only. What are the implications for the perturbed matter? In particular, what happens to superfluid elements when they cross into a region which is above the critical temperature during an oscillation cycle? This problem has two natural limits; it depends on the heat conduction and how fast the temperature of the superfluid element equilibrates with its surrounding. If heat is only slowly transferred, then this superfluid element may temporarily move into the single fluid region without losing its identity. Mathematically this means that there is no condition imposed on $W_{\rm n}$ at this boundary; in return, we would require the associated Lagrangian pressure variation, $X_{\rm n}$, to vanish as the boundary is a free boundary of the superfluid. The opposite limit is when the heat conduction is much faster than the time scale of the oscillations, which means that a superfluid element loses its character immediately after its transit into the single fluid region. This essentially locks the velocities at the interface and as a result the superfluid displacement $W_{\rm n}$ is linked to the single fluid displacement W. Since we assumed that the protons behave like a normal fluid in this case, their displacement $W_{\rm p}$ is also linked to the single fluid displacement W. Essentially, we will use the "lockstep-condition" at interfaces between single and multi-fluids in the form of

$$W_{\rm n}(R^*) - W_{\rm p}(R^*) = 0, \tag{4.250}$$

$$W_{\rm p}(R^*) = W(R^*), \tag{4.251}$$

where R^* is the location of such an interface. All variables have obviously to be evaluated on the respective side of the interface. These are the first of our "multi-fluid conditions". We note that this condition takes a slightly different form if the multi-fluid layer has an elastic component; we then deal with quantities associated with the *confined* and *free* components and hence we write

$$W_{\rm c}(R^*) - W_{\rm f}(R^*) = 0, \tag{4.252}$$

$$W_{\rm c}(R^*) = W(R^*). \tag{4.253}$$

We collect all conditions in Table 4.3; we have copied the junction conditions for purely single fluid interfaces from Table 3.1 in the single fluid part of this thesis and we have also used the condition $[T_2]_r = 0$ from (3.115) wherever an elastic component is present.

Table 4.3: The junction condition matrix. It summarises the junction conditions imposed on the perturbation variables at different interfaces. We do not show the conditions $[H_0]_r = [H_1]_r = [K]_r = 0$ which are valid at any interface. For an interface, located at radius r, between layers I and II, they can be found and understood as follows: Locate the nature of layer I in the first column and the nature of layer II in the top row; the junction conditions are then found in the intersecting cell of the matrix. A pure "continuity condition" written like "$[Q]_r = 0$" means that the corresponding quantity is well-defined in both layers and is continuous across the interface. Where a junction condition is written like "$Q_1 = Q_2$", this means that the quantity on the left-hand side, Q_1, is well-defined in layer I, whereas Q_2 is well-defined in layer II. Both quantities have to be evaluated on the respective side of the interface and their values are identical at the interface. We point out that this matrix is symmetric in the sense that junction conditions found in cell (ij) are found in cell (ji) just with their sides of the equation swapped.

	fluid	two-fluid	elastic	elastic/fluid
fluid	$[W]_r = 0$	$W = W_\mathrm{p}$ $0 = W_\mathrm{n} - W_\mathrm{p}$	$[W]_r = 0$ $[T_2]_r = 0$	$W = W_\mathrm{c}$ $0 = W_\mathrm{c} - W_\mathrm{f}$ $[T_2]_r = 0$
two-fluid	$W_\mathrm{p} = W$ $W_\mathrm{n} - W_\mathrm{p} = 0$	$[W_\mathrm{n}]_r = 0$ $[W_\mathrm{p}]_r = 0$ $[V_\mathrm{n}]_r = 0$	$W_\mathrm{p} = W$ $W_\mathrm{n} - W_\mathrm{p} = 0$ $[T_2]_r = 0$	$W_\mathrm{p} = W_\mathrm{c}$ $W_\mathrm{n} = W_\mathrm{f}$ $V_\mathrm{n} = V_\mathrm{f}$ $[T_2]_r = 0$
elastic	$[W] = 0$ $[T_2]_r = 0$	$W = W_\mathrm{p}$ $0 = W_\mathrm{n} - W_\mathrm{p}$ $[T_2]_r = 0$	$[W] = 0$ $[V]_r = 0$ $[T_2]_r = 0$	$W = W_\mathrm{c}$ $0 = W_\mathrm{c} - W_\mathrm{f}$ $V = V_\mathrm{c}$ $[T_2]_r = 0$
elastic/fluid	$W_\mathrm{c} = W$ $W_\mathrm{c} - W_\mathrm{f} = 0$ $[T_2]_r = 0$	$W_\mathrm{c} = W_\mathrm{p}$ $W_\mathrm{f} = W_\mathrm{n}$ $V_\mathrm{f} = V_\mathrm{n}$ $[T_2]_r = 0$	$W_\mathrm{c} = W$ $W_\mathrm{c} - W_\mathrm{f} = 0$ $V_\mathrm{c} = V$ $[T_2]_r = 0$	$[W_\mathrm{f}]_r = 0$ $[W_\mathrm{c}]_r = 0$ $[V_\mathrm{f}]_r = 0$ $[V_\mathrm{c}]_r = 0$ $[T_2]_r = 0$

Let us now come back to the case where a single fluid has a boundary with a multi-fluid. As just explained, we apply a lockstep-condition for the superfluid component. Whilst this was a purely physical argument (and actually an approximation) based on time scales of certain reactions and should be investigated further in order to account

for the actual time scales of the problem, we can take a more fundamental approach for the junction condition between the single fluid and the normal component of the multi-fluid. We consider these two components, irrespective of the presence of the superfluid, and locate the interface (the radius where the temperature is critical) at $r = r_i + \xi^r$, where ξ^r is the single fluid displacement. Obviously, we can also define this location using the displacement of the normal fluid (as seen from within the multi-fluid), i.e. $r = r_i + \xi^r_{\rm p}$. These radii define a hypersurface and we can determine the induced three-metric on this hypersurface. Its continuity (in particular the continuity of the $r\theta$-component, see Section 3.6.1 for details) then implies the condition

$$W = W_{\rm p}, \tag{4.254}$$

at the interface (where both quantities obviously have to be evaluated on that side of the interface where they are defined). Should the multi-fluid under consideration have an elastic component, then the same analysis holds if we consider the confined component instead of the normal fluid. Physically, this means that the elastic matter pushes the single fluid out of its way. We then implement the condition

$$W = W_{\rm c}. \tag{4.255}$$

Another important case is where the neutron superfluid extends across the crust-core interface (see Section 4.7). If the star is old enough, so that the neutrons in the outer core as well as the inner crust are superfluid and that the inner crust is elastic, then we will find a multi-fluid system on either side of the crust-core boundary. In the outer core, we have a normal proton fluid whereas in the crust we have an elastic component; both of these components are penetrated by a neutron superfluid. Again, we take our point of view that we can consider either the neutron superfluid separately or the combination of proton fluid and elastic matter. In the former case of a neutron superfluid, there is no obvious crust-core boundary apart from the fact that the number density of neutrons in the core, $n_{\rm n}$, and the number density of the free neutrons in the crust, $n_{\rm f}$, differ (a density discontinuity within the fluid!). However, as we have discussed earlier, if we take the location of this boundary as a starting point for an analysis of the fundamental forms, we find that irrespective of any (number) density discontinuity, we find that the radial displacement is continuous. In this case this implies the condition

$$W_{\rm n} = W_{\rm f}, \tag{4.256}$$

which physically means that there will be no void in the neutron superfluid. An analogous argument, but now for the elastic component in the crust and the proton fluid in the core yields the condition

$$W_{\rm p} = W_{\rm c}. \tag{4.257}$$

This is analogous to condition (4.255).

For completeness, we need to consider the cases where we have some sort of interface within a multi-fluid (e.g. due to a phase transition) where the nature of the matter on both sides of the interface is identical; e.g. we find a multi-fluid system with or without an elastic component. In such cases, we will proceed as before and consider the superfluid component separate from the elastic component (or the normal component). The analysis will be identical to the one in the previous paragraph and yields the intuitive results

$$[W_{\mathrm{c}}]_r = [W_{\mathrm{f}}]_r = 0 \quad \text{for multi-fluids } \textit{with} \text{ an elastic component,} \tag{4.258}$$

and

$$[W_{\mathrm{p}}]_r = [W_{\mathrm{n}}]_r = 0 \quad \text{for multi-fluids } \textit{without} \text{ an elastic component.} \tag{4.259}$$

These results tell us that there will be no gaps in either component.

Our discussion of the junction conditions is nearly complete. However, we still need more conditions in order to connect two multi-fluid layers or two elastic layers. We follow Finn's argument [32] and demand that *within* the elastic crust, the tangential displacement has to be continuous. While a fluid can freely slip along the solid crust (in general, we have $[V]_r \neq 0$ at its boundaries), we forbid that two solid layers, which may be physically distinct due to a phase transition, can slip along each other. This imposes the conditions

$$[V]_r = 0, \quad \text{or} \quad [V_{\mathrm{c}}]_r = 0 \tag{4.260}$$

at an interface where both sides are purely elastic or permeated by a superfluid, respectively, and

$$V = V_{\mathrm{c}} \tag{4.261}$$

at the boundary of the superfluid component within the elastic crust. We find the last junction conditions by demanding the same physical behaviour for the superfluid components of multi-fluid layers, i.e.

$$[V_{\mathrm{f}}]_r = 0 \tag{4.262}$$

for the neutron superfluid in the crust,

$$[V_{\mathrm{n}}]_r = 0 \tag{4.263}$$

for the superfluid component in the core, and

$$V_{\mathrm{n}} = V_{\mathrm{f}} \tag{4.264}$$

at the crust-core boundary which is permeated by a neutron superfluid.

This completes the discussion of the junction conditions. We show them in the junction condition matrix in Table 4.3. We also point out that by construction, all these conditions are independent. This is essential as otherwise we would attempt to solve an under-determined system of equations.

Table 4.4: The number of independent variables in a layer dependant on its nature.

nature of layer	fluid	two-fluid	elastic	elastic/fluid
number of independent variables	4	6	6	8

While we have motivated an extensive set of independent junction conditions, we also need to assure that they suffice to uniquely (up to an arbitrary amplitude) determine the interior solution. According to Section 3.7.1, we decompose our star into n layers, each of which has a certain composition which is one of the following: perfect fluid, elastic, multi-fluid or multi-fluid with elastic component. For each layer, we find k_i linearly independent solutions. In Table 4.4 we show the number of independent variables for each type of layer. The total number of linearly independent solutions, say $n_{\rm sol}$, that we have to link to each other through the entire star is then

$$n_{\rm sol} = \sum_{i=1}^{n} k_i = \sum_{i=1}^{n-1} k_i + 4. \tag{4.265}$$

Note that we *always* have a perfect fluid ocean (the crust never extends to the surface of the star), i.e. $k_n = 4$; the inner-most layer never has an elastic component, either, so we have $k_1 = 4$ or $k_1 = 6$, depending on the age of the star and whether its central temperature is below the critical temperature or not. Let us now count the junction conditions as given in the junction condition matrix, i.e. Table 4.3 (remember that in fact each cell implicitly has three more entries than shown due to the continuity of the metric perturbations H_0, H_1 and K). In conjunction with the values in Table 4.4 we find that the number of junction conditions j_i applied at interface i between the layers i and $i+1$ obeys the simple relation

$$j_i = \frac{1}{2}\left(k_i + k_{i+1}\right). \tag{4.266}$$

We have to add up all these j_i's for $i = 1, \ldots, n-1$, plus the boundary conditions applied at the star's surface (one condition, $X(R) = 0$) and at the centre (the Taylor expansions around $r = 0$ yield $\frac{1}{2}k_1$ boundary conditions, see Sections 3.2.1 and 4.5.1). The total number of junction conditions then is

$$n_{\rm junc} = \frac{1}{2}k_1 + \sum_{i=1}^{n-1} j_i + 1. \tag{4.267}$$

A simple calculation using (4.266) and $k_n = 4$ yields

$$n_{\text{sol}} - n_{\text{junc}} = 1, \tag{4.268}$$

which means that we have precisely one fewer junction condition than independent solutions. This is as desired as it allows us to freely specify the amplitude of the interior solution.

4.10 Results

4.10.1 Various Test Cases

We will apply the new formalism to our model neutron star. Our first results will be a comparison of the spectra obtained using the variational approach (applied to a single fluid) against our results from the DL85 formulation.

Variational Approach vs. Perfect Fluid Formulation

In Section 4.6, we have derived equations governing perturbations of a perfect fluid using the variational approach. Physically, these equations (4.182) are equivalent to the DL85 equations (3.33) (including stratification) as they describe the same problem, however, in two different ways. We show a comparison of the high frequency domains of the spectra obtained for our model neutron star ($\rho_c = 1 \cdot 10^{15}\,\mathrm{g\,cm^{-3}}$, $R = 11.77\,\mathrm{km}$, $M = 1.447\,M_\odot$) once using the variational approach and once using the DL85 formulation in Figure 4.5. They are essentially identical—as expected; the relative difference of the frequencies of the f- and p-modes is in the order of 10^{-4}, usually considerably less.

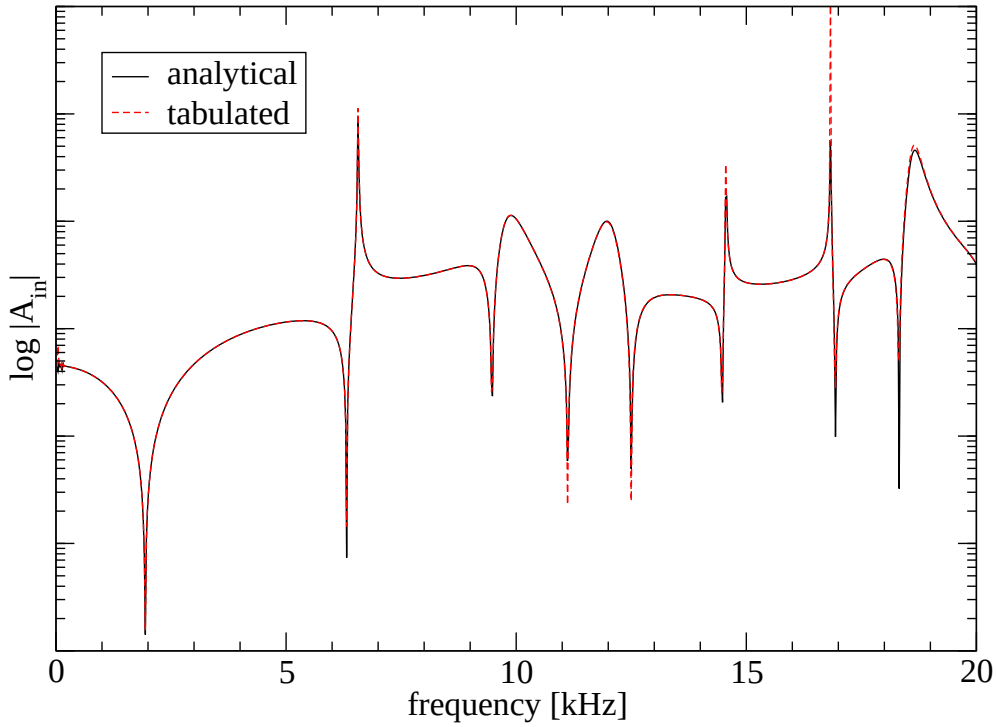

Figure 4.5: Comparison of the high frequency spectra obtained using two different formulations of the same problem. The dashed line is obtained using the DL85 formulation and a tabulated version of our EoS; the solid line is obtained using the single fluid limit equations (cf. (4.182)) which involve the analytical representation of the EoS. The spectra are virtually identical.

In Figure 4.6, we compare the g- and i-mode spectra as determined from the different

formalisms. As for the high frequency part of the spectrum, we find a very high degree of agreement. The agreement is a little less striking than for the high frequency modes and we find that it depends on the mode class as well. The relative difference in frequency is less than $5 \cdot 10^{-3}$ for the g-modes while the agreement for the i-modes is about one order of magnitude better; their frequencies differ by less than $4 \cdot 10^{-4}$.

We find similarly good agreement for the w-modes as well, the discrepancy is less than $5 \cdot 10^{-5}$.

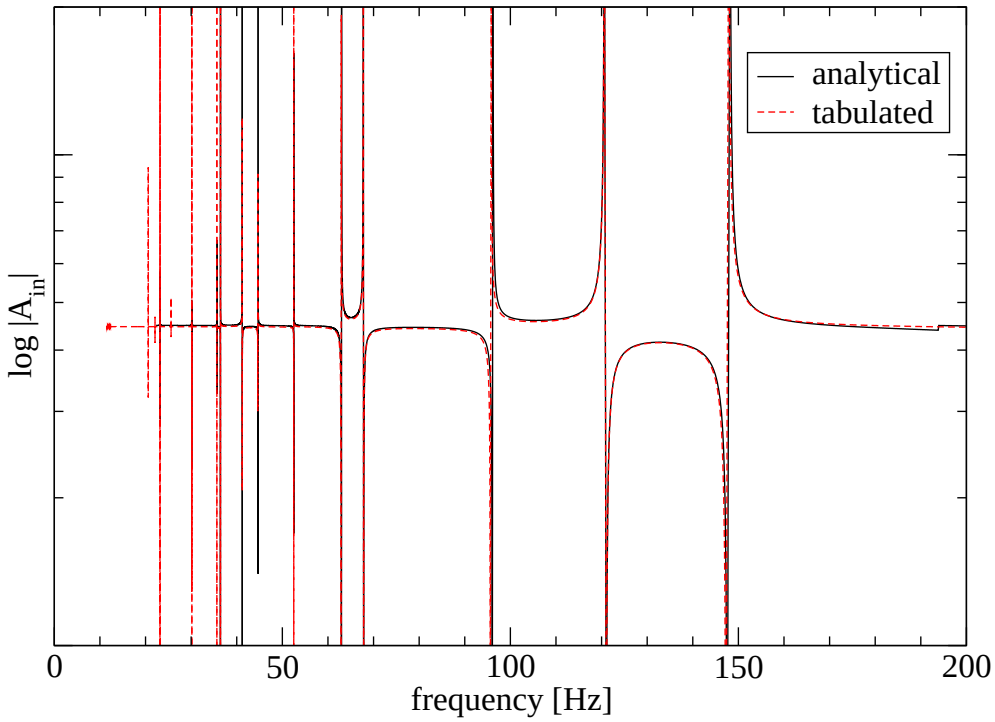

Figure 4.6: As Figure 4.5 but now for the low frequency part of the spectrum. The spectra coincide to a high degree, too.

Even though the physical content of the two sets of evolution equations is identical, they make use of a completely different set of variables to describe the neutron star core. There are several aspects as to why we should expect some small discrepancy in the results. First, the finite numerical precision will inevitably lead to different rounding errors at different places which affects the final results. Secondly, the background models are actually not precisely identical; while we prescribe a certain central energy density (and hence a pressure) for the DL85 formulation of the problem, we need to start with a central number density in the new formulation. We have chosen $n_{\mathrm{n}}(0) = 0.5067\,\mathrm{fm}^{-3}$ which is equivalent to $\rho_c = 1.000136 \cdot 10^{15}\,\mathrm{g\,cm}^{-3}$; compared to our DL85 model with $\rho_c = 1 \cdot 10^{15}\,\mathrm{g\,cm}^{-3}$ this is a tiny but nonetheless existent discrepancy in the background model which affects radius and mass of the star and hence the frequencies of (some) modes to a similar extent. Furthermore, when using the DL85 formulation, we decided to produce a tabulated version of the SLy4 force for our DL85

implementation rather than extending this code to calculate all background quantities analytically at runtime. With 215 given points, our tabulated EoS for the core is very accurate; however, interpolation in between the points introduces some small error, too. In particular the numerical computation of the adiabatic index γ will be afflicted with some approximation error.

Overall, the results of the two formalisms agree very well with each other and we are able to explain the small discrepancies in the results. Since the new formalism comes into effect only in the core of the neutron star (in the crust we continue to use the DL85 formalism and the tabulated DH EoS), we expect the modes in this region to be affected most. This is indeed the case; the g-modes, which arise only due to the composition gradient in the star's core, have the largest discrepancy.

Multi-Fluid Stars

We are convinced that the variational approach gives identical results in the single fluid case. Our next test will concern the multi-fluid formulation. In the simplest scenario, we assume that the entire star is superfluid and there is no entrainment between the two fluids (which means that both fluids are coupled only via the space-time); we need to apply equations (4.163) for the special case of no electrons or muons throughout the star (how this special set of equations is obtained from the full equations is explained in the same section). This case has been studied by Comer et al. [35] (CLL99 thereafter) in the first numerical multi-fluid study on neutron star oscillations. They used a polytropic EoS for each fluid; in particular, their choice of master function is

$$\Lambda(n_{\mathrm{n}}^2, n_{\mathrm{p}}^2) = -mn_{\mathrm{n}} - \sigma_{\mathrm{n}} n_{\mathrm{n}}^{\beta_{\mathrm{n}}} - mn_{\mathrm{p}} - \sigma_{\mathrm{p}} n_{\mathrm{p}}^{\beta_{\mathrm{p}}}, \tag{4.269}$$

where m is the nucleon mass and for simplicity the difference between neutron and proton mass is neglected. The σ_{x} and β_{x} are coefficients of the polytropic EoS. An immediate consequence of this master function is that $\mathcal{A}^{\mathrm{np}} = \mathcal{A}^{\mathrm{np}}{}_0^0 = 0$. We have to comment briefly on the boundary conditions at the surface of the star since we did not cover this particular case (which is a test case only) when we discussed these in Section 4.9. In the perfect fluid case, we demand the Lagrangian pressure to vanish at the surface of the star, $X(R) = 0$. Here, we will have two individual fluids extending to the surface of our model; we demand that both their corresponding partial Lagrangian pressure variations vanish, $X_{\mathrm{n}}(R) = X_{\mathrm{p}}(R) = 0$.

We use Model Two of CLL99 in order to test our code. The polytropic parameters of this model are

$$\sigma_{\mathrm{n}} = 0.2, \qquad \beta_{\mathrm{n}} = 2.5, \tag{4.270}$$

$$\sigma_{\mathrm{p}} = 0.5, \qquad \beta_{\mathrm{p}} = 2.0, \tag{4.271}$$

and the central neutron number density is $n_{\mathrm{n}}(0) = 1.3\,\mathrm{fm}^{-3}$. Chemical equilibrium ($\mu_{\mathrm{n}} = \mu_{\mathrm{p}}$) enforces $n_{\mathrm{p}}(0) = 0.741$ and the resulting star has a radius of $R = 7.957\,\mathrm{km}$ and a mass of $M = 1.361\,M_{\odot}$. Our model neutron star is slightly larger and heavier than the one constructed by CLL99, however, the difference is less than 0.5 % and will not significantly affect the comparison with their results.

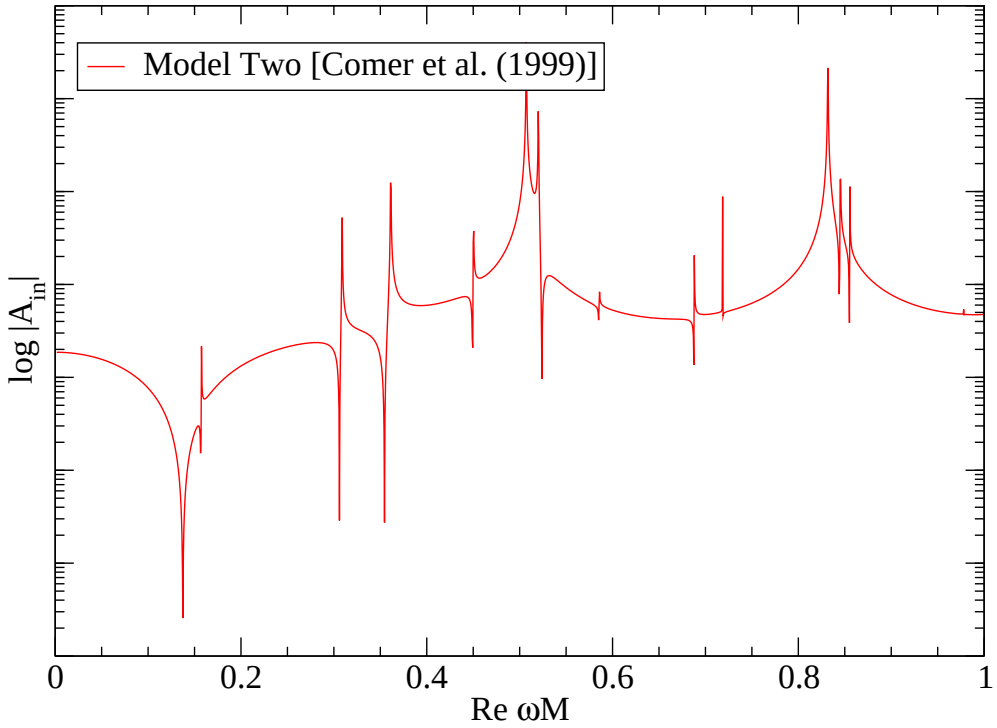

Figure 4.7: The high frequency domain of the spectrum of Model Two of CLL99. Most notably, there is an additional mode at $\mathrm{Re}(\omega M) \approx 0.16$, which is some duplicate of the f-mode due to the second fluid.

We determine the frequencies and damping times of the first few f-, p- and w-modes of this model and show them in Table 4.5. The first pair of columns is for the w-modes, the second pair is for the *ordinary* f- and p-modes, and the last pair is for the new class of *superfluid* modes; before we explain their nature, let us comment on our quantitative results. We observe an excellent agreement with the values published in CLL99; our results generally agree to at least three significant digits (even though the bulk properties of the star are slightly different)—the largest discrepancy of about 1 % is for the ordinary f-mode, all other modes differ by at most 0.5 %.

We show the spectrum of Model Two in Figure 4.7. The most prominent change is another smaller spike to the right of the f-mode at $\mathrm{Re}(\omega M) \approx 0.16$. A closer investigation reveals that actually every expected p-mode is also accompanied (the frequency difference becomes larger for higher order p-modes) by another new mode. These modes are due to the presence of the second fluid and we call them *superfluid* modes. We denote the n-th mode by $\bar{s}_n$ with an overbar in order to distinguish them

Table 4.5: Complex eigenfrequencies of Model Two of CLL99 which are in excellent agreement with their published values (where provided). The first pair of columns shows the strongly damped w-modes (not the $\bar{w}$-modes); the second pair and third pair of columns show the frequencies and damping times of the ordinary (f and p_1 to p_4) and superfluid modes ($\bar{s}_0$ to $\bar{s}_4$), respectively.

Highly damped modes (w)		Slowly damped modes ($f, p, \bar{s}$)			
		ordinary		superfluid	
$\mathrm{Re}(\omega M)$	$\mathrm{Im}(\omega M)$	$\mathrm{Re}(\omega M)$	$\mathrm{Im}(\omega M)$	$\mathrm{Re}(\omega M)$	$\mathrm{Im}(\omega M)$
0.428	0.397	0.1374	$7.171 \cdot 10^{-5}$	0.1568	$4.113 \cdot 10^{-7}$
0.510	0.194	0.3060	$6.539 \cdot 10^{-6}$	0.3545	$5.057 \cdot 10^{-6}$
0.853	0.316	0.4493	$3.154 \cdot 10^{-7}$	0.5239	$5.624 \cdot 10^{-8}$
1.190	0.369	0.5854	$5.611 \cdot 10^{-8}$	0.6877	$3.238 \cdot 10^{-8}$
1.523	0.406	0.7185	$3.223 \cdot 10^{-9}$	0.8443	$6.295 \cdot 10^{-9}$

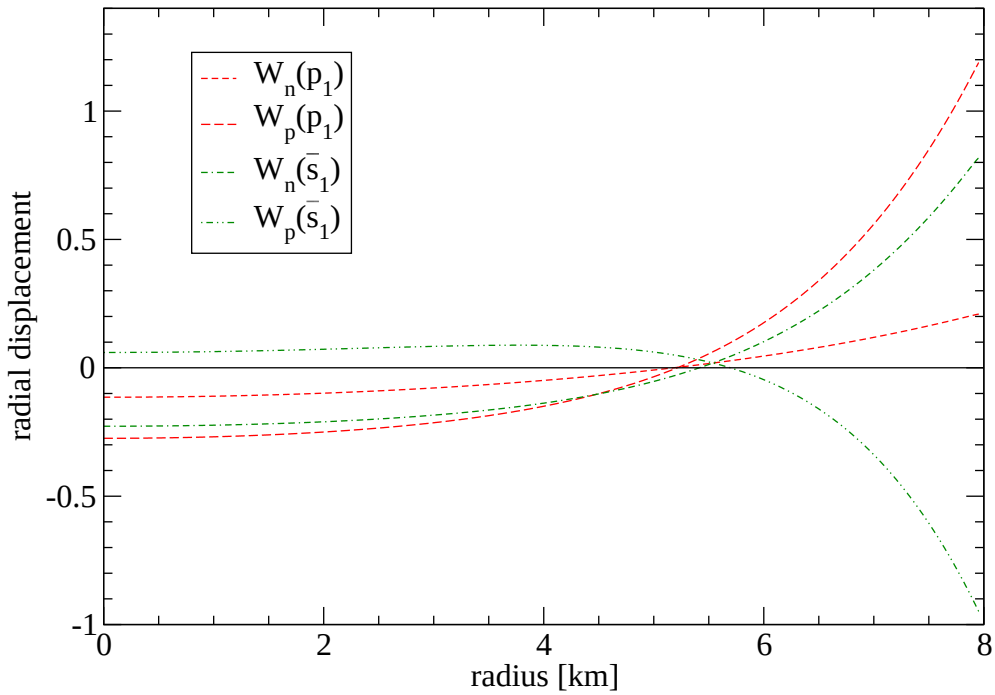

Figure 4.8: The eigenfunctions of the radial displacements of the first ordinary (dashed lines) and superfluid (dash-dotted lines) pressure mode. While the displacements of neutrons and protons are in phase for the ordinary mode, they are out of phase in case of the superfluid mode.

from the shear modes. By their eigenfunction, these different modes are quite easy to distinguish. As an example, we show the eigenfunctions of the two radial displacement variables W_{n} and W_{p} of the p_1- and the $\bar{s}_1$-mode in Figure 4.8; they clearly exhibit one node in radial direction as we expect from p-modes. The key feature of this graph is that the motion of the two fluids are in phase in case of the ordinary mode; for the superfluid mode, which has a slightly higher frequency, the neutrons and protons are counter-moving—their motion is out of phase. This also explains the different damping times which in many cases are much longer for the superfluid modes than for the ordinary modes. When the two fluids in a superfluid mode are counter-moving, the mass distribution of the whole star changes much less than it would if the two fluids were comoving; hence, the impact on space-time is lower and subsequently the gravitational wave emission due to this mode is reduced. This immediately raises the question if it could be that a particular oscillation mode is such that the motions of the fluids counteract each other in a way so that no gravitational radiation is emitted at all. Andersson et al. [36] have proven that such modes can exist only in stars whose matter obeys an EoS which belongs to a very special (and unrealistic) class; thus, we will always expect some gravitational radiation from each mode.

We have also calculated the damping times of the five lowest f- and p-modes; we show them in Table 4.5 and plot them in Figure 4.9. The graph suggests that the damping times of the ordinary modes are exponentially decreasing (the crosses lie nearly on a straight line) with mode frequency; there is also no sign of a "kink" between the first and second p-mode which we observed in the case of the perfect fluid star we considered earlier (cf. Section 3.10.1). The damping times of the superfluid modes, however, seem irregular. They are often but not always considerably longer than the damping time of the respective ordinary mode and amongst the first five damping times we cannot detect any pattern; in order to rule out numerical errors, we performed a convergence test on these modes, see Section 4.10.1. Unfortunately, the finite precision of the numerics prevents us from reliably determining damping times of higher order modes.

We do not show the very low frequency domain of the spectrum. Even though we demonstrated in Section 4.6, where we discussed the single fluid limit of the multi-fluid equations, that the variational approach accounts by construction for stratification, which generally leads to the existence of g-modes, we do not observe any evidence for gravity modes in this two-fluid neutron star model. This is in accordance with the analysis of Andersson & Comer [82]; they showed that a two-fluid star, consisting of individual neutron and proton fluids, does not support g-modes. However, the two fluids give rise to two independent sets of high-frequency modes; these are, firstly, the ordinary f- and p-modes which we already know from single fluid stars and are acoustic waves travelling with the speed of sound, and secondly, a similar set of superfluid modes which exist as a result of the two independent fluids; the frequencies of the latter

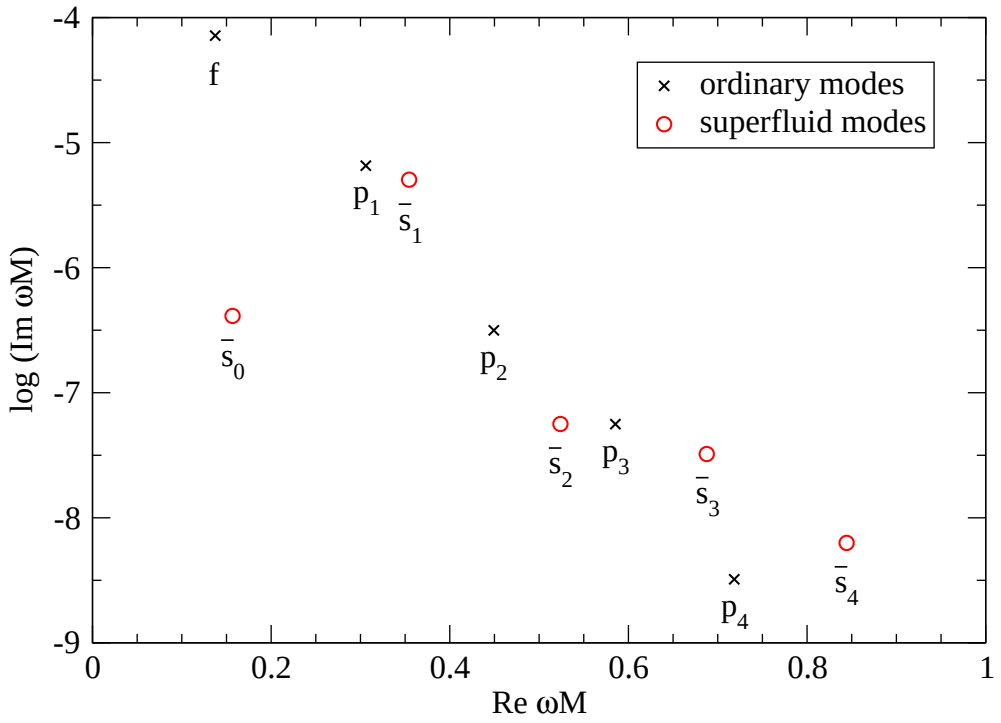

Figure 4.9: The complex frequencies of the slowly damped modes of Model Two of CLL99. The crosses are for the ordinary modes; they lie—to good approximation—on a straight line which suggests exponential decrease of the damping time with mode frequency. The circles denote the frequencies of the superfluid modes and there is no obvious pattern.

modes are governed by the proton speed of sound. Both sets of modes share the same characteristics; they have an infinite number of members and their frequencies obey $\mathrm{Re}(\omega_n) \to \infty$ as $n \to \infty$ (where n is the number of nodes in the radial direction); both sets are intertwined in the high frequency spectrum of the star. The findings from our test runs above confirm these analytical results.

Convergence Test for the Superfluid Modes

For completeness, we perform a convergence test on the frequencies and damping times of the superfluid modes as their damping times appear to be irregular; this irregularity may be a numerical artefact due to the fact that the imaginary part of the eigenfrequency ω is several orders of magnitude smaller than the real part. If we, for example, demand an accuracy of 10^{-5}, we should not expect to find reliable results for the damping time of the mode $\bar{s}_3$ as $\mathrm{Im}(\omega(\bar{s}_3))/\mathrm{Re}(\omega(\bar{s}_3)) < 10^{-7}$.

As in Section 3.10.1, we keep the accuracy of the background fixed at 10^{-12} and vary merely the accuracy of the perturbations; we show the results for the convergence test of the mode $\bar{s}_3$ in Figure 4.10; a straight line given as in equation (3.186) approximates

the results best with the coefficients

$$\left.\begin{aligned} a &= 0.5423 \pm 0.0529 \\ b &= -2.556 \pm 0.359 \end{aligned}\right\} \quad \text{for the real part,} \tag{4.272}$$

$$\left.\begin{aligned} a &= 0.5609 \pm 0.0701 \\ b &= 0.07831 \pm 1.09 \end{aligned}\right\} \quad \text{for the imaginary part.} \tag{4.273}$$

As expected, the accuracy of the damping times (related to the y-intercept given by b) is worse compared to the accuracy of the frequency. (The error of 1.09 in the y-intercept for the fit of the imaginary part appears to be large but can be put into perspective by noting that the value of b is very close to zero just by coincidence.) However, the convergence speed of both components is nearly the same; the convergence is clearly visible and we find comparable results for all other superfluid modes as well as the normal fluid pressure modes. The apparent irregularity of the damping times of the superfluid modes is, hence, no numerical artefact.

We would like to point out one more peculiarity of the convergence tests which are visible only for slowly damped modes. As both the frequency and the damping time are encoded in the same quantity—the complex variable ω—and the damping time (the imaginary part of ω) is usually between 5 and 10 (or more) orders of magnitude smaller than the frequency (the real part), we would expect a much more inaccurate solution for the damping time than for the frequency. However, our convergence tests show a somewhat different behaviour in several cases. E.g. in Figure 4.10, the damping time is accurate to only about two fewer digits than the frequency, even though their magnitude differs by seven orders of magnitude. We have no obvious explanation for that, but we could argue that it is possible, due to the smallness of the imaginary part, firstly, to treat it as a perturbation to a purely real-valued variable ω, and secondly, that the real and imaginary part of the perturbation equations (which are coupled only via the appearance of ω^2) fully decouple if such a decomposition is assumed (and quadratic terms of the imaginary part are neglected by means of linearisation). This way, frequency and damping time can be calculated separately and would both be accurate to some desired level. However, the actual realisation of such a decomposition is very tedious and not prioritised in this study, which is why we cannot show further details here.

4.10.2 The Perturbations of a Realistic Multi-Fluid Star

We have demonstrated that our implementation of the multi-fluid approach reproduces literature values to excellent agreement. We can move on and investigate the dynamics of our model neutron star, which we have considered to consist of a single fluid in Section 3.10.3, in more detail now. Instead of treating the neutron star core as a single

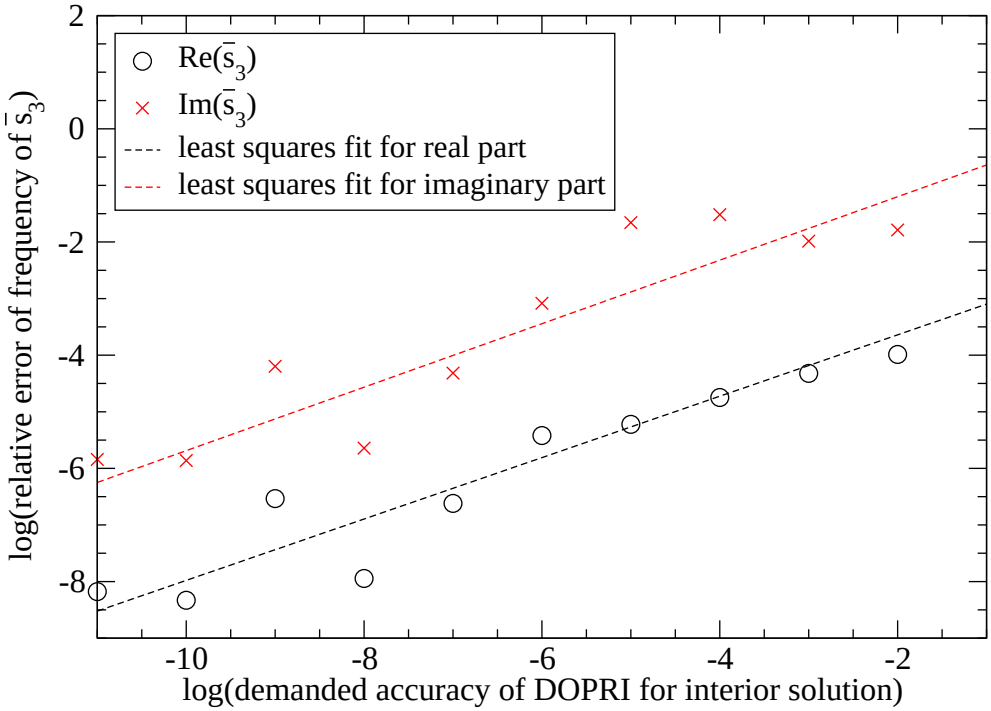

Figure 4.10: The convergence test for the $\bar{s}_3$-mode. We show the relative error of both the real and imaginary part of the frequency of this mode and plot it against the demanded accuracy of the DOPRI solver. The convergence of the solution is clearly visible; the straight, dashed lines are least squares fits to the respective data points. Note that the two plotted quantities (real and imaginary part) are not fully independent and we expect the imaginary part to be less accurate as it is several orders of magnitude smaller than the real part.

fluid and using a tabulated version of the EoS, we will now specifically consider the core to consist of neutrons, protons, electrons and possibly muons and account for the possibility of superfluidity. As a reminder, our neutron star model has the following characteristica: a central neutron number density of $n_{\mathrm{n}}(0) = 0.5067\,\mathrm{fm}^{-3}$ (equivalent to $\rho_c = 1 \cdot 10^{15}\,\mathrm{g\,cm}^{-3}$), which leads to a radius of $R = 11.771\,\mathrm{km}$ and a mass of $M = 1.447\,M_\odot$. The EoS we use will again consist of two parts; the DH EoS for the crust and the SLy4 force for the core. As we consider multi-fluids now, we will use the analytical representation of the core EoS instead of resorting to a tabulated variant.

As a first test case, we assume that the entire core of the star is superfluid while the crust behaves like a perfect fluid. We point out that we will not encounter such a neutron star model when we use the cooling sequence for more realistic results later; a mature neutron star constructed as part of our cooling sequence will indeed have an entirely superfluid core, however, it would also possess a crystallised crust and our simulations would account for thermal pressure. We neglect both of these properties for testing purposes. We can then compare these results to the case where we model the star as perfect fluid (at zero temperature).

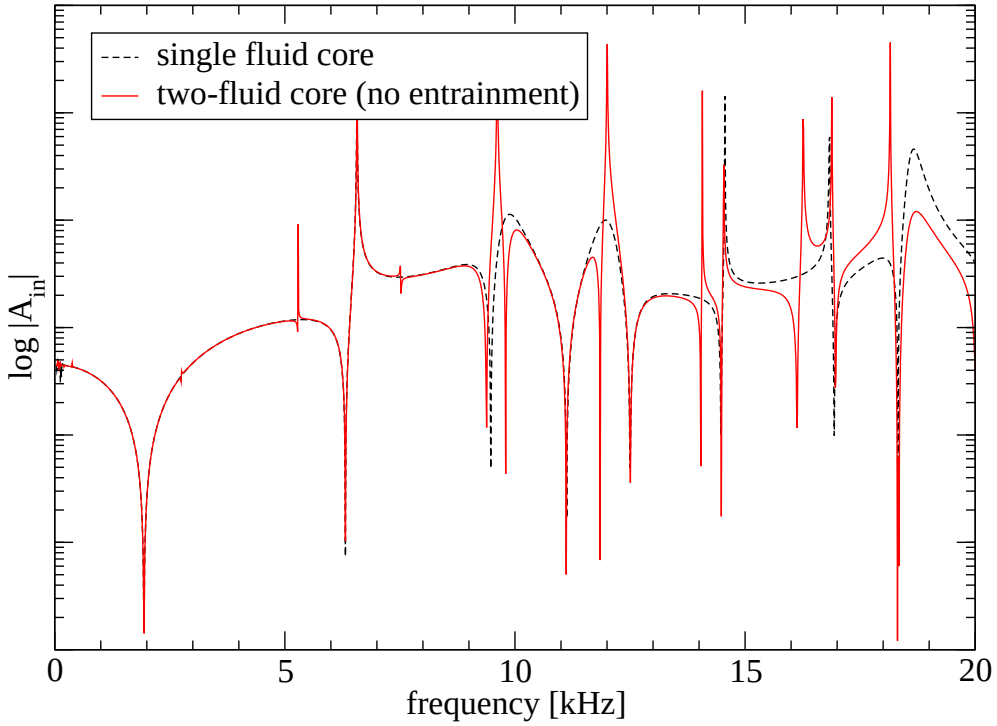

Figure 4.11: The high frequency spectra of our model neutron star (both at zero temperature). The dashed line is for the star modelled entire as a perfect fluid, the solid line is for the star where we treated the whole core as a two-fluid system. We have also artificially set the entrainment to zero.

In Figure 4.11, we show the high frequency spectra of our neutron star model at zero temperature. We compare the spectrum for the star when it is modelled entirely as a perfect fluid, to the spectrum when the whole core is considered superfluid. We have also switched entrainment off for this particular test, $\mathcal{A}^{\rm np} = 0$. We make two key observations: firstly, all pressure modes of the single fluid system are still eigenmodes of the multi-fluid system (the frequencies are altered only marginally), secondly, we find a series of new modes in the spectrum. These new modes are due to the presence of the superfluid component in the neutron star core.

When we try to assign the modes to the sets of ordinary and superfluid modes based on their eigenfunctions, we are confronted with a new difficulty. While this assignation was fairly easy in the polytropic case, this is not possible in an unambiguous way anymore. The key difference is that the two individual fluids (the neutron and the proton fluid) are physically more different than they are in the polytropic case; in that case, the corresponding eigenfunctions of the displacement, $W_{\rm n}$ and $W_{\rm p}$, bore similarity to each other and were easy to classify as counter- or co-moving. We do not find this behaviour in our realistic neutron star model anymore; the eigenfunctions of $W_{\rm n}$ and $W_{\rm p}$ of a particular mode are in most of the cases quite different in their overall behaviour and exhibit a quite different number of nodes in the radial direction (which previously

used to be a criterion for the determination of the order of a p-mode). We find that the linear combination $\tilde{W} := \mu_{\rm n} n_{\rm n} W_{\rm n} + \mu_{\rm p} n_{\rm p} W_{\rm p}$, which appears in the differential equation (4.163b) for K' (and reduces to $(\rho + p)W$ in the case of identical displacements), serves as a good indicator for the nature of a mode; while the individual displacements $W_{\rm n}$ and $W_{\rm p}$ may have very different characteristics, we observe that $\tilde{W}$ allows us classify a mode according to the number of its nodes. Another important point is that the eigenfunction of a mode may exhibit a radial node within the crust (or, more general, in a region of the star which is modelled as a single fluid) which would be hidden if we looked at the variables $W_{\rm x}$ only; these are not defined for a single fluid.

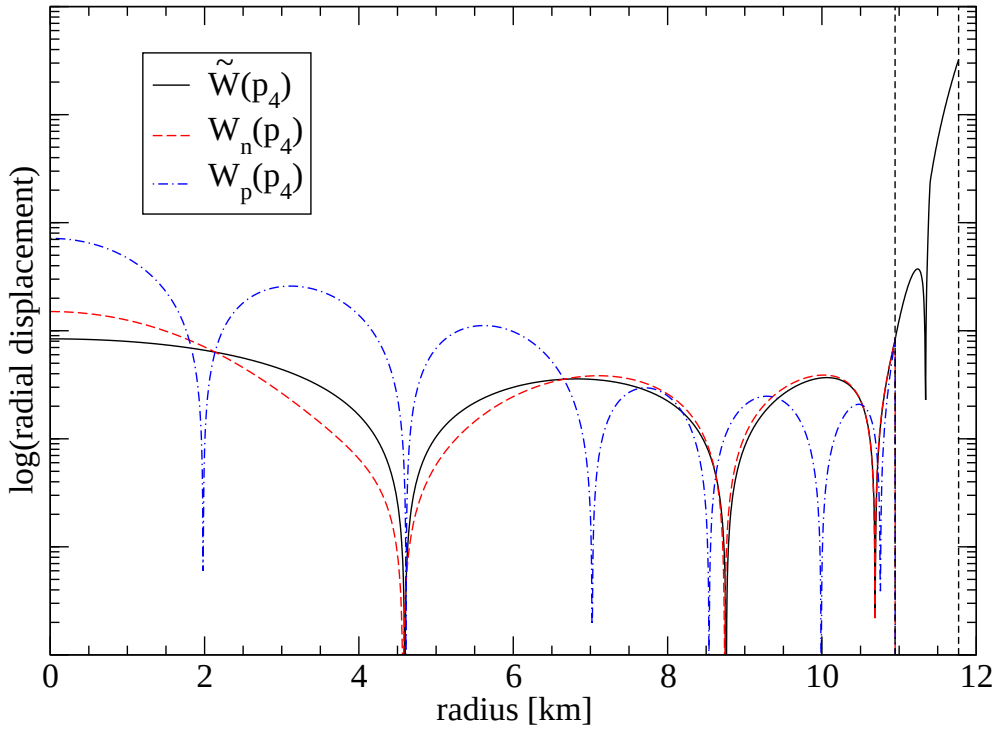

Figure 4.12: The radial displacements $W_{\rm n}$ and $W_{\rm p}$ as well as their linear combination $\tilde{W}$ (see text for details) of the p_4-mode. The proton eigenfunction is clearly different from the neutron or the combined eigenfunction. Note that $W_{\rm n}$ or $W_{\rm p}$ are not defined in the single fluid part of the star (the crust). The model star has a two-fluid core (with no entrainment), a single fluid crust, and sustains no thermal pressure; we show the crust-core interface as well as the surface of the star with dashed lines.

As an example, we show the radial displacements of the p_4-mode at 12.51 kHz in Figure 4.12 which is also an eigenmode of the purely single fluid system (at 12.50 kHz). The combined eigenfunction $\tilde{W}$ clearly exhibits four nodes in the radial direction (and is essentially identical to the eigenfunction of W in the corresponding p_4-mode in the single fluid star). While the neutron eigenfunction $W_{\rm n}$ is nearly identical in the core region (it is not defined outside the core), the proton eigenfunction $W_{\rm p}$ displays an entirely different behaviour; it exhibits six nodes within the core region and they are at locations very different from the nodes of the neutron eigenfunction.

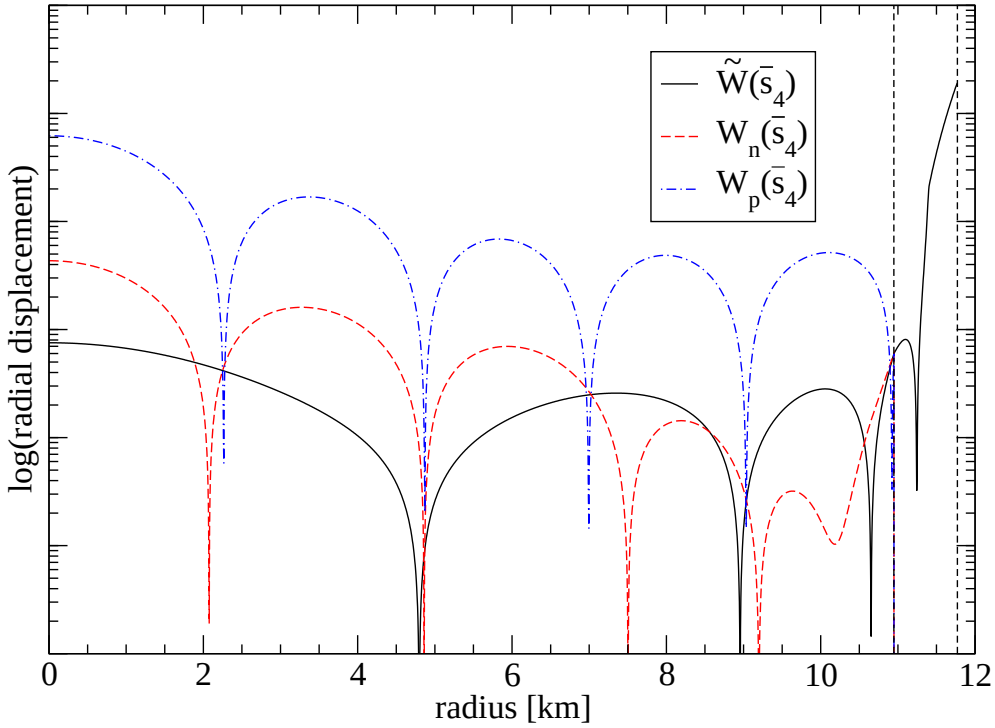

Figure 4.13: As Figure 4.12 but for the superfluid mode at 11.85 kHz. The eigenfunction $\tilde{W}$ exhibits four nodes in the radial direction and it looks very similar to $\tilde{W}$ in the other graph (the radial nodes are only a few tenths of metres apart). However, the displacement eigenfunctions $W_{\rm n}$ and $W_{\rm p}$ differ drastically from $\tilde{W}$; in amplitude as well as number and location of nodes.

We continue this example and show the same graph in Figure 4.13 but for the mode at 11.85 kHz; its eigenfunction $\tilde{W}$ also exhibits four nodes in the radial direction. We denote it therefore with $\bar{s}_4$. We do not show it explicitly, but the eigenfunctions $\tilde{W}(p_4)$ and $\tilde{W}(\bar{s}_4)$ are very similar; their radial nodes are only a few tenths of metres apart and their overall amplitudes do not differ very much. We observe that the displacement eigenfunctions $W_{\rm n}$ and $W_{\rm p}$ of the individual fluids have essentially no characteristics in common with their linear combination $\tilde{W}$; they have four and five radial nodes within the core, respectively. We also see that the amplitude of the proton eigenfunction is about one order of magnitude larger than that of the neutron eigenfunction. Looking at both graphs in Figures 4.12 and 4.13, we realise that the distinction of co- and counter-moving fluids, which was obvious in the polytropic case, turns out not to be as useful in the realistic case.

Our approach of dividing the high frequency modes into ordinary and superfluid ones is by comparing to the single fluid spectrum; p-modes which are also eigenmodes of the single fluid star go into the ordinary bin while the others go into the superfluid bin. The result of this procedure is shown in Table 4.6, where we list the frequencies and damping times of the f- and some p-modes for the single fluid star as well as for the

Table 4.6: The frequencies and damping times of the first few f-, p- and $\bar{s}$-modes of our neutron star. We compare the single fluid model to the two-fluid model where we assume the entire core to be superfluid. We have grouped the high frequency modes by the number of radial nodes in $\tilde{W}$ as described in the text. Where a mode p_n or $\bar{s}_n$ exhibits a different number of nodes than n, we note the number in brackets next to the frequency.

	Single Fluid Core		Two-Fluid Core				
			ordinary		superfluid		
Mode	f [kHz]	τ [ms]	f [kHz]	τ [ms]	f [kHz]	τ [ms]	
f	1.938	186	1.938	186	2.750 (1)	1.67e6	$\bar{s}_0$
p_1	6.315	4071	6.317	4116	5.287	4.70e5	$\bar{s}_1$
p_2	9.476	1.65e6	9.381	2.43e6	7.522	1.92e6	$\bar{s}_2$
p_3	11.12	2.15e6	11.11	2.13e6	9.797 (2)	4.85e6	$\bar{s}_3$
p_4	12.50	7.13e6	12.51	7.82e6	11.85	4e8	$\bar{s}_4$
p_5	14.48	2.9e7	14.48	5e8	14.04 (8)	–	$\bar{s}_5$
p_6	16.94	2e8	16.97	–	16.13	–	$\bar{s}_6$
p_7	18.32	–	18.31	–	18.34	–	$\bar{s}_7$
p_8	20.18	–	20.02	–	20.61	–	$\bar{s}_8$
p_9	22.31	–	22.27	–	22.62 (12)	–	$\bar{s}_9$

star with a two-fluid core; for higher order p-modes, our code is not able to determine the damping times reliably or does not converge at all. Whenever the number n of nodes in the radial direction does not correspond to the order of the eigenmode, we show the actual number of nodes in parentheses. For example, we find two superfluid modes with two nodes but none with three nodes. Another outlier is the mode at 14.04 kHz which surprisingly exhibits eight radial nodes instead of five.

We repeat this calculation with entrainment, i.e. we consider our model neutron star again with no elastic crust, no thermal pressure and a two-fluid core while accounting for entrainment. We compare the spectrum of this star to the spectrum of the single fluid star in Figure 4.14. As before we find that p-modes of the single fluid star are—in most cases—still eigenmodes of the two-fluid star. However, the discrepancy when accounting for entrainment is a bit larger than in the star without entrainment. We encounter the same difficulties as in the case without entrainment when we try to split the modes into ordinary and superfluid modes: we resort to the linear combination $\tilde{W}$ (defined as above) in order to determine the order of a p-mode; the eigenfunctions of the individual displacements W_{n} and W_{p} show a similarly "arbitrary" behaviour with no obvious link (regarding amplitude or location and number of nodes) to $\tilde{W}$.

We show the frequencies and damping times (where accessible to us) of the entrained model in Table 4.7. In two rows, there appears "N/A" for the frequency and

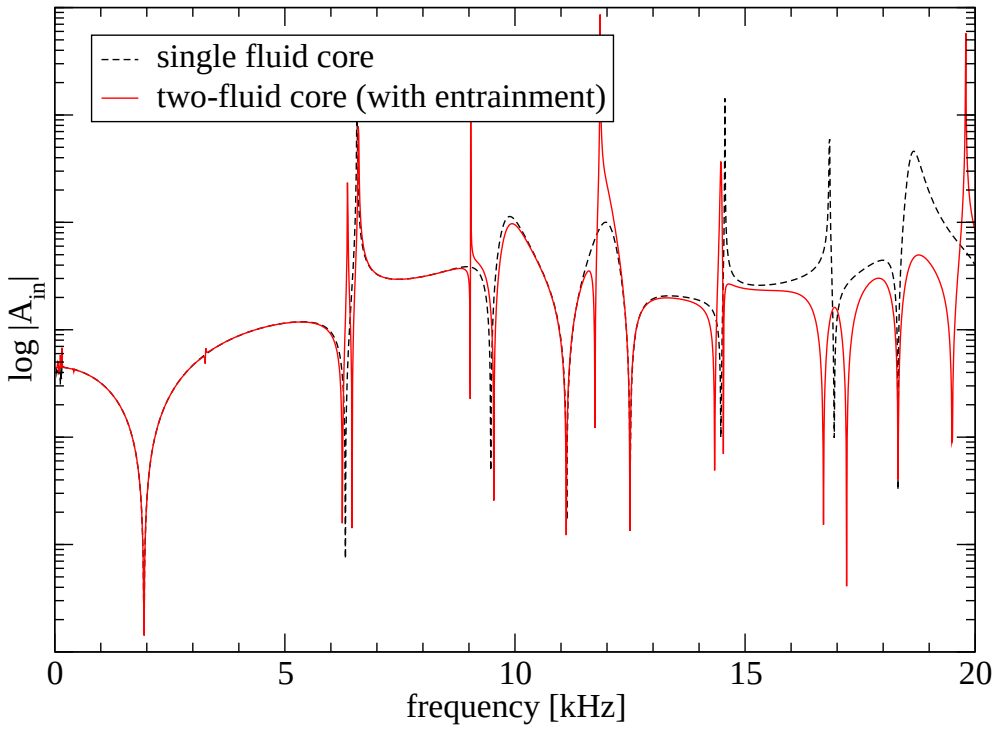

Figure 4.14: As Figure 4.11 but with entrainment switched on. While the ordinary modes are hardly affected, the superfluid modes got shifted to higher frequencies.

Table 4.7: As Table 4.6, but we account for entrainment in the core.

	Single Fluid Core		Two-Fluid Core				
			ordinary		superfluid		
Mode	f [kHz]	τ [ms]	f [kHz]	τ [ms]	f [kHz]	τ [ms]	
f	1.938	186	1.938	186	3.274 (1)	1.35e6	$\bar{s}_0$
p_1	6.315	4071	6.251	5768	6.460	1.389e4	$\bar{s}_1$
p_2	9.476	1.65e6	9.540	1.62e6	9.027	2e9	$\bar{s}_2$
p_3	11.12	2.15e6	11.12	1.67e6	N/A	N/A	$\bar{s}_3$
p_4	12.50	7.13e6	12.50	7.69e6	11.74	3e8	$\bar{s}_4$
p_5	14.48	2.9e7	14.34	3.8e7	14.53	–	$\bar{s}_5$
p_6	16.94	2e8	16.70	–	17.21	–	$\bar{s}_6$
p_7	18.32	–	18.33	–	N/A	N/A	$\bar{s}_7$
p_8	20.18	–	19.50	–	20.21	–	$\bar{s}_8$
p_9	22.31	–	22.28	–	22.20 (12)	–	$\bar{s}_9$

damping time; that is, we are unable to find superfluid modes with three or seven nodes, respectively. Instead of continuously counting the superfluid modes, we decide that it makes more sense to skip some ordinals. This way, we ensure that the superfluid mode $\bar{s}_n$ has n nodes (apart from a few exceptions) and its frequency is usually comparable to the frequency of the ordinary mode p_n.

4.10.3 The Return of the g-modes

In Section 4.10.1, we discussed the tests of our multi-fluid code against other formulations of the equations or literature values using simple neutron star models. For the multi-fluid models, there was no need to discuss the low-frequency spectrum since Andersson & Comer have proved mathematically that it is void of eigenmodes [82]; a high resolution run quickly confirmed this result (up to a certain finite but high resolution). However, the observant reader will have noticed that the very low frequency part (at frequencies below 500 Hz) of the spectra in Figures 4.11 and 4.14 is not smooth. It turns out that this is not an artefact of our numerical implementation but something physical is going on there. We will therefore reconsider the low frequency problem.

Andersson & Comer [82] studied the perturbation equations of multi-fluid stars in the Newtonian limit; the advantage of this approach is that these equations are easier to handle since the underlying theory is simpler (compared to general relativity), however, we can expect quantitatively comparable results. Their investigation of two-fluid stars, consisting of a neutron and a proton fluid, reveals that such stars do not support g-modes at non-zero frequencies. This is somewhat counter-intuitive as one might have expected one set of g-modes for each of the two fluids; however, the presence of two individual fluids counteracts the buoyant forces (when a fluid element of one fluid is shifted out of equilibrium then, rather than experiencing buoyancy, a fluid element of the other fluid moves accordingly eliminating the buoyant force on the former fluid element), preventing the existence of low-frequency modes in such stars.

What is going on at low frequencies in Figure 4.11? Instead of zooming into this region, we will first consider a simpler neutron star model; more precisely, we will strip off the perfect fluid region (which is calculated using a rather complicated, tabulated EoS) surrounding the star's core and investigate only an entirely superfluid neutron star core, for which we use our analytically given SLy4 force. We construct this neutron star model by prescribing the same central neutron number density of $n_{\mathrm{n}}(0) = 0.5067\,\mathrm{fm}^{-3}$ but then discontinue the integration of the background equations once we reach the bottom of the core at 10.948 km; it has a mass of $M = 1.437\,M_{\odot}$. Another important value is the radius $R_{\mu} = 10.648\,\mathrm{km}$, which is where muons start to appear; only the outermost 300 m of the core consist of muon-free matter, most of it is an npeμ-conglomerate. We note that these dimensions obviously depend on the central density of the star; in a less compact star, we have to penetrate the star much deeper before we find muons.

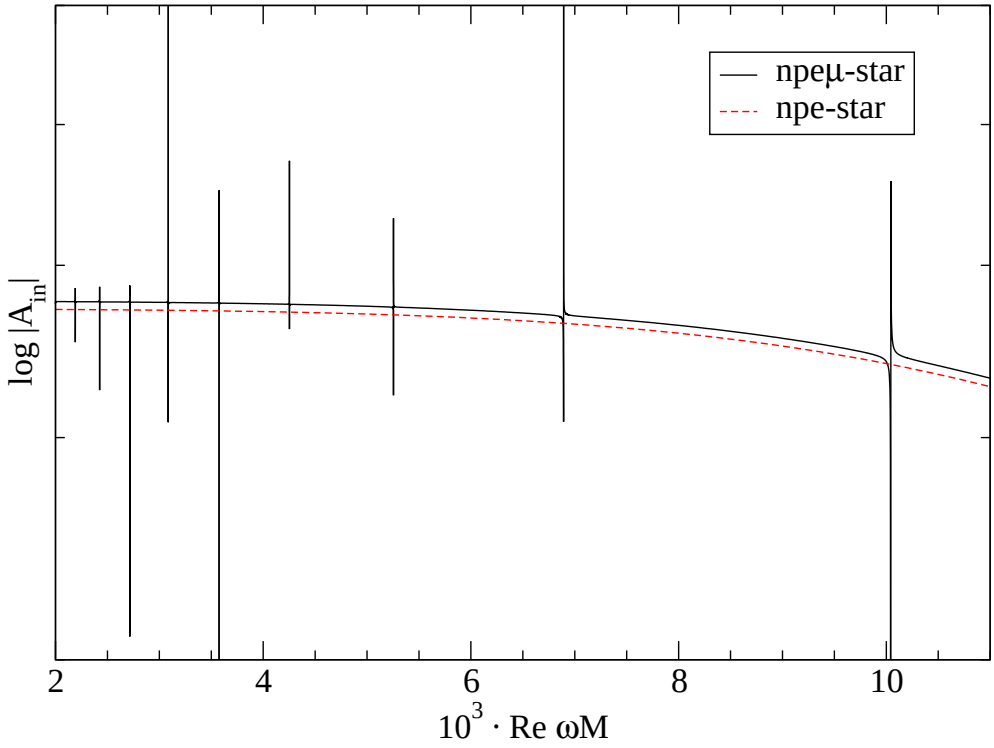

Figure 4.15: The low frequency domain of the spectra of superfluid neutron star *cores* (see text for explanation). The solid line is for a core consisting of npeμ-matter, whereas the dashed line is for muon-free matter. It is obvious that the presence of muons gives rise to low frequency modes.

We show the low frequency spectrum in Figure 4.15, where we find a series of modes below $\mathrm{Re}(\omega M) \approx 0.186$ (for clarity we zoom in on a region at lower frequencies); these modes are indeed g-modes. To understand their origin (after we have argued that superfluid stars do *not* support g-modes), we show the spectrum of a purely npe-core in the same graph; it is perfectly void of modes. The new modes are apparently closely linked to the presence of muons in the core. This makes sense since only the muons introduce a composition gradient *within the proton fluid*; this in turn means that a fluid element of the proton fluid is, in fact, subject to buoyant forces originating from the proton fluid. In contrast, when we remove the muons from the star, charge-neutrality imposes the condition $n_\mathrm{p} = n_\mathrm{e}$ throughout the star which means that the composition of the proton fluid is constant; a fluid element of the proton fluid will not experience buoyancy when traveling within the proton fluid.

This discussion makes clear that g-modes are a feature of individual, stratified fluids. A composition gradient between two interpenetrating (super-)fluids will not give rise to g-modes and this is what has been proven in [82]. Taking this further, if both fluids were to have a composition gradient, then (without proof) we would expect to find two sets of g-modes. However, in our simulations merely the proton fluid is intrinsically stratified whereas the neutron fluid is not; thus, we will find one set of g-modes.

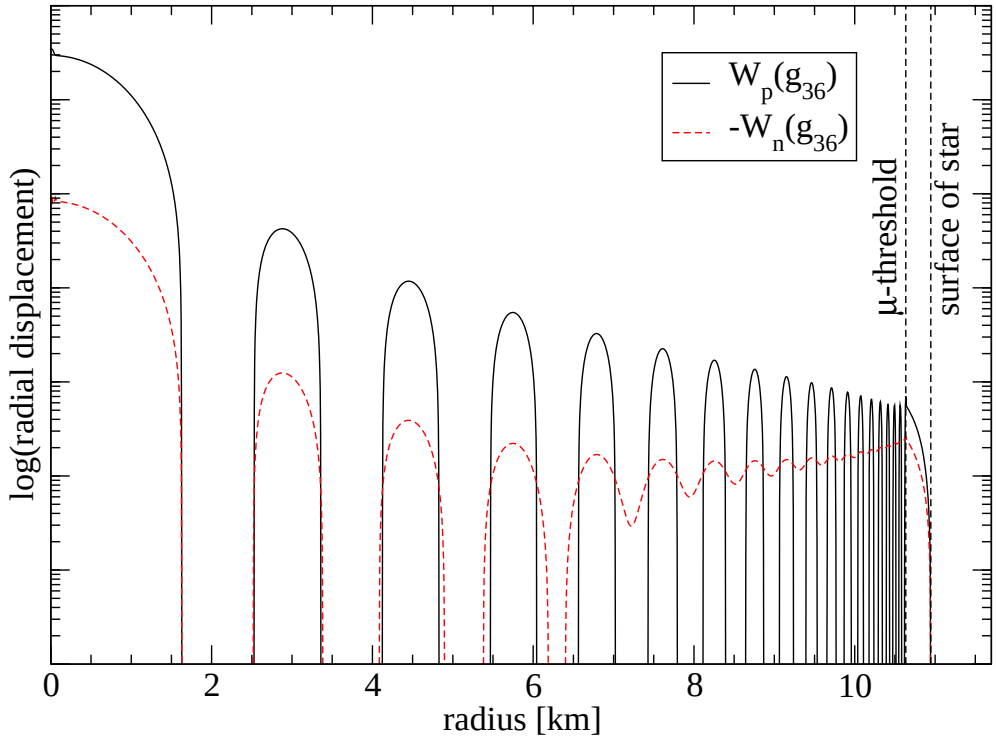

Figure 4.16: The radial displacement eigenfunctions of the mode g_{36} of the npeμ-core. The two dashed vertical lines are for the appearance of muons in the core and for the surface of the core, respectively. The eigenfunctions show clear characteristics of a g-mode: the amplitude is largest at the center of the star and the radial nodes accumulate towards the outer boundary of stratification. Furthermore, it is obvious that the radial nodes are confined to the region with muons present. The eigenfunction associated with the neutron fluid exhibits nodes only in the deep core. We have chosen to display $W_{\rm p}$ along with the negative of $W_{\rm n}$ in order to clearly show their behaviour in the outer layers of the core (plotting the magnitude would have made the graph less clear); hence, the motion of protons and neutrons is *out of phase* in the deep core.

In Figure 4.16, we show the eigenfunction of the 36th g-mode of our neutron star core which we find at $\mathrm{Re}(\omega M) = 6.1678 \cdot 10^{-4}$. We have intentionally chosen this rather high order for several reasons. Firstly, because we can; it demonstrates the high accuracy of our code and it poses no difficulty to isolate this mode from others in close vicinity in the spectrum and the 36 nodes in radial direction are well resolved. We could have shown the eigenfunctions of a mode with even higher order but we chose not to do so for the clarity of presentation. Secondly, we clearly see that the characteristic behaviour of the g-mode is well confined to that region of the star where muons exist; the amplitude is largest in the center of the star whereas the nodes accumulate towards the boundary of the stratified region—there are no nodes within the small muon-free layer of 300 m thickness at the outer edge of the core. This provides another clear link to the presence of muons. Thirdly, it is merely the radial displacement $W_{\rm p}$ of the proton fluid that actually exhibits nodes; the radial motion of the neutron fluid

(shown by W_{n} in the graph) follows the proton fluid to some extent but it exhibits nodes only deep in the core. There, their motion is *out of phase* with the protons (note that we have plotted the negative of W_{n}); we find this behaviour in general: when the radial displacement of both proton and neutron fluid exhibits nodes then the nodes are located at very similar locations and both fluids are out of phase. Anyway, the lack of nodes in the neutron displacement in conjunction with the presence of the nodes in the proton fluid proves the fact that the proton fluid is the origin of the g-modes; the neutron fluid plays more of an observer role.

When we enclose this naked core by the DH crust, the spectrum gets enriched by the interface modes due to the phase transitions there; the g-modes are not affected as their origin lies entirely in the core (the physics of which remains untouched). The frequencies of the i-modes are identical to the ones we found for a barotropic star in Section 3.10.3. Since there is nothing new, we will not further elaborate on this case.

4.10.4 The Temporal Evolution of the Stellar Spectrum

The next logical step after we have considered an entirely superfluid core surrounded by a fluid crust, is to advance to more realistic neutron star models. This implies that we have to account for the superfluid gap as well as the crust crystallisation. In the following, we will summarise how we determine the structure of our model neutron star and what approximations we make for simplicity.

In order to do this in a somewhat realistic way, we will reuse the cooling sequence which we already considered in the first chapter; given a temperature profile, we will not only determine where the crust is solid but also in which region of the core neutrons or protons are superfluid. For the crust, we will strictly use the criterion $\Gamma_m > 173$ (with Γ_m as defined in equation (3.95)) from Section 3.5.1 in order to determine where the crust has solidified, whereas in the core we will employ the gap model described in Section 4.7. That is, we consider crust and core essentially separately. In reality, the free neutrons in the crust will form a superfluid in a certain region, too, and permeate the elastic crust (or the perfect fluid where matter has not solidified yet). However, we will account for thermal pressure due to neutrons and protons in the crust in the same way as we have laid out in Section 3.4. In the core region, we use the superfluid gap model to determine whether *any* of the present species is superfluid but we will not distinguish between different superfluids; once the temperature drops below any of the four critical temperatures at some point in the core, we consider this location to be superfluid and then employ the two-fluid equations in this region. As a last approximation, we use the cooling sequence as calculated for a perfect fluid star; that is, even though we consider superfluid cores, we do not account for its effect on the cooling process. This is in line with the ad hoc EoS which we use to construct our neutron star models; both EoS and temperature profiles are parameters of our simulations which can easily be exchanged once more realistic data are available.

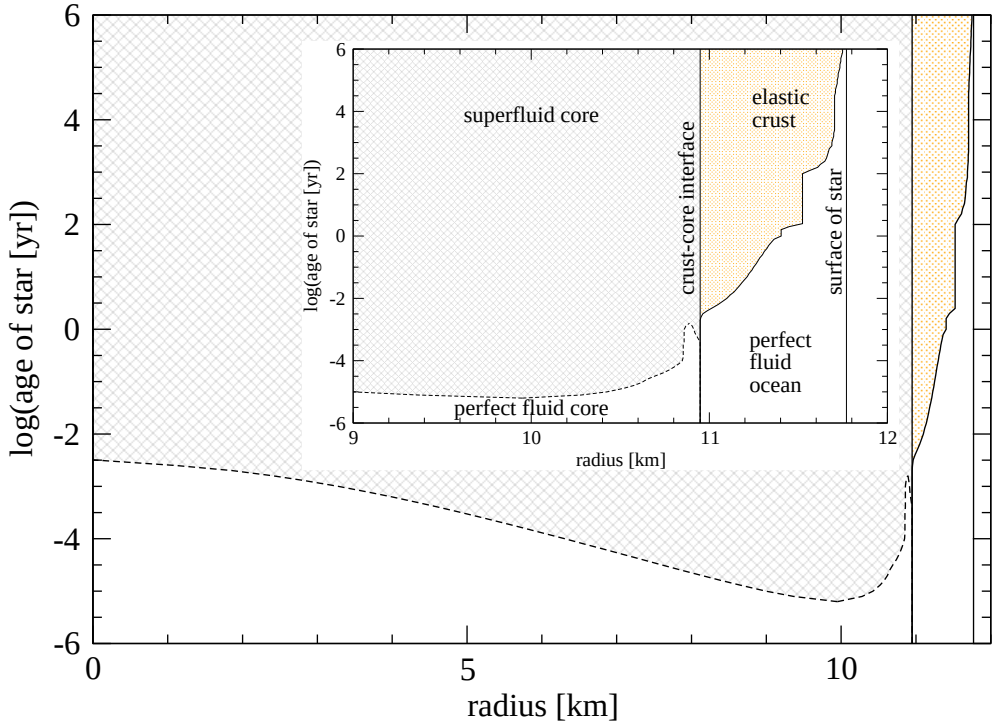

Figure 4.17: The evolution of the state of the neutron star matter. The inset zooms in on the outer layers of the star in order to make the features more clearly visible. At approximately $t \approx 4.2\,\mathrm{min}$, the neutrons in the outer layer of the core become superfluid (note that the superfluid region does not extend to the crust-core interface); as the star cools, the superfluid region grows. After about $t \approx 4.4\,\mathrm{hr}$, a thin superfluid layer forms next to the crust-core interface (in fact, it extends into the crustal region of the star but we do not account for superfluidity outside the core at this stage). Both superfluid regions merge when the star is $t \approx 13.9\,\mathrm{hr}$ old and from this time onwards, the entire core of the star is superfluid (the region shaded in grey). The crust starts to crystallise at $t \approx 22\,\mathrm{hr}$ and its formation is as described in Section 3.5; the yellow shaded area depicts the region where the crust is solid.

We show the resulting radial profiles of our cooling sequence in Figure 4.17; this figure can be seen as an extension of Figure 3.1 where we have shown only the crustal region (since we treated the entire core solely as a single fluid). We now show the entire star and zoom in on the outer layers of the star in the inset figure. The region shaded in grey is the region where our model star is superfluid, the region shaded in yellow is elastic; both regions are separated by the crust-core interface and do not overlap. After about $t \approx 4.2\,\mathrm{min}$, a small superfluid regions emerges in the outer core at a radius of $r \approx 10\,\mathrm{km}$. This region grows quickly, primarily towards the center of the star. Up until about 1.1 days into the neutron star's life, its center is still above the critical temperature for the onset of superfluidity. Hence, we find a perfect fluid ball in the center of the star, enclosed by a superfluid shell of increasing thickness. However, before the central perfect fluid ball shrinks away, we notice a very thin superfluid layer forming at the crust-core boundary (at $t \approx 4.4\,\mathrm{hr}$). In reality, this layer would extend

into the crustal region of the star but we do not account for this fact at the moment. This second, thin layer exists for roughly 9.5 hours before the two superfluid regions merge into one region at $t \approx 13.9\,\mathrm{hr}$. Then, from the age of 1.1 days onwards, the entire core behaves as a two-fluid system. At this time the crust has already started to crystallise for a while (since $t \approx 22\,\mathrm{hr}$). We have described this process in detail in Section 3.5.1 and will therefore not repeat it here; the only difference being that the core now is a two-fluid system rather than a single fluid system.

Table 4.8: The layering of our model neutron star after about half a day ($t \approx 11.4\,\mathrm{hr}$) assuming the cooling sequence as described in Section 2.3.1. The crust has not crystallised yet; in the core of the neutron star, two regions have cooled below the critical temperature and are superfluid.

nature of layer	thickness [km]	region
perfect fluid	2.816	neutron star core
two-fluid	8.053	
perfect fluid	0.035	
two-fluid	0.045	
fluid ocean	0.823	neutron star crust

Table 4.9: The layering of our model neutron star after about $t \approx 21.9\,\mathrm{hr}$. Compared to the structure shown in Table 4.8, the superfluid layers in the core have grown and merged and the crust has started to crystallise.

nature of layer	thickness [km]	region
perfect fluid	1.116	neutron star core
two-fluid	9.833	
elastic crust	0.005	neutron star crust
fluid ocean	0.818	

After this discussion, it becomes obvious that the layering of the star in the radial direction can be fairly complex. In particular at an age where the core is nearly (but not entirely) superfluid and the crust has already started crystallising. For clarity, we pick two time points from our cooling sequence with a particularly complex layering structure and show the respective layers in Tables 4.8 and 4.9; the age of our neutron star is 11.4 hr and 21.9 hr, respectively. In the former case, we need five layers to describe our star, in the latter, we need four layers; their nature as well as their thickness is also given in the tables. We want to highlight that our code determines the necessary number of layers, their nature and thickness as well as the appropriate junction conditions

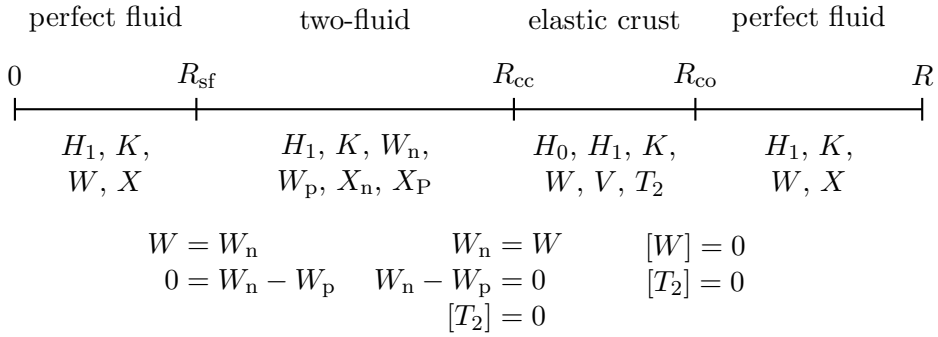

Figure 4.18: The schematic representation (not to scale) of the radial structure of our neutron star at an age of 21.9 hr, cf. Table 4.9. At this age, the star is described by four distinct layers, the nature of which is displayed in the top row; the interfaces between them are located at $R_{\rm sf} = 1.116\,{\rm km}$ (boundary of superfluidity within the core), $R_{\rm cc} = 10.948\,{\rm km}$ (core-crust interface), $R_{\rm co} = 10.953\,{\rm km}$ (crust-ocean interface). Directly below the horizontal line, we show for each region which perturbation variables are integrated within them; the applied junction conditions are aligned with the respective interfaces (we have omitted the continuity of H_0, H_1 and K as well as the boundary conditions at the center and surface of the star for clarity).

across the boundaries as given in Table 4.3 fully automatically once a temperature profile is given. As an example, the particular model at an age of 21.9 hr is split into four layers (one of them is quite thin with 5 metres width only); we show a schematic representation as generated by our code in Figure 4.18. Our code integrates $2 + 6 + 6 + 3 = 17$ linearly independent solutions within the layers (the number of solutions in the inner- and outermost layer are reduced due to boundary conditions) which are linked by 16 junction conditions across the three boundaries. This uniquely defines the inner problem (up to an arbitrary amplitude).

When we account for superfluidity of the free neutrons in the crust or employ more realistic cooling models (accounting for superfluidity in the core or heat sources etc.), we cannot rule out the possibility that even more layers are necessary for an accurate description of the star. No problem, our code is ready.

Let us now have a look at the spectra of the neutron stars along our cooling sequence. As usual, we combine the spectra into one graph that displays the evolution of the mode frequencies, see Figure 4.19 where we show the high frequency domain (up until $f = 20\,{\rm kHz}$) of the spectrum; we will explain below as to why we do not show the time evolution further than $\log(t/{\rm yr}) = -2.3$. At the very beginning of our cooling sequence, the entire star is too hot to have superfluid components and the crust has obviously not crystallised yet; thus, we observe the spectrum of a perfect fluid star with one f-mode and the first six p-modes. After about 4.2 minutes ($\log(t/{\rm yr}) = -5.1$), parts of the core matter becomes superfluid; the spectrum immediately gets enriched by the superfluid modes and the ordinary modes are essentially unaltered. The superfluid mode with the lowest frequency, $\bar{s}_0$, has a frequency of 2.471 kHz to start with and

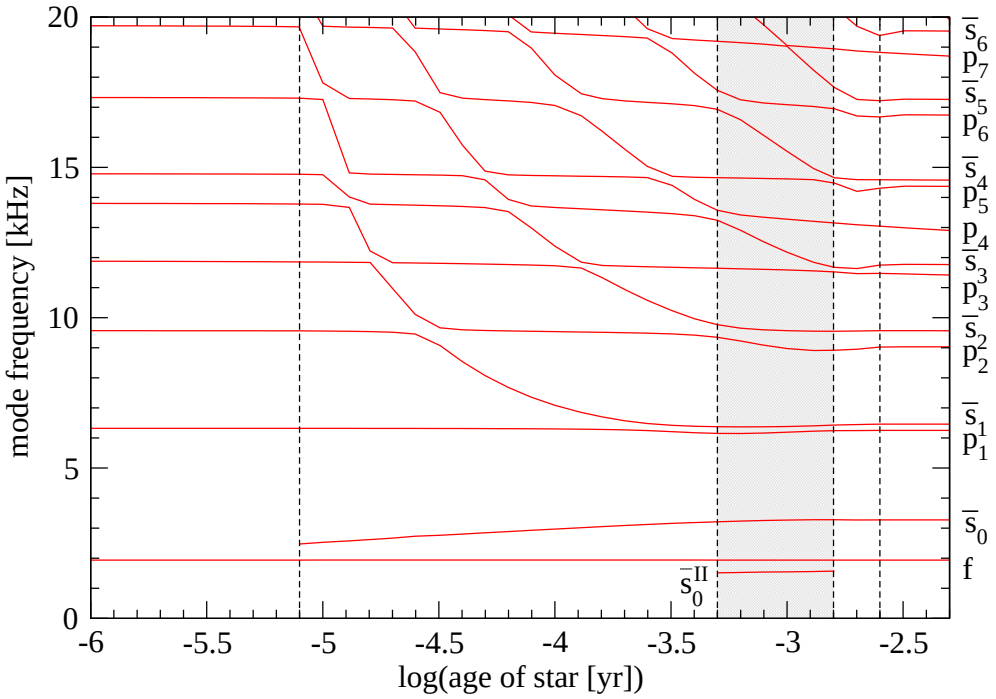

Figure 4.19: The evolution of the high frequency spectrum of our neutron star model over time. The vertical, dashed line at $\log(t/\mathrm{yr}) = -5.1$ depicts the earliest time at which we find superfluid matter in the core; the time period during which we find two separate superfluid layers (cf. Figure 4.17) is shaded in grey; for completeness, we show the beginning of the crystallisation of the crust which happens at $\log(t/\mathrm{yr}) = -2.6$. In the very early stages, we observe a perfect fluid spectrum. Once the neutrons become superfluid, we find associated superfluid modes; the frequency of the superfluid $\bar{s}_0$-mode remains fairly constant whereas the higher order modes decrease in frequency as the superfluid region grows. In the grey shaded region, as long as we have another very thin superfluid layer, we find another superfluid mode which we name $\bar{s}_0^{\mathrm{II}}$. All modes exhibit avoided crossings.

slowly increases to 3.274 kHz while the superfluid region grows; however, its frequency is subject to only small variations throughout the neutron star's life. On the contrary, the higher order superfluid modes show a behaviour similar to that of the shear modes; when then superfluid layer is thin, they have a high frequency (the frequency of $\bar{s}_1$ lies at ≈ 20 kHz in the beginning) and the expansion of the superfluid region comes with a considerable decrease in frequency. We have no intuitive explanation as to why the lowest order superfluid mode, $\bar{s}_0$, displays such a different behaviour compared to the other superfluid modes; the same behaviour has been observed by Lin et. al [37] who investigated the spectrum of a neutron star with one superfluid layer at different temperatures. The pressure modes remain largely unaffected; however, they exhibit avoided crossings with the superfluid modes. Towards the right edge of the graph, we find, aside the well-known f- and p-modes, also the first seven superfluid modes. At this point, the neutron star core is entirely superfluid and the region of superfluidity

will not grow anymore; this is reflected by the fact that the frequencies of the superfluid modes are virtually unaffected in the upcoming stages of the neutron star's life.

The area shaded in grey covers the time period from about 4.4 hr to about 13.9 hr in our cooling sequence. This is the time during which the thin, superfluid layer at the crust-core boundary is still detached from the larger superfluid region deeper in the core (see Figure 4.17); the thickness of this layer (the part of it which lies within the core) can reach up to $\approx 54\,\mathrm{m}$. While this layer exists, we find one more superfluid mode in our spectrum just below the f-mode; its frequency monotonically increases from 1.514 kHz to 1.571 kHz. We name this mode $\bar{s}_0^{\mathrm{II}}$ since it is the superfluid mode of lowest order associated with the second superfluid layer. In fact, we would expect another full set of superfluid modes, however, the frequencies of the higher order modes exceed the frequency domain which we cover for our eigenmode search. The superfluid mode $\bar{s}_0^{\mathrm{II}}$ comes and goes as quickly as the thin layer appears, with no trace before or after.

The fact that the cut-off in our evolution graph is only briefly after the crust starts to solidify and when the shear modes start to enter the spectrum is no coincidence. Firstly, since we have the core and the crust completely decoupled in our neutron star model, there is not much exciting physics to be expected. It is straightforward to explain how the graph continues while the star matures; the fundamental, pressure and superfluid modes remain at (essentially) constant frequency since none of the physics relevant for these classes of modes (radii of star or superfluid region, sound speeds) is affected; this spectrum is then overlaid by the pure shear mode spectrum (see e.g. Figure 3.41, but remove the f- and p_1-mode from this graph). Finally, one only needs to account for the avoided crossings exhibited by the various modes. Secondly, we have severe difficulties in producing a well resolved graph, in particular for the time period $\log(t/\mathrm{yr}) \in [-2.3, 0]$ during which the crust quickly gains in width and in return the shear modes drop drastically in frequency. This undertaking was feasible for a perfect fluid core with only a few pressure modes but our endeavours were without success when accounting for a superfluid core; there are too many superfluid modes and subsequently avoided crossing which need to be resolved. A higher time resolution in the cooling sequence would be necessary. However, we content ourselves with the spectrum of a mature neutron star at an age of 10 years which we show in Figure 4.20; this spectrum provides evidence that our code is able to deal with realistic neutron star models which account for phase transitions, composition gradients, thermal pressure, an elastic crust as well as superfluidity using a realistic EoS in linearised general relativity.

4.11 Summary of Multi-Fluid Calculations

We have extended our work to account for superfluidity in neutron star cores. For this, we have laid out the derivation of the equations of motion, which describe the dynamics

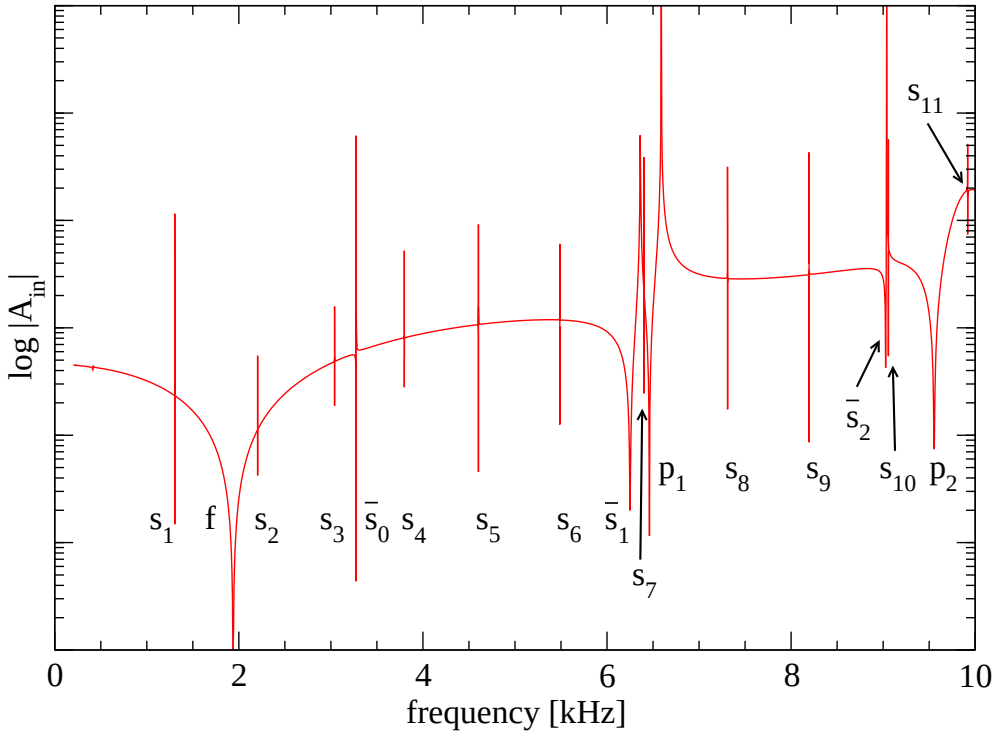

Figure 4.20: The spectrum of our model neutron star at an age of 10 years up to 10 kHz. We find the f-mode, the first two p-modes, the first three superfluid modes and the first eleven shear modes. The graph has been produced with an overall resolution of $\Delta f = 5.58\,\mathrm{Hz}$; in order to resolve the shear modes (which in some cases appear only as tiny blips at that resolution), we increased the resolution in their near environment up to $\Delta f = 4.5 \cdot 10^{-4}\,\mathrm{Hz}$. Note that while the two modes $\bar{s}_2$ and s_{10} cannot be resolved graphically here, they are easily distinguishable at higher resolution; they lie 28.7 Hz apart.

of multi-fluid systems, starting from a fundamental action principle. Guided by the calculation in [84], we extended previous work to account for the presence of leptons in the star's core which are locked to the protons. We derived equations of motions for a two-fluid system consisting of npeμ-matter where one fluid is made of the neutrons while the other fluid comprises the charged particles which are electromagnetically locked to each other.

As equation of state, we use the analytic representation of the SLy4 force as proposed by Chamel [38] which is well suited for the use in multi-fluid calculations since it provides all necessary coefficients and includes entrainment.

We derived the perturbation equations for a superfluid neutron star core; we find that when the background is assumed to be in β-equilibrium, variables associated with the leptons in the perturbation equations can be replaced by baryonic variables to large extent. The limiting cases of muon-free matter (as in the outer layers of the outer core) or even lepton-free matter (as an academic concept) can then easily be deduced.

The solid crust will be permeated by a neutron superfluid a sufficiently low tem-

peratures; we have derived a set of perturbation equations also for this case. An essential ingredient for the calculation of this particular region of the star, are the partial derivatives of the chemical potentials. While the equivalent quantities for neutron star cores have been published a few years ago, this is not the case for the crustal region. Chamel [94] kindly provided us with a set of values, however, temporal constraints did not allow us to produce reliable results in time for this thesis; we are currently working on this particular case.

We have revisited the junction condition problem within two-fluid systems. The issue with physically counter-intuitive results, as described in Section 3.6.4 for single fluid systems, persists. We proceeded in a similar way and considered each fluid in the multi-fluid system separately; we found a sufficient number of junction conditions based on physical arguments.

Our first results demonstrate numerically the equivalence of the DL85 formulation and the perturbation equations derived from the variational approach. We also compare our results for two-fluid systems against literature values and found excellent agreement. We calculated the damping times of the slowly damped modes; like in the single-fluid case, they are challenging to calculate. Our results suggest an exponential increase in damping time for the ordinary modes, while the damping times of the superfluid do not show a regular pattern.

The presence of leptons in the core is crucial for the determination of the low frequency spectrum of a superfluid neutron star; when we considered a bare superfluid neutron star core, we found that the presence of muons, which leads to an instrinsic stratification of the proton fluid, gives rise to g-modes in such stars. As expected (and mathematically argued) there are no g-modes in the spectrum of a muon-free neutron star core.

Finally, we attach the DH EoS for the crustal region of the neutron star to the core EoS and investigate the spectrum of a neutron star model, which we have constructed using a realistic EoS, accounting for density discontinuities, a stratified superfluid core, and thermal pressure in the elastic crust. The regions in which the core is superfluid and in which the crust is elastic are determined (automatically by our code) by making use of the Coulomb criterion for the crystallisation of the crust and using modern models for the superfluid energy gap. We find all expected modes in the spectrum; ordinary (f- and p-) modes, superfluid modes, gravity modes, shear modes and gravitational wave modes. The superfluid gap model we employ in conjunction with the thermal profiles suggest the formation of a second superfluid layer next to the core-crust boundary for a short period of time. This second superfluid layer gives rise to another set of superfluid modes; we locate the lowest order mode of this new set in our spectrum. The higher order modes have frequencies beyond our search range. We obtained the evolution of the high frequency domain of the spectrum from our simulations and find avoided crossings between ordinary and superfluid modes. Concerning older stars,

whose spectrum is vastly enriched by all types of oscillation modes, we are still able to clearly distinguish them.

The numerical limitations are identical to the single fluid case; we find a fairly sharp noise cut-off at low frequencies of about $10 - 20\,\mathrm{Hz}$ which makes the location of modes impossible; at the other end of the spectrum, we find weak noise entering at roughly $10 - 20\,\mathrm{kHz}$ which makes the eigenmode determination a bit more challenging but not impossible.

Chapter 5

Conclusion and Outlook

In this thesis, we have taken considerable steps towards the aim of developing the computational technology for the accurate determination of spectra of realistic neutron stars. While the different physical properties of neutron stars have been investigated regarding their impact on the stellar dynamics individually during the past decades, we have now taken many of them into account in a new comprehensive code written from scratch using modern coding practices. We have made the effort to introduce as few simplifications as possible or, where accurate data are not yet available, to implement the most recent results in such a way so that revised data can easily be accounted for. We make the widely used assumption that the deviations from equilibrium are small and we can, thus, linearise the Einstein equations.

Our numerical code produces satisfactory results for all kinds of modes under consideration. We give a comprehensive list here: we find the fundamental and pressure modes, accounting for space-time perturbations gives us gravitational wave modes, density discontinuities result in interface modes, stratification gives rise to composition gravity modes, the thermal pressure introduces thermal gravity modes, shear modes appear due to the elastic crust, and if we consider a superfluid core we find superfluid modes. The identification of all these oscillation modes works reliably to high accuracy; merely the low frequency spectrum is hidden to us due to numerical noise.

This leads us immediately to potential paths of continuation of this work. As for the modes present in our spectra, the origin of the new branch of fast damped w-modes which we discovered needs to be investigated to greater detail in order to ascertain either their physical existence or appearance as an artefact due to the particular numerical solution of the (exterior) problem. For slowly damped modes, it would be interesting to learn more about the damping times, in particular the irregular pattern that is displayed by the superfluid modes. We also encourage further research on the numerical noise that emerges in mode searches at low frequencies.

Apart from these improvements on the code, there are obviously other physical properties of the star which need to be taken into account. Most prominently (since

we have derived the equations already), the superfluidity of the free neutrons in the crustal region is the next natural step to take. In fact, we are currently implementing this feature and hope to obtain new results soon. For the sake of completeness, thermal pressure in the core of the multi-fluid star should also be taken into account, even though this will lead to only small corrections in the spectrum.

While our code incorporates a wide range of physics, we are still quite far from a fully realistic description. Most obvious in the list of neglected reality are magnetic fields and rotation. The latter not only strongly affects the mode spectrum in that it breaks the degeneracy of quadrupole (and higher order) modes and, of course, introduces a new family of oscillations driven by the Coriolis force, it also leads to the instability of particular oscillation classes which may be of high relevance for the explanation of the seemingly existent upper limit (notably lower than the Kepler limit) on observed rotation rates of neutron stars.

Furthermore, it is imperative when accounting for superfluidity to distinguish neutron Cooper pairs and proton Cooper pairs (and also the different states in which they can be found). This leads to the presence of regions in mature neutron stars which are near the superfluid transition; thermal effects may have significant impact on the dynamics of the system. Another direction of research concerns modifications of the background model; the spin-down of sufficiently mature stars inevitably leads to an increasingly strained crust. We have not taken this possiblity into account yet but this case certainly requires further consideration.

We have laid out a mathematical description of neutron star dynamics which incorporates many different aspects of neutron star physics; the used formalism explicitly allows for extension to include more physics. Accordingly, our code is written in such a way that it can accompany the gradual adolescence of the mathematical models. It provides the compulsory link between symbols and nature and once a reasonably accurate description of lifelike neutron stars has been developed, one is equipped with an efficient tool for calculating the spectra of realistic neutron star models which provide valuable information for the realisation of gravitational wave asteroseismology.

Appendix A

The Perturbations of the Conjugated Momenta

The variations of the momentum covectors μ^{x}_{ν} as given in (4.33) are

$$\delta\mu^{\mathrm{x}}_{\lambda} = \delta\mathcal{B}^{\mathrm{x}} n^{\mathrm{x}}_{\lambda} + \mathcal{B}^{\mathrm{x}}\delta n^{\mathrm{x}}_{\lambda} + \sum_{\mathrm{y}\neq\mathrm{x}} \left(\delta\mathcal{A}^{\mathrm{xy}} n^{\mathrm{y}}_{\lambda} + \mathcal{A}^{\mathrm{xy}}\delta n^{\mathrm{y}}_{\lambda}\right). \tag{A.1}$$

Our aim is to have $\delta\mu^{\mathrm{x}}_{\lambda}$ expressed solely in the variations $\delta n^{\mathrm{x}}_{\lambda}$ and $\delta g_{\mu\nu}$ since we know how to express these in terms of the displacement vectors and the metric perturbations. In order to achieve this, we need to rewrite the variations $\delta\mathcal{B}^{\mathrm{x}}$ and $\delta\mathcal{A}^{\mathrm{xy}}$ as

$$\delta\mathcal{B}^{\mathrm{x}} = \sum_{\mathrm{z}_1} \frac{\partial\mathcal{B}^{\mathrm{x}}}{\partial n^2_{\mathrm{z}_1}}\delta n^2_{\mathrm{z}_1} + \sum_{\mathrm{z}_1}\sum_{\mathrm{z}_2>\mathrm{z}_1} \frac{\partial\mathcal{B}^{\mathrm{x}}}{\partial n^2_{\mathrm{z}_1\mathrm{z}_2}}\delta n^2_{\mathrm{z}_1\mathrm{z}_2}, \tag{A.2}$$

$$\delta\mathcal{A}^{\mathrm{xy}} = \sum_{\mathrm{z}_1} \frac{\partial\mathcal{A}^{\mathrm{xy}}}{\partial n^2_{\mathrm{z}_1}}\delta n^2_{\mathrm{z}_1} + \sum_{\mathrm{z}_1}\sum_{\mathrm{z}_2>\mathrm{z}_1} \frac{\partial\mathcal{A}^{\mathrm{xy}}}{\partial n^2_{\mathrm{z}_1\mathrm{z}_2}}\delta n^2_{\mathrm{z}_1\mathrm{z}_2}. \tag{A.3}$$

For the sake of generality, we have used z_1 and z_2 as constituent indices. Even though these formulae are not very complicated, they already look messy. If we were to perfrom the whole calculation in full, we would end up with numerous triple sums and lengthy expressions which obscures the main purpose of this calculation. We will, therefore, resort to our special case of the four constituents n, p, e and μ for which the only non-vanishing entrainment parameter is $\mathcal{A}^{\mathrm{np}}$; the other five mixed coefficients are zero. We will also make use of the fact that

$$\mathcal{B}^{\mathrm{n}} = \mathcal{B}^{\mathrm{n}}(n^2_{\mathrm{n}}, n^2_{\mathrm{np}}, n^2_{\mathrm{p}}), \tag{A.4}$$

$$\mathcal{B}^{\mathrm{p}} = \mathcal{B}^{\mathrm{p}}(n^2_{\mathrm{n}}, n^2_{\mathrm{np}}, n^2_{\mathrm{p}}), \tag{A.5}$$

$$\mathcal{A}^{\mathrm{np}} = \mathcal{A}^{\mathrm{np}}(n^2_{\mathrm{n}}, n^2_{\mathrm{np}}, n^2_{\mathrm{p}}), \tag{A.6}$$

$$\mathcal{B}^{\mathrm{e}} = \mathcal{B}^{\mathrm{e}}(n^2_{\mathrm{e}}), \tag{A.7}$$

$$\mathcal{B}^{\mu} = \mathcal{B}^{\mu}(n^2_{\mu}), \tag{A.8}$$

which removes numerous partial derivatives from the calculation. In fact, we will show the calculation only for neutron momentum covector $\delta\mu^{\mathrm{n}}_{\nu}$ since the proton equivalent can simply be obtained by swapping n and p throughout the calculation and the leptonic covectors are special cases of vanishing entrainment coefficients.

First, we simplify (A.2) to

$$\delta\mathcal{B}^{\mathrm{n}} = \sum_{\mathrm{z=n,p}} \frac{\partial\mathcal{B}^{\mathrm{n}}}{\partial n^2_{\mathrm{z}}}\delta n^2_{\mathrm{z}} + \sum_{\mathrm{z_1=n,p}} \sum_{\mathrm{z_2}\neq\mathrm{z_1}} \frac{\partial\mathcal{B}^{\mathrm{n}}}{\partial n^2_{\mathrm{z_1 z_2}}}\delta n^2_{\mathrm{z_1 z_2}} \tag{A.9}$$

$$= \frac{\partial\mathcal{B}^{\mathrm{n}}}{\partial n^2_{\mathrm{n}}}\delta n^2_{\mathrm{n}} + \frac{\partial\mathcal{B}^{\mathrm{n}}}{\partial n^2_{\mathrm{p}}}\delta n^2_{\mathrm{p}} + \frac{\partial\mathcal{B}^{\mathrm{n}}}{\partial n^2_{\mathrm{np}}}\delta n^2_{\mathrm{np}}, \tag{A.10}$$

$$\delta\mathcal{A}^{\mathrm{np}} = \sum_{\mathrm{z=n,p}} \frac{\partial\mathcal{A}^{\mathrm{np}}}{\partial n^2_{\mathrm{z}}}\delta n^2_{\mathrm{z_1}} + \sum_{\mathrm{z_1=n,p}} \sum_{\mathrm{z_2}\neq\mathrm{z_1}} \frac{\partial\mathcal{A}^{\mathrm{np}}}{\partial n^2_{\mathrm{z_1 z_2}}}\delta n^2_{\mathrm{z_1 z_2}} \tag{A.11}$$

$$= \frac{\partial\mathcal{A}^{\mathrm{np}}}{\partial n^2_{\mathrm{n}}}\delta n^2_{\mathrm{n}} + \frac{\partial\mathcal{A}^{\mathrm{np}}}{\partial n^2_{\mathrm{p}}}\delta n^2_{\mathrm{p}} + \frac{\partial\mathcal{A}^{\mathrm{np}}}{\partial n^2_{\mathrm{np}}}\delta n^2_{\mathrm{np}}, \tag{A.12}$$

and then plug these into the expression for the variation of the momentum covector

$$\delta\mu^{\mathrm{n}}_{\lambda} = \delta\mathcal{B}^{\mathrm{n}} n^{\mathrm{n}}_{\lambda} + \mathcal{B}^{\mathrm{n}}\delta n^{\mathrm{n}}_{\lambda} + \delta\mathcal{A}^{\mathrm{np}} n^{\mathrm{p}}_{\lambda} + \mathcal{A}^{\mathrm{np}}\delta n^{\mathrm{p}}_{\lambda} \tag{A.13}$$

$$= \left(\frac{\partial\mathcal{B}^{\mathrm{n}}}{\partial n^2_{\mathrm{n}}}\delta n^2_{\mathrm{n}} + \frac{\partial\mathcal{B}^{\mathrm{n}}}{\partial n^2_{\mathrm{p}}}\delta n^2_{\mathrm{p}} + \frac{\partial\mathcal{B}^{\mathrm{n}}}{\partial n^2_{\mathrm{np}}}\delta n^2_{\mathrm{np}}\right) n^{\mathrm{n}}_{\lambda} + \mathcal{B}^{\mathrm{n}}\delta n^{\mathrm{n}}_{\lambda}$$
$$+ \left(\frac{\partial\mathcal{A}^{\mathrm{np}}}{\partial n^2_{\mathrm{n}}}\delta n^2_{\mathrm{n}} + \frac{\partial\mathcal{A}^{\mathrm{np}}}{\partial n^2_{\mathrm{p}}}\delta n^2_{\mathrm{p}} + \frac{\partial\mathcal{A}^{\mathrm{np}}}{\partial n^2_{\mathrm{np}}}\delta n^2_{\mathrm{np}}\right) n^{\mathrm{p}}_{\lambda} + \mathcal{A}^{\mathrm{np}}\delta n^{\mathrm{p}}_{\lambda} \tag{A.14}$$

Next, we make use of the identities

$$\delta n^2_{\mathrm{x}} = -\delta\left(n^{\mathrm{x}}_{\mu} n^{\mathrm{x}}_{\nu} g^{\mu\nu}\right) \tag{A.15}$$

$$= -2n^{\mu}_{\mathrm{x}}\delta n^{\mathrm{x}}_{\mu} + n^{\mu}_{\mathrm{x}} n^{\nu}_{\mathrm{x}}\delta g_{\mu\nu} \tag{A.16}$$

and similarly

$$\delta n^2_{\mathrm{xy}} = -n^{\mu}_{\mathrm{x}}\delta n^{\mathrm{y}}_{\mu} - n^{\mu}_{\mathrm{y}}\delta n^{\mathrm{x}}_{\mu} + n^{\mu}_{\mathrm{x}} n^{\nu}_{\mathrm{y}}\delta g_{\mu\nu}, \tag{A.17}$$

for which we have used the identity $\delta g^{\mu\nu} = -g^{\mu\lambda} g^{\nu\sigma}\delta g_{\lambda\sigma}$. After appropriate grouping, we arrive at

$$\delta\mu^{\mathrm{n}}_{\lambda} = -\left(2\frac{\partial\mathcal{B}^{\mathrm{n}}}{\partial n^2_{\mathrm{n}}} n^{\mathrm{n}}_{\lambda} n^{\mu}_{\mathrm{n}} + 2\frac{\partial\mathcal{A}^{\mathrm{np}}}{\partial n^2_{\mathrm{n}}} n^{\mathrm{p}}_{\lambda} n^{\mu}_{\mathrm{n}} + \frac{\partial\mathcal{B}^{\mathrm{n}}}{\partial n^2_{\mathrm{np}}} n^{\mathrm{n}}_{\lambda} n^{\mu}_{\mathrm{p}} + \frac{\partial\mathcal{A}^{\mathrm{np}}}{\partial n^2_{\mathrm{np}}} n^{\mathrm{p}}_{\lambda} n^{\mu}_{\mathrm{p}}\right)\delta n^{\mathrm{n}}_{\mu}$$
$$+ \left(\frac{\partial\mathcal{B}^{\mathrm{n}}}{\partial n^2_{\mathrm{n}}} n^{\mu}_{\mathrm{n}} n^{\nu}_{\mathrm{n}} + \frac{\partial\mathcal{B}^{\mathrm{n}}}{\partial n^2_{\mathrm{p}}} n^{\mu}_{\mathrm{p}} n^{\nu}_{\mathrm{p}} + \frac{\partial\mathcal{B}^{\mathrm{n}}}{\partial n^2_{\mathrm{np}}} n^{\mu}_{\mathrm{n}} n^{\nu}_{\mathrm{p}}\right) n^{\mathrm{n}}_{\lambda}\delta g_{\mu\nu} + \mathcal{B}^{\mathrm{n}}\delta n^{\mathrm{n}}_{\lambda}$$
$$- \left(2\frac{\partial\mathcal{B}^{\mathrm{n}}}{\partial n^2_{\mathrm{p}}} n^{\mathrm{n}}_{\lambda} n^{\mu}_{\mathrm{p}} + 2\frac{\partial\mathcal{A}^{\mathrm{np}}}{\partial n^2_{\mathrm{p}}} n^{\mathrm{p}}_{\lambda} n^{\mu}_{\mathrm{p}} + \frac{\partial\mathcal{B}^{\mathrm{n}}}{\partial n^2_{\mathrm{np}}} n^{\mathrm{n}}_{\lambda} n^{\mu}_{\mathrm{n}} + \frac{\partial\mathcal{A}^{\mathrm{np}}}{\partial n^2_{\mathrm{np}}} n^{\mathrm{p}}_{\lambda} n^{\mu}_{\mathrm{n}}\right)\delta n^{\mathrm{p}}_{\mu}$$
$$+ \left(\frac{\partial\mathcal{A}^{\mathrm{np}}}{\partial n^2_{\mathrm{n}}} n^{\mu}_{\mathrm{n}} n^{\nu}_{\mathrm{n}} + \frac{\partial\mathcal{A}^{\mathrm{np}}}{\partial n^2_{\mathrm{p}}} n^{\mu}_{\mathrm{p}} n^{\nu}_{\mathrm{p}} + \frac{\partial\mathcal{A}^{\mathrm{np}}}{\partial n^2_{\mathrm{np}}} n^{\mu}_{\mathrm{n}} n^{\nu}_{\mathrm{p}}\right) n^{\mathrm{p}}_{\lambda}\delta g_{\mu\nu} + \mathcal{A}^{\mathrm{np}}\delta n^{\mathrm{p}}_{\lambda} \tag{A.18}$$

We have now arrived at a point where the expression looks quite messy with no obvious possibility for further simplification.

As our aim is to find expressions for $\delta\mu^{\mathrm{n}}_{\lambda}$ for our particular system, we will now apply the appropriate values. First, we will calculate the spatial components of (A.18), i.e. $\lambda = i$. This leads very quickly to a simple expression since we have $n^{\mathrm{x}}_i = 0$. We find

$$\delta\mu^{\mathrm{n}}_i = \mathcal{B}^{\mathrm{n}}\delta n^{\mathrm{n}}_i + \mathcal{A}^{\mathrm{np}}\delta n^{\mathrm{p}}_i. \tag{A.19}$$

Let us now study the time component. The calculation will, unfortunately, not be as quick. As a very first step, we use that all number density currents have a time component only, $n^{\mu}_{\mathrm{x}} = n_{\mathrm{x}}(e^{-\nu/2}, 0, 0, 0)$,

$$\begin{aligned}
\delta\mu^{\mathrm{n}}_t = &+ \left(2\frac{\partial\mathcal{B}^{\mathrm{n}}}{\partial n^2_{\mathrm{n}}}n_{\mathrm{n}}n_{\mathrm{n}} + 2\frac{\partial\mathcal{A}^{\mathrm{np}}}{\partial n^2_{\mathrm{n}}}n_{\mathrm{p}}n_{\mathrm{n}} + \frac{\partial\mathcal{B}^{\mathrm{n}}}{\partial n^2_{\mathrm{np}}}n_{\mathrm{n}}n_{\mathrm{p}} + \frac{\partial\mathcal{A}^{\mathrm{np}}}{\partial n^2_{\mathrm{np}}}n_{\mathrm{p}}n_{\mathrm{p}}\right)\delta n^{\mathrm{n}}_t \\
&- \left(\frac{\partial\mathcal{B}^{\mathrm{n}}}{\partial n^2_{\mathrm{n}}}n_{\mathrm{n}}n_{\mathrm{n}} + \frac{\partial\mathcal{B}^{\mathrm{n}}}{\partial n^2_{\mathrm{p}}}n_{\mathrm{p}}n_{\mathrm{p}} + \frac{\partial\mathcal{B}^{\mathrm{n}}}{\partial n^2_{\mathrm{np}}}n_{\mathrm{n}}n_{\mathrm{p}}\right)e^{-\nu/2}n_{\mathrm{n}}\delta g_{tt} + \mathcal{B}^{\mathrm{n}}\delta n^{\mathrm{n}}_t \\
&+ \left(2\frac{\partial\mathcal{B}^{\mathrm{n}}}{\partial n^2_{\mathrm{p}}}n_{\mathrm{n}}n_{\mathrm{p}} + 2\frac{\partial\mathcal{A}^{\mathrm{np}}}{\partial n^2_{\mathrm{p}}}n_{\mathrm{p}}n_{\mathrm{p}} + \frac{\partial\mathcal{B}^{\mathrm{n}}}{\partial n^2_{\mathrm{np}}}n_{\mathrm{n}}n_{\mathrm{n}} + \frac{\partial\mathcal{A}^{\mathrm{np}}}{\partial n^2_{\mathrm{np}}}n_{\mathrm{p}}n_{\mathrm{n}}\right)\delta n^{\mathrm{p}}_t \\
&- \left(\frac{\partial\mathcal{A}^{\mathrm{np}}}{\partial n^2_{\mathrm{n}}}n_{\mathrm{n}}n_{\mathrm{n}} + \frac{\partial\mathcal{A}^{\mathrm{np}}}{\partial n^2_{\mathrm{p}}}n_{\mathrm{p}}n_{\mathrm{p}} + \frac{\partial\mathcal{A}^{\mathrm{np}}}{\partial n^2_{\mathrm{np}}}n_{\mathrm{n}}n_{\mathrm{p}}\right)e^{-\nu/2}n_{\mathrm{p}}\delta g_{tt} + \mathcal{A}^{\mathrm{np}}\delta n^{\mathrm{p}}_t
\end{aligned} \tag{A.20}$$

Next, we will replace δn^{x}_t by

$$\delta n^{\mathrm{x}}_t = \delta\left(n^{\mathrm{x}}u^{\mathrm{x}}_t\right) = n_{\mathrm{x}}\delta u^{\mathrm{x}}_t + u_t\delta n_{\mathrm{x}} = -e^{\nu/2}\delta n_{\mathrm{x}} + \frac{1}{2}e^{-\nu/2}n_{\mathrm{x}}\delta g_{tt} \tag{A.21}$$

This yields after cancellation and appropriate grouping

$$\begin{aligned}
\delta\mu^{\mathrm{n}}_t = &- \left(\mathcal{B} + 2\frac{\partial\mathcal{B}^{\mathrm{n}}}{\partial n^2_{\mathrm{n}}}n_{\mathrm{n}}n_{\mathrm{n}} + 2\frac{\partial\mathcal{A}^{\mathrm{np}}}{\partial n^2_{\mathrm{n}}}n_{\mathrm{p}}n_{\mathrm{n}} + \frac{\partial\mathcal{B}^{\mathrm{n}}}{\partial n^2_{\mathrm{np}}}n_{\mathrm{n}}n_{\mathrm{p}} + \frac{\partial\mathcal{A}^{\mathrm{np}}}{\partial n^2_{\mathrm{np}}}n_{\mathrm{p}}n_{\mathrm{p}}\right)e^{\nu/2}\delta n_{\mathrm{n}} \\
&+ \mathcal{B}^{\mathrm{n}}\frac{1}{2}e^{-\nu/2}n_{\mathrm{n}}\delta g_{tt} \\
&- \left(\mathcal{A}^{\mathrm{np}} + 2\frac{\partial\mathcal{B}^{\mathrm{n}}}{\partial n^2_{\mathrm{p}}}n_{\mathrm{n}}n_{\mathrm{p}} + 2\frac{\partial\mathcal{A}^{\mathrm{np}}}{\partial n^2_{\mathrm{p}}}n_{\mathrm{p}}n_{\mathrm{p}} + \frac{\partial\mathcal{B}^{\mathrm{n}}}{\partial n^2_{\mathrm{np}}}n_{\mathrm{n}}n_{\mathrm{n}} + \frac{\partial\mathcal{A}^{\mathrm{np}}}{\partial n^2_{\mathrm{np}}}n_{\mathrm{p}}n_{\mathrm{n}}\right)e^{\nu/2}\delta n_{\mathrm{p}} \\
&+ \mathcal{A}^{\mathrm{np}}\frac{1}{2}e^{-\nu/2}n_{\mathrm{p}}\delta g_{tt}.
\end{aligned} \tag{A.22}$$

Now, we define new variables

$$\mathcal{B}^{\mathrm{n}0}_{\ 0} = \mathcal{B} + 2\frac{\partial\mathcal{B}^{\mathrm{n}}}{\partial n^2_{\mathrm{n}}}n_{\mathrm{n}}n_{\mathrm{n}} + 2\frac{\partial\mathcal{A}^{\mathrm{np}}}{\partial n^2_{\mathrm{n}}}n_{\mathrm{p}}n_{\mathrm{n}} + \frac{\partial\mathcal{B}^{\mathrm{n}}}{\partial n^2_{\mathrm{np}}}n_{\mathrm{n}}n_{\mathrm{p}} + \frac{\partial\mathcal{A}^{\mathrm{np}}}{\partial n^2_{\mathrm{np}}}n_{\mathrm{p}}n_{\mathrm{p}}, \tag{A.23a}$$

$$\mathcal{A}^{\mathrm{np}0}_{\ 0} = \mathcal{A}^{\mathrm{np}} + 2\frac{\partial\mathcal{B}^{\mathrm{n}}}{\partial n^2_{\mathrm{p}}}n_{\mathrm{n}}n_{\mathrm{p}} + 2\frac{\partial\mathcal{A}^{\mathrm{np}}}{\partial n^2_{\mathrm{p}}}n_{\mathrm{p}}n_{\mathrm{p}} + \frac{\partial\mathcal{B}^{\mathrm{n}}}{\partial n^2_{\mathrm{np}}}n_{\mathrm{n}}n_{\mathrm{n}} + \frac{\partial\mathcal{A}^{\mathrm{np}}}{\partial n^2_{\mathrm{np}}}n_{\mathrm{p}}n_{\mathrm{n}}, \tag{A.23b}$$

and equivalent variables $\mathcal{B}^{\mathrm{x}}$ for $\mathrm{x} = \mathrm{p}, \mathrm{e}, \mu$, which allow us to write the variation of the

momentum covectors in the compact form

$$\delta\mu_t^{\mathrm{n}} = -e^{\nu/2}\left[\mathcal{B}^{\mathrm{n}0}{}_0\delta n_{\mathrm{n}} + \mathcal{A}^{\mathrm{np}0}{}_0\delta n_{\mathrm{p}}\right] + \frac{1}{2}\mu_{\mathrm{n}}e^{-\nu/2}\delta g_{tt}, \tag{A.24}$$

$$\delta\mu_t^{\mathrm{p}} = -e^{\nu/2}\left[\mathcal{B}^{\mathrm{p}0}{}_0\delta n_{\mathrm{p}} + \mathcal{A}^{\mathrm{np}0}{}_0\delta n_{\mathrm{n}}\right] + \frac{1}{2}\mu_{\mathrm{p}}e^{-\nu/2}\delta g_{tt}, \tag{A.25}$$

$$\delta\mu_t^{\mathrm{e}} = -e^{\nu/2}\mathcal{B}^{\mathrm{e}0}{}_0\delta n_{\mathrm{e}} + \frac{1}{2}\mu_{\mathrm{e}}e^{-\nu/2}\delta g_{tt}, \tag{A.26}$$

$$\delta\mu_t^{\mu} = -e^{\nu/2}\mathcal{B}^{\mu 0}{}_0\delta n_{\mu} + \frac{1}{2}\mu_{\mu}e^{-\nu/2}\delta g_{tt}, \tag{A.27}$$

We arrive at another very important result if we calculate the variation of the chemical potential. We do this exemplary for the neutron chemical potential, but equivalent statements hold for the other species, too. We have

$$\delta\mu_t^{\mathrm{n}} = \delta\left(\mu_{\mathrm{n}}u_t\right) = u_t\delta\mu_{\mathrm{n}} + \mu_{\mathrm{n}}\frac{1}{2}u^t\delta g_{tt}, \tag{A.28}$$

which we can use to in conjunction with (A.24) to solve for $\delta\mu_{\mathrm{n}}$. We find

$$\delta\mu_{\mathrm{n}} = \mathcal{B}^{\mathrm{n}0}{}_0\delta n_{\mathrm{n}} + \mathcal{A}^{\mathrm{np}0}{}_0\delta n_{\mathrm{p}}. \tag{A.29}$$

This immediately tells us that we can abandon the complicated expressions (A.23) for $\mathcal{B}^{\mathrm{x}0}_{\ 0}$ and $\mathcal{A}^{\mathrm{xy}0}_{\ 0}$ if we have access to the partial derivatives of the chemical potentials since we can identify (in general)

$$\frac{\partial\mu_{\mathrm{x}}}{\partial n_{\mathrm{x}}} = \mathcal{B}^{\mathrm{x}0}_{\ 0} \quad \text{and} \quad \frac{\partial\mu_{\mathrm{x}}}{\partial n_{\mathrm{y}}} = \mathcal{A}^{\mathrm{xy}0}_{\ 0}. \tag{A.30}$$

Note that it is necessary to have knowledge about the chemical potentials of the species *away* from chemical equilibrium in order to correctly calculate these partial derivatives.

Bibliography

[1] C. J. Krüger, W. C. G. Ho, and N. Andersson. Seismology of adolescent neutron stars: Accounting for thermal effects and crust elasticity. *ArXiv e-prints*, February 2014.

[2] J. M. Weisberg, J. H. Taylor, and L. A. Fowler. Gravitational waves from an orbiting pulsar. *Scientific American*, 245:74–82, October 1981.

[3] J. M. Weisberg, D. J. Nice, and J. H. Taylor. Timing Measurements of the Relativistic Binary Pulsar PSR B1913+16. *ApJ*, 722:1030–1034, October 2010.

[4] J. Goodricke and J. Bayer. A Series of Observations on, and a Discovery of, the Period of the Variation of the Light of the Star Marked δ by Bayer, Near the Head of Cepheus. In a Letter from John Goodricke, Esq. to Nevil Maskelyne, D. D. F. R. S. and Astronomer Royal. *Royal Society of London Philosophical Transactions Series I*, 76:48–61, 1786.

[5] A. S. Eddington. Stars, Gaseous, On the pulsations of a gaseous star. *MNRAS*, 79:2–22, November 1918.

[6] A. G. Kosovichev, J. Schou, P. H. Scherrer, P. H. Goode, W. A. Dziembowski, E. J. Rhodes, Jr., and SOI Structure Inversion Team. Spherical and aspherical structure of the sun: First year of SOHO/MDI observations. In F.-L. Deubner, J. Christensen-Dalsgaard, and D. Kurtz, editors, *New Eyes to See Inside the Sun and Stars*, volume 185 of *IAU Symposium*, page 157, 1998.

[7] L. Samuelsson and N. Andersson. Neutron star asteroseismology. Axial crust oscillations in the Cowling approximation. *MNRAS*, 374:256–268, January 2007.

[8] H. Sotani, K. D. Kokkotas, and N. Stergioulas. Torsional oscillations of relativistic stars with dipole magnetic fields. *MNRAS*, 375:261–277, February 2007.

[9] Y. Levin. QPOs during magnetar flares are not driven by mechanical normal modes of the crust. *MNRAS*, 368:L35–L38, May 2006.

[10] Y. Levin. On the theory of magnetar QPOs. *MNRAS*, 377:159–167, May 2007.

[11] H. Sotani, K. D. Kokkotas, and N. Stergioulas. Alfvén quasi-periodic oscillations in magnetars. *MNRAS*, 385:L5–L9, March 2008.

[12] H. Sotani, A. Colaiuda, and K. D. Kokkotas. Constraints on the magnetic field geometry of magnetars. *MNRAS*, 385:2161–2165, April 2008.

[13] A. Colaiuda, H. Beyer, and K. D. Kokkotas. On the quasi-periodic oscillations in magnetars. *MNRAS*, 396:1441–1448, July 2009.

[14] P. Cerdá-Durán, N. Stergioulas, and J. A. Font. Alfvén QPOs in magnetars in the anelastic approximation. *MNRAS*, 397:1607–1620, August 2009.

[15] S. K. Lander, D. I. Jones, and A. Passamonti. Oscillations of rotating magnetized neutron stars with purely toroidal magnetic fields. *MNRAS*, 405:318–328, June 2010.

[16] M. Gabler, P. Cerdá-Durán, N. Stergioulas, J. A. Font, and E. Müller. Imprints of Superfluidity on Magnetoelastic Quasiperiodic Oscillations of Soft Gamma-Ray Repeaters. *Physical Review Letters*, 111(21):211102, November 2013.

[17] K. S. Thorne and A. Campolattaro. Non-Radial Pulsation of General-Relativistic Stellar Models. I. Analytic Analysis for L $\geq$ 2. *ApJ*, 149:591, September 1967.

[18] L. Lindblom and S. L. Detweiler. The quadrupole oscillations of neutron stars. *ApJS*, 53:73–92, September 1983.

[19] S. Detweiler and L. Lindblom. On the nonradial pulsations of general relativistic stellar models. *ApJ*, 292:12–15, May 1985.

[20] T. G. Cowling. The non-radial oscillations of polytropic stars. *MNRAS*, 101:367–+, 1941.

[21] K. D. Kokkotas and B. F. Schutz. W-modes - A new family of normal modes of pulsating relativistic stars. *MNRAS*, 255:119–128, March 1992.

[22] M. Leins, H.-P. Nollert, and M. H. Soffel. Nonradial oscillations of neutron stars: A new branch of strongly damped normal modes. *Phys. Rev. D*, 48:3467–3472, October 1993.

[23] A. Reisenegger and P. Goldreich. A new class of g-modes in neutron stars. *ApJ*, 395:240–249, August 1992.

[24] A. Passamonti, B. Haskell, N. Andersson, D. I. Jones, and I. Hawke. Oscillations of rapidly rotating stratified neutron stars. *MNRAS*, 394:730–741, April 2009.

[25] E. Gaertig and K. D. Kokkotas. Relativistic g-modes in rapidly rotating neutron stars. *Phys. Rev. D*, 80(6):064026, September 2009.

[26] L. S. Finn. G-modes of non-radially pulsating relativistic stars - The slow-motion formalism. *MNRAS*, 222:393–416, September 1986.

[27] L. S. Finn. G-modes in zero-temperature neutron stars. *MNRAS*, 227:265–293, July 1987.

[28] T. E. Strohmayer. Density Discontinuities and the g-Mode Oscillation Spectra of Neutron Stars. *ApJ*, 417:273, November 1993.

[29] H. Sotani, K. Tominaga, and K.-I. Maeda. Density discontinuity of a neutron star and gravitational waves. *Phys. Rev. D*, 65(2):024010, January 2002.

[30] G. Miniutti, J. A. Pons, E. Berti, L. Gualtieri, and V. Ferrari. Non-radial oscillation modes as a probe of density discontinuities in neutron stars. *MNRAS*, 338:389–400, January 2003.

[31] B. L. Schumaker and K. S. Thorne. Torsional oscillations of neutron stars. *MNRAS*, 203:457–489, May 1983.

[32] L. S. Finn. Non-radial pulsations of neutron stars with a crust. *MNRAS*, 245:82–91, July 1990.

[33] L. Samuelsson and N. Andersson. Axial quasi-normal modes of neutron stars: accounting for the superfluid in the crust. *Classical and Quantum Gravity*, 26(15):155016, August 2009.

[34] P. S. Shternin, D. G. Yakovlev, C. O. Heinke, W. C. G. Ho, and D. J. Patnaude. Cooling neutron star in the Cassiopeia A supernova remnant: evidence for superfluidity in the core. *MNRAS*, 412:L108–L112, March 2011.

[35] G. L. Comer, D. Langlois, and L. M. Lin. Quasinormal modes of general relativistic superfluid neutron stars. *Phys. Rev. D*, 60(10):104025, November 1999.

[36] N. Andersson, G. L. Comer, and D. Langlois. Oscillations of general relativistic superfluid neutron stars. *Phys. Rev. D*, 66(10):104002, November 2002.

[37] L.-M. Lin, N. Andersson, and G. L. Comer. Oscillations of general relativistic multifluid/multilayer compact stars. *Phys. Rev. D*, 78(8):083008, October 2008.

[38] N. Chamel. Two-fluid models of superfluid neutron star cores. *MNRAS*, 388:737–752, August 2008.

[39] D. I. Jones, N. Andersson, and N. Stergioulas. Time evolution of the linear perturbations of a rotating Newtonian polytrope. *MNRAS*, 334:933–940, August 2002.

[40] E. Gaertig and K. D. Kokkotas. Oscillations of rapidly rotating relativistic stars. *Phys. Rev. D*, 78(6):064063, September 2008.

[41] W. Kastaun. Inertial modes of rigidly rotating neutron stars in Cowling approximation. *Phys. Rev. D*, 77(12):124019–+, June 2008.

[42] C. Krüger, E. Gaertig, and K. D. Kokkotas. Oscillations and instabilities of fast and differentially rotating relativistic stars. *Phys. Rev. D*, 81(8):084019, April 2010.

[43] S. Chandrasekhar. Solutions of Two Problems in the Theory of Gravitational Radiation. *Phys. Rev. Lett.*, 24(11):611–615, March 1970.

[44] J. L. Friedman and B. F. Schutz. Secular instability of rotating Newtonian stars. *ApJ*, 222:281–296, May 1978.

[45] D. D. Doneva, E. Gaertig, K. D. Kokkotas, and C. Krüger. Gravitational wave asteroseismology of fast rotating neutron stars with realistic equations of state. *Phys. Rev. D*, 88(4):044052, August 2013.

[46] N. Stergioulas, T. A. Apostolatos, and J. A. Font. Non-linear pulsations in differentially rotating neutron stars: mass-shedding-induced damping and splitting of the fundamental mode. *MNRAS*, 352:1089–1101, August 2004.

[47] B. Zink, O. Korobkin, E. Schnetter, and N. Stergioulas. Frequency band of the f-mode Chandrasekhar-Friedman-Schutz instability. *Phys. Rev. D*, 81(8):084055, April 2010.

[48] H. Dimmelmeier, N. Stergioulas, and J. A. Font. Non-linear axisymmetric pulsations of rotating relativistic stars in the conformal flatness approximation. *MNRAS*, 368:1609–1630, June 2006.

[49] K. H. Lockitch, N. Andersson, and J. L. Friedman. Rotational modes of relativistic stars: Analytic results. *Phys. Rev. D*, 63(2):024019, January 2001.

[50] K. H. Lockitch, J. L. Friedman, and N. Andersson. Rotational modes of relativistic stars: Numerical results. *Phys. Rev. D*, 68(12):124010, December 2003.

[51] A. Stavridis, A. Passamonti, and K. Kokkotas. Nonradial oscillations of slowly and differentially rotating compact stars. *Phys. Rev. D*, 75(6):064019–+, March 2007.

[52] A. Passamonti, A. Stavridis, and K. D. Kokkotas. Nonaxisymmetric oscillations of differentially rotating relativistic stars. *Phys. Rev. D*, 77(2):024029–+, January 2008.

[53] W. Ho. private communication.

[54] E. H. Gudmundsson, C. J. Pethick, and R. I. Epstein. Structure of neutron star envelopes. *ApJ*, 272:286–300, September 1983.

[55] C. J. Jog and R. A. Smith. Mixed lattice phases in cold dense matter. *ApJ*, 253:839–841, February 1982.

[56] F. Douchin and P. Haensel. A unified equation of state of dense matter and neutron star structure. *A&A*, 380:151–167, December 2001.

[57] Samuelsson, L. *Stellar Models in General Relativity.* PhD thesis, Stockholm University, sep 2003.

[58] G. Baym and D. Pines. Neutron starquakes and pulsar speedup. *Annals of Physics*, 66:816–835, 1971.

[59] G. Shen, C. J. Horowitz, and S. Teige. New equation of state for astrophysical simulations. *Phys. Rev. C*, 83(3):035802, March 2011.

[60] W. C. G. Ho, K. Glampedakis, and N. Andersson. Magnetars: super(ficially) hot and super(fluid) cool. *MNRAS*, 422:2632–2641, May 2012.

[61] N. Andersson, K. D. Kokkotas, and B. F. Schutz. A new numerical approach to the oscillation modes of relativistic stars. *MNRAS*, 274:1039–1048, June 1995.

[62] N. Andersson, K. D. Kokkotas, and B. F. Schutz. Space-time modes of relativistic stars. *MNRAS*, 280:1230–1234, June 1996.

[63] F. Frescura and C. Engelbrecht. Stellar perturbations via Lie derivatives. unpublished oral presentation, July 2011.

[64] T. Regge and J. A. Wheeler. Stability of a Schwarzschild Singularity. *Physical Review*, 108:1063–1069, November 1957.

[65] S. L. Detweiler and J. R. Ipser. A Variational Principle and a Stability Criterion for the Non-Radial Modes of Pulsation of Stellar Models in General Relativity. *ApJ*, 185:685–708, October 1973.

[66] M. Prakash, I. Bombaci, M. Prakash, P. J. Ellis, J. M. Lattimer, and R. Knorren. Composition and structure of protoneutron stars. *Phys. Rep.*, 280:1–77, 1997.

[67] J. M. Lattimer, C. J. Pethick, D. G. Ravenhall, and D. Q. Lamb. Physical properties of hot, dense matter: The general case. *Nucl. Phys. A*, 432:646–742, 1985.

[68] N. Chamel and P. Haensel. Entrainment parameters in a cold superfluid neutron star core. *Phys. Rev. C*, 73(4):045802, April 2006.

[69] M. Prakash, T. L. Ainsworth, J. P. Blaizot, and H. Wolter. Features of hot dense nuclear matter. In *Windsurfing the Fermi Sea*, pages 357–381, 1987.

[70] R. T. Farouki and S. Hamaguchi. Thermal energy of the crystalline one-component plasma from dynamical simulations. *Phys. Rev. E*, 47:4330–4336, June 1993.

[71] C. W. Misner, K. S. Thorne, and J. A. Wheeler. *Gravitation.* W. H. Freeman, 1973.

[72] B. F. Schutz. Junction conditions across perturbed contact discontinuities. *MNRAS*, 192:503, August 1980.

[73] E. D. Fackerell. Solutions of Zerilli's Equation for Even-Parity Gravitational Perturbations. *ApJ*, 166:197, May 1971.

[74] S. Chandrasekhar. On the Equations Governing the Perturbations of the Schwarzschild Black Hole. *Royal Society of London Proceedings Series A*, 343:289–298, May 1975.

[75] S. Chandrasekhar. *The mathematical theory of black holes.* New York : Oxford University Press, 1992.

[76] H. Sundqvist and G. Veronis. A simple finite-difference grid with non-constant intervals. *Tellus*, 22:26, 1970.

[77] E. Balbinski, S. Detweiler, L. Lindblom, and B. F. Schutz. The accuracy of the quadrupole approximation for the gravitational radiation from pulsating stars. *MNRAS*, 213:553–561, April 1985.

[78] Y. Kojima. Two Families of Normal Modes in Relativistic Stars. *Progress of Theoretical Physics*, 79:665–675, March 1988.

[79] R. F. Tooper. Adiabatic Fluid Spheres in General Relativity. *ApJ*, 142:1541, November 1965.

[80] W. H. Press, S. A. Teukolsky, W. T. Vetterling, and B. P. Flannery. *Numerical recipes in C++ : the art of scientific computing.* Cambridge University Press, 2002.

[81] V. Ferrari and M. Germano. Scattering of Gravitational Waves by Newtonian Stars. *Royal Society of London Proceedings Series A*, 444:389–398, February 1994.

[82] N. Andersson and G. L. Comer. On the dynamics of superfluid neutron star cores. *MNRAS*, 328:1129–1143, December 2001.

[83] P. N. McDermott, H. M. van Horn, and C. J. Hansen. Nonradial oscillations of neutron stars. *ApJ*, 325:725–748, February 1988.

[84] N. Andersson and G. L. Comer. Relativistic Fluid Dynamics: Physics for Many Different Scales. *Living Reviews in Relativity*, 10:1, January 2007.

[85] M. Prakash, J. M. Lattimer, and T. L. Ainsworth. Equation of state and the maximum mass of neutron stars. *Physical Review Letters*, 61:2518–2521, November 1988.

[86] G. L. Comer and R. Joynt. Relativistic mean field model for entrainment in general relativistic superfluid neutron stars. *Phys. Rev. D*, 68(2):023002, July 2003.

[87] D. G. Yakovlev, A. D. Kaminker, O. Y. Gnedin, and P. Haensel. Neutrino emission from neutron stars. *Phys. Rep.*, 354:1–155, November 2001.

[88] L. Villain and P. Haensel. Non-equilibrium beta processes in superfluid neutron star cores. *A&A*, 444:539–548, December 2005.

[89] A. D. Kaminker, P. Haensel, and D. G. Yakovlev. Nucleon superfluidity vs. observations of cooling neutron stars. *A&A*, 373:L17–L20, July 2001.

[90] N. Andersson, G. L. Comer, and K. Glampedakis. How viscous is a superfluid neutron star core? *Nuclear Physics A*, 763:212–229, December 2005.

[91] M. E. Gusakov and E. M. Kantor. Velocity-dependent energy gaps and dynamics of superfluid neutron stars. *MNRAS*, 428:L26–L30, January 2013.

[92] M. Karlovini and L. Samuelsson. Elastic stars in general relativity: I. Foundations and equilibrium models. *Classical and Quantum Gravity*, 20:3613–3648, August 2003.

[93] N. Andersson. private communication.

[94] N. Chamel. private communication.